WARWICK
THE UNIVERSITY OF WARWICK

3D coupled pore-network modelling of flow and solute transport through porous media, from laminar to turbulent flow

by

Amr A. El-Zehairy

A thesis submitted in partial fulfilment of the requirements
for the degree of

Doctor of Philosophy in Engineering

University of Warwick, Department of Engineering

January 2020

Table of Contents

List of figures

List of tables

In Table 5-3, different porous media with different properties are presented, therefore, the presented Darcy permeability (K_D) and Reynold's number values are not expected to match with each other. For instance, when the average bead diameter of the sample increases, the permeability (K_D) increases as it is easier for the flow to move through the medium. Moreover,

Acknowledgements

I would like to thank my supervisors, Dr Mohaddeseh Mousavi Nezhad and Professor Ian Guymer for what they have done. Dr Vahid Niasar is acknowledged for his support. Professor Mark Williams and Dr Nadia Kourra are acknowledged for doing the CT-scanning of the porous medium used in the experiments.

Dr Bagus Muljadi, Dr Ali Raeini and Professor Marin Blunt are acknowledged for providing the pore-network extraction code and part of the CT- images used in this study.

I also would like to thank Dr Branko Bijeljic from Imperial College and Professor Michael Chappell from the University of Warwick for reviewing and examining my dissertation.

The financial support from the Newton-Mosharafa programme, which is a collaboration between the British Council and the Egyptian Ministry of Higher Education, is acknowledged.

My gratitude extends to my parents, brothers and the whole family who supported me during this journey. My friends Karim Adel, Mohamed Taha, Ahmed Eissa, Ahmed Khaled, Zeina AL-Nabulsi, Mihaela Porumb, Mohamed Elghorab, Lijuan Liu, Yanjie Zhu, Stela Makri and Vasiliki Ioannidou are acknowledged for their useful discussions.

Mr Ian Baylis and Ms Kerrie Hatton are acknowledged for the technical and administrative support.

Declaration

This thesis is submitted to the University of Warwick in support of my application for the degree of Doctor of Philosophy. I declare that the work in this thesis has been composed by myself and no portion of this work has been submitted in support of an application for another degree at any other university or institute. The work has been my own except where indicated.

List of journal publications as a result of this work

El-Zehairy, A. A., Nezhad, M. M., Joekar-Niasar, V., Guymer, I., Kourra, N., & Williams, M. A. (2019). Pore-network modelling of non-Darcy flow through heterogeneous porous media. Advances in Water Resources, 131, 103378. doi: https://doi.org/10.1016/j.advwatres.2019.103378

El-Zehairy, A. A., Nezhad, M. M., Joekar-Niasar, V. (2019). Pore-network modelling of solute transport in Newtonian non-Darcy flow in porous media. (to be submitted)

Abstract

Subsurface hydrology including flow and solute transport modelling is essential for designing many engineering processes such as seepage, remediation of contaminated groundwater, improved oil recovery, etc. The processes involved in such activities are observed across a wide range of length and timescales; from nanometres to kilometres and from nanoseconds to years. The recent growth in imaging technologies has shown that the size of a single pore in a porous medium may range from 0.1 nm to a few centimetres (Marry & Rotenberg, 2015). Therefore, to perform reliable field-scale simulations, a deep understanding of the processes happening at the pore-scale level and their consequences at larger scales is needed (Mehmani, 2014). Most of the previous work that modelled flow and solute transport at the pore-scale assumed laminar flow and applied Darcy's law. However, in some cases, such as the flow of gases through porous media, flow near wellbores, and flow through the hyporheic zone, non-Darcy flow can be observed. It is not clear how solute transport processes are affected by the flow behaviour in the non-Darcy (Forchheimer) and turbulent flow regimes. In this work, a pore-network model (PNM) capable of simulating flow and solute transport within the Darcy, Forchheimer and turbulent flow regimes was developed. One of the aims of this work is to determine the onset of non-Darcy flow and the onset of turbulence, after which Darcy's law loses its validity. Using PNM, any porous medium can be simplified into large pores connected to each other's by narrow pores, then analytical or semi-analytical equations can be implemented to model the flow and transport processes through the medium. The proposed model was verified against experimental data of a packed spheres sample and other data in the literature. X-ray Computed Tomography scans of the packed spheres, sandstone and carbonate samples were used to extract the equivalent pore-network. It was found that the onset of non-Darcy flow is highly dependent on the medium degree of heterogeneity, and in heterogeneous media, the onset velocity could be up to three orders of magnitude smaller compared to the homogenous media. In porous media with coarse particles, the assumption of fully developed flow in each pore is not valid and using the Hagen-Poiseuille equation does not predict the flow behaviour properly. After the onset of non-Darcy flow, if Darcy's law is applied, this causes overestimation (up to ~10 times) of the Péclet number and the longitudinal dispersion coefficient (D_L). In the turbulent flow regime, D_L increased, due to the effect of turbulent diffusion, by a factor up to 1.6 compared to the D_L value obtained under the Forchheimer flow conditions.

Nomenclature

A	Sample cross-sectional area
A_1	Coefficient of X^2 in the quadratic equation $A_1 X^2 + A_2 X + A_3 = 0.0$
A_2	Coefficient of X in the quadratic equation $A_1 X^2 + A_2 X + A_3 = 0.0$
A_3	The constant term in the quadratic equation $A_1 X^2 + A_2 X + A_3 = 0.0$
$A`$	Ergun equation first constant
a	Pore cross-sectional area
a_{i}	Cross-sectional area of pore body i
$a_{\mathrm{i-j}}$	Cross-sectional areas of the pore throat that connects the two connected pore bodies i and j
$B`$	Ergun equation second constant
BTC	Breakthrough curve
C	Concentration
C_i	Concentration at pore-unit i
C_o	Concentration of injected solute
$\bar{C}$	Average concentration
Cc	Dimensionless jet contraction-area ratio (Vena-contraction)
d_{p}	Diameter of a spherical particle
d_{PTh}	Pore throat diameter
d_{m}	Mean beads diameter
d	Diameter
$d_{\mathrm{i-j}}$	Diameter of pore throat that connects the two pore bodies i and j
D_m	Coefficient of molecular diffusion
D^{eff}	Effective diffusion coefficient
D_{L}	Longitudinal dispersion coefficient
d_{l}	Largest diameter of the beads
d_s	Smallest diameter of the beads
F	Diffusive mass flux
F_{o}	Forchheimer number
f	Friction factor
f_{pore}	Pore Friction factor
g	The gravitational acceleration
g_{pore}	Pore conductance
$g_{\mathrm{i-j,tot}}$	Conductance of the pore throat and the two connected pore bodies i and j.
G	Shape factor
h	Head
J	Dispersion flux
k	A factor used to calculate the conductance and its value depends on the cross-sectional shapes of the pore

K_c	Contraction coefficient
kd	Dimensionless momentum coefficients
K_{D}	Medium Darcy permeability
K_e	Expansion coefficient
K_{F}	Medium Forchheimer permeability
$K_F^{`}$	Modified Forchheimer permeability
K_{app}	Apparent permeability
K^*	Dimensionless apparent permeability
$K_{\mathrm{i-j,tot}}$	Hydraulic conductivity of the pore throat and the two connected pore bodies i and j
L_{charc}	Characteristic length
L	Sample length
L_{i-j}	Pore throat length that connects the two connected pore bodies i and j
L_i	Pore body length
$L_{i-j,tot}$	Length of pore throat and the connected two pore bodies i and j
L_{h}	Length of the entrance region
L_{pore}	Pore length
L_{x}	Length in *x*-direction
L_{y}	Length in *y*-direction
L_{z}	Length in *z*-direction
N_x	Number of pore bodies in *x*-direction
N_y	Number of pore bodies *y*-direction
N_z	Number of pore bodies *z*-direction
N_{PB}	Number of pore bodies
N_{PTh}	Number of pore throats
$N_{\mathrm{i-j}}$	The coordination number of pore body i.
P	Pressure
PB	Pore body
PN	Pore-network
PNM	Pore-network model/modelling
PTh	Pore throat
Pe	Péclet number
P_{r}	Probability
ΔP_{i-j}^{tot}	Total pressure loss for any pore throat that connects the two pore bodies i and j
$\Delta P_{\mathrm{i-j,tot}}^{\mathrm{v}}$	Viscous pressure loss between the two pore bodies i and j
$\Delta P_{\mathrm{i-j,tot}}^{\mathrm{f}}$	Frictional pressure loss between the two pore bodies i and j
$\Delta P_{\mathrm{i-j}}^{\mathrm{exp}}$	Pressure loss due to expansion
$\Delta P_{\mathrm{i-j}}^{\mathrm{cont}}$	Pressure loss due to contraction
p	Perimeter

$p_{\mathrm{i-j}}$	Perimeter of pore throat that connects the two pore bodies i and j
q	Discharge
$q_{\mathrm{i-j}}$	Discharge through any pore throat that connects the two pore bodies i and j
r	Radius
$r_{\mathrm{i-j}}$	Radius of pore throat that connects the two pore bodies i and j
r_c	Radius of the largest inscribed circle
r_e	Radius of the circle that has area equal to the void area
r_{eff}	Effective radius
r_{pore}	Pore radius
r_{PTh}	Pore throat radius
$\mathrm{R.PB_{max}}$	Maximum pore body radius
$\mathrm{R.PB_{avg}}$	Average pore body radius
$\mathrm{R.PB_{min}}$	Minimum pore body radius
$\mathrm{R.PTh_{max}}$	Maximum pore throat radius
$\mathrm{R.PTh_{avg}}$	Average pore throat radius
$\mathrm{R.PTh_{min}}$	Minimum pore throat radius
REV	Representative elementary volume
Re	Reynold's number based on characteristic length
Re_K	Reynold's number based on fluid superficial velocity and the square root of the medium permeability
$\hat{R}e_K$	Reynold's number based on fluid interstitial velocity and the square root of the medium permeability
s_p	Sphericity
S_v	Medium specific surface area
t	Time
T	Dimensionless time
u	Intrinsic or interstitial velocity
u_{avg}	Average interstitial velocity
u_{x}	*x*-component of interstitial velocity
$u_{\mathrm{i-j}}$	Average fluid velocity through the pore throat that connects the two pore bodies i and j.
u_{L}	Average pore velocity in longitudinal direction
$u_{*\mathrm{i-j}}$	Shear velocity in pore throat that connects the two pore bodies i and j.
V	Volume
V_o	Voltage
v	Superficial velocity
$\boldsymbol{D}_{\mathrm{PTh}}^{\mathrm{eff}}$	Pore throat effective diffusion coefficients vector
$\boldsymbol{L}_{\mathrm{PTh}}$	Pore throat lengths vector
$\boldsymbol{V}_{\mathrm{PU}}$	Pore-unit volumes vector
$\boldsymbol{V}_{\mathrm{PTh}}$	Pore throat volumes vector

$\boldsymbol{q}_{\mathrm{PU}}$	Pore-unit total absolute discharges vector
$\boldsymbol{q}_{\mathrm{PTh}}$	Pore throat discharges vector
$\boldsymbol{t}_{\mathrm{PU}}$	Vector of pore-unit residence times
$\boldsymbol{t}_{\mathrm{PTh}}$	Vector of pore throat residence times based on advection.
$\grave{\boldsymbol{t}}_{\mathrm{PTh}}$	Vector of pore throat residence times based on dispersion.
$\boldsymbol{u}_{\mathrm{PTh}}$	Vector of average velocities through the pore throats
κ	Kozeny-Carman constant
ϕ	Medium porosity
κ_o	A factor used to calculate the effective diffusion coefficient and its value depends on the cross-sectional shapes of the pore
α	Dimensionless kinetic-energy coefficient
α_L	Longitudinal dynamic dispersivity
β	Non-Darcy (Forchheimer) coefficient
β`	Modified Non-Darcy (Forchheimer) coefficient
μ	Fluid dynamic viscosity
ρ	Fluid density
δ	Power law coefficient
γ	Fluid specific weight
ε	Surface roughness
σ	Standard deviation
σ^2	Variance
τ	Tortuosity

Chapter 1

Introduction

1.1 Motivations

Flow and solute transport modelling through porous media are of high interest to many researchers and can be used to mimic flow near groundwater wells, in hydraulic fractures and at the bottom of canals and water bodies. The zone underneath a water body or a stream bed, which is called the hyporheic zone, is subjected to many flow and biogeochemical exchange processes between the surface water and groundwater and has been the focus of much research (Winter et al., 1998). Such flow and transport processes can be observed across a wide range of length and timescales; from nanometres to kilometres and from nanoseconds to years (Figure 1-1). Reliable field-scale simulations are highly dependent on understanding the flow and transport processes happening at the pore-scale and their consequences at larger scales (Mehmani, 2014). Most of macro-scale models do not provide details about the basic processes and prevailing factors at the pore-scale (Meng & Yang, 2017). Some phenomena such as capillary pressure and solute dispersion cannot be understood from macro-scale simulations, but need initially to be understood at the pore-scale level (Bear & Cheng, 2010). Moreover, most of macro-scale models do not allow one to simulate the macroscopic behaviour as a result of changing the porous medium characteristics at the pore-scale, e.g. changing the pore size distribution (Sorbie et al., 1989). Most of the previous studies that modelled flow and solute transport, at the pore-scale, through porous media focused on Darcy flow and assumed that the relationship between the pressure gradient and discharge through the medium is linear. However, in some cases, such as the flow of gases through porous media, flow near a wellbore, flow through the hyporheic zone, and flow through coarse porous media, non-Darcy flow can be observed. It is not fully understood how solute transport processes are affected by the flow behaviour in the Forchheimer and turbulent flow regimes. Nevertheless, the effect of changing the pore

space structure and topology on flow and solute transport within the non-Darcy flow regime needs more investigations. In order to gain an in-depth understanding of these processes at the pore-scale, this research focuses on modelling single phase flow and solute transport in porous media within the Darcy, Forchheimer and turbulent macro-scale flow regimes. For this purpose, a pore-network modelling (PNM) approach has been chosen among other pore-scale simulation approaches as it is computationally less demanding and, in some cases, it can provide information that cannot be obtained by using other approaches (Joekar-Niasar & Hassanizadeh, 2012).

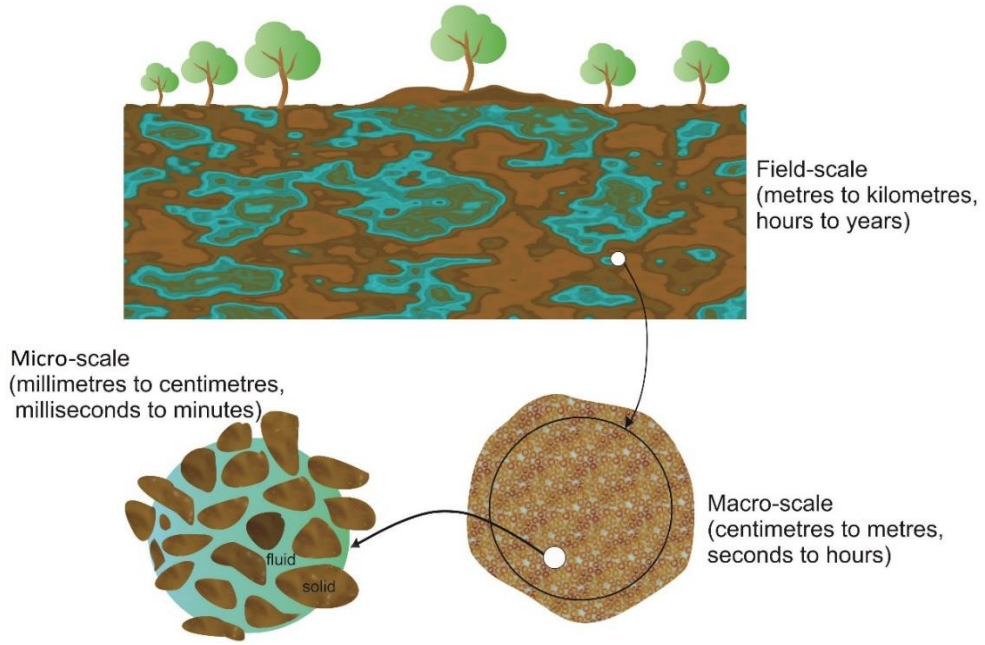

Figure 1-1 Different length and timescales for flow and transport processes through porous media, after Wood et al. (2007). In this work, pore scale is defined as the scale of a single pore in a medium, the micro-scale ranges from 0.5 to 5 mm, and the macro-scale ranges from 50 to 200 mm.

One of the applications of PNM is the process of geological carbon dioxide (CO_2) storage, in which CO_2 emissions from industrial factories are captured, compressed, transferred, injected and stored for hundreds or thousands of years in subsurface reservoirs such as depleted oil reservoirs. The aim of carbon dioxide storage is to reduce the greenhouse effect of CO_2 emissions and to enhance coal and natural gas productivity. The CO_2 injection process is performed at high pressure and temperature rates which makes it difficult to mimic experimentally, moreover, the process should be

designed in a way that does not allow CO_2 to escape from the pores of the reservoir. The CO_2 injection process into pores is affected by buoyance, capillary and viscosity forces, therefore, it requires a good understanding of the pore structures and the interplay between these forces. For such a case, PNM provides an affordable option for understanding and designing the process (Andrew et al., 2013; Ellis and Bazylak, 2012; Middleton et al., 2012).

1.2 Aims and Objectives

The main aim of this research is to gain an in-depth understanding of the effect of porous media structure and topology on the non-Darcy flow and pressure fields, and to assess the effect of turbulence and inertial force on the transport processes happening at the pore-scale and, accordingly, at the macro-scale. Special attention has been given to the macro-scale Forchheimer and turbulent flow regimes, as the laminar Darcy flow regime has been extensively studied by many research, (e.g. Bruderer & Bernabé, 2001; Bijeljic et al., 2004; Bijeljic & Blunt, 2007; Mehmani et al., 2014; Babaei & Joekar-Niasar, 2016). The main aim has been achieved by conducting the following specific tasks:

- Using Computed Tomography (CT) scans of micro-scale (0.5-5.0 mm) beadpacks, sandstone and carbonate samples to gain information about their micro-scale structure and to extract their equivalent pore-networks.
- Developing a pore-network model to simulate steady state single phase flow through porous media within different flow regimes (Darcy, Forchheimer and turbulent).
- Defining the boundaries between the different flow regimes.
- Verifying the developed pore-network flow model experimentally using macro-scale (50-200 mm) packed spheres samples and using available data in the literature.
- Coupling the flow simulation model with a solute transport model to simulate the transient propagation of conservative solutes through porous media.

- Verifying the solute transport model experimentally and using certain data from the literature.

1.3 Thesis Contents

This thesis is divided into eight chapters as follows:

Chapter 2 provides a detailed literature review including the modelling of fluid flow through porous media at the pore-scale and at the macro-scale, flow modelling and dispersion through a single capillary tube, defining the boundaries between different flow regimes in porous media and in a single capillary tube, simulating the transport of a conservative solute through porous media, different methods used to generate a pore-network equivalent to a specific medium, and defining some research gaps.

Chapter 3 shows the experimental setup of the flow and solute transport experiments, in addition to the details of sample preparation and CT-scanning of the porous medium used in the experiments.

Chapter 4 explains the developed pore-network model for simulating non-Darcy (Forchheimer) flow through porous media with different degrees of heterogeneity. In this chapter, the details of determining the onset of non-Darcy flow are presented.

Chapter 5 explains the developed general pore-network model for simulating the macro-scale Darcy, Forchheimer and turbulent flow regimes through porous media. It also presents the method followed to detect the boundaries between these different flow regimes.

Chapter 6 provides the details of solute transport modelling within the non-Darcy (Forchheimer) flow regime, and how the inertial forces affect the transport process.

Chapter 7 provides the details of a general solute transport pore-network model which is capable of simulating solute transport within all possible flow regimes.

Chapter 8 provides the final conclusions on the work performed and some proposed future work.

Chapter 2

Background and literature review

Experimental work needs time and effort, and in some cases, it may have limitations either due to difficulties or uncertainties in measuring some quantities as well as the complexity of the process. In such cases, computational methods can provide an alternative tool for achieving an insight into an understanding of the process. The computational methods used to study fluid flow in fully saturated porous media can be divided into macro-scale continuum models and pore-scale models. A key advantage of the pore-scale models is their capability in describing details of the physical and chemical processes occurring at the pore-scale, and their consequences at the micro and macro scales (Joekar-Niasar & Hassanizadeh, 2012).

In this Chapter, most of the previous work related to pore-scale and macro-scale flow modelling, the boundaries between different flow regimes, flow and dispersion through a single capillary tube, solute transport through porous media and different methods used to extract pore-networks are reviewed.

2.1 Flow modelling at the macro-scale

To simulate single phase, incompressible, fully saturated, steady flow through rigid porous media at the macro-scale, Darcy's law (Equation 2.1) (Darcy, 1856) is usually applied, neglecting the non-linear inertial effects according to Stokes law and assuming that the flow is in the laminar regime. Darcy's law, which is a linear relationship between the pressure gradient, $\frac{\Delta P}{L}$ $\left(\frac{\mathrm{Pa}}{\mathrm{mm}}\right)$, between two points separated by a distance, L (mm), and the flow superficial velocity, $v = \frac{q}{A}$ (mm/s), where q (mm^3/s) is the volumetric fluid discharge and A (mm^2) is the whole cross-sectional area perpendicular to the flow direction, is given by:

$$-\frac{\Delta P}{L} = \frac{\mu}{K_D} v \qquad 2.1$$

where ΔP (Pa) is the pressure loss over the length L, μ (Pa·s) is the fluid dynamic viscosity and K_D (mm^2) is the Darcy permeability.

However, for relatively high velocities, the above equation is not valid anymore, the inertial terms cannot be neglected and the relationship between the pressure gradient ($\frac{\Delta P}{L}$) and the flow superficial velocity (v) becomes non-linear (Muljadi et al., 2015). In other words, the flow regime changes from the laminar creeping flow regime (when viscous forces are dominant and larger if compared to the insignificant inertial forces, and Stokes law is applied (Kirby, 2010)) to the laminar non-Darcy flow regime which is also called the Forchheimer flow regime (Kececioglu & Jiang, 1994; Bağcı et al., 2014). In cases such as flow through the hyporheic zone, near groundwater wells, through fractures or porous domains with relatively high porosity (e.g. porous media composed of coarse sand or gravel particles) and the flow of gases through porous media, non-Darcy flow may be observed. For the non-Darcy flow regime, the well-known Forchheimer's equation is normally applied (Forchheimer, 1901). Forchheimer's equation (Equation 2.2) is an extension of Darcy's law which was developed by adding a quadratic velocity term to Darcy's equation in order to account for the non-linear inertial effects in the flow, as follows:

$$-\frac{\Delta P}{L} = \frac{\mu}{K_F} v + \rho \beta v^2 \qquad 2.2$$

where K_F (mm^2) is the Forchheimer permeability that is very close to, but not the same as, Darcy permeability (K_D) as will be shown later, ρ (Kg/m·mm^2) is the fluid density and β (mm^{-1}) is the non-Darcy coefficient which is also known as the Forchheimer coefficient and is a medium dependent parameter.

In porous media, the inertial effects can be expressed in the form of drag forces, and as was shown by experiments (Fand et al., 1987; Kececioglu & Jiang, 1994), the pressure loss in such cases is proportional to the summation of two terms (see Equation 2.2); one term includes the fluid velocity and represents the force exerted to overcome fluid viscosity, while the other term includes the squared value of fluid velocity and represents the

force exerted to overcome fluid and solid medium interactions. The second term represents the inertial effects which is a function of the medium geometry, permeability and Reynold's number (Vafai & Tien, 1981; Zeng & Grigg, 2006). These inertial effects are accounted for in the Navier-Stokes equations in terms of local and convective accelerations and they result from tortuosity and the diverging-converging nature of the medium (Balhoff & Wheeler, 2009). In Equation 2.2, the non-Darcy coefficient (β) accounts for the inertial effects due to convergence, divergence and tortuosity in the flow path geometry (Thauvin & Mohanty, 1998; Balhoff & Wheeler, 2009). Normally, the β coefficient and the onset of a non-Darcy flow regime are determined experimentally, whereas some authors developed empirical relationships that predict β as a function of the medium permeability, K_D (mm^2), porosity, ϕ (%) and tortuosity, τ (-). In order to determine β and K_F from Forchheimer's equation, a linearised form of Forchheimer's equation was proposed by Forchheimer (1901), which is presented in Equation 2.3.

$$\frac{\Delta P}{L\mu v} = \frac{1}{K_{app}} = \frac{1}{K_F} + \beta\frac{\rho v}{\mu} \qquad 2.3$$

Forchheimer (1901) proposed using a Forchheimer plot, which is a plot describing the relation between $\frac{\Delta P}{L\mu v}$ or $\frac{1}{K_{app}}$ (mm^2), where K_{app} is the apparent permeability, and $\frac{\rho v}{\mu}$ (1/mm). The resulting plot should be a straight line with slope β and intercept $\frac{1}{K_F}$.

To simulate single phase, incompressible, non-Darcy (Forchheimer) flow in fully saturated porous media at the macro-scale, typically the Navier-Stokes equations are used, simplified, averaged over the simulation domains (fluid and solid phases), and then solved numerically. For example, Zimmerman et al. (2004) and Zhang and Xing (2012) solved Navier-Stokes equations for nonlinear flow using a finite-element mesh, Aly and Asai (2015) simulated non-Darcy flows through porous media by the incompressible smooth particle hydrodynamics method, and Belhaj et al. (2003) used the Forchheimer equation, which is a simplified form of the Navier-Stokes equations, to derive a finite difference model for Darcy and non-Darcy flow

in porous media. However, there are other models that can be used to simulate non-Darcy flow such as the Barree and Conway model, the hydraulic radius model, A. V. Shenoy's Model, and the Fractal Model. Further details about these models can be found in the review by Wu et al. (2016).

Many researchers have found that Forchheimer's equation is capable of reproducing their experimental results (Blake, 1922; Fancher & Lewis, 1933; E. Lindquist, 1933; Brownell et al., 1947; Mobasheri & Todd, 1963; Sunada, 1965; Ahmed, 1967; Kim, 1985), while others (Forchheimer, 1930; Barree & Conway, 2004, 2005) reported that Forchheimer's equation is not a good match for their experiments. It is important to notice that Forchheimer's equation has some limitations and it requires modifications of its coefficient values (K_F and β) before it can be applied to the turbulent flow regime, i.e. for a specific medium, Forchheimer's equation cannot be used to describe the flow behaviour in all flow regimes with constant values of K_F and β.

To simulate single phase, incompressible, turbulent flow in fully saturated porous media at the macro-scale, typically the Navier-Stokes equations (Equation 2.4 and 2.5) are used, averaged over the simulation domains (fluid and solid phases), and then solved numerically. This system of equations is not closed, i.e. the number of unknowns is more than the number of equations, and cannot be solved without further simplifications or additional closure models (Ferdos & Dargahi, 2016). Many commercial Computational Fluid Dynamics (CFD) software tools, such as ANSYS CFX, Fluent and OpenFOAM, provide numerical solutions for equations 2.4 and 2.5, given by:

$$\rho \frac{Du}{Dt} = -\nabla P + \rho g + \mu \nabla^2 u \qquad 2.4$$

where u (mm/s) is the velocity vector, g (mm/s^2) is the gravitational acceleration, and t (s) is time.

The left-hand side of Equation 2.4 represents the inertial term, while on the right-hand side, the first term is the pressure term, the second term is the

body force due to gravity, and the third term is the effect of viscosity. Equation 2.4 is solved along with:

$$\frac{\partial \rho}{\partial t} + \rho \frac{\partial u_1}{\partial x} + \rho \frac{\partial u_2}{\partial y} + \rho \frac{\partial u_3}{\partial z} = 0 \qquad 2.5$$

where u_1, u_1, and u_3 are the velocity components in the *x*, *y* and *z* directions, respectively.

For the laminar and Forchheimer flow regimes, Equations 2.4 and 2.5 can be simplified which results in the Darcy's (i.e. Equation 2.1) and Forchheimer's (i.e. Equation 2.2) equations (Whitaker, 1996; Bear & Cheng, 2010).

The Kozeny-Carman equation (Equation 2.6) is a widely accepted equation for laminar flow through beadpacks that relates the medium Darcy permeability (K_D) to the medium porosity (ϕ), specific surface area (S_v) and a constant called the Kozeny–Carman constant (κ) which considers irregularity in bead shape and tortuosity of the medium. It was first developed by Kozeny (1927) and later modified by Carman (1937), and given by:

$$K_\mathrm{D} = \frac{\emptyset^3}{S_v^2\, \kappa\, (1-\emptyset)^2} \qquad 2.6$$

where S_v (1/mm) can be considered equal to $\frac{6}{d}$ (1/mm) for spherical particles of diameter *d* (Muljadi et al., 2015).

Ergun (1952) extended the Kozeny-Carman equation for non-Darcy flow in a form (Equation 2.7) similar to Forchheimer's equation, given by:

$$-\frac{\Delta P}{L} = A` \frac{\mu\ (1-\emptyset)^2}{s_p^2\, d_m^2\, \emptyset^3} v + B` \frac{\rho\, (1-\emptyset)}{s_p\, d_m\, \emptyset^3} v^2 \qquad 2.7$$

where *A`* and *B`* are dimensionless constants known as Ergun's first and second constants, d_m (mm) is the mean bead diameter and s_p (-) is the particle shape factor (sphericity). A linearised form of Equation 2.7 can be obtained by dividing the equation by *v*. Then, by fitting a straight line through the experimental results, *A`* and *B`* can be determined from the intercept and slope of the straight line. Different authors provided different values for A` and B`. For instance, Ergun (1952) suggested the values of

150 and 1.75 (for different gases through various-sized spheres, sand and pulverized coke), while Leva (1959) proposed 200 and 1.75 and Macdonald et al. (1979) recommended 180 and a range from 1.8 to 4.0 (for spherical glass beads, cylindrical fibres, consolidated media, variety of material with different porosities and a wide variety of coarse granular media) (Niven, 2002).

Ergun related the pressure gradient through a granular medium to the summation of two terms; the first term represents the pressure required to overcome viscous forces, while the second term represents the pressure loss due to inertial forces (kinetic energy losses) (Niven, 2002).

Fand et al. (1987) carried out laboratory experiments aimed at defining the boundaries of different flow regimes through different porous media (uniform and non-uniform spherical beads) and developing some empirical correlations between the pressure gradient and velocity for these different regimes. In their experiments, they used porous media composed of spherical beads with uniform diameters (2.098, 3.072 and 4.029 mm) and others with non-uniform diameters (mean diameters of 3.690, 3.276 and 2.759 mm). The beads were packed in a stainless-steel water tube of 86.6 mm internal diameter and 457.2 mm length. Water was driven through the beads either by an electric pump or by gravity using a constant head tank, and the discharge rates were measured by a calibrated orifice plate. The pressure drop through the beads was measured either by a differential pressure cell (at low pressure values) or by manometers (at high pressure values). Using Reynold's number (*Re*) based on the flow superficial velocity and the average diameter of the beads (d_m) (Equation 2.12), they concluded that Darcy flow was observed for $Re \leq 2.3\left(\frac{d_m}{d_l}\right)$, where d_l is the largest diameter of the beads used. They also found that their measurements follow Forchheimer's equation when $5\left(\frac{d_m}{d_s}\right) \leq Re \leq 80\left(\frac{d_m}{d_l}\right)$, where d_s is the smallest diameter of the beads used. For all samples composed of uniform and non-uniform beads, the fully turbulent flow regime was observed when $Re > 120$. Fand et al. (1987) used a different coefficient value $(\kappa = 5.34)$ for the Kozeny-Carman equation instead of the widely

accepted value of 5 for spheres. Within the Forchheimer flow regime, Fand et al. (1987) obtained values of 182 and 1.92 for Ergun's first and second constants, whereas, for the turbulent flow regime they proposed values of A` = 225 and B` = 1.61. Finally, when Fand et al. (1987) plotted the normalised dimensionless pressure $\left(\frac{\Delta P\, d_{\mathrm{m}}}{L\, \mu\, v}\right)$ versus R_e, they suggested that the transition regimes between Darcy and Forchheimer regimes and between Forchheimer and turbulent regimes can be considered as points instead of defining a range of Reynold's number for these transition regimes, and this results in a negligible error (<7%) in terms of the flow behaviour. This error was estimated as the maximum difference between the exact value of $\frac{\Delta P\, d_{\mathrm{m}}}{L\, \mu\, v}$ in the transition regime and the corresponding value at the point that represents the transition regime, when $\frac{\Delta P\, d_{\mathrm{m}}}{L\, \mu\, v}$ is plotted versus R_e.

A similar experimental study was carried out by Kececioglu and Jiang (1994) on two randomly packed uniform beads of 3 mm and 6 mm diameter. The beads were packed in a 920 mm long Plexiglas cylindrical tube with internal diameter of 57.15 mm. Water was driven through the beads either by gravity or by using an electric pump. The discharge rates, which ranged from 5070 to 4920×10^3 mm^3/s, were measured by a flowmeter. The pressure drop through the beads was measured either by a differential pressure transducer (at low pressure values) or by manometers (at high pressure values). The aim of their work was to define the boundaries between different flow regimes. Kececioglu and Jiang (1994) used a Reynold's number, $\hat{R}e_K$, (Equation 2.17) based on the fluid interstitial velocity and the square root of the medium permeability (as a characteristic length instead of the particles average diameter). They presented their pressure gradient results in the form of normalised dimensionless pressure $\left(\frac{\Delta P\, K_{\mathrm{D}}}{L\, \mu\, v}\right)$ versus $\hat{R}e_K$, and in this form, the change of the slope of their results represents different flow regimes (pre-Darcy, Darcy, Forchheimer and turbulent). They concluded that the pre-Darcy,

Darcy, Forchheimer and turbulent flow regimes were observed when $\hat{R}e_K < 0.06$, $0.06 < \hat{R}e_K < 0.12$, $0.34 < \hat{R}e_K < 2.3$ and $\hat{R}e_K > 3.4$, respectively.

2.2 Flow modelling at the pore-scale

On the other hand, pore-scale models can be subdivided into percolation models (e.g. Wilkinson, 1984), Lattice-Boltzmann (LB) models (e.g. Kuwata and Suga, 2015), smoothed particle hydrodynamics (SPH) approach (e.g. Bandara et al. 2013), level-set models (e.g. Amiri and Hamouda, 2013), pore-network models (e.g. Joekar-Niasar et al. 2009) (Joekar-Niasar & Hassanizadeh, 2012) and direct numerical simulations (DNS) (e.g., Muljadi et al., 2015). In the following literature, due to the wide range of methodologies and applications for each method, a short summary of each method is given, then the most relevant pore-network modelling studies are summarised.

Percolation models are stochastically based approaches used to predict the random movement of a fluid through a medium, and they were first implicitly introduced by Flory (1941) and Stockmayer (1943). They can be divided into Bernoulli percolation models (further subdivided into bond and site percolation models) and first-passage percolation models (Wierman, 1982). In percolation models, the porous medium is represented by a network composed of bonds (throats) and sites (pores). In bond percolation models (Figure 2-1a), the bonds of the network are allowed to pass a fluid with probability P_r, or the bonds are blocked (or unoccupied) with probability 1- P_r. For single phase flow, the open bonds represent zones in the porous media with higher permeability while the blocked bonds represent less permeable or impermeable zones. If there is an open bond between any two sites, then the two sites are connected to each other. Any set of connected sites surrounded by blocked bonds is referred to as a "cluster". In site percolation models (Figure 2-1b), the sites of the network are occupied by fluid with probability P_r, or the sites are blocked (or vacant) with probability 1- P_r. Any two neighbouring sites are connected if both of them are occupied by a fluid. Clusters are formed if groups of sites are connected to each other while surrounded by vacant sites. One of the most

critical issues in percolation models is the critical probability, which is the minimum fraction of lattice bonds or sites that should be occupied to create an interconnected path from one side to the other side of the network (Sahimi, 2011a). The first passage percolation models are considered as a generalised form of Bernoulli percolation (Kesten, 1987). More details about each of these percolation models can be found in the work done by Wierman (1982). The major disadvantage of percolation models is that they are static and cannot reveal any transient process information (Joekar-Niasar & Hassanizadeh, 2012).

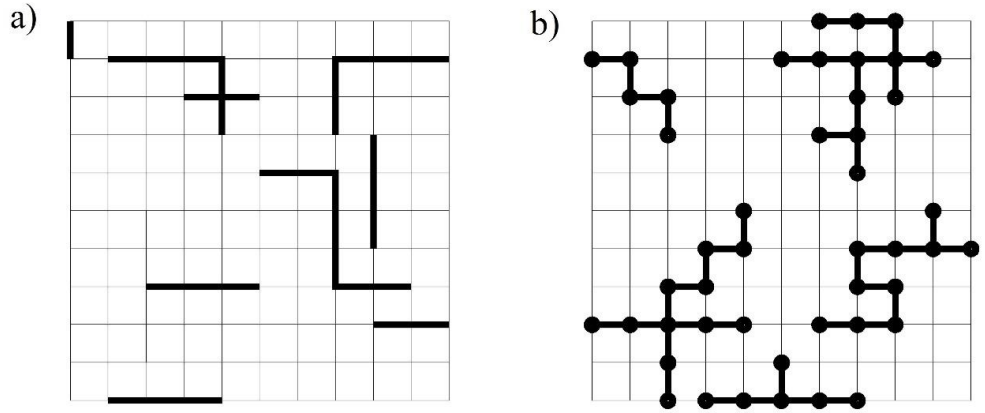

Figure 2-1 Percolation in a square network; a) bond percolation, b) site percolation, after Ghanbarian et al. (2013).

In computational fluid dynamics, typically, the Navier-Stokes equations are simplified, averaged over the simulation domains, then solved numerically at the macro-scale using the finite difference, the finite volume or the finite element method. An alternative technique, applied in the Lattice-Boltzmann method (LBM), is to use the molecular dynamics concept to identify the location and velocity of fluid particles at the micro-scale. It is not necessary to identify the location and velocity of all fluid particles in the volume of interest, but the basic idea is to develop a simplified kinetic model that conserves the essential physics of the microscopic processes and results in macroscopic behaviour that obeys the desired macroscopic equations (for instance, the Navier-Stokes equations) (Chen & Doolen, 1998). LBM originates from the Lattice Gas Automaton (Frisch et al., 1986) which represents a simplified, imaginary molecular dynamic for discretised space, time and particle velocities. In the LBM, the lattice is occupied by fictitious

particles that represent the fluid. The microscopic particle movements are constricted to take place between regularly spaced lattice nodes while obeying a set of collision rules that organise the particles' movement through the lattice and how they scatter when they collide with each other. Different discretisations can be considered for 2D and 3D simulations, e.g. D2Q9, D3Q15, D3Q19, D3Q27, where D2 and D3 represent whether the simulation is either two or three dimensional, while Q9, for instance, states that there are 9 discrete velocity directions (Figure 2-2) (Chen & Doolen, 1998; Junk, 2001; Newman & Yin, 2011; Sahimi, 2011b; Chukwudozie et al., 2012; Al-Zoubi, 2014; Kuwata & Suga, 2015). Chen and Doolen (1998) provided an extensive review of LBM for fluid flow, nevertheless, LBMs have been proved to be computationally very expensive and require supercomputers in order to be able to obtain sufficient or meaningful results, especially for multiphase flow (Pan et al., 2004; Blunt et al., 2013).

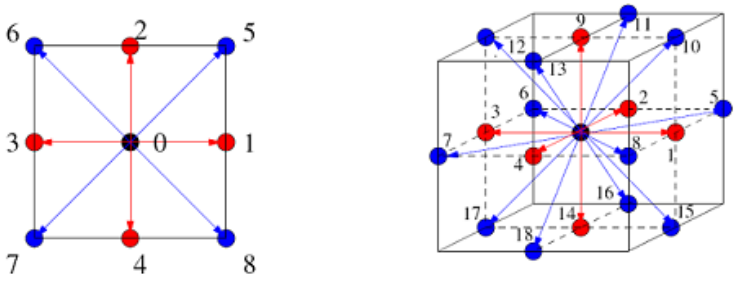

Figure 2-2 Velocity vectors for D2Q9 (left) and D3Q19 (right), by Al-Zoubi (2014).

The SPH method is a meshless, Lagrangian (i.e. using a moving coordinate system (Shadloo et al., 2016)), particle-based method in which the fluid is simulated by a finite number of independent moving particles. These particles carry the fluid physical properties, e.g. location, mass, pressure and velocity, while any change in the particle motions or properties should obey the governing equations. In fluid dynamics, the governing equations are the Lagrangian form of the mass and momentum balance equations. The SPH discretised equations can be obtained by approximating the two governing partial differential equations as ordinary differential equations discretised in time. Then, by using kernel and particle approximation techniques, approximate numerical solutions can be obtained for the flow. For the

kernel approximation technique, the field of interest for a specific particle is obtained by interpolating the values of all particles located within a predefined smoothing radius around the particle under concern, while the particle approximation technique is a further approximation process using interpolation. Full details of this method can be found in the reviews performed by Z-B. Wang et al. (2016) and Shadloo et al. (2016). Generally speaking, the SPH approach can easily capture the interface in the case of multiphase flow, however, it has been proven to be computationally expensive (Tartakovsky et al., 2015).

Direct numerical simulation (DNS) has been used mainly to simulate creeping flow in porous media (e.g. Mostaghimi et al., 2012), however, it could be used to simulate other flow regimes as well (see Muljadi et al., 2015). The method was initially developed by Orszag and Patterson (1972) and Rogallo (1981). Using DNS, the Navier-Stokes equations are solved numerically using a fine mesh based on the pore structure obtained via a micro-CT scan of the medium, while the solid domain is defined as an impermeable boundary surrounding the pores. On the other hand, DNS has been extensively used to simulate turbulent flow in pipes and open channels using a fine mesh and small-time steps in a way that resolves all the crucial turbulent scales. One of the advantages of DNS is that it considers the irregularities in the pore shapes and it can represent the geometry of porous media with complex structures better than other pore-scale methods. Using large mesh elements or large time steps leads to some errors at the small scales that will be transferred to the large scale and corrupt the solution. Consequently, DNS is quite computationally expensive, but at the same time, it helps to gain an insight into an understanding of turbulence physics which cannot be done easily in the laboratory (Poinsot et al., 1995; Moin & Mahesh, 1998; Alfonsi, 2011).

The level set method is an Eulerian (using a reference coordinate system to transfer fluid properties from an element to another (Shadloo et al., 2016)) Computational Fluid Dynamics (CFD) approach that was originally developed by Osher and Sethian (1988). It is an implicit, mesh-based

method which is mainly used for tracking the surface of interaction in the case of two or multiphase flow. A level set function is used to define the distance to the surface of interaction at every point in the domain. The level set function has a zero value at the interface between the two phases, a positive value in one phase, and for the other phase it has a negative sign (Johansson, 2011; Hilton, 2012). The motion of the interface depends on the velocity field which can be assigned externally or by implementing the Navier-Stokes equations (Enright, 2002). The level set method sometimes produces physically unrealistic results and in general requires a large number of time steps, i.e. a long running time (Amiri & Hamouda, 2013). More details about the level set method can be found in the work by Osher and Sethian (1988) and Osher and Fedkiw (2003).

2.3 Flow simulation using pore-network modelling

Using Pore-Network Modelling (PNM), any porous medium can be simplified into large pores called Pore Bodies (PBs) connected to each other by narrow pores called Pore Throats (PThs). Then classical analytical or semi-analytical equations governing the flow and transport in pipes are used to simulate the fluid flow and transport processes at the pore-scale. Moreover, the magnitude of the medium parameters (e.g. Darcy permeability, friction coefficient and longitudinal dispersion coefficient) are determined for the whole medium. The basic principles of PNM were initiated by Fatt (1956a, b,c) who constructed a 2D network of capillary tubes with different radii to simulate the pore space. Many publications have been built based on Fatt's (1956) work, who assumed volumeless nodes between the tubes (Celia et al., 1995). For instance, the majority of networks now represent pore throats by tubes that connect nodes (pore bodies). Generally, pore bodies are represented by spheres while pore throats are represented by cylinders or conical shapes, however, other shapes such as star-shape or hyperbolic triangular cross-sections have also been used (Joekar-Niasar et al., 2010). Connectivity is usually assigned by the coordination number, which is the number of pore throats connected to a pore body. The coordination number contributes to defining the topology of

the pore-network. Pore-networks can be classified into four types; i) structured or ii) unstructured according to the spatial location of pore bodies, and iii) regular or iv) irregular according to the coordination number (Figure 2-3), and all pore-network types can be constructed either in 2D or 3D (Joekar-Niasar & Hassanizadeh, 2012).

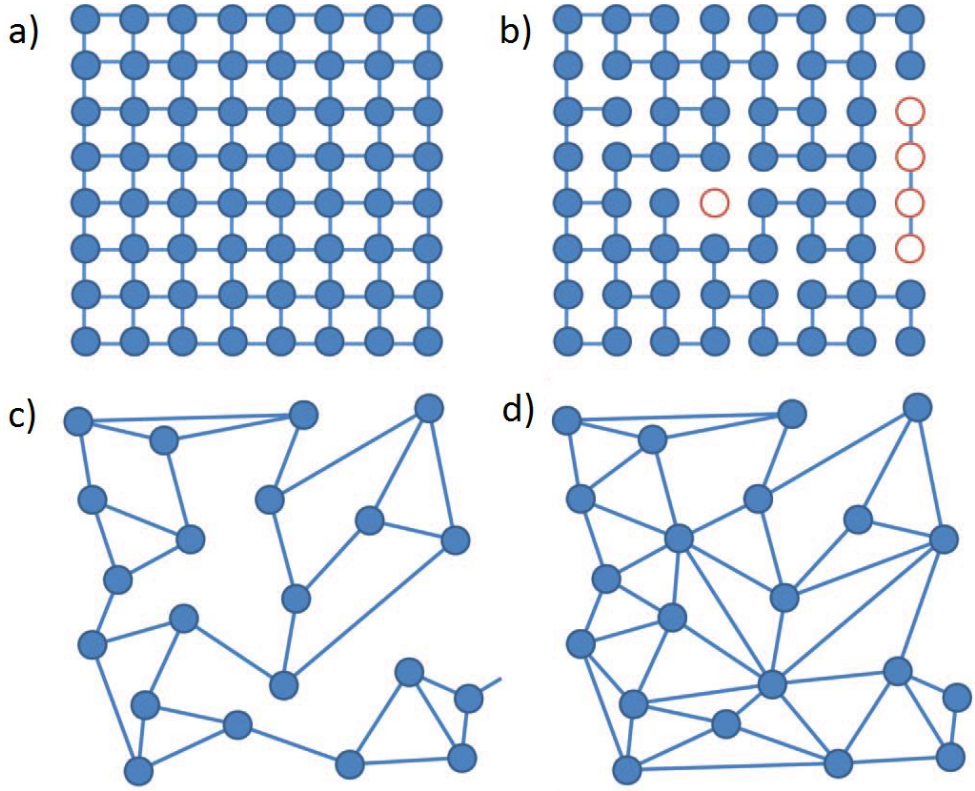

Figure 2-3 Types of pore-networks: a) structured regular, b) structured irregular (isolated pores are shown in red), d) unstructured regular, and e) unstructured irregular, by Joekar-Niasar and Hassanizadeh (2012).

After Fatt (1956a, b, c), many authors have used PNM for different applications; e.g. single-phase (Pan et al., 2001), two-phase (Oren et al., 1998; Al-Gharbi & Blunt, 2005; Joekar-Niasar & Hassanizadeh, 2011), multi-phase flow (Blunt, 1998; Piri & Blunt, 2005), prediction of permeability (Bryant et al., 1993), non-Newtonian flow (Lopez et al., 2003; Valvatne et al., 2005), Darcy and non-Darcy flow (Thauvin & Mohanty, 1998; Martins et al., 2007; Balhoff & Wheeler, 2009), solute dispersion (Bruderer & Bernabé, 2001; Babaei & Joekar-Niasar, 2016), reactive transport (Li et al., 2006; Algive et al., 2010; Kim et al., 2011), interfacial area and capillary pressure (Held & Celia, 2001), evaporation (Freitas &

Prat, 2000), gas drive process (Bora et al., 2000) and gas condensation (Wang & Mohanty, 1999; Jamiolahmady et al., 2000).

2.3.1 Flow through a single capillary tube

Flow through macro-scale "commercial" pipes is governed by the Darcy-Weisbach equation, Equation 2.8, (Weisbach, 1845; Darcy, 1857), given by:

$$\Delta h = \frac{\Delta P}{\gamma} = f \frac{L}{2r} \frac{u^2}{2g} \qquad 2.8$$

where Δh (mm) and ΔP (Pa) are the head loss and the pressure loss between the two ends of the tube, γ (N/m·mm^2) is the fluid specific weight which is equal to the fluid density ρ (Kg/m·mm^2) times the gravitational acceleration, g (mm/s^2), f (-) is the tube friction factor, u (mm/s) is the average fluid velocity through the tube, and L (mm) and r (mm) stand for the tube length and radius, respectively.

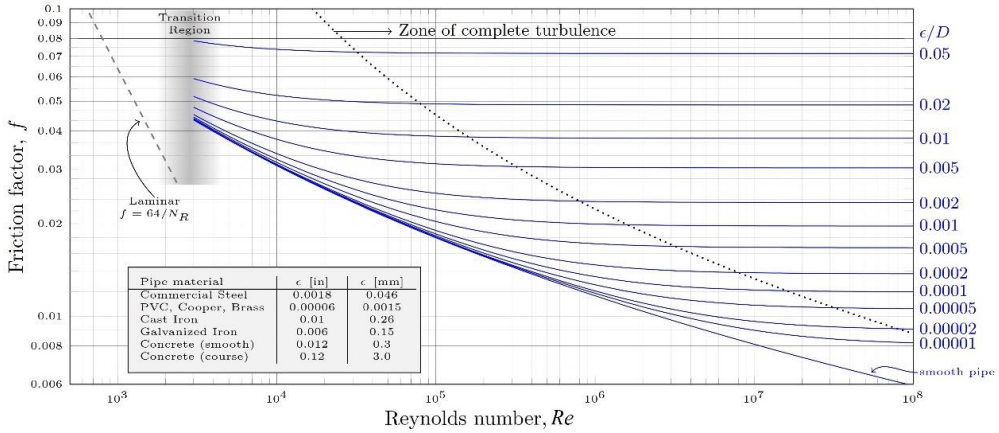

Figure 2-4 Moody Diagram for macro-scale pipes (Moody, 1944), obtained from (https://kdusling.github.io/teaching/Applied-Fluids/Notes/FrictionLosses).

Typically, the friction factor of the tube is determined from a Moody Diagram (Figure 2-4), then the pressure needed to pass a fluid at a specifically required discharge rate is obtained from Equation 2.8 using iterations. A Moody Diagram can be divided into four zones (Peiyi & Little, 1983):

a) The laminar flow zone when the Reynold's number (*Re*) < 2200. In this zone, *f* depends only on *Re*.

b) The transition zone when $2200 < Re < 4000$. In this zone, f is related to the initial turbulence and pressure waves.

c) The first part of the turbulent flow regime when $4000 < Re < Re_{critical}$ ($Re_{critical}$ is represented by the dashed curve in Figure 2-4). In this zone, f depends on both the Reynolds number (Re) and the relative roughness of the tube (ε/D), and the curves of f follow the Colebrook equation (Equation 5.2) (Colebrook & White, 1937).

d) A complete turbulence zone or completely rough tube when $Re > Re_{critical}$. In this zone, the curves of f appear as a group of horizontal lines and the value of f is dependent only on the relative roughness of the tube. When using PNM, implementing a suitable value of the friction factor for each of these zones at the pore-scale results in a smooth transition between the macro-scale flow regimes.

Many previous studies investigated flow through microtubes aiming to investigate if the flow governing equations of macro-scale commercial pipes are valid for microtubes and to revise the boundaries (Re values) between different flow regimes (laminar, transition and turbulent). Some of these studies confirmed that the limits between the flow regimes are the same for micro and macro-tubes (Chung et al., 2002; Hegab et al., 2002; Judy et al., 2002; Sharp & Adrian, 2004; Rands et al., 2006; Wibel & Ehrhard, 2009), while others (Peiyi & Little, 1983; Peng et al., 1994; Gui & Scaringe, 1995; Harms et al., 1999; Mala & Li, 1999; Weilin et al., 2000; Zeighami et al., 2000; Wu & Cheng, 2003; Li et al., 2005) confirmed early transition from laminar to turbulent flow in microtubes; i.e. the Re at the onset of the transition and turbulent flow regimes in microtubes is less than the widely accepted values of 2200 and 4000, respectively, for macro-tubes. A summary of these studies is given in Table 2-1 and Table 2-2. Moreover, most of the studies that observed early transition to turbulence attributed this to the relatively high surface roughness in the microchannels (Li et al., 2005).

Despite the fact that macro-scale tubes are several orders of magnitude larger than microtubes, most of the previous experimental work suggested

that the flow in both systems is statistically and structurally the same. Therefore, all previous correlations and governing equations of macro-scale tubes are applicable to microtubes and any experimentally observed deviations from these governing equations can be considered as scaling effects, not new effects. In conclusion, macro-scale governing equations can be used as the starting point of modelling flow through microtubes (Weilin et al., 2000; Olsen, 2008).

Table 2-1 Studies that observed earlier onset of transition and turbulent flow in microchannels.

Reference	*Experimental method*	*Re at onset of transition flow*	*Re at onset of turbulence*
Peiyi and Little (1983)	Pressure and discharge measurements through very fine channels used for microminiature Joule-Thomson refrigerators with hydraulic diameter 45-83 μm.	350	NA
Peng et al. (1994)	Pressure and discharge measurements of water through rectangular microchannels with hydraulic diameters of 0.133-0.367 mm and height/width ratios of 0.333-1.	200-700	400-1500
Gui and Scaringe (1995)	Flow and heat transfer through chemical etched microchannels with hydraulic diameters up to 388 μm.	1400	NA
Harms et al. (1999)	Pressure and discharge measurements through deep rectangular microchannels, 251 μm wide and 1000 μm deep.	1500	2000
Mala and Li (1999)	Pressure and discharge measurements of water through cylindrical microtubes of fused silica and stainless steel with diameters ranging from 50 to 254 μm.	500	1500
Weilin et al. (2000)	Pressure measurements through silicon trapezoidal microchannels with hydraulic diameters ranging from 51 to 169 μm.	500	NA
Zeighami et al. (2000)	Study of transition to turbulent in 150 μm×100 μm×1 cm Silicon microchannels by using micron-resolution particle imaging velocimetry (μPIV).	1200	1600

Wu and Cheng (2003)	Pressure and discharge measurements of water through smooth silicon trapezoidal microchannels with hydraulic diameters ranging from 25.9 to 291.0 μm.	1500	2000
Li et al. (2005)	Investigation of flow through 320×320 μm square microchannel using microscopic particle image velocimetry (μPIV).	1535	2630-2853

Table 2-2 Studies that did not observe earlier onset of transition and turbulent flow in microchannels.

Reference	*Experimental method*	*Re at onset of transition flow*	*Re at onset of turbulence*
Chung et al. (2002)	Visualization of deionized water and nitrogen gas flowing through capillary tubes with 100 μm inner diameter.	2000	NA
Judy et al. (2002)	Measurement of discharge and pressure drop through microtubes with hydraulic diameters ranging from 15 to 150 μm for three different fluids (water, methanol, isopropanol), two different tube materials (fused silica, stainless steel), and two different tube cross section geometries (circular, square).	They did not detect any distinguishable deviation from the macro-scale viscous flow theory.	
Hegab et al. (2002)	Investigating fluid flow and heat transfer through rectangular aluminium microchannels with hydraulic diameters ranging from 112 to 210 μm and aspect ratios from 1.0 to 1.5.	2000	4000
Sharp and Adrian (2004)	Flow and pressure drop through glass microtubes with diameters ranging from 50 to 247 μm.	1800-2300	NA
Rands et al. (2006)	Measurements of flow, pressure drop and viscous heating-induced temperature rise through microtubes with varying lengths and diameters ranging from 16.6 to 32.2 μm.	2100-2500	NA

Wibel and Ehrhard (2009)	μPIV measurements of velocity through stainless-steel rectangular microchannels with a hydraulic diameter of ~133 μm.	1900-2000	NA

To apply the Darcy-Weisbach equation, Equation 2.8, (Weisbach, 1845; Darcy, 1857) for a tube, the friction factor (*f*) is obtained, either from a Moody Diagram or from the equivalent equations, assuming that the flow is "fully developed" through the whole tube length. A fully developed flow is achieved when the velocity profile becomes fully developed (e.g. parabolic velocity profile in case of laminar flow) and remains constant after the hydrodynamic entrance region as shown in Figure 2-5 (Çengel & Cimbala, 2006). When a fluid enters a tube, its velocity profile is more likely to be uniform, then, due to the no-slip condition and the effect of friction between the fluid and the tube wall, the fluid particles in contact with the tube wall slow down until their velocities reach zero. Meanwhile, the layers at the centre of the pipe speed up to compensate for the reduction of velocity and maintain a constant discharge rate through the tube. This process results in a developing velocity profile through the entrance region as shown in Figure 2-5. The friction between the pipe wall and the fluid is related to the velocity profile and this friction is highest at the pipe entrance, then it decreases until it reaches a constant value when the flow becomes fully developed and the velocity profile remains unchanged (Figure 2-6). Consequently, the pressure drop is higher at the entrance region compared to the fully developed region and if the effect of the entrance region is taken into considerations, it will increase the average friction factor (*f*) of the whole pipe. For long pipes, the effect of the entrance region can be neglected and the whole pipe length can be used in the calculations, however, for short pipes this increase in the friction factor may be significant (Çengel & Cimbala, 2006).

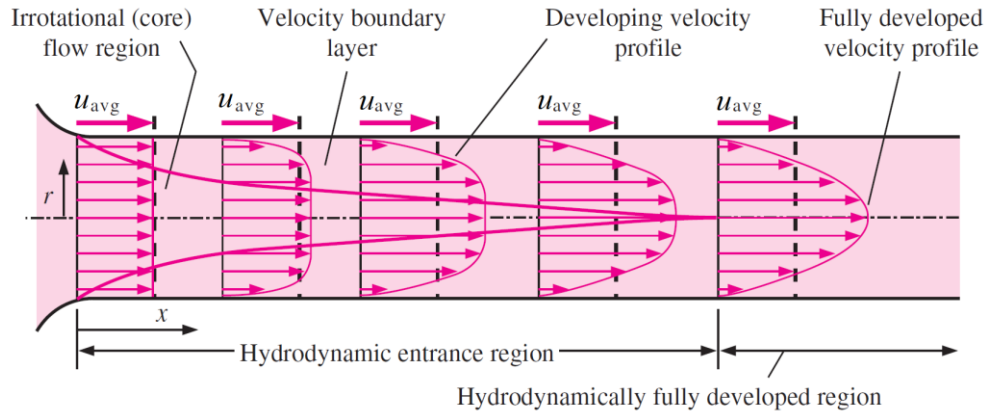

Figure 2-5 The development of an average velocity (parabolic) profile for laminar flow through a circular pipe. For turbulent flow, the velocity profile is flatter or fuller, by Çengel and Cimbala (2006). u_{avg} in the figure denotes the average velocity at any cross-section of the pipe.

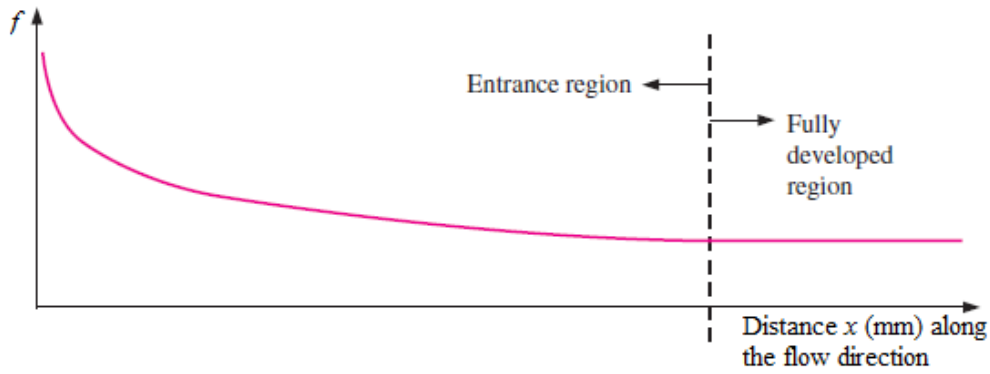

Figure 2-6 The variation of friction factor, f (-), for a pipe from the entrance region to the fully developed region, modified after Çengel and Cimbala (2006).

For laminar flow, the length of the entrance region, $L_{h,\ laminar}$ (mm), can be approximately estimated as proposed by Kays and Crawford (1993) and Shah and Bhatti (1987) (as mentioned by Çengel and Cimbala (2006)) as

$$L_{h,\ laminar} \cong 0.05\ Re \times\ d; \qquad 2.9$$

where d (mm) is the pipe diameter.

For turbulent flow, the length of the entrance region, $L_{h,\ turbulent}$ (mm), can be approximately estimated as proposed by Bhatti and Shah (1987) and Zhi-qing (1982) (as mentioned by Çengel and Cimbala (2006)) as

$$L_{h,\ turbulent} \cong 1.359\ d\ \times Re^{0.25}. \qquad 2.10$$

Çengel and Cimbala (2006) proposed that the $L_{\text{h, turbulent}}$ is shorter for turbulent flow compared to laminar flow, and it is less dependent on Reynold's number, so it can be considered as

$$L_{\text{h, turbulent}} \cong 10\, d. \qquad 2.11$$

2.3.2 Single phase flow within the Darcy (laminar) and non-Darcy (Forchheimer) flow regimes

Simulation of single-phase laminar Darcy flow in a fully saturated medium using PNM allows one to estimate the medium Darcy permeability (K_{D}). Additionally, it could be used either to obtain an initial guess of the pressure distribution throughout a pore-network (PN) for simulating non-Darcy flow (e.g. Balhoff & Wheeler, 2009; Thauvin & Mohanty, 1998) or as part of a specific study, e.g. simulation of solute transport using PNM in the Darcy flow regime (Babaei & Joekar-Niasar, 2016). In such cases, the conductance of each pore (g_{pore}) is calculated analytically from the Hagen-Poiseuille equation (Equation 4.2) (Hagen, 1839; Poiseuille, 1841), while the overall medium Darcy permeability is estimated from Darcy's law (Equation 2.1). The methodology describing this process is shown in detail in Section 4.2.

According to my knowledge, there are only five studies that have modelled non-Darcy flow in porous media using PNM. One of these earliest studies was conducted by Thauvin and Mohanty (1998), nevertheless, their study was limited only to a 3D regular structured pore-network, i.e. all pore bodies were located on equally spaced lattice nodes and each pore body, except the pore bodies at the boundaries, was connected to six pore throats. In their isotropic pore-network, pore bodies were represented by spheres, while pore throats were represented by circular tubes. The pore body and pore throat radii were assigned arbitrarily using a Weibull distribution. At the pore-scale, they evaluated the viscous pressure loss through each pore throat by using the Hagen-Poiseuille equation and used an approximate equation for evaluating the pressure loss due to the change in flow direction. In order to simulate the converging-diverging flow behaviour, Thauvin and Mohanty (1998) modified two equations, $K_e = \left\{1 - \left(\frac{r_{i-j}}{r_j}\right)^2\right\}\left(\frac{r_{i-j}}{r_j}\right)^2$ and

$K_c = \left\{1.45 - 0.45\left(\frac{r_{i-j}}{r_i}\right)^2 - \left(\frac{r_{i-j}}{r_i}\right)^4\right\}$ where K_e and K_c are the expansion and contraction coefficients respectively, while r_{i-j}, r_i, r_j are the pore throat and pore body radii respectively, for pressure loss due to sudden expansion (diverging flow) and sudden contraction (converging flow) after Bird et al. (1960), but they did not explain the reason for these modifications. At the macro-scale, they used Darcy's law and Forchheimer equation to estimate the medium Darcy permeability (K_D) and Forchheimer coefficient (β). Moreover, they did not validate their model and the performance of the model for simulating flow through real porous media has not been tested.

A following study by Wang et al. (1999), who extended the work of Thauvin and Mohanty (1998) and used the same previous modified equations after Bird et al. (1960), was conducted for anisotropic pore-networks, and it was also limited to regular structured pore-networks. They used the same Weibull distribution to assign pore throat and pore body radii, however, in their pore-networks they considered the spatial correlation between pore bodies and the adjacent pore throats. They generated anisotropic pore-networks by either changing the pore throat radii in one direction with respect to the other two directions, removing some pore throats in a specific direction or changing the spatial correlation in a specific direction. They used a tensorial form of Forchheimer's equation and concluded that, in most of the anisotropic cases, the Forchheimer coefficient increases while Darcy permeability decreases.

Later, Lao et al. (2004) performed a non-Darcy flow study using Forchheimer's equation for irregular unstructured pore-networks, but their study was conducted only in 2D and the maximum value of the coordination number in their pore-networks was set to 3, which might not represent real porous media with larger coordination number, and they also assumed volumeless nodes. Lao et al. (2004) generated different pore-networks with cylindrical tubes from known porosity and pore size distributions; a Gaussian distribution, a Beta distribution and experimentally measured distributions. Then, for a large number of pore-networks, they used a Monte-Carlo technique to estimate the mean and variance of the pore-

network properties. In contrast to Thauvin and Mohanty (1998), Lao et al. (2004) concluded that the change in flow direction at each node has the largest effect on the non-Darcy coefficient (β), however, this conclusion might be specific for their pore-networks that assumed volumeless nodes (PBs). Finally, Lao et al. (2004) provided an empirical relationship that predicts the non-Darcy coefficient, β (1/mm), from Darcy permeability, K_{D} (mm^2), porosity, ϕ (-), and tortuosity, τ (-).

Lemley et al. (2007) extended Lao et al.'s (2004) work for irregular unstructured 3D pore-networks composed of cylindrical tubes, but the upper limit of the coordination number in their networks was 3 and they also assumed volumeless node. Lemley et al. (2007) generated pore-networks with different porosity, pore throat lengths, diameters and orientations following the pore size probability density functions (PDFs) for glass beads and Berea sandstone provided by Yanuka et al. (1986). They used a Monte-Carlo technique very similar to the method used by Lao et al. (2004) to estimate the average values of Darcy permeability (K_D) and Forchheimer coefficient (β). For glass beads, they obtained a relationship between K_D and β that recalls Ergun's equation (Ergun & Orning, 1949), while for Berea sandstone they obtained a trend similar to the previous data presented by Jones (1987) with one order of magnitude difference.

The most recent study for non-Darcy flow through 3D irregular unstructured pore-networks using Forchheimer's equation was performed by Balhoff and Wheeler (2009). In order to account for the inertial effects in their model, they did not use the equations provided by Bird et al. (1960) and approximated in Thauvin and Mohanty (1998) and Wang et al. (1999)'s models arguing that these equations are valid only for turbulent flow, despite the fact that these equations can be derived from Bernoulli, continuity and momentum equations, so they are valid for all flow conditions including laminar flow. Balhoff and Wheeler (2009) also did not use the equation derived by Koplik (1982), which was specific for laminar flow, but they approximated the geometry of pore throats by axisymmetric sinusoidal ducts and calculated the pressure loss through these throats by

solving the Navier-Stokes equations using a finite element method (FEM). After performing the FEM simulations for pore throats with different dimensions, they provided a relatively complex approximated equation that describes the pressure loss due to expansion and contraction through each pore throat and depends on the flow rate and pore throat and pore body geometries. However, their equation was developed from axisymmetric ducts, and they defined the geometries of these ducts by a sinusoidal equation that implies the pore bodies at the two ends of a pore throat to have equal size, a scenario that is not likely to happen in real porous media. Balhoff and Wheeler (2009) applied their model to different pore-networks extracted from a computer-generated sphere packing and from a computer-generated synthetic sandstone by using a modified Delaunay tessellation (MDT) algorithm developed by Al-Raoush et al. (2003). When they provided Forchheimer plots, most of their results showed a concave downward deviation from the Forchheimer equation solution at high velocities. They attributed this deviation to the inertial effects due to the change in flow direction at each node, which was not considered in their model.

2.3.3 Single phase flow within the turbulent flow regimes

To my knowledge, the only work that modelled turbulent flow using PNM is that by Martins et al. (2007). They developed a method to generate different 2D regular pore-networks (with different coordination number values, pore throat orientations and boundary conditions) equivalent to beadpacks by considering only the beadpack porosity and average particle diameter. Their networks were composed of pore bodies and pore throats represented by spheres and cylinders, respectively. The pore body and pore throat diameters were assigned using a log-normal distribution. For flow modelling, they tried to develop a model which is able to simulate flow through the Darcy, Forchheimer and turbulent flow regimes by predefining the boundaries between different flow regimes at the pore-scale. They considered that the limit of the laminar flow regime, in each pore throat, is when the pore throat Reynold's number (*Re*, based on pore throat diameter

and average velocity) is equal to 2300 and the beginning of the turbulent flow regime is when Re = 5000, however, these values were obtained from studying flow through macro-scale commercial pipes which have very large dimensions compared to the dimensions of voids in porous media. Many studies (e.g. Dybbs & Edwards, 1984; Ma & Ruth, 1993; Thauvin & Mohanty, 1998; Zeng & Grigg, 2006; Horton & Pokrajac, 2009) found that the onset of non-Darcy (Forchheimer) flow and the onset of turbulence occur earlier in porous media; for example, Dybbs and Edwards (1984) proposed that the onset of non-Darcy flow occurs when $Re \approx 1$ and the onset of turbulence occurs when $Re \approx 300$. Generally speaking, the onset of non-Darcy flow and the onset of turbulence are highly dependent on the medium properties and the degree of heterogeneity (El-Zehairy et al., 2019) as will be discussed in Chapter 4. To model the pressure loss through pore throats, Martins et al. (2007) used the Hagen-Poiseuille (Hagen, 1839; Poiseuille, 1841) equation to determine the pore throat friction factor when the pore throat $Re < 2300$, while for the turbulent flow regime (when the $Re > 5000$) they used the Blasius equation (Blasius, 1913). For the transition flow regime, when $2300 \leq Re \leq 5000$, they determined the pore throat friction factor by using linear interpolation between the friction factor value obtained from the Hagen-Poiseuille equation at Re = 2300 and the friction factor value obtained from the Blasius equation at Re = 5000. Regarding the inertial effects due to expansion and contraction, they used a constant factor of 1.5 as the summation of the sudden expansion and sudden contraction coefficients, despite the fact that that these coefficients are dependent on the pore throat and pore body geometries. Finally, Martins et al. (2007) were able to obtain results that agree with previous experimental work by fitting the values of the coordination numbers together with the values of the sudden expansion and sudden contraction coefficients.

2.4 Boundaries between different flow regimes in porous media

Over the last four decades, different methods (e.g. visual inspection, Laser-Doppler anemometry, particle image velocimetry, magnetic resonance imaging) have been used to investigate the fluid behaviour at the pore-scale and its consequences on the macroscopic flow regimes. In porous media,

unlike flow in straight pipes, the transition from Darcy to turbulent flow occurs gradually and it is important not to consider any deviation from Darcy's law as an indication of the onset of turbulence (Hlushkou & Tallarek, 2006). When the fluid velocity increases and after a certain point, the relationship between the pressure gradient and fluid velocity becomes nonlinear (Equation 2.2). This point is considered as the onset of non-Darcy flow and can be determined "when the pressure loss due to the linear term becomes less than 99% of the total pressure loss" (Comiti et al., 2000; Muljadi et al., 2015). While at very high velocities, the inertial forces become dominant compared to the viscous forces, this leads to the occurrence of some turbulent eddies and the flow can be considered as fully turbulent.

At the macro-scale, the flow regimes in porous media can be classified into three main regimes; a Darcy flow regime, a non-Darcy (Forchheimer) flow regime and a turbulent flow regime. These are the main flow regimes considered by Bear (1972) and they are the main focus of this work. However, some authors (e.g. Kececioglu & Jiang, 1994; Kundu et al., 2016) defined a pre-Darcy flow regime, while others proposed additional transition flow regimes from Darcy to Forchheimer and from Forchheimer to turbulent (e.g. Kececioglu & Jiang, 1994; Fand et al., 1987). In the pre-Darcy regime, the fluid velocities are very low, the pressure gradient is non-linearly related to the flow superficial velocity, and the fluid shows non-Newtonian behaviour which might be due to capillary-osmotic forces in the medium (Kundu et al., 2016).

Horton and Pokrajac (2009) defined different flow regimes in porous media based on the length scale; i.e. if the study is performed either at the pore-scale or at the macro-scale. For macro-scale studies, they defined the previously mentioned three main regimes (Darcy, Forchheimer and turbulent flow regimes). While, for pore-scale studies, following Dybbs and Edwards (1984), these authors defined the following four regimes (steady laminar linear, steady laminar nonlinear, unsteady laminar or transition, and turbulent) for a single representative pore (Figure 2-7a):

1) steady laminar (linear): when the fluid velocities and Reynold's numbers are low, and the inertial effects can be neglected compared to the viscous forces. In this regime, the pressure gradient is linearly related to the fluid velocity.
2) steady laminar (nonlinear): when the inertial effects start to affect the fluid flow, and the relationship between the pressure gradient and the fluid velocity becomes nonlinear.
3) unsteady laminar (i.e. transition): when the inertial effects are large enough to cause instabilities or oscillations in the streamlines.
4) turbulent: occurs at very high flow velocities when the fluid flow is chaotic and turbulent.

Different criteria (by different authors), based on different characteristic lengths (L_{charc}) and velocities, have been used to identify flow regimes in porous media. For example, Dwivedi and Upadhyay (1977) mentioned the following three forms of Reynold's number for porous media:

$$Re = \frac{\rho\, v\, L_{charc}}{\mu} = \frac{\rho\, v\, d_m}{\mu}, \quad 2.12$$

$$Re` = \frac{\rho\, v\, d_m}{\mu\, \phi}, \quad 2.13$$

$$Re`` = \frac{\rho\, v\, d_m}{\mu\, (1-\phi)}. \quad 2.14$$

While Ergun (1952) recommended the following equation for evaluating the Reynold's number, after Zeng and Grigg (2006):

$$Re``` = \frac{\rho\, u\, d_m}{\mu\, (1-\phi)} \quad 2.15$$

Other authors (e.g. Muljadi et al., 2015), preferred using the permeability based Reynold's number, in which $\sqrt{K_D}$ replaces the characteristic length, L_{charc} (mm), in the conventional Reynold's number (*Re*) in Equation 2.12, so that

$$Re_K = \frac{\rho\, v \sqrt{K_D}}{\mu} \quad 2.16$$

where $\sqrt{K_D}$ is the Brinkman screening length (Durlofsky & Brady, 1987).

Kececioglu and Jiang (1994) used a Reynold's number based on the fluid interstitial velocity, u (mm/s), the porosity and the square root of the medium permeability (Equation 2.17):

$$\hat{R}e_K = \frac{\rho\, u \sqrt{\frac{K_D}{\phi}}}{\mu}. \qquad 2.17$$

Several authors (e.g. Cornell and Katz, 1953; Zeng and Grigg, 2006) recommended using Forchheimer's number (Equation 2.18) due to the difficulty in determining the characteristic length (L_{chrac}) in the standard Reynold's number, and given by:

$$F_o = \frac{K_D\, \beta\, \rho\, v}{\mu}. \qquad 2.18$$

In PNM, different characteristic lengths have also been used for the standard Reynold's number (Equation 2.12), i.e. mean bead diameter, d_{m} (mm), mean pore throat diameter, d_{PTh} (mm), and mean pore throat radius, r_{PTh} (mm). Table 2-3 summarise some previous studies and the criteria used in each study to determine the onset of a non-Darcy Forchheimer flow regime after Zeng and Grigg (2006). To wrap up the information provided in Table 2-3, there are two main criteria that can be used to determine the onset of non-Darcy flow in porous media; the Reynold's number (*Re*) and the Forchheimer's number (F_{o}). For the Reynold's number the critical value for the onset of non-Darcy flow varies from *Re* = 0.4 to 100, while for Forchheimer's number the critical value for the onset of non-Darcy flow varies from F_{o} = 0.005 to 0.2. Due to the ambiguity in defining the characteristic length for different porous media, using F_{o} is recommended (Zeng & Grigg, 2006). Nevertheless, the onset of non-Darcy flow is dependent on the medium's degree of heterogeneity (see Chapter 4).

Table 2-3. The onset of non-Darcy Forchheimer flow according to different studies, after Zeng and Grigg (2006).

Author	*criterion*	*Method and samples*	*Onset of non-Darcy flow*
Chilton and Colburn (1931)	$Re = \frac{\rho\, v\, d_m}{\mu}$	Experiments on packed particles.	The onset non-Darcy flow occurs in the range of *Re* = 40 to 80.

Fancher and Lewis (1933)	$Re = \frac{\rho\, v\, d_m}{\mu}$	Experiments of crude oil, water and air flow through unconsolidated sands, lead shot, and consolidated sandstones.	Re = 10 − 1000 for unconsolidated samples & Re = 0.4−3 in loosely consolidated samples.
Green and Duwez (1951)	$F_o = \frac{K_D\, \beta\, \rho\, v}{\mu}$	N_2 flow experiments through different porous metal samples.	The non-Darcy behaviour initiated at F_o = 0.1–0.2.
Ergun (1952)	$Re``` = \frac{\rho\, u\, d_m}{\mu\,(1-\phi)}$	Experiments of gas flow through packed particles.	The onset of non-Darcy flow occurs when $Re``` = 3 - 10$.
Bear (1972)	$Re = \frac{\rho\, v\, d_m}{\mu}$	Various data from the literature.	The critical value for the onset of non-Darcy flow is when Re = 3 to 10.
Scheidegger (1974)	$Re = \frac{\rho\, v\, d_m}{\mu}$	N. A.	The critical value for the onset of non-Darcy flow is when Re = 0.1–75.
Hassanizadeh and Gray (1987)	$Re = \frac{\rho\, v\, L_{charc}}{\mu}$	Various experimental data from the literature.	The critical value for the onset of non-Darcy flow occurred when Re = 1−15 and they suggested Re = 10 as an average critical value.
Blick and Civan (1988)	$Re = \frac{\rho\, v\, d_m}{\mu}$	A capillary–orifice model to simulate fluid flow in porous media.	Based on their model, the critical Re for the onset of non-Darcy flow is 100.
Ma and Ruth (1993)	$Re = \frac{\rho\, u\, d_{PTh}}{\mu}$ and $Fo = \frac{K_D\, \beta\, \rho\, v}{\mu}$	They numerically modelled non-Darcy flow using a diverging–converging model.	The critical Re is 3–10, while the corresponding Fo is 0.005–0.02.
Thauvin and Mohanty (1998)	$Re = \frac{\rho\, v\, r_{PTh}}{\mu}$	They used PNM to simulate the porous media.	Their result showed that the critical Re is 0.11.

Andrade et al. (1999)	$F_o = \frac{K_D \beta \rho v}{\mu}$	Flow simulation through disordered porous media.	The critical F_o is 0.01–0.1.

To determine the onset of turbulence in porous media, visual inspection can be used as was done by Dybbs and Edwards (1984). They used a dye to visualise the flow streamlines in porous media composed of either Plexiglas sphere packing or rods arranged in a complex 3D geometry. They determined the onset of the turbulent flow regime when the streamlines start to fluctuate inside the pores and the fluid moves in a chaotic manner. Other experimental studies (e.g. Fand et al., 1987; Kececioglu & Jiang, 1994) presented their results in the form of a normalised dimensionless pressure gradient $\left(\frac{\Delta P\, K_D}{L\, \mu\, v}\right)$ versus Reynold's number, and in this form, the change in the slope of their results represents different flow regimes. A more advanced method to determine the onset of the Forchheimer and turbulent flow regimes is to use particle image velocimetry (PIV) which allows one to visualise and track the instantaneous movement of fluid particles and to determine the velocity field (magnitude and direction) over time. From the velocity field measurements, obtained by Horton and Pokrajac (2009) inside the pores of a regular structured medium composed of uniform spheres, they were able to estimate the velocity moments, skewness and kurtosis, and to further determine the onset of the Forchheimer and turbulent flow regimes at the pore-scale. Figure 2-7 shows the onset of different flow regimes obtained by several studies using $Re`$ (Equation 2.13) and summarised by Horton and Pokrajac (2009). The figure shows that, at the macro-scale, there is no specific value or narrow range of Reynold's number that can be used as a criterion for the onset of turbulence, which is attributed to different medium geometries and degrees of heterogeneity in each study. However, there is agreement between the only available two studies by Dybbs and Edwards (1984) and Horton and Pokrajac (2009) who determined the limits between different flow regimes by experimental measurement inside the pores. These two studies observed transitions of flow properties at $Re` \approx 150$, which represents the onset of transition flow and at $Re` \approx 300$, which represents the onset of turbulent flow.

It is important to take into considerations that flow through the pores of a porous medium differs from flow through a single long straight micro-tube. The chaotic nature of porous media causes an early occurrence of the transition and turbulent flow regimes inside the pores compared to singular micro-tubes. As shown in Section 2.3.1, there is an ongoing debate regarding determination of Reynold's number values at the boundaries between different flow regimes in micro-tubes. Some authors found that the limits of macro-tubes are the same for micro-tubes, while others found early occurrence of the transition and turbulent flow regimes in micro-tubes. However, even those who observed early occurrence of the transition and turbulent flow regimes in micro-tubes determined Reynold's number values larger than the values obtained by Dybbs and Edwards (1984) and Horton and Pokrajac (2009) when flow was observed inside the pores of the medium. Therefore, the Reynold's number values at the onset of the transition and turbulent flow regimes determined by Dybbs and Edwards (1984) and Horton and Pokrajac (2009) (at $Re` \approx 150$ and $Re` \approx 300$, respectively) will be used later in Chapter 5.

a) Pore-scale

Laminar		Transition	Turbulent
Steady		Unsteady	
Linear	Nonlinear		

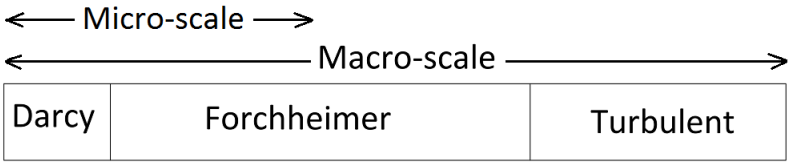

b)

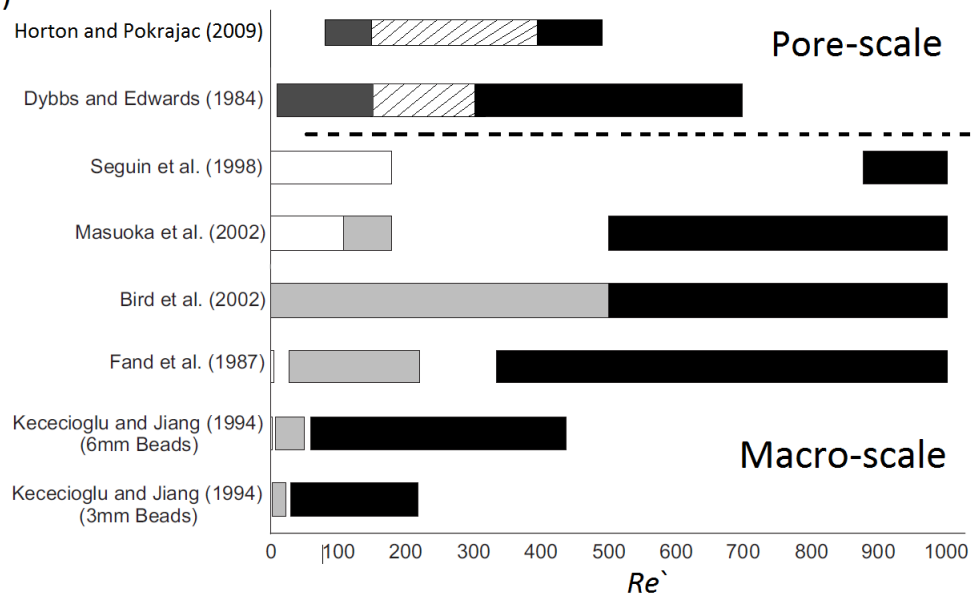

Figure 2-7 a) Classification of the pore- and macro-scale flow regimes. b) Boundaries of flow regimes. For pore-scale studies, the flow regimes are presented as follows: i) steady linear laminar (white), ii) steady, nonlinear laminar-inertial core (dark grey), iii) unsteady transition (hatched), and iv) turbulent (black). For macro-scale studies, the flow regimes are presented as follows: i) Darcian (white), ii) Forchheimer (light grey), and iii) turbulent (black). The flow regimes are determined using $Re`$ (Equation 2.13), and the figure is modified after Horton and Pokrajac (2009).

In the following chapters, different porous samples are used to verify the proposed pore-network flow and solute transport models. At the micro-scale (0.5-5 mm), beadpack, Bentheimer sandstone, Berea sandstone, and Estaillades carbonate samples are used. At the macro-scale (50-200 mm),

two samples composed of randomly packed and regularly structured uniform spheres are used. The micro-scale samples are considered as a special case or a small crop of the macro-scale sample, but in the used samples, the size of pores in micro-scale samples is smaller than the size of pores in macro-scale samples (see Figure 4-3). The pore-scale is meant to be the length scale of a single pore body and pore throat.

2.5 Modelling of solute transport through porous media

The transport process in porous media is of high interest to many scientists and can affect groundwater wells, oil wells and agricultural activities. Pollutants can be classified into the following species; dissolved or immiscible, and conservative or reactive. Dissolved pollutants/solutes are aqueous phase pollutants which spread within the water due to advection, diffusion and dispersion, while immiscible pollutants are non-aqueous phase liquids (NAPL). Conservative pollutants are those which do not react with the porous medium solid matrix, nor with other pollutants and are not affected by biological activities. Reactive solutes may interact with the fluid (water) through chemical reactions, adsorption and/or biodegradation (van der Zee & Leijnse, 2013). The focus of this work is on dissolved conservative solutes.

The system shown in Figure 2-8 is a container that contains a saline solution and distilled water separated by a removable barrier. All saline molecules are subjected to a random movement resulting from its Brownian motion related to the thermal energy of the liquid. When the barrier between the saline solution and the distilled water is removed, the molecules' random movement causes some saline molecules to move from the saline solution to the distilled water. The number of saline molecules that crosses the boundary between the saline solution and the distilled water is proportional to the concentration gradient. The constant of proportionality is equal to the coefficient of molecular diffusion, D_m (mm^2/s). Therefore, Fick's first law of diffusion states that the diffusive flux (F) is proportional to the concentration gradient as per Equation 2.19 (Zheng & Bennett, 2002),

$$F = -D_{\mathrm{m}} \frac{\partial C}{\partial L} \qquad 2.19$$

where F is the diffusive mass flux (mol/mm^2·s), and $\frac{\partial C}{\partial L}$ (mol/mm^4) is the concentration gradient.

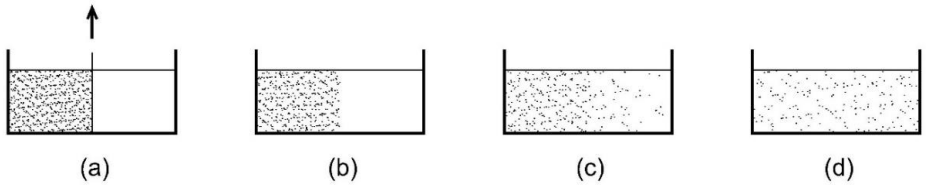

Figure 2-8 Illustration of molecular diffusion; a) a container with saline solution and distilled water separated by a removable barrier, b) saline molecular distribution right after removing the barrier, c) saline molecular distribution at time t_1 after removing the barrier, and d) final saline molecular distribution, after Zheng and Bennett (2002).

At the macro-scale, solute transport in porous media can be modelled using the following 1D Advection-Dispersion Equation (ADE) (Ogata & Banks, 1961):

$$\frac{\partial C}{\partial t} = D_{\mathrm{L}} \frac{\partial^2 C}{\partial x^2} - u \frac{\partial C}{\partial x} \qquad 2.20$$

where C (mol/mm^3) is the concentration of the conservative solute, u (mm/s) is the fluid average pore velocity and x is the longitudinal spatial coordinate in the mean flow direction, D_{L} (mm^2/s) is the longitudinal dispersion coefficient and t is the elapsed time. Advection is the movement of solute particles within the moving fluid, while dispersion is a result of two processes; a non-uniform velocity field and molecular diffusion (Bijeljic et al., 2004). When a solute is injected into a flowing water or fluid, the longitudinal dispersion coefficient (D_{L}) is a measure of the solute spreading along the flow's direction (Hart, 2013). Therefore, the longitudinal dispersion coefficient (D_{L}) can be thought of as the summation of two components that account for the hydrodynamic effects and molecular diffusion as per Equation 2.21 (Kulasiri, 2013):

$$D_{\mathrm{L}} = \alpha_{\mathrm{L}} u_{\mathrm{L}} + D_{\mathrm{m}} \qquad 2.21$$

where α_L (mm) is the longitudinal dynamic dispersivity, u_L (mm/s) is the average pore velocity in the longitudinal direction, and D_m (mm^2/s) is the coefficient of molecular diffusion. In most of solute transport applications, the effect of diffusion can be neglected compared to the effect of advection, then Equation 2.21 can be rewritten as $D_L \approx \alpha_L u_L$.

In porous media, the dispersion flux in the longitudinal direction, J (mol/mm^2·s), is proportional to the concentration gradient, dC/dL (mol/mm^4). Additionally, due to the fluid movement, the dispersion flux (J) is assumed to be proportional to the average fluid seepage velocity in the longitudinal direction, u_L (mm/s), while the longitudinal dispersivity, α_L (mm), is the proportionality constant. These assumptions result in the final form of Equation 2.22 (Kulasiri, 2013); given by:

$$J \approx -\alpha_L u_L \frac{dC}{dL} \ . \qquad 2.22$$

The term "Fickian transport" originates from the fact that in a manner similar to Fick's law, the dispersion flux (J) in the longitudinal direction is proportional to the concentration gradient (Equation 2.22). In Fickian transport, the concentration spread within the medium follows a Gaussian distribution (Lee & Buchberger, 2001). However, in some cases, mainly due to medium heterogeneity, the concentration distribution deviates significantly from being Gaussian, the 1D ADE is not valid, and such a process is called "Non-Fickian transport" which is out of the scope of this work.

Once a solute is injected into a porous medium, it needs some time to travel through the medium in order to be "asymptotically Fickian"; i.e. when the longitudinal dispersion coefficient reaches a constant value over time. This time is needed for solute particles to undergo a wide range of independent velocities. Once the asymptotically Fickian state is reached, the variance, σ^2 (mm^2), of the Gaussian distribution increases linearly with time (Jha et al., 2011; Mostaghimi, 2012).

Different approaches have been reported in the literature to estimate the longitudinal dispersion coefficient (D_L) from experimental or numerical

concentration profiles. One approach is to use the variance of the Gaussian distribution as per Equation 2.23 (Bruderer & Bernabé, 2001), but this approach requires extensive calculations (Lee & Buchberger, 2001),

$$D_L = \frac{1}{2}\frac{d\sigma_x^2(t)}{dt} = \frac{1}{2}\frac{\sigma_{x_2}^2(t_2) - \sigma_{x_1}^2(t_1)}{t_2 - t_1} \quad 2.23$$

where $\sigma_x^2(t)$ is the solute particle positions variance at time *t* after injecting the solute pulse in the medium.

A second method proposed by Fried and Combarnous (1971) when a solute of concentration C_o is injected at the inlet boundary of a medium, and the concentration (C/C_o) versus distance (x) profile is plotted at time *t*. The concentration profile can be approximated by a normal distribution function and a transition mixing zone (with width *w* (mm)) is generated between C/C_o = 0.16 and C/C_o = 0.84. Then, D_L can be estimated according to equation 2.25 (Fried & Combarnous, 1971), where

$$w = 2\sigma = 2\sqrt{2D_L t} = x_{0.16} - x_{0.84} \quad 2.24$$

then,

$$D_L = \frac{(x_{0.16} - x_{0.84})^2}{8t} = \frac{w^2}{8t} \quad 2.25$$

where *t* (s) is the time at which the concentration versus distance graph is plotted.

Another approach, used in this study, is to estimate D_L by fitting the analytical solution of the 1D ADE (Ogata & Banks, 1961) to the BTC obtained from PNM, and this can be done using CXTFIT computational software (Toride et al., 1995). The 1D ADE is valid under the assumptions that the porous medium is homogeneous, isotropic, saturated with fluid, and the transport is Fickian (Kulasiri, 2013; Sahimi, 2011b). A similar method was used before to obtain the longitudinal dispersion coefficient in some laboratory and field studies, pore-network modelling and other numerical studies (Coats & Smith, 1964; Zaretskiy et al., 2010; Köhne et al., 2011; Babaei & Joekar-Niasar, 2016; Oostrom et al., 2016). CXTFIT makes use of the analytical solution of the 1D ADE. Using a nonlinear least-squares

parameter optimisation approach, CXTFIT can quantify the solute transport parameters. CXTFIT can be used either in a forward mode to estimate the concentration as a function of time, distance or both, or in an inverse mode to estimate transport parameters (e.g. the coefficient of longitudinal dispersion and the retardation factor) from known experimental or numerical results.

Dispersion in porous media has been investigated before using different methodologies either experimentally or numerically. For instance, Pfannkuch (1963) provided a summary of 175 values of the longitudinal dispersion coefficient (D_L) determined experimentally by Rifai et al. (1956), Day (1956), Ebach and White (1958), Carberry and Bretton (1958), Blackwell (1959), Blackwell et al. (1959), Raimondi et al. (1959) and Brigham (1969) for graded sands and other single-grained materials. From this summary and by plotting the longitudinal dispersion coefficient scaled by the coefficient of molecular diffusion (D_L/D_m) versus Péclet number (*Pe*), *Pe* is defined as the rate of transport by advection to the rate of transport by diffusion as per Equation 6.4 (Bear, 1972), Pfannkuch (1963) classified the transport process through porous media into 5 zones. Starting from low flow velocities, zone I is the diffusion dominated zone, where the value of D_L/D_m is constant. In zone II, when $0.4 < Pe < 5$, the effect of molecular diffusion is comparable to mechanical dispersion. In zone III, molecular diffusion acts in the transversal direction against the longitudinal spread of solute by mechanical dispersion and the power law $\left[\frac{D_L}{D_m} = \alpha\,(Pe)^{\delta}\right]$ can be applied with $\alpha \approx 0.5$ and $1 < \delta < 1.2$. In zone IV, mechanical dispersion is dominant and D_L/D_m is linearly dependent on *Pe*, as far as Darcy's law is valid. The last zone (zone V) is a pure mechanical dispersion zone, but the flow inertial effects should not be neglected. The slope of the curve in zone V tends to be less than the slope in zone IV (Bear, 1972; Lal & Shukla, 2004).

Several researchers have studied dispersion experimentally using nuclear magnetic resonance (NMR) where fluid molecules can be tracked using their nuclear spins, instead of using tracers. For instance, Ding and Candela

(1996) used NMR to measure longitudinal and transverse dispersion through 15 μm diameter packed plastic beads for Reynold's number < 1. They noticed a transfer from the diffusion dominated regime to the dispersion dominated regime at $Pe \sim 1$. Despite the fact that the NMR is limited to a length scale of 100 μm or less, i.e. NMR can be used to determine only pore-scale processes, Ding and Candela (1996) used a Fourier transformation to obtain the macro-scale dispersion coefficients from the NMR pore-scale data. They concluded that further theoretical work is needed to obtain better results. Seymour and Callaghan (1997) used an NMR method to study flow and dispersion of water through 90.7 μm diameter packed spheres. They determined the fluid density, velocity, flow propagation, velocity fluctuation and dispersion using an NMR imaging technique and showed that their methodology provided good results, compared to previous results in the literature, for a length scale of ~ 90 μm. However, for a larger scale, an averaging technique should be used. Kandhai et al. (2002) used NMR to evaluate the effect of hold-up dispersion, i.e. the influence of stagnant zones on dispersion. They used random packings of porous particles with 34 μm and 50 μm average diameter, and they concluded that the effect of porous particle hold-up increases the dispersion significantly. The NMR method was successfully used by Khrapitchev and Callaghan (2003) who investigated the pre-asymptotic dispersion (over time) and the asymptotic Fickian dispersion through randomly packed 500 μm diameter uniform spheres. Khrapitchev and Callaghan (2003) deduced that the asymptotic dispersion can be reached after a several order of magnitude larger length than the beads' average diameter.

Stöhr (2003) used an imaging technique to measure dispersion through sharp-edged silica grains and spherical plexiglass beads with average bead diameters of 0.8 mm and 0.6 mm, respectively. He implemented a refractive index matching method (Budwig, 1994) to detect the dynamics of the dye through the 3D structure of the media. Stöhr concluded that his obtained D_L values follow the power law with $\delta = 1.2$. Similarly, Theodoropoulou (2007) used an image analysis technique to experimentally detect the

concentration of a conservative solute through a transparent artificial glass-etched pore-network. Additionally, she developed a 2D macro-scale finite element model to simulate Darcy flow and solute transport through a 2D domain similar to her pore-network and she verified the numerical results against the experimental measurements. When she compared the D_L values calculated from the method of moments, which accounts for transverse dispersivity, to D_L values estimated by fitting the breakthrough curves to the analytical solution of the 1D ADE, she concluded that the latter method underestimates D_L. Another study was performed by Moroni and Cushman (2001) who used a 3D particle tracking velocimetry scanning technique to obtaine the trajectories of a tracer (air bubbles) flowing through glycerol in a homogenous porous medium composed of 1.9 cm spheres. By obtaining the 3D dispersion tensor from image analysis, they concluded that the longitudinal dispersion tensor becomes Fickian after travelling through five to six pore diameters, before this the dispersion is convolution-Fickian and time dependent.

Despite the fact that most of solute transport studies have focused on the asymptotic dispersion rates, Maier et al. (2000) applied a random walk particle tracking technique using a Lattice-Boltzmann (LB) method to investigate the pore-scale pre-asymptotic time dependent (transient) behaviour of dispersion. Compared to previous results, Maier et al. (2000) presented results that showed shorter time and lower rates of longitudinal dispersion. They also found that the time needed to reach asymptotic longitudinal dispersion rates scales with Péclet number, *Pe* (-), in a manner similar to mechanical dispersion.

Using DNS, Mostaghimi et al. (2012) modelled Stoke's flow on a micro-Computed Tomography (micro-CT) scan of Berea sandstone. They proposed a finite difference scheme to simulate the linear flow and pressure fields, while dispersion was modelled by considering the effect of advection and diffusion. Advection was modelled using a streamline tracing technique whereas a random-walk method was used to simulate diffusion. Mostaghimi et al. (2012) were able to detect the diffusion dominated, power law and pure advection regimes, however, when they compared their results to

various results in the literature, they found that their results underestimate the dispersion compared to bead packs. They attributed this to the neglected inertial effects in their flow simulations.

Only few studies have tried to investigate the inertial effects on dispersion through porous media. For instance, starting from the pore-scale and using a volume averaging technique, Wood (2007) developed a macro-scale numerical solution for dispersion of conservative solutes in porous media. The main focus of Wood's work was to investigate the inertial effects on both longitudinal and transverse dispersion coefficients. Using FEM, Wood (2007) determined a solution for the ancillary closure problems, a set of equations that governs the relation between pore-scale and macro-scale physics, over a small unit cell considered as a representative elementary volume (REV) of the medium. Wood (2007) found that the inertial forces affect the longitudinal dispersion coefficient (D_L) much less than the transverse dispersion coefficient (D_T). When the inertial effects are considered, D_L increased by a factor of 1.13 while D_T increased by a factor of up to 40, compared to D_L and D_T for Stoke's flow. He attributed these unsatisfactory results to the use of very simple unit cell and suggested the use of more complex unit cells in future studies. Nezhad et al. (2019) investigated experimentally the flow inertial effects on dispersion through two samples composed of randomly packed uniform spheres with 1.85 and 3 mm diameter. Most of their results were obtained in the mechanical dispersion regime and they concluded that the onset of non-Darcy flow occurred earlier, i.e. at a lower *Re*, in the fine medium (1.85 mm spheres) compared with the coarse medium (3 mm spheres). Nevertheless, reducing the particle size of the porous medium caused higher dispersion in comparison to the medium with larger particle size. However, their obtained D_L values were several orders of magnitude higher than the data in the literature, and they attributed this to the large D_m value of tracer used in their experiments.

2.6 Pore-network modelling of solute transport

2.6.1 Dispersion in pipes

Taylor (1953, 1954) and later Aris (1956) investigated the motion of a passive tracer in a steady state laminar flow through a single circular tube. By studying the Fickian advection-diffusion in a tube, they stated that the effective diffusion coefficient in a single capillary tube, D^{eff} (mm^2/s), can be expressed as $D^{eff} = D_m + \frac{u^2 r^2}{48\, D_m}$, where u (mm/s) is the mean fluid velocity through the tube, r (mm) is the tube radius and D_m (mm^2/s) is the coefficient of molecular diffusion. Taylor stated that his solution is valid when $\frac{4\,L}{r} \gg \frac{u\,r}{D_m} \gg 6.9$, where L is the tube length, however, this condition was found to be severe and Gill and Sankarasubramanian (1970) stated that the Taylor-Aris solution $\left(D^{eff} = D_m + \frac{u^2 r^2}{48\, D_m}\right)$ is valid when $T \geq 0.5$, where T (-) is the dimensionless time, given as $T = \frac{D_m t}{r^2}$, and t is the residence time in the capillary tube. When $T \geq 0.5$, the effective diffusion coefficient should be constant over time. In summary, the transport process in a capillary tube can be divided into three cases: Case 1 (asymptotic Fickian regime), when the fluid flows relatively slowly (i.e. the dimensionless residence time (T) ≥ 0.5) through the capillary tube. For this case, the effect of both advection and molecular diffusion should be considered and the Taylor-Aris solution is valid. Case 2 (pure advection); purely advective flow that occurs when the fluid flows relatively fast (i.e. the dimensionless residence time (T) < 0.01) through a capillary tube and the effect of molecular diffusion can be neglected compared to the advective transport. The results obtained by Bailey and Gogarty (1962) and Ananthakrishnan et al. (1965) confirmed that purely advective flow occurs when the dimensionless residence time is less than or equal to 0.01. A third case (pre-asymptotic time dependent regime), not tested by Taylor, is a transition case between case 1 and case 2 that occurs when $0.01 < T < 0.5$, i.e. the asymptotic state has not been achieved and the transport process is not purely advective. In case 3, the effective diffusion coefficient $[D^{eff}(t)]$ is time dependent and can be expressed as a small percentage of the

asymptomatic effective diffusion coefficient [D^{eff}]. Many authors have investigated this transition case (case 3) and provided an estimation of the effective diffusion coefficient as a function of the residence time, (e.g. Bailey & Gogarty, 1962; Ananthakrishnan et al., 1965; Lighthill, 1966; Gill & Sankarasubramanian, 1970; Chatwin, 1977; Vedel & Bruus, 2011; Meng & Yang, 2017). However, the only work that provides an explicit equation for $D^{eff}(t)$ was performed by Lee (2004), Figure 2-9, Equation 6.3. Lee (2004)'s equation can accurately predict the analytical solution proposed by Gill and Sankarasubramanian (1970).

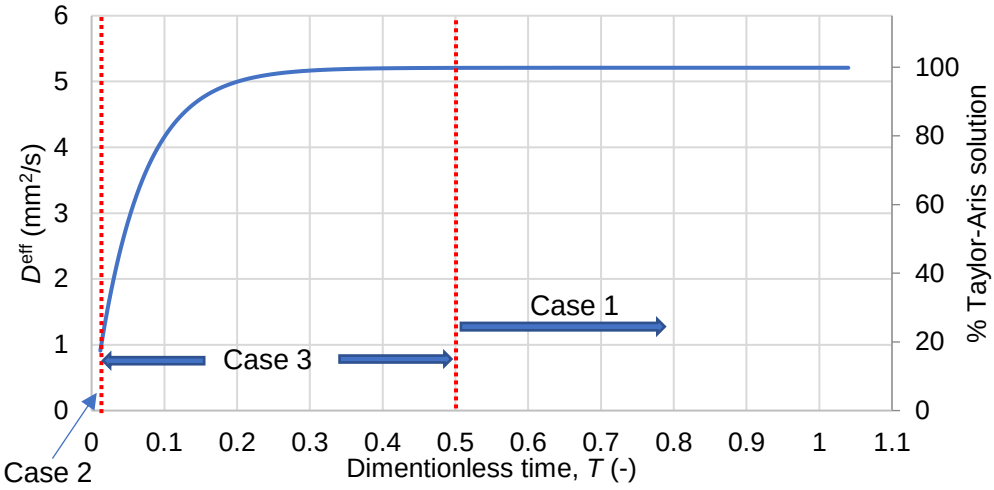

Figure 2-9 The time dependent effective diffusion coefficient [D^{eff} (t)] vs. dimensionless time (T) for a 1 mm diameter circular tube, after Lee (2004) equation (Equation 6.3).

The mixed cell method (MCM), the method applied in this study, is based on the assumption that dispersion occurs mainly in pore throats, the fluid is perfectly mixed at each pore, and when the PNM approach is used, the mass balance equations are adapted for each node (pore body) (Mehmani et al., 2014). For a pore-network that represents a specific medium, once D^{eff} is defined for each pore throat in the pore-network, the mass balance equation (6.1) is adopted at each pore body and the resulting breakthrough curve can be used to obtain the longitudinal dispersion coefficient (D_L). A common mistake in most of the previous solute transport studies performed using pore-network modelling and applying the mixed cell method using the

Taylor-Aris equation $\left(D^{\text{eff}} = D_{\text{m}} + \frac{u^2 r^2}{48\, D_{\text{m}}}\right)$ is that they did not check the residence time needed to reach an asymptotic state for each pore throat, such behaviour may result in overestimating the longitudinal dispersion coefficient (D_{L}) predictions for the medium. Despite the flow at the macro-scale being relatively slow (Darcy), at the pore-scale there might be some pore throats with high velocities or short lengths leading to T < 0.5. For such cases, the transport process might be purely advective or affected by both advection and diffusion, but the solute residence time is not long enough to reach an asymptotic state, i.e. the effective diffusion coefficient is time dependent.

Taylor (1954b) estimated the effective diffusion coefficient of a passive tracer in a circular tube under turbulent flow conditions. He expressed the effective diffusion coefficient as $D^{\text{eff}} = 10.1\, r\, u_*$, where u_* (mm/s) is the shear velocity. This relationship is valid when the solute is fully mixed across the tube, i.e. when the ADE is valid. In most turbulent flow applications, the fully mixed condition is more likely to be achieved as a result of turbulent diffusion and rapid radial mixing (Hart et al., 2016). Taylor proposed that for an injected solute, the distance required for the solute to be fully mixed is equal to 100 times the tube radius. To my knowledge, no previous studies have investigated the value of the effective diffusion coefficient in short pipes under turbulent flow conditions.

The previously mentioned information for estimating D^{eff} will be applied to two different samples; the packed spheres (d_{m} = 1.84 mm) sample used in the experimental work and a Berea sandstone sample (see Chapter 6).

2.6.2 Pore-network modelling of Dispersion

Solute transport using pore-network modelling has been investigated before (Bruderer & Bernabé, 2001; Bijeljic et al., 2004; Bijeljic & Blunt, 2006; Köhne et al., 2011; Babaei & Joekar-Niasar, 2016) but only within the Darcy flow regime. Bruderer and Bernabé (2001) used pore-network modelling to simulate dispersion through 2D pore-networks with different degrees of heterogeneity. They modelled advection using a particle tracking

technique while diffusion was modelled as a discrete random walk. They observed a transition from Taylor-Aris dispersion in homogenous pore-networks, where the longitudinal dispersion coefficient is proportional to the square of the Péclet number ($D_L \propto Pe^2$), to the so-called mechanical dispersion in highly heterogeneous pore-networks, where the longitudinal dispersion coefficient is proportional to the Péclet number ($D_L \propto Pe$).

Bijeljic et al. (2004) investigated the longitudinal dispersion for a 2D pore-network equivalent to a Berea sandstone sample. They applied a Lagrangian-based transport model for a wide range of Péclet numbers and confirmed that diffusion dominates at low Péclet numbers ($Pe \leq 0.1$), while the transition regime, in which combined effects of advection and diffusion occur, was noticeable at $0.1 < Pe < 10$. They divided the advection dominated regime into two zones; the first zone when $10 < Pe < 400$ and the second when $Pe > 400$. They referred to the first zone as the boundary-layer dispersion regime, when advection dominates the mixing process, but particles still have some time to encounter low velocities near the solid matrix (pore throat walls) where diffusion can be observed. In this zone the power law coefficient (δ) was equal to 1.19, $\frac{D_L}{D_m} \approx P_e^{\delta}$. They referred to the second zone as the mechanical dispersion regime, when $Pe > 400$ and the longitudinal dispersion coefficient (D_L) is linearly dependent on Pe. Later, Bijeljic and Blunt (2007) used the same pore-network used by Bijeljic et al. (2004) to study transverse dispersion and concluded that the ratio between the longitudinal and the transverse dispersion coefficients is not constant and it is inappropriate to assume that the longitudinal dispersion coefficient is always one order of magnitude larger than the transverse dispersion coefficient.

Köhne et al. (2011) simulated solute transport, for both non-reactive and adsorbed solutes, through different intact soil samples using pore-network modelling and applying the mixed cell method. They used X-ray and Minkowski functions (Thompson, 1996) to generate pore-networks equivalent to the used soil samples and verified their results by performing laboratory experiments on the same samples. They acknowledged that using

Minkowski functions was a good predictive tool for producing the equivalent pore-networks and consequently for the pore-network simulations of the conservative solute.

Using pore-network modelling and the MCM, Babaei and Joekar-Niasar (2016) investigated the effect of the correlation length, which is known to increase with heterogeneity (Bruderer & Bernabé, 2001), for stochastically generated pore-networks, on the transport regime. They created a transport phase diagram with three regimes (diffusion-controlled, mixed advection-diffusion and advection-controlled regimes) at various correlation lengths ranging from small correlation length, which corresponds to an uncorrelated pore-network, to strongly correlated pore-networks with a larger correlation length. They concluded that the correlation length affects more the advection-controlled regime by causing an increase in the longitudinal dispersion coefficient in correlated (heterogeneity) pore-networks compared to uncorrelated (homogenous) pore-networks.

Jha et al. (2011) investigated the effect of diffusion on the dispersion coefficient by applying a particle tracking technique and using the PNM approach. They created a representative pore-network from a computer-generated random packing of equal spheres following the methodology proposed by Bryant and Blunt (1992). Jha et al. (2011) investigated, separately, the effect of streamlines splitting and joining at each pore body, the velocity gradient in pore throats due to the parabolic velocity profile in the direction perpendicular to the pore throat axis, and diffusion. They concluded that the advection movement causes solute particles to undergo a range of independent velocities and this leads to an asymptotically Fickian dispersion. However, when they considered the effect of velocity variation in the transverse direction in pore throats due to the parabolic velocity profile, they noticed that solute particles next to the pore throat walls are not free to move and this causes non-Fickian convective spreading. Finally, when they superimposed diffusion on advection, diffusion allowed solute particles near pore throat walls to enter the main flow streams and this allows all solute particles to undergo a wide range of velocities leading to a Fickian behaviour of dispersion.

Based on optimisation and using PNM, Mehmani et al. (2014) developed a streamline splitting method (SSM) to determine how the inflowing streamlines are distributing among the outflowing streamlines at each pore body. The SSM showed better results for investigating transverse dispersion in porous media compared to the results obtained from the MCM and the Continuous-Time Random Walk (CTRW) method. However, the Mehmani et al. (2014) study was limited to the Darcy flow regime.

2.7 Generation of pore-networks

In order to construct a 3D pore-network that is able to represent a real porous medium, there are three different approaches that can be followed. The first approach is called the grain-based model which was initiated by Bryant and Blunt (1992) and is used to generate a pore-network equivalent to a packing of grains by considering information about the grain diameters and locations. This approach was further extended to generate pore-networks from grains affected by swelling, compaction or sedimentation. While the second approach is to construct a representative pore-network using statistical distributions of basic morphologic parameters, e.g. pore body and pore throat size distributions, throat length distribution, coordination number distribution, spatial correlation between: adjacent pore bodies, adjacent pore throats, and neighbouring pore throats and pore bodies. Pore-network models can predict medium parameters (e.g. permeability) similar to the measured values by carefully choosing the pore body, pore throat and coordination number distributions of the pore-network. However, by using this second approach, the generated pore-network may not represent a typical morphology of the real medium, but it is similar statistically only to the modelled porous media. Moreover, the second approach is simple and can quickly simulate fluid flow properties in complex (heterogeneous) porous structures (Al-Raoush et al., 2003; Dong & Blunt, 2009; Gao et al., 2012; Xiong et al., 2016). The third approach is to directly map the porous media, e.g. from a 3D micro X-ray Computed Tomography image (CT-image), focused ion beams, scanning electron microscopy, nuclear magnetic resonance, mercury intrusion porosimetry,

and gas adsorption (Xiong et al., 2016). The third approach provides a direct spatial correspondence between the porous medium structure and the network structure. In the following review, the most relevant network generation approaches are summarised, however, readers interested in other methods are referred to the review paper by Xiong and Jivkov (2015).

Bryant and Blunt (1992) used 8000 measured coordinates of randomly packed uniform ball bearings provided by Finney (1968) to construct a representative pore-network of the medium. They performed Delaunay triangulation on the central 3367 spheres of the Finney pack. The vertices of the resulting tetrahedrons from Delaunay triangulation represent the bearing centres, while the inner volume of the tetrahedron represents a void space (pore body) (Figure 2-10). Each tetrahedral face represented a narrow entrance (pore throat) to the larger volume inside the tetrahedron. As each cell in the domain was represented by a tetrahedron, each pore body had 4 connected pore throats represented by the four faces of the tetrahedron, i.e. the coordination number was 4. Bryant and Blunt (1992) estimated the spherical pore body volume as the volume of the tetrahedral Delaunay cell minus the volume of the sphere segments located inside that cell. They also defined the pore throat length to be the distance between the adjoining Delaunay cells, while the cylindric pore throat radius is defined as the effective radius, r_{eff} (mm), as shown in Figure 2-11.

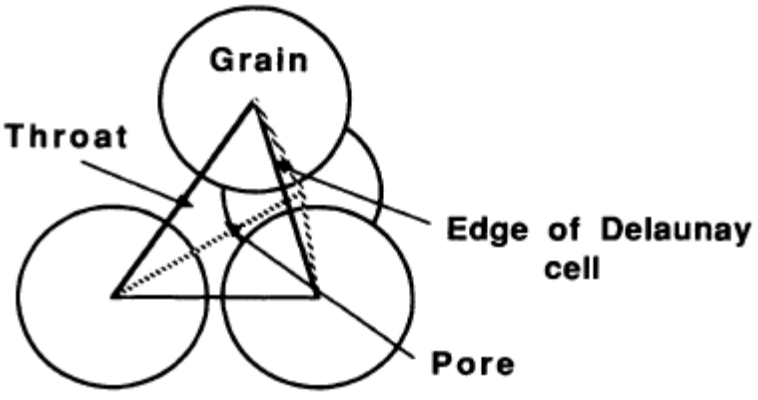

Figure 2-10 A Delaunay tetrahedral cell in a random packing of uniform spheres. The centre of the tetrahedral cell represents the pore body, while

each of the tetrahedral cell four faces represents a pore throat. The vertices of the cells represent the sphere centres, by Bryant and Blunt (1992).

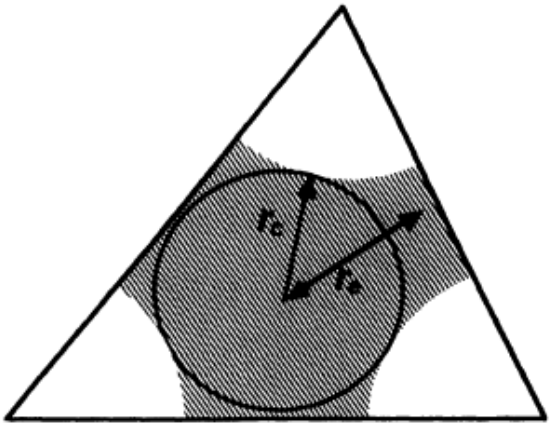

Figure 2-11 One face of a Delaunay cell with two definitions of an equivalent pore throat radius. r_c (mm) is radius of the largest inscribed circle that can fit in the void space within the cell face. r_e (mm) is the radius of the circle that has an area equal to the void area (shaded in grey). The pore throat radius is estimated as $r_{eff} = 0.5\ (r_c+r_e)$, by Bryant and Blunt (1992).

Bryant et al. (1993) extended the previous work of Bryant and Blunt (1992) and used the same Finney coordination measurements (Finney, 1968) to obtain the simplicial cell (Delaunay cell) tessellation of 2000 central spheres of that packing. They acknowledged that the basis of their approach belongs to Mason (1967, 1971). In their pore-network, each cell was represented by a tetrahedron, so each cell had a fixed coordination number of four. Bryant et al. (1993) approximated their pore-network by a group of flow paths (pore throats) which simulate the bonds between cells. They divided each bond into a number of segments (12 segments) along its flow path axis. Each of these segments is represented by a conical frustum as shown in Figure 2-12. They defined the geometry of each conical frustum by assigning an inlet face radius, outlet face radius and axial length which all depend on the geometry of each Delaunay cell. They concluded that their proposed pore throat geometries provide a better estimation of the permeability.

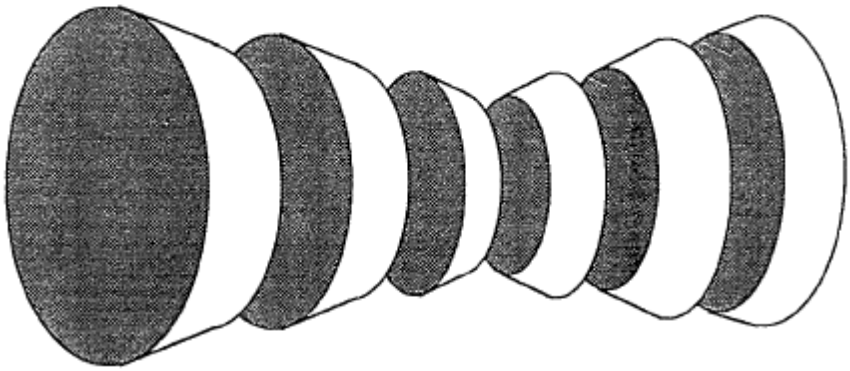

Figure 2-12 A group of conical frusta used for estimating the conductance of each pore throat, by Bryant et al. (1993).

Gao et al. (2012) presented two methods for generating pore-networks from porous media. The first method produces a pore-network from a random computer simulated packing of sphere. That method requires knowledge of all sphere radii and locations for which they used the PFC3D discrete element code. They used an algorithm (Chan & Ng, 1988) to construct the tetrahedral Delaunay tessellation between spheres. Then, they developed a method to solve the problem resulting from the division of a single void (pore body) into several zones by the tetrahedral tessellation. That method depended on defining three different interconnectivity levels between neighbouring pore bodies according to the extent of their overlapping. Later, depending on the interconnectivity level between each two neighbouring pore bodies, they assigned pore throat geometries as Biconical abscissa Asymmetric CONcentric (BACON) shapes. The second method produces a lattice structured (the pore body centres are located on regular lattice nodes and the pore bodies are separated by equal distances) pore-network equivalent to the porous medium. In that method, the regular spacing between pore bodies was adjustable according to the porosity of the simulated porous medium. They started by connecting each pore body to the nearest neighbouring 26 pore bodies using pore throats in different directions and with variable lengths. They used a statistical distribution (e.g. Gaussian or log-normal distribution) to assign random pore body radii, and then correlate each pore body size and its corresponding coordination number. All pore throats were assigned a BACON shape using two power

functions. They concluded that the second method can be used as a predictive approach for quantitative analysis of flow though porous media.

Joekar-Niasar et al. (2008) used two regularly structured 3D lattice pore-networks to investigate the relationships between capillary pressure, saturation, interfacial area and relative permeability. Their first pore-network, called the tube model, consisted of cylindrical pore throats only, while the second pore-network consisted of both spherical pore bodies and cylindrical pore throats. They used a truncated random log-normal number generator to assign the pore throat radii for the first network and the pore body radii for the second pore-network. They used a fixed coordination number of 6 for both types of networks and for the second pore-network they developed a procedure to assign a pore throat radius in a way that accounts for the correlation between the pore throat and its two neighbouring pore bodies. Joekar-Niasar et al. (2008) concluded that the second pore-network produced more accurate and realistic results compared to the oversimplified tube model.

In Babaei and Joekar-Niasar (2016) work, the authors statistically generated pore-networks with different degrees of heterogeneity. Firstly, they filled the domain with randomly generated points that act as pore body centres, and they set a threshold for the minimum distance between any two neighbouring points to avoid pore bodies overlapping. Secondly, they generated correlated fields for pore body radii using the field generator developed by Nowak et al. (2008). The degree of heterogeneity in each pore-network was changed by changing the correlation length scale. Then, they used a Delaunay triangulation methodology to generate the connections between points (pore bodies), where the vertices of the triangulations represent pore body centre coordinates and the edges represent pore throats. As Delaunay triangulation results in a large number of pore throats/edges, they excluded some extra-long pore throats. Finally, they used the depth average search algorithm to label the network.

Al-Raoush et al. (2003) showed two different methods to construct a pore-network from 3D CT-images of unconsolidated porous media. For both

methods, they used a computer-generated packing of spheres. The first method was based on the medial-axis (MA) analysis of a digital image of the pore space. The medial axis of an object is known as the skeleton of that object that runs along its geometrical middle. In order to obtain the medial axis of the image, they used the 3DMA software package (Lee et al., 1994; Lindquist et al., 1996). The obtained medial axis represents the flow paths (pore throats) while the intersections of these paths represent pore bodies. Then they used a voxel-based calculation method to determine the inscribed radius of each pore body and pore throat. The second method was based on a modified Delaunay tessellation (MDT) of the grain locations. This method followed the same approach used by Bryant and Blunt (1992) except that they added some modifications for large pore bodies that occupy more than one tetrahedron. For this specific case, they allowed the merging between tetrahedrons into one larger polyhedral.

Dong and Blunt (2009) used a maximal ball algorithm to extract the pore-network equivalent to a medium from its CT-image. The maximal ball algorithm searches for the largest sphere that can be centred on each voxel of the image and just touches the grain. This process may result in some balls being included or intersecting with each other, in such cases all the smaller balls are discarded and the rest are considered as maximal balls. Finally, the largest maximal balls are defined as pore bodies, while the smallest maximal balls between pore bodies are defined as pore throats. The outputs from that code are pore body and pore throat radii, pore body Cartesian coordinates, pore body coordination numbers, pore throat lengths, pore body and pore throat volumes, and pore body and pore throat shape factors. Dong and Blunt (2009) obtained a good match for the resulting permeability of the pore-networks extracted using their method, however, they did not verify their method for the case of non-Darcy flow and they concluded that their pore-network extraction code underestimates the pore throats' size and tends to generate many small pore throats.

The most recent pore-network extraction code, used throughout this thesis, was developed by Raeini et al. (2017) in which they used a medial axis transform and coarse discretisation of the 3D CT-image combined with

single phase flow direct numerical simulation (DNS) to parameterise the pore-network. First, they identified pore bodies and pore throats by using a maximal ball algorithm in a way similar to that used by Dong and Blunt (2009). Second, they discretised the void space into pores, these pores are further divided into smaller elements called "half-throat connections". Then, by using single phase flow direct numerical simulation on the underlaying CT-image at different discretisation levels, they defined the parameters (e.g. volume, cross-sectional area, and conductivity) of each half-throat. Finally, they defined the connectivity between pore throats and pore bodies, and the outputs files that contain pore body and pore throat radii, pore body Cartesian coordinates, pore body coordination numbers, pore throat lengths, pore body and pore throat volumes, and pore body and pore throat shape factors. The generated pore bodies and pore throats may have either triangular, square or circular cross sections. The shape of the pore cross-sections is selected based on the level of irregularity over the wall of the narrow pores which is quantified with shape factor parameter, G (-). The shape factor is a dimensionless parameter, defined as $G = \frac{a}{p^2}$, where a (mm^2) is the average cross-sectional area of the pore throat or the pore body and p is its average perimeter (Mason and Morrow, 1991; Valvatne and Blunt, 2004). The value of the shape factor decreases when the shape of the pore space wall surface becomes irregular. According to the geometrical definitions of 2D geometries, the value of the shape factor ranges from zero, for a slit shape triangle, to $\frac{\sqrt{3}}{36}$ for an equilateral triangle, whilst for squares and circles, the shape factor has values of $\frac{1}{16}$ and $\frac{1}{4\pi}$ (Figure 2-13), respectively (Oren et al., 1998; Valvatne & Blunt, 2004). The shape factor definition for more complex geometries such as hyperbolic polygonal cross-sections can be found in Joekar-Niasar et al. (2010).

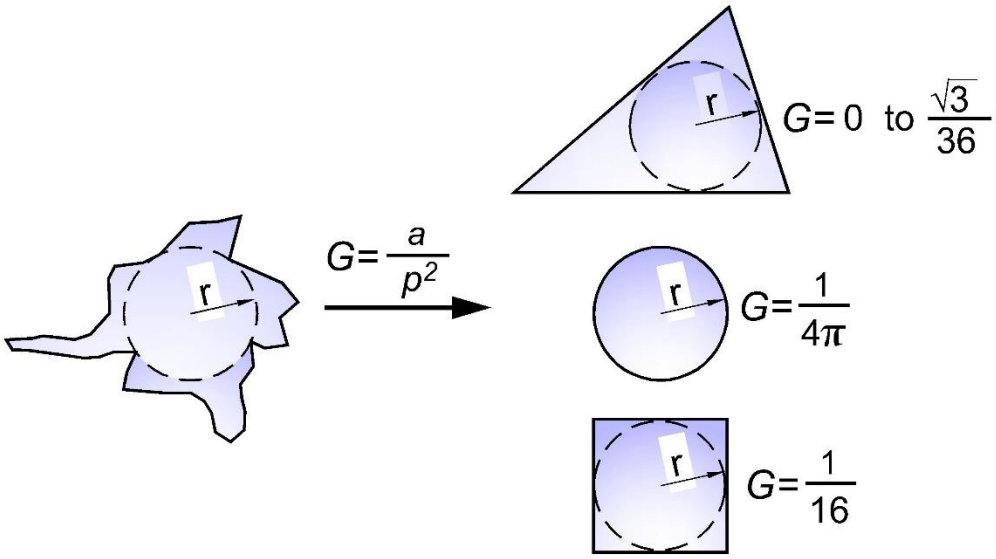

Figure 2-13 The dimensionless shape factor of any pore, after Dong (2007).

2.8 Summary and research gaps

All previously mentioned pore-scale modelling methods (percolation models, Lattice-Boltzmann models, smoothed particle hydrodynamics approach, level-set models and direct numerical simulations) are computationally more expensive compared to pore-network models which are computationally affordable for simulating larger domains. Nevertheless, when PNM is used, the pore geometries are idealised into simple geometries that represent the main features of the pores, and this may result in losing some geometrical information (Joekar-Niasar & Hassanizadeh, 2012). Blunt et al. (2002) stated that if the complex pore geometry of a medium can be effectively represented, then pore-scale models can provide accurate predictions of the flow behaviour. Therefore, to minimize the information that might be lost when generating a pore-network, and to accurately represent the void space, the state of the art pore-network extraction code developed by Raeini et al. (2017) has been used throughout the presented work.

To my knowledge, there are only five previous studies that modelled non-Darcy flow using PNM (Thauvin & Mohanty, 1998; Wang et al., 1999; Lao et al., 2004; Lemley et al., 2007; Balhoff & Wheeler, 2009) and none of these considered the effect of pore body and pore throat shape factors (G) on the flow simulation, which is considered of high importance for natural

porous media that are usually composed of pores with irregular shapes. It is also necessary for simulating two or multi-phase flow within the non-Darcy flow regime. Moreover, based on the above literature, it was found that a new 3D pore-network model, capable of simulating non-Darcy flow and which can overcome all the limitations in the above five pore-network modelling studies; i.e. fixed value for the maximum coordination number (Lao et al., 2004; Lemley et al., 2007), 2D simulations only (Lao et al., 2004), uncertainty in some equations that calculate the inertial effects due to expansion and contraction (Thauvin & Mohanty, 1998; Wang et al., 1999; Lao et al., 2004; Balhoff & Wheeler, 2009), the use of regular structured pore-networks only (Thauvin & Mohanty, 1998; Wang et al., 1999), lack of calibration (Thauvin & Mohanty, 1998; Wang et al., 1999) and neglecting the effect of pore shape factors, is needed. It is important to determine the threshold (the onset of non-Darcy flow) after which this model should be applied and Darcy's law is no longer valid. It is also noted that none of the above-mentioned studies that used pore-network modelling for non-Darcy flow investigated in detail the onset of non-Darcy flow. However, Thauvin and Mohanty (1998) mentioned that Darcy's law was valid for Reynold's numbers < 0.11, but this value was specific only for the regular structured pore-network used in their study. Nevertheless, Lemley et al. (2007) followed the value recommended by Janicek and Katz (1955) and mentioned that the onset of non-Darcy flow is usually observed when the Forchheimer's number (Equation 2.18) is greater than or equal 0.1, however, this value was obtained from studying gas flow through different porous media.

The work of Martins et al. (2007) was the only developed pore-network model to simulate turbulent flow, however, they assumed a constant value for the expansion and contraction coefficients for each pore throat and they were able to obtain results that agree with previous experimental work by fitting the values of this coefficient and the coordination numbers of the pore-network. Moreover, they applied Blasius equation to obtain the friction factor for each pore throat in the turbulent flow regime, but they did not verify if the flow is fully developed in each pore throat.

To my knowledge, all solute transport pore-network modelling studies were limited to the Darcy flow regime. The effect of non-Darcy flow and inertial forces on solute transport in porous media has never been investigated yet using PNM. The two studies (by Wood (2007) and Nezhad et al. (2019)) which investigated the inertial effects on dispersion did not provide satisfactory results. Moreover, all previous PNM studies that used the Taylor-Aris equation to model solute transport using the MCM, did not check the residence time needed to reach an asymptomatic state for each pore throat in the pore-network which may produce misleading results.

Based on the above summary, and referring to Figure 2-7a, at the pore-scale, flow and solute transport within the laminar linear and laminar nonlinear flow regimes will be modelled in Chapter 4 and Chapter 6. In Chapter 5 and Chapter 7, flow and solute transport within all possible flow regimes, including the pore-scale laminar, transition and turbulent flow regimes, will be modelled. The models presented in these chapters are proposed to overcome most of the mentioned limitations in the previous studies and to cover some of the previously mentioned research gaps which have not been investigated before. Moreover, the experimental work presented in Chapter 3, is performed to verify the proposed flow and solute transport models within all possible macro-scale flow regimes.

Chapter 3

Sample preparation, scanning and experimental work

3.1 Introduction

Most of the previous work that used pore-network modelling to simulate flow through porous media assumed Darcy flow and applied the Hagen-Poiseuille (Hagen, 1839; Poiseuille, 1841) analytical equation at the pore-scale. They did not verify their models assuming that using analytical equations is sufficient, however, this is not the case for the Forchheimer and turbulent flow regimes where semi-analytical equations are used. There are two sources of uncertainties that may affect the results of the proposed Forchheimer and turbulent flow PNM simulation codes. The first is the proposed system of equations used for flow simulation, while the second is the approximations associated with the method used to generate a pore-network equivalent to a specific medium and the uncertainties resulting from simplifying the irregular pore shapes into simple shapes for which analytical or semi-analytical equations can be applied (Balhoff & Wheeler, 2009). It is very difficult to test a model's performance with two main sources of uncertainties. Therefore, the laboratory experiments presented in this chapter were proposed to minimise the uncertainties that might affect the simulation results. A packed spheres sample was prepared for the laboratory experiments, then the same sample was CT-scanned and its CT-image was used to produce an equivalent pore-network using the state-of-the-art pore-network extraction code developed by Raeini et al. (2017). To my knowledge, no previous work used a medium CT-scan to simulate turbulent flow through porous media, i.e. using any previous data in the literature to verify the proposed turbulent flow code is prone to some uncertainties associated with the method used to generate a pore-network that represents the medium used in the literature.

This chapter explains the procedures followed to prepare and scan the packed spheres sample used for the flow and solute transport experimental tests. The experimental facilities, procedures and results are presented. Two

types of experiments were conducted on the packed spheres sample; a) steady state flow tests to measure the discharge, velocity and pressure loss within the Darcy, Forchheimer and turbulent flow regimes, and b) solute transport tests to measure the breakthrough curves and magnitude of dispersion coefficients through the sample.

3.2 Sample preparation and experimental setup

The spheres' average diameter and the dimensions of the packed spheres sample were designed to achieve all flow conditions (Darcy, Forchheimer and turbulent flow regimes) using the existing laboratory facilities at the School of Engineering, at the University of Warwick. For that purpose, the samples and results of the previous experimental work conducted by Fand et al. (1987), Kececioglu and Jiang (1994) and Bağcı et al. (2014) on packed spheres were studied and their data were used as a reference. The proposed sample is composed of uniform spherical glass beads with average diameter (d_m) of 1.84 ± 0.14 mm. The spheres were packed in a Perspex circular pipe of 300 mm length and 50 mm internal diameter. Two fine steel meshes were used at both ends of the sample to hold the spheres in place. The packing process was done in layers and each layer was compacted to achieve minimum porosity of the sample (36%). The sample length was proposed to achieve head loss, through the sample, ranging from a few millimetres up to ~2.5 m, while the sample diameter was chosen equal to the diameter of the main recirculating pipe of the test rig. The porous sample was placed in a recirculating pipe system (a diagram is shown in Figure 3-1) with a sump of approximately 2.5 m^3. Water was used as the working fluid at different discharge rates ranging from ~0.001 to 0.18 l/s, and for each run, the discharge rate was measured manually since the readings of the provided digital flowmeter (Siemens Sitrans FM Magflo MAG 5100W flowmeter) were fluctuating especially at low discharges. The discharge was measured by collecting the volume of water over a specific time period. Depending on the discharge, the collected water volume ranged from ~0.1 to 2 litres and the collection time was measured using a digital stopwatch with ± 0.01 s accuracy. A 2-Litre measuring cylinder was used to measure the volume of water collected with ± 10.00 ml accuracy, while at very low discharges

another 0.25 Litre measuring cylinder with ± 2.0 ml accuracy was used. The head loss measurements were done using two manometer tubes located 50 mm after the sample inlet and before the sample outlet to eliminate the effect of boundaries on the flow, i.e. the head loss was measured through a distance of 200 mm in the porous medium (Figure 3-1). To ensure the accuracy of manometric measurements at low pressure gradients, an SPI digital depth gauge with accuracy ± 0.01 mm was used to measure the manometric heads inside fixed, 25 mm wide manometric tubes. While at larger head differences (> 500 mm), graduated cylinders were used to measure the manometric head difference with ± 1 mm accuracy. Moreover, before taking any measurements, water was allowed to run through the recirculating system for a period sufficient to remove any air from the system.

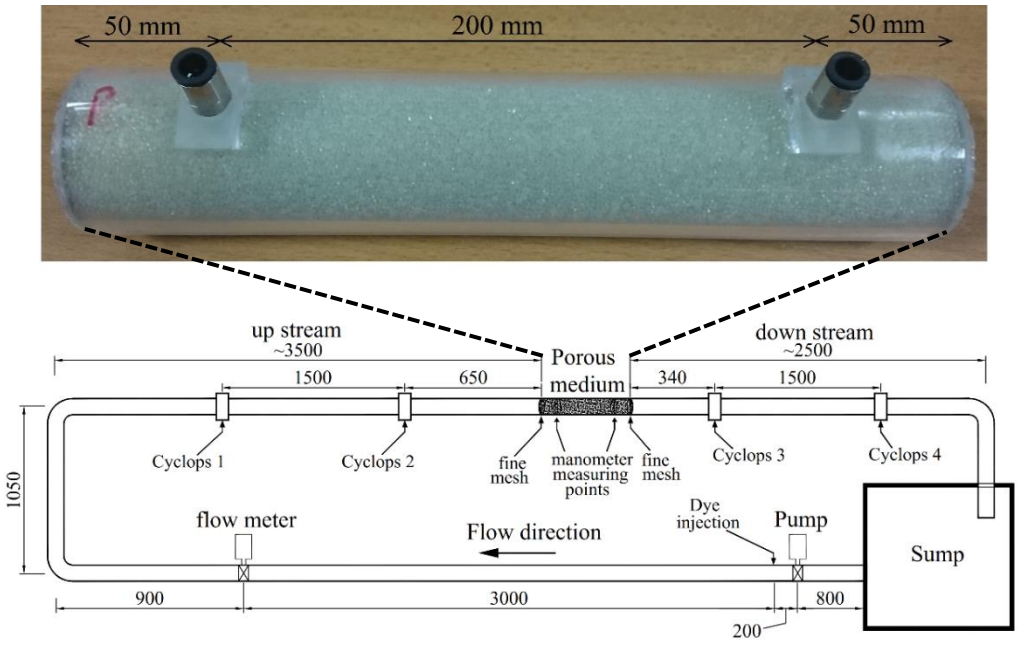

Figure 3-1 A schematic diagram of the laboratory test rig and a photograph of the packed spheres sample showing the position of the manometer measuring points, all dimensions are in millimetres.

The solute transport tests were done at different discharge rates on the same packed spheres sample. The tests were performed using a conservative fluorescent dye (Rhodamine WT), with molecular diffusion (D_m) equal to 2.9×10^{-10} (m^2/s) (Chandler, 2012), as a tracer. A peristaltic pump was used to inject the dye at the beginning of the upstream recirculating pipe (20 cm

after the water pump, Figure 3-1) to ensure that the dye has travelled a long distance and is fully mixed with water before measuring its concentration using a Turner Designs Cyclops-7 Submersible Sensor (referred to as "Cyclops"). Four Cyclops sensors were used to measure the dye concentration over time for each test and their locations are shown in Figure 3-1. The dye was injected continuously over time until the concentration detected at all Cyclops sensors reached a constant value over time. The solute transport tests were done using a methodology similar to that used by Guymer and Stovin (2011) to determine the dispersion through surcharged manhole structures. Following that methodology, and by recording the breakthrough curves (BTCs) at Cyclops 2 and Cyclops 3, then by fitting the BTCs to the 1D ADE, the longitudinal dispersion coefficient ($D_{L,\ pipe+medium}$) is determined for the whole system (the porous medium and the recirculating pipe) in between these two Cyclops sensors. Then, by recording the BTCs at Cyclops 1 and Cyclops 2, or at Cyclops 3 and Cyclops 4, the longitudinal dispersion coefficient ($D_{L,\ pipe}$) of the recirculating pipe only is determined. Finally, for each run, the longitudinal dispersion coefficient of the porous medium is determined by subtracting the value of $D_{L,\ pipe}$ from $D_{L,\ pipe+medium}$.

The Turner Designs Cyclops-7 Submersible Sensor has a front LED which produces a green light, and a front sensor that receives back the fluoresced light (Figure 3-2 a). Each Cyclops sensor is connected to a data logger and a power supply that provides an electric current with voltage range from 3 to 15 Volts. The received fluoresced light is converted into a voltage output which can be interpreted as dye concentration using a calibration plot. Three different modes (gain settings) can be used for the Cyclops sensor; X1 which can detect concentration from 0 to 1000 parts per billion (PPb), X10 which can detect concentration from 0 to 100 PPb and X100 which can detect concentration from 0 to 10 PPb. When the gain increases, the concentration range decreases and the sensitivity of the Cyclops sensor increases. In this work only gain X1 and X10 were used and the Cyclops sensor calibration plots were developed for each gain. A 12-volt battery and a control box (Figure 3-2 b-c) were used for switching easily from one gain

to another. To calibrate the Cyclops sensors, a linear calibration plot needs to be established using samples with known concentrations. The Cyclops' manual recommends using different samples, with known concentration, in a non-fluorescent glass beaker placed on a non-reflective black surface. Then, a linear relationship between the output voltage and the known concentration can be established. When this calibration method was followed, the obtained calibration plot was not accurate because the measurements were affected by the surrounding room lighting and also because the signals received from a Cyclops sensor placed in a glass beaker differ from the signals received from the same Cyclops sensor mounted in the test rig. So, following Hart (2013), the succeeding calibration procedures were used to calibrate the Cyclops while mounted in the test rig. The sump of the test rig was filled with a known volume of clear water, then the proposed amount of dye was added to the sump to yield a dilution with known concentration (Figure 3-3). The dye was mixed manually in the sump, then the flow was allowed to circulate for a few minutes to ensure that the dye was completely mixed with water. The sump of the test rig was filled with different known concentrations and the signal from all the cyclops sensors mounted in the test rig for these known concentrations were obtained to construct the calibration plot shown in Figure 3-7. Next to the mounted Cyclops sensors, the circulating tube was wrapped with black paper to minimise the error resulting from the room lighting. After calibration, and before performing the experiments, the water in the sump was replaced with clear water.

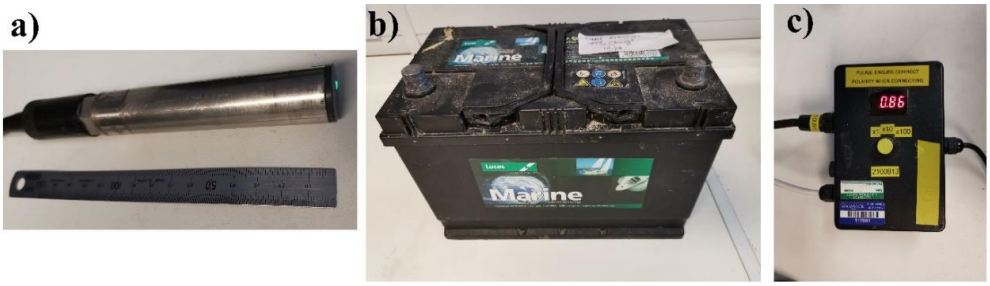

Figure 3-2 Photographs of the a) Cyclops sensor, b) 12-Volt battery and c) power unit.

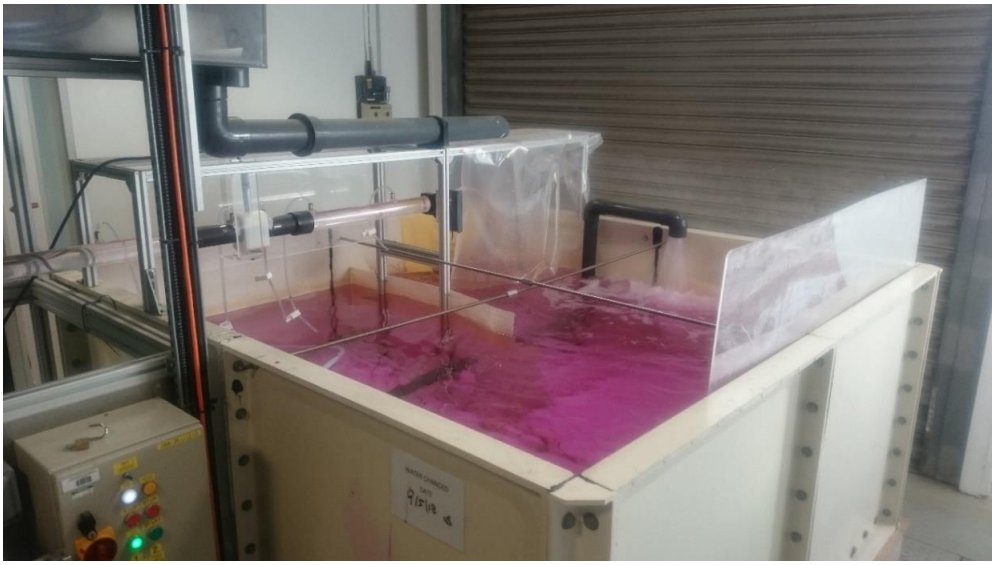

Figure 3-3 Filling the sump with a known concentration during the Cyclops sensor Calibration process.

3.3 X-ray scanning and determining the REV of the sample

Before performing the proposed flow and solute transport experiment, the packed spheres sample was scanned using a micro X-ray Computed Tomography (XCT) scanner to produce a 3D image of the sample micro-structure (see Figure 3-5). The obtained 3D XCT-image was used later as input to the pore-network extraction code. The scanning process was done at Warwick Manufacturing Group (WMG). Four XCT scans were performed to examine the packed spheres sample utilising Nikon XT H 225/320 LC (Figure 3-4) and the settings provided in Table 3-1. The XCT settings were chosen to achieve optimum penetration and minimise noise. A physical radiation filter was used to reduce beam hardening and cupping errors. The resolution of the scans (33 μm) was achieved based on the diameter of the specimen. The four scans were combined together to provide the full volume of the middle part (between the two manometer measuring points) of the sample.

Figure 3-4 The (Nikon XT H 225/320 LC) micro X-ray Computed Tomography scanner, located at Warwick Manufacturing Group (WMG), used to scan the packed spheres sample.

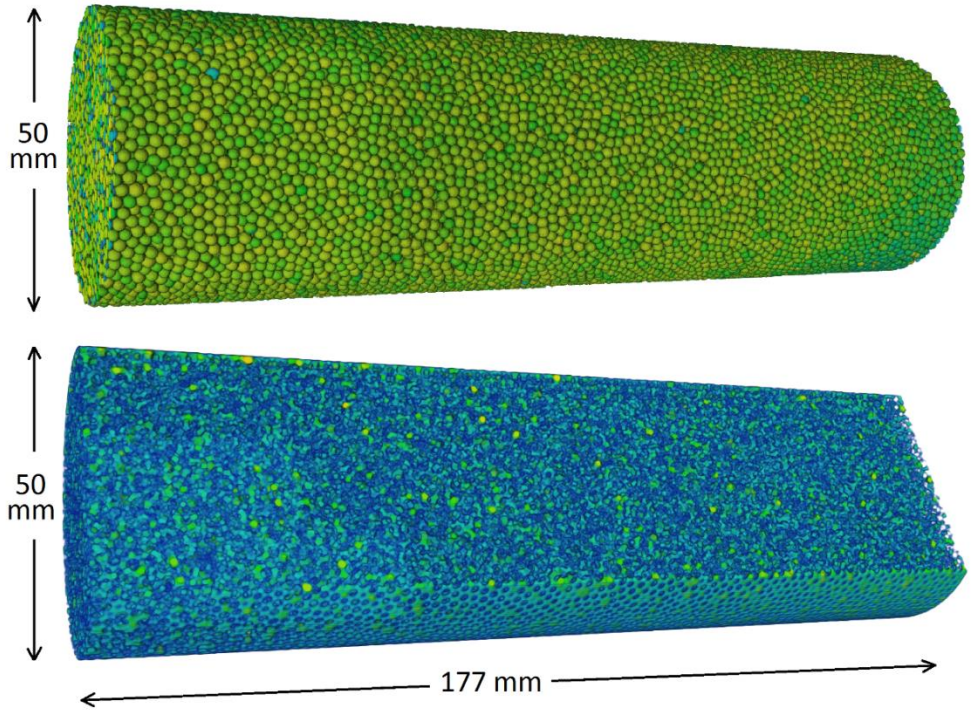

Figure 3-5 The packed spheres sample field of view and a longitudinal cross-section through the sample.

Table 3-1 The micro-XCT scanning settings.

XCT scanning settings	
Voltage (kV)	145
Current (μA)	145
Exposure time (s)	2
Gain (dB)	24
Filtration Sn (mm)	0.25
Resolution (μm)	33
Number of projections	3142

All pore-scale modelling methodologies, described in Section 2.2, have limitations regarding the size of the sample. These limitations are attributed to the available computational power, and for this reason, modelling the flow behaviours for large samples is not possible and required the use of other upscaling techniques. Thus, all pore-scale modelling methodologies perform their computations on a Representative Elementary Volume (REV). An REV can be defined as a representative portion or subvolume of the medium, when selecting such a volume at different locations in the sample, the resulting parameters (ϕ, K_D or β) of the subvolumes should not vary significantly (Bear, 1972), as seen in Figure 3-6. The scanned middle part of the packed spheres sample, which has the dimensions of 50 mm × 50 mm × 177 mm, was used to determine the REV because using the whole volume for simulations required computational resources more than those available. To find an REV which represents the properties of the whole sample, a conventional approach was followed, and a code was developed to generate random coordinates for cubic subvolumes with different cube lengths (5, 10, 15, 20, 25, 30, 35 and 50 mm), and 10 different crops at random locations were tested for each cube size. For each single crop of the XCT image, a pore-network was extracted using the pore-network extraction code developed by Raeini et al. (2017), and the developed pore-network non-Darcy flow model, shown in Chapter 4, was used to estimate the porosity, ϕ (%), Darcy-permeability (Equation 2.1), K_D (mm^2), and non-Darcy coefficient (Equation 2.3), β (1/mm).

Figure 3-6 shows an idealised relationship for the values of a medium parameter at different cubic subvolume lengths of the medium, after Costanza-Robinson et al. (2011). Three zones (I, II and III) are shown in

Figure 3-6. In zone I, the fluctuations in the parameter value (e.g. porosity) are due to pore-scale heterogeneity, i.e. due to the change of pore size from one location to another in the sample. In zone II, the parameter value is independent of the REV length and it should be representative of the medium at large scale. A minimum size for the REV is the size at the left-hand boundary of zone II. In zone III, these changes in the parameter value are associated with the macro-scale heterogeneity of the medium. In a heterogeneous porous media, zone II may be difficult to define.

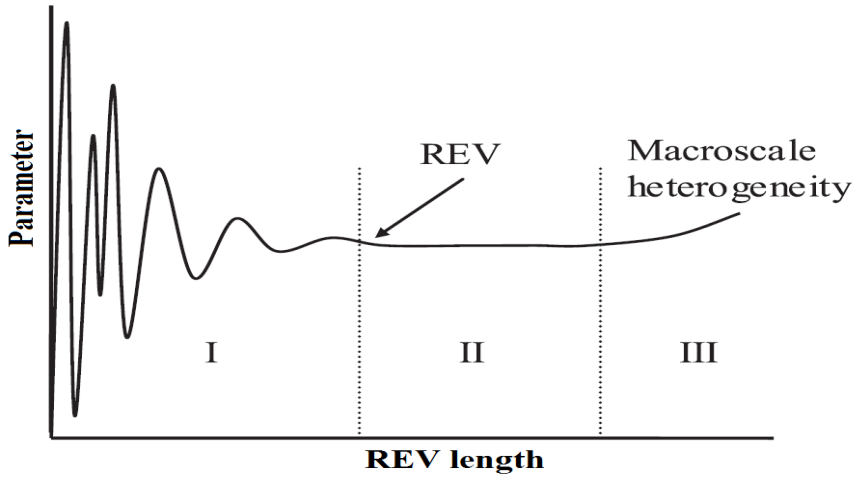

Figure 3-6 Conceptual schematic representing the idealised relationship between a parameter (e.g. ϕ, K_D or β) and the scale of the measurement (REV length), by Costanza-Robinson et al. (2011).

3.4 Results

3.4.1 The Cyclops calibration plots

The calibration plots, shown in Figure 3-7, were obtained from the Cyclops sensors' calibration process for X1 and X10 gains. The plots show a linear relationship between the output voltage received from the Cyclops sensor and the concentration. The correlation coefficient, obtained by fitting a straight line through the values, for all relationships is 0.999 or higher.

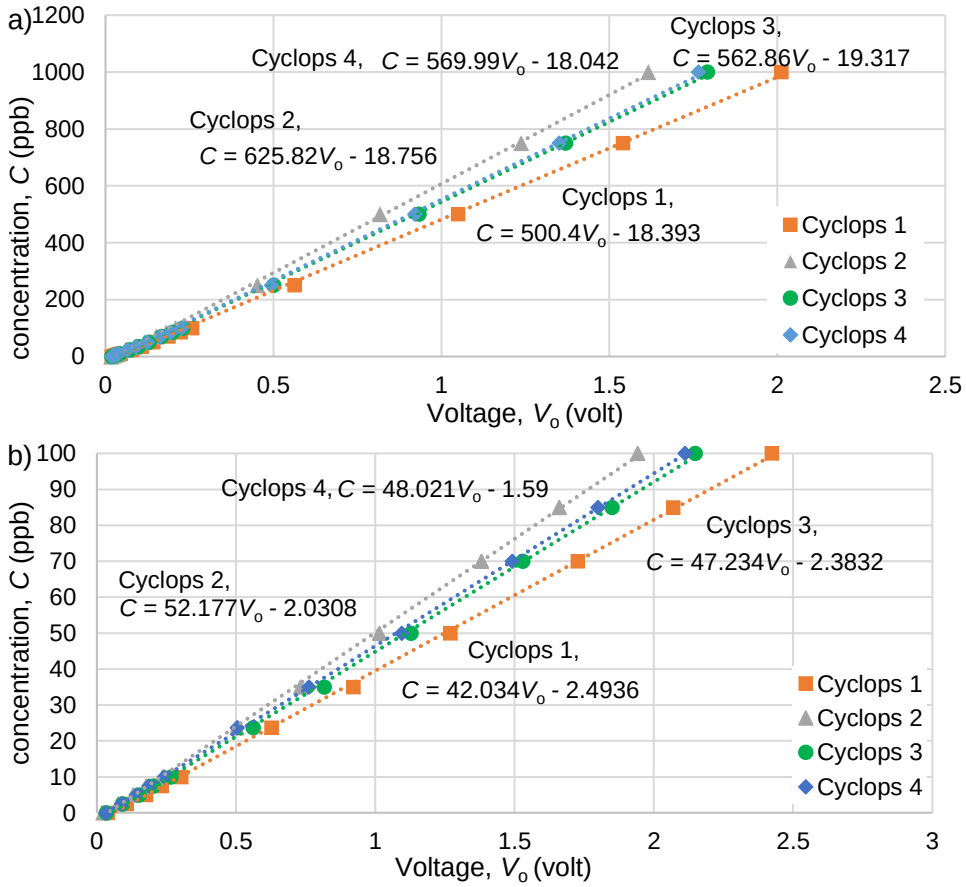

Figure 3-7 The calibration plot of the four Cyclops sensors, for a) X1 gain and b) X10 gain. The correlation coefficient for all relationships is 0.999 or higher.

3.4.2 Determining the REV size

Figure 3-8 shows the obtained porosity, Darcy-permeability and non-Darcy coefficient values for different subvolume cube lengths (5, 10, 15, 20, 25, 30, 35 and 50 mm) of the packed spheres sample. It can be produced by applying the proposed non-Darcy flow model (Chapter 4) to the pore-networks extracted from all subvolume crops of the packed spheres' XCT-image (see Section 3.3). In Figure 3-8, a suitable REV might be a subvolume cube with 30 or 35 mm length, which is a common value of the plateaus in figures 3-8(a-c) associated with minimum fluctuation, i.e. minimum standard deviation. However, this is not the case for the relatively small sample of 50 mm diameter used in the laboratory, considering its large average bead diameter of 1.84 mm. For this specific case, using an REV length less than 50 mm results in eliminating the effect of the containing pipe wall or boundaries. Due to the small size of the sample, the

boundaries of the containing pipe have a high effect on the estimated medium parameters as shown in Figure 3-8. For that reason, an REV length of 50 mm was selected to consider the effect of the external pipe on the medium structure and on the flow behaviour through the medium.

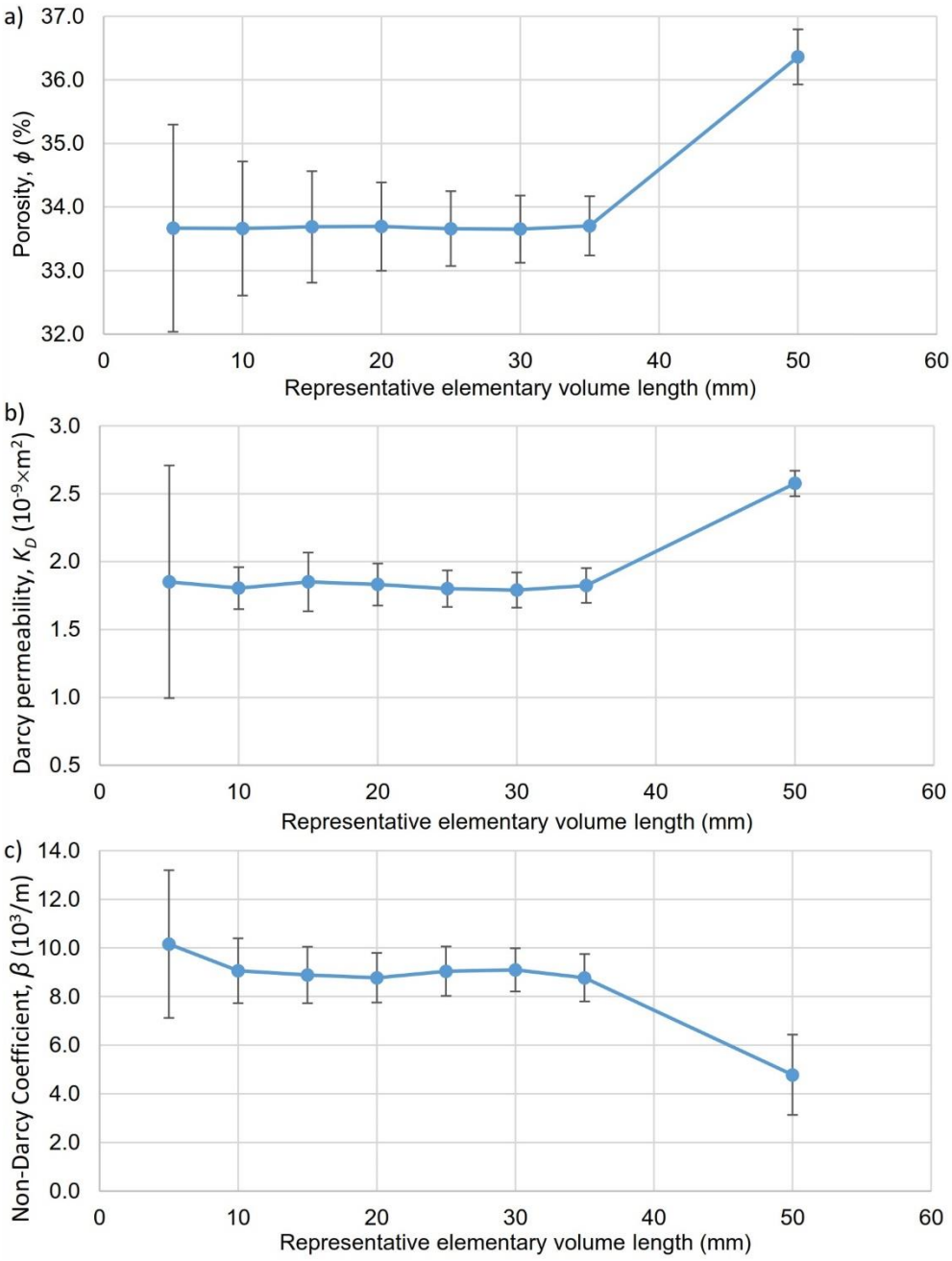

Figure 3-8 Variation of a) porosity, b) Darcy-permeability and c) the non-Darcy coefficient for different cubic subvolumes (10 crops for each REV length) of the packed spheres (d_m = 1.84 mm) sample. The values in blue represent the mean of 10 different values for each REV length, while the

error bars represent the standard deviation of these estimated 10 values of each parameter.

3.4.3 Flow test experimental results

During the flow test experiments, the measured discharge ranged from 0.001 to 0.18 l/s. Figure 3-9 shows the dimensionless head gradient ($\Delta h/L$) versus flow superficial velocity (v), where v (mm/s) represents the discharge divided by the whole cross-sectional area of the sample. The head loss measurements were obtained through the intermediate 200 mm of the sample. The plot shown in Figure 3-9, shows a linear relationship at very low velocities (when v < 4 mm/s), and within this range, Darcy's law (Equation 2.1) was applied to estimate the medium Darcy permeability, K_D (mm^2). Figure 3-10 and Figure 3-11 demonstrate the normalized dimensionless pressure gradient $\left(\frac{\Delta P\, K_D}{L\, \mu\, v}\right)$ versus Reynold's number (Re (-) and Re_K (-)). For Re (Equation 2.12), the characteristic length was chosen equal to the average particle diameter of the packed spheres (d_m = 1.84 mm), while for Re_K (Equation 2.16) the characteristic length is equal to the square root of the sample Darcy permeability. In Figure 3-10 and Figure 3-11, the change of the slope of the results represents different flow regimes, and from the figures the onset of non-Darcy flow and the onset of turbulent flow are determined when Re is equal to 7.5 and 98, and when Re_K is equal to 0.19 and 2.54, respectively. Using a Forchheimer plot (Section 2.1) as presented in Figure 3-12, the Forchheimer coefficients for the non-Darcy, β (1/mm), and turbulent flow regimes, β` (1/mm), can be determined. From the experimental results, the values of $K_D$, $\beta$ and $\beta$` are equal to $2{,}250\times10^{-12}$ m^2 ± 7%, 10,871 m^{-1} ± 11% and 7,568 m^{-1} ± 11%, respectively.

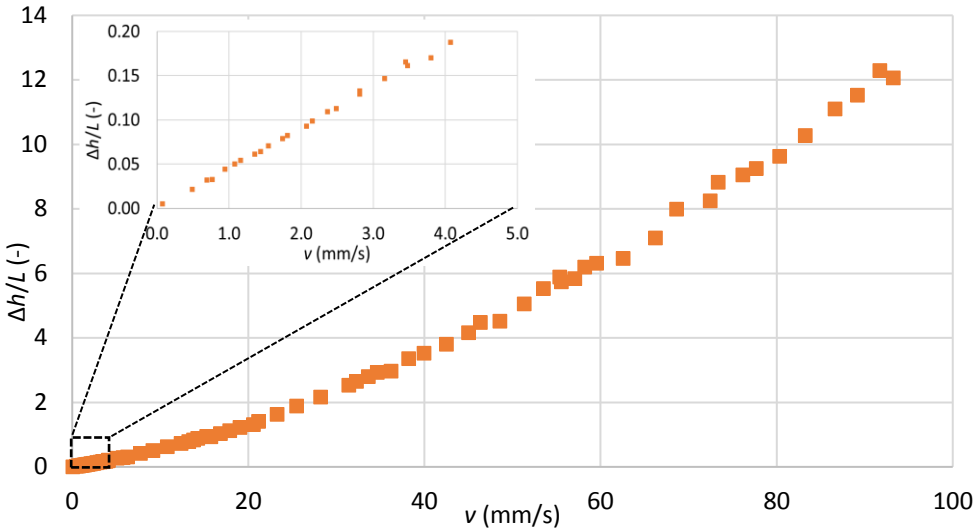

Figure 3-9 The head gradient ($\Delta h/L$) vs. flow superficial velocity (v), obtained from flow test experiment for the middle part (L = 200 mm) of the packed spheres (d_m = 1.84 mm) sample.

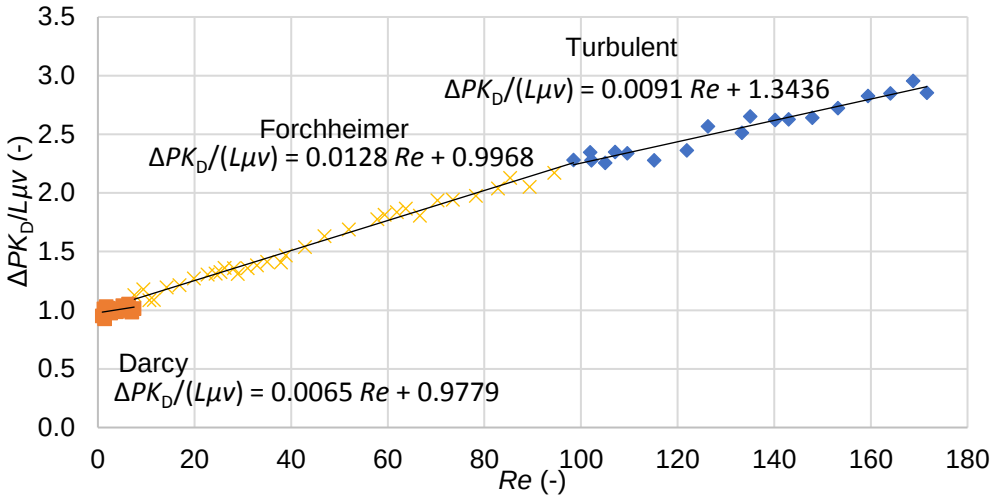

Figure 3-10 The normalised dimensionless pressure ($\Delta PK_D/L\mu v$) versus Reynold's number (Re) for the packed spheres (d_m = 1.84 mm) sample. The change of the slope of the results represents different flow regimes.

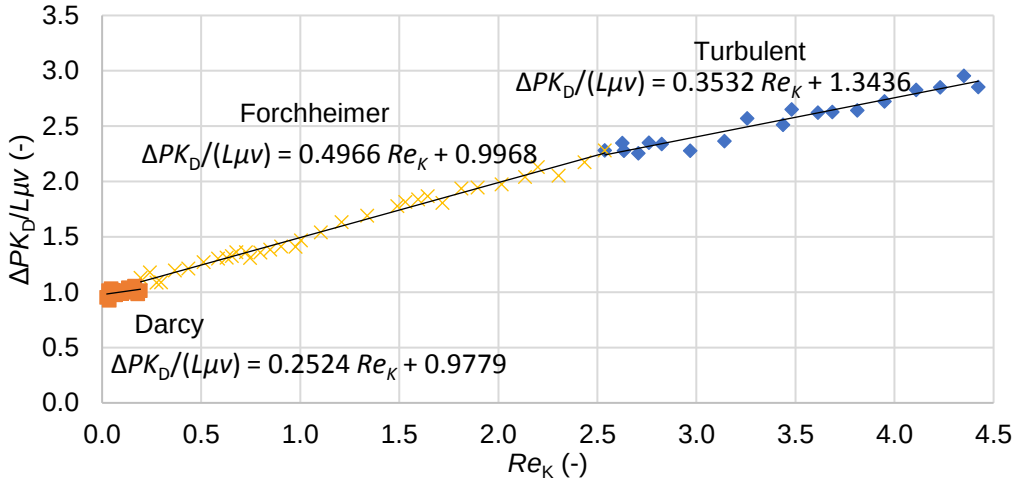

Figure 3-11 The normalised dimensionless pressure ($\Delta PK_D/L\mu v$) versus Permeability based Reynold's number (Re_K) for the packed spheres (d_m = 1.84 mm) sample. The change of the slope of the results represents different flow regimes.

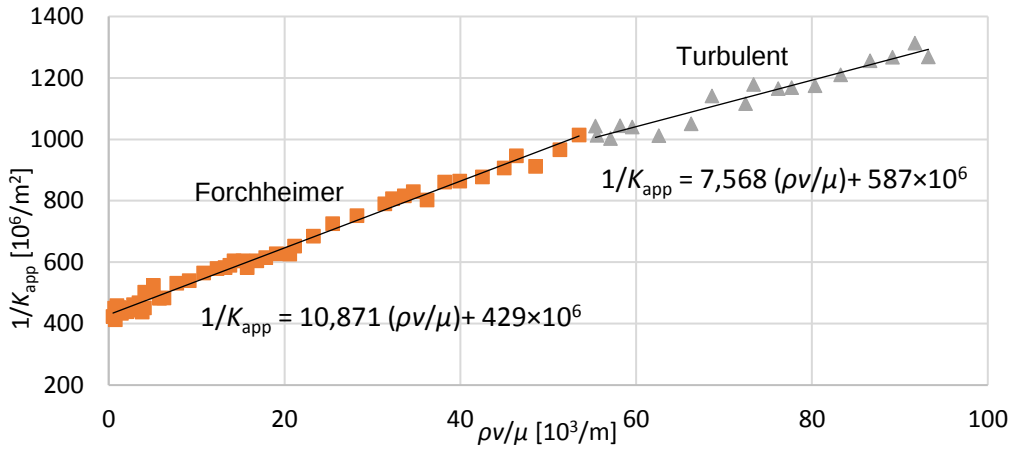

Figure 3-12 A Forchheimer plot for the packed spheres (d_m = 1.84 mm) sample.

Table 3-2 shows the obtained values for the onset of non-Darcy flow and the onset of turbulent flow, using two different criteria (Re and Re_K), compared to different values in the literature. From the table, it can be noticed that the permeability of the samples increases with increasing average bead diameter, while the onset of non-Darcy flow and the onset of turbulence occur earlier in finer material. The onset of non-Darcy flow and the onset of turbulence obtained from the laboratory experiments are in agreement with the values in the literature presented in Table 3-2, however, it is noticed that the onset of non-Darcy flow obtained by Fand et al. (1987) is lower than all the values shown in the table. This might be because of

some uncertainties in their laboratory experiments for this sample (d_m = 2.098 mm), as they noticed a change in the sample structure and its permeability after passing high flow discharges through the sample.

Table 3-2 The onset of non-Darcy flow and the onset of turbulent flow for the packed spheres sample (d_m = 1.84 mm), compared to data in the literature.

Sample	$K_D \times 10^{-6}$ *(mm²)*	*Onset velocity (mm/s)*		*Onset of non-Darcy flow*		*Onset of turbulent flow*	
		Non-Darcy	*turbulence*	*Re*	Re_K	*Re*	Re_K
Experimental results, d_m = 1.84 mm	2,250 ± 7%	4.1 ± 3%	53.5 ± 4%	7.50 ± 3%	0.19 ± 7%	98.00 ± 4%	2.54 ± 8%
Fand et al. (1987), d_m = 2.098 mm	3,885	1.74	47.7	2.30-5.0	0.068-0.15	80.00-120.00	2.37-3.57
Kundu et al. (2016), d_m = 2.5 mm	5,488	7.24	N.A.	18.10	0.20	N.A.	N.A.
Bağcı et al. (2014), d_m = 3 mm	6,423	7.5	77.5	22.45	0.59	232.50	6.21

3.4.4 Solute transport test experimental results

Due to some limitations, the solute transport experiments covered only the turbulent flow regime. While performing the solute transport experiments in the Darcy and Forchheimer flow regimes, it was noticed that the obtained results were unreasonable and difficult to interpret compared to the results obtained within the turbulent flow regime (see Figure 3-13). In Figure 3-13a, within the Forchheimer flow regime, the highest concentration measured at all Cyclops sensors is not the same, and the dye was detected at Cyclops 3 earlier than at Cyclops 2 (see Figure 3-1 for the Cyclops sensor positions), both of these observations are unreasonable. By investigating the reason behind these observations, it was found that, in the Darcy and Forchheimer flow regimes, the dye was not fully mixed with water in the recirculating pipe and therefore the Cyclops sensors did not detect accurate measurements of the concentration. In the turbulent flow regime, the flow is chaotic and characterised by high velocities, eddies and velocity fluctuations which led to rapid mixing. According to Taylor (1954a), for laminar flow, the solute can be fully mixed in a pipe cross-section when

$\frac{4\,L}{r} \gg \frac{u\,r}{D_m} \gg 6.9$, where L (mm) is the pipe length, r (mm) is the pipe radius and u (mm/s) is the average velocity through the pipe. According to Taylor's condition, and the experimental configurations shown in Figure 3-1, the recirculating pipe length required for the solute to be fully mixed, before it reaches the Cyclops sensors, within the Darcy and Forchheimer flow regimes should range from 266 to 28827 m, depending on the discharge value, which is practically impossible. For this reason, the solute transport experiments were performed only within the turbulent flow regime. For the laminar and Forchheimer flow regimes, the condition proposed by Taylor (1954a) can be achieved by using smaller diameter and larger length of the recirculating pipe, but in this case the head loss through the small recirculating pipe will be higher than the maximum head that can be delivered by the pump. Another option is to use a mixing chamber to achieve fully mixed conditions, but the propeller motion may create some eddies and affect the flow.

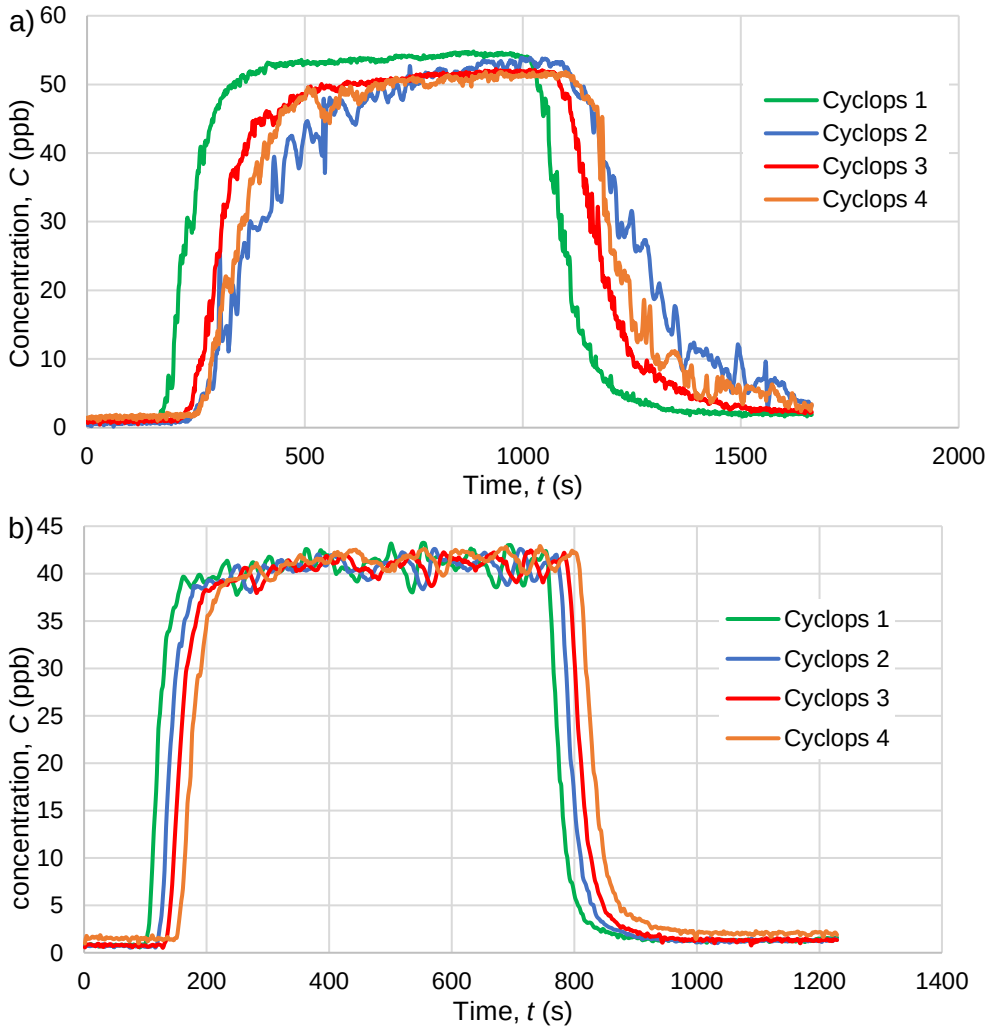

Figure 3-13 The breakthrough curves for two selected cases, a) for Forchheimer flow when the porous medium *Re* = 76.50 and b) for turbulent flow when the porous medium *Re* = 140.20.

As explained in Section 3.2, for each run, a first step to determine the longitudinal dispersion coefficient for the porous medium ($D_{L,\ medium}$) and for the circulating pipe ($D_{L,\ pipe}$) is to fit the measured breakthrough curves to the analytical solution of the 1D ADE (as shown in Figure 3-14). After analysing the results, it was found that the longitudinal dispersion coefficient ($D_{L,\ medium}$) obtained for the porous medium is small compared to the value of $D_{L,\ pipe+medium}$. Also, the values of $D_{L,\ pipe+medium}$ and $D_{L,\ pipe}$ were comparable to each other, despite the fact that $D_{L,\ pipe+medium}$ should always be larger than $D_{L,\ pipe}$, which led to a relatively large error in the estimated values of $D_{L,\ medium}$. Sometimes the obtained $D_{L,\ medium}$ values

were negative, but these values were excluded from the results shown in Figure 3-15.

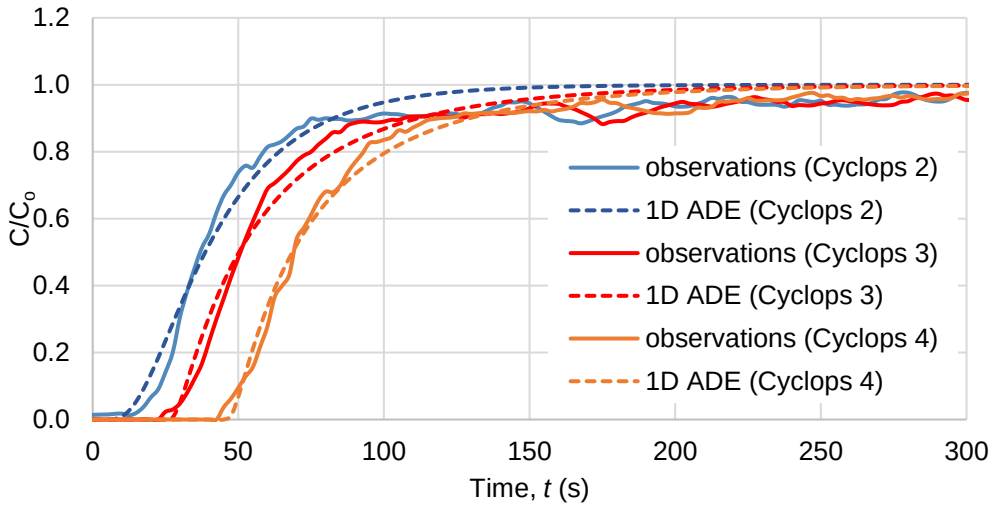

Figure 3-14 Fitting the observed breakthrough curves to the 1D ADE (Equation 2.20). The observed concentration is normalised by the maximum concentration obtained during the test, and *Re* = 140.20 for the porous medium.

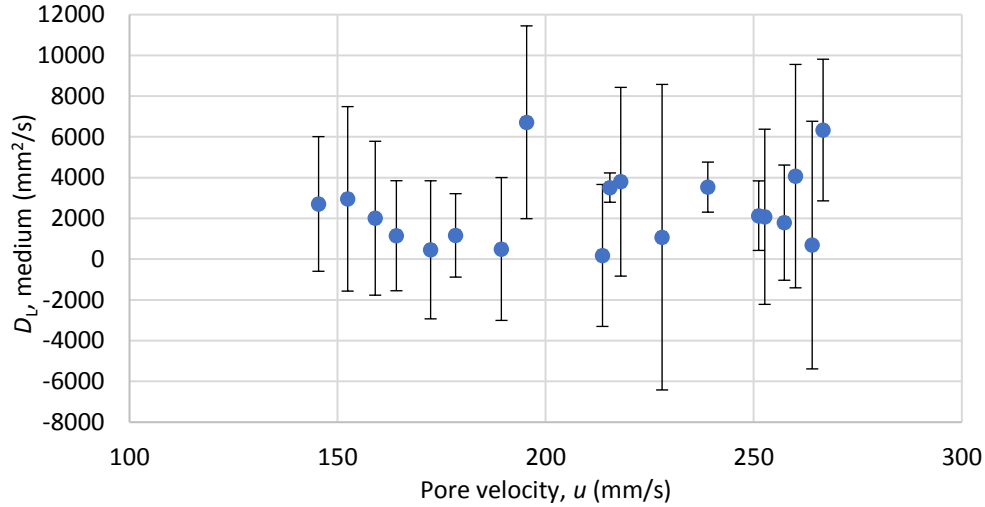

Figure 3-15 The obtained longitudinal dispersion coefficient ($D_{L,\ \text{medium}}$) of the packed spheres sample at different pore velocities (u) within the turbulent flow regime. The error bars represent the root mean square error.

3.5 Comparing experimental results to model results

In the following chapters, the experimental results presented in this chapter are compared to the results obtained from the models developed. None of the experimental results obtained or parameters, apart from the CT-scans,

are used as inputs to the proposed models. The coefficient of determination (R^2) is used to measure the goodness of fit between the experimental and numerical results. The coefficient of determination (R^2) is given by:

$$R^2 = 1 - \frac{\sum(y_i - f_i)^2}{\sum(y_i - \bar{y})^2} \quad 3.1$$

where y_i is the experimentally observed value, f_i is the numerically predicted value and $\bar{y}$ is the mean of the experimentally observed values. R^2 is also used to measure the goodness of fit between the obtain numerical results and results in the literature.

3.6 Conclusion

The experimental facilities and procedures of the flow tests and solute transport experiments were explained. In addition, the porous medium (packed spheres) sample preparation and design were discussed. The details of the X-ray Computed Tomography (XCT) scanning and determining the representative elementary volume (REV) of the porous sample were demonstrated.

The boundaries of the external containing pipe of the packed spheres sample were found to have a high effect on the estimated medium parameters, such as porosity and permeability. Thus, a cube of 50 mm length, which is equal to the sample diameter, was selected as an REV to consider the effect of the external pipe on the medium structure and flow behaviour.

The steady state flow test experiments extended from the Darcy flow regime to the turbulent flow regime and the corresponding discharge ranged from 0.001 to 0.18 l/s. The onset of non-Darcy flow and the onset of turbulence, determined by plotting the normalised dimensionless pressure gradient versus Reynold's number (*Re*), were observed at *Re* equal to 7.5 and 98, respectively, which agrees well to the previously published studies of Fand et al. (1987) and Kundu et al. (2016).

For solute transport test experiments, within the Darcy and Forchheimer flow regimes, the dye was not fully mixed with the water and the Cyclops sensors did not provide accurate measurements for the concentration.

Within the turbulent flow regime, the velocity fluctuations and eddies enhanced the process of rapid mixing and the dye was cross-sectionally fully mixed with the water. The longitudinal dispersion coefficient for the porous medium was relatively small compared to the longitudinal dispersion coefficient of the recirculating pipe and the porous medium together, and this results in large errors when estimating the longitudinal dispersion coefficient values for the porous medium.

Chapter 4

Pore-network modelling of Darcy and non-Darcy flow

In this chapter, the PNM algorithm developed for modelling Darcy and non-Darcy flow in porous media is explained. The proposed model has been applied on four porous media with different degrees of heterogeneity and additionally on the packed spheres sample used in the experimental work. The pore-networks of all samples have been extracted from their CT-images. The onset of non-Darcy flow has been determined and compared to previous studies and to the values obtained using existing empirical relationships. The proposed model results are compared to the DNS results performed on the same media (by Mostaghimi et al. (2012) and Muljadi et al. (2015)) and to the experimental results shown in Chapter 3.

4.1 Introduction

Based on the literature review in Section 2.3.2, it has been found that a new 3D pore-network model, capable of simulating non-Darcy flow and overcoming all the limitations in the previous non-Darcy flow pore-network modelling studies, is needed. Therefore, the main objective of this chapter is to develop a pore-network model that can represent the flow characteristics and predict the properties of the porous media within the non-Darcy flow regime. It is important to determine the velocity threshold, i.e. the onset of non-Darcy flow, above which this model should be applied and Darcy's law is not valid.

The reliability of predictions from pore-network modelling depends firstly on how accurately the approximated pore-network represents the porous medium; and secondly, on the accuracy of the equations and the numerical schemes used for simulating the physical or chemical process in the porous medium (Balhoff & Wheeler, 2009). Among the three different approaches that can be followed to generate a pore-network (explained in Section 2.7), in this study, for verification purposes, the third method is used to extract

the pore-networks from the available CT-image of each sample using the pore-network extraction code developed by Raeini et al. (2017).

The proposed model has been applied to simulate flow through five pore-networks extracted from the 3D CT-images of beadpack, Bentheimer sandstone, Estaillades carbonate, packed spheres, and Berea sandstone samples. The beadpack, Bentheimer sandstone and Estaillades carbonate are the same samples used for modelling non-Darcy flow using direct numerical simulation by Muljadi et al. (2015). The packed spheres sample is the same medium used in the experimental work (Chapter 3) it is referred to, throughout the whole thesis, as the "packed spheres" sample. Berea sandstone is the sample used to simulate flow and dispersion using direct numerical simulation by Mostaghimi et al. (2012). The beadpack, Bentheimer, Estaillades and Berea CT-images are obtained either from the Imperial Collage website (https://www.imperial.ac.uk/earth-science/research/research-groups/perm/research/pore-scale-modelling/micro-ct-images-and-networks/) or through direct contact with the authors. The properties of these CT-images together with the CT-image of the REV of the packed spheres sample (determined in Section 3.4.2) are shown in Table 4-1.

4.2 Method

4.2.1 Darcy and Non-Darcy flow modelling

4.2.1.1 Viscous pressure loss at the pore-scale

The average velocity through any pore, u_{pore} (mm/s), is related to the pressure loss through the pore, ΔP_{pore} (Pa), using the Darcy-Weisbach equation (Weisbach, 1845; Darcy, 1857), Equation 2.8 $\left(\Delta h_{pore} = \frac{\Delta P_{\text{pore}}}{\gamma} = f_{\text{pore}} \frac{L_{\text{pore}}}{2\, r_{\text{pore}}} \frac{u_{\text{pore}}^2}{2g}\right)$. For fully developed laminar flow, the pressure loss through the pore is caused mainly by fluid viscosity and the pore friction factor is only a function of Reynold's number (*Re*) (e.g. for circular cross-sections, $f_{\text{pore}} = \frac{64}{Re}$) (Çengel & Cimbala, 2006; Rennels & Hudson, 2012), and Equation 2.8 can be rewritten as

$$q_{\text{pore}} = K_{\text{pore}}\,\Delta P^{\text{v}}_{\text{pore}} = \frac{g_{\text{pore}}}{L_{\text{pore}}}\Delta P^{\text{v}}_{\text{pore}} \qquad 4.1$$

where q_{pore} (mm^3/s) is the flow rate through the pore, K_{pore} (mm^3/Pa·s) is the hydraulic conductivity, g_{pore} (mm^4/Pa·s) is the fluid conductance that can be calculated using Equation 4.2 and $\Delta P^{\text{v}}_{\text{pore}}$ (Pa) represents the viscous pressure loss through the pore.

For a circular capillary tube (either a pore body or a pore throat), the conductance g_{pore} is given analytically by the Hagen–Poiseuille equation (Hagen, 1839; Poiseuille, 1841) as follows

$$g_{\text{pore}} = k\frac{a^2 G}{\mu} = \frac{1}{2}\frac{a^2 G}{\mu} \qquad 4.2$$

where a (mm^2) is the pore cross-sectional area.

For other cross-sectional shapes such as equilateral triangular and square cross sections, analytical expression can also be derived with k (-) equal to 3/5 and 0.5623 respectively (Patzek & Silin, 2001; Valvatne & Blunt, 2004). It has been also found that the conductance of irregular triangles (scalene triangle) can be approximated by Equation 4.2, using the same constant (k = 3/5) as for an equilateral triangle (Oren et al., 1998; Valvatne & Blunt, 2004). According to Oren et al. (1998), the pore cross-sectional area (a) can be related to the shape factor (G) as

$$a = \frac{r^2_{\text{pore}}}{4G}. \qquad 4.3$$

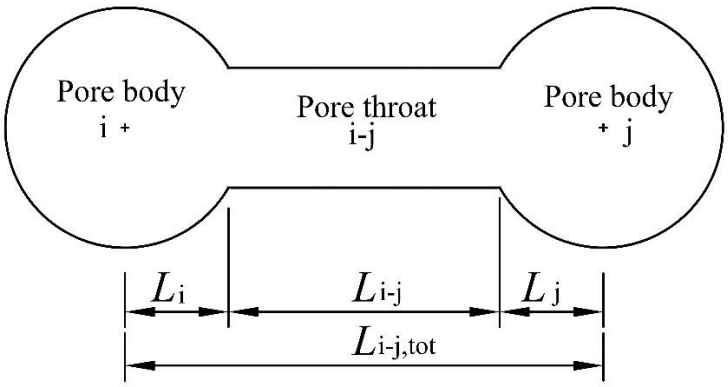

Figure 4-1 Schematic of a pore throat (i-j) and two pore bodies (i and j).

For a pore-network, the conductance $\left(g_{\mathrm{i-j,tot}}\right)$ between any two pore bodies (i and j) is the harmonic mean of the conductances through the pore throat and the two connected pore bodies as per Equation 4.4 (Oren et al., 1998; Valvatne & Blunt, 2004; Raoof & Hassanizadeh, 2012):

$$\frac{L_{\mathrm{i-j,tot}}}{g_{\mathrm{i-j,tot}}} = \frac{L_{\mathrm{i}}}{g_{\mathrm{i}}} + \frac{L_{\mathrm{i-j}}}{g_{\mathrm{i-j}}} + \frac{L_{\mathrm{j}}}{g_{\mathrm{j}}} \qquad 4.4$$

where i-j indicates the connecting throat, $L_{\mathrm{i\text{-}j}}$ (mm) is the pore throat length excluding the lengths of the two connected pore bodies i and j, L_{i} (mm) and L_{j} (mm) are the pore body lengths from the pore throat interface to the pore body centre, and $L_{\mathrm{i-j,tot}}$ (mm) is the length between the two pore body centres (Figure 4-1).

To determine the viscous pressure loss between any two pore bodies (i and j), Equation 4.1 can be rewritten as

$$q_{\mathrm{i-j}} = K_{\mathrm{i-j,tot}}\,\Delta P^{\mathrm{v}}_{\mathrm{i-j,tot}} = \frac{g_{\mathrm{i-j,tot}}}{L_{\mathrm{i-j,tot}}}\Delta P^{\mathrm{v}}_{\mathrm{i-j,tot}} \qquad 4.5$$

where $q_{\mathrm{i-j}}$ ($\mathrm{mm^3/s}$) is the discharge through any pore throat that connects the two pore bodies i and j, $K_{\mathrm{i-j,tot}}$ ($\mathrm{mm^3/Pa{\cdot}s}$) is the hydraulic conductivity, $\Delta P^{\mathrm{v}}_{\mathrm{i-j,tot}}$ (Pa) represents the viscous pressure loss between the two pore bodies i and j.

4.2.1.2 Pore-scale pressure loss due to inertial effects

For relatively high flow velocities, the inertial effects cannot be neglected as in the Darcy creeping flow regime. The inertial effects due to expansion, i.e. when flow moves from a pore throat to a connected pore body, and contraction, i.e. when flow moves from a pore body to a connected pore throat, cause additional pressure loss that should be considered in the calculation of the total pressure loss through any pore throat. In the model developed, the pressure losses due to the inertial effects, expansion and contraction, are expressed using equations 4.6 and 4.7 (Kays, 1950; Abdelall et al., 2005; Guo et al., 2010; Momen et al., 2016):

$$\Delta P_{\mathrm{i-j}}^{\mathrm{exp}} = K_{\mathrm{e}} \frac{\rho u_{\mathrm{i-j}}^2}{2} = \left[\left(\frac{a_{\mathrm{i-j}}}{a_{\mathrm{j}}} \right)^2 \left(2\, kd_{\mathrm{j}} - \alpha_{\mathrm{j}} \right) + \alpha_{\mathrm{i-j}} - 2\, kd_{\mathrm{i-j}} \left(\frac{a_{\mathrm{i-j}}}{a_{\mathrm{j}}} \right) \right] \frac{\rho u_{\mathrm{i-j}}^2}{2}, \quad 4.6$$

$$\Delta P_{\mathrm{i-j}}^{\mathrm{cont}} = K_{\mathrm{c}} \frac{\rho u_{\mathrm{i-j}}^2}{2} = \left\{ \frac{1 - \left[\alpha_{\mathrm{i-j}} \left(\frac{a_{\mathrm{i-j}}}{a_{\mathrm{i}}} \right)^2 - 2\, kd_{\mathrm{i-j}} + 1 - \left(\frac{a_{\mathrm{i-j}}}{a_{\mathrm{i}}} \right)^2 \right] Cc^2 - 2Cc}{Cc^2} \right\} \frac{\rho u_{\mathrm{i-j}}^2}{2}. \quad 4.7$$

where, in Equation 4.6, $\Delta P_{\mathrm{i-j}}^{\mathrm{exp}}$ (Pa) is the pressure loss due to expansion, K_e (-) is the expansion coefficient, $a_{\mathrm{i-j}}$ (mm^2) and a_{j} (mm^2) are the cross-sectional areas of the pore throat and the connected pore body j, and $u_{\mathrm{i-j}}$ (mm/s) is the average fluid velocity through the pore throat that connects the two pore bodies i and j. *kd* and α are the dimensionless momentum and kinetic-energy coefficients which depend on the velocity profile in each pore.

In Equation 4.6, $\Delta P_{\mathrm{i-j}}^{\mathrm{cont}}$ (Pa) is the pressure loss due to contraction, K_c (-) is the contraction coefficient, a_{i} is the cross-sectional area of the connected pore body i, and *Cc* (-) is the dimensionless jet contraction-area ratio (Vena-contraction) which can be estimated using Equation 4.8 (Geiger, 1964) as follows:

$$Cc = 1 - \frac{1 - \frac{a_{\mathrm{i-j}}}{a_{\mathrm{i}}}}{2.08 \left(1 - \frac{a_{\mathrm{i-j}}}{a_{\mathrm{i}}} \right) + 0.5371}. \quad 4.8$$

For laminar flow, when the velocity is low and its profile is parabolic, *kd* is equal to 1.33, 1.39 and 1.43 for circular, square and equilateral triangular cross-sections respectively, while α is equal to 2 for circular cross-sections. For turbulent flow, when the velocity is high and its profile is almost uniform, *kd* and α are equal to ~1.0 (Kays, 1950).

It has been found that using *kd* and α equal to 1.0 provides a better representation of non-Darcy flow which is characterised by higher velocities compared to the Darcy flow (El-Zehairy et al., 2019). This also agrees with the experimental findings of Abdelall et al. (2005) and Guo et al. (2010) performed on small channels. They showed that when using *kd* = 1.33 or α = 2.0 in equations 4.6 and 4.7, this result in overestimation of K_{e} and K_{c} in

most of the cases they tested. Moreover, when flow passes through a sudden expansion or contraction, this creates eddies and turbulence that make a uniform velocity profile a better approximation for the flow. Using *kd* and α equal to 1.0, equations 4.6 and 4.9 can be simplified and this results in the well-known Borda-Carnot equations (Crane, 1942; Bird et al., 1960).

The total pressure loss for any pore throat in the network is the summation of pressure losses due to viscosity, expansion and contraction, and can be given according to Equation 4.9 as follows:

$$\Delta P_{\mathrm{i-j}}^{\mathrm{tot}} = \Delta P_{\mathrm{i-j,tot}}^{\mathrm{v}} + \Delta P_{\mathrm{i-j}}^{\mathrm{exp}} + \Delta P_{\mathrm{i-j}}^{\mathrm{cont}} = \left[\frac{L_{\mathrm{i-j,tot}}}{g_{\mathrm{i-j,tot}}}\right] q_{\mathrm{i-j}} + K_{\mathrm{e}} \frac{\rho q_{\mathrm{i-j}}^2}{2a_{\mathrm{i-j}}^2} + K_{\mathrm{c}} \frac{\rho q_{\mathrm{i-j}}^2}{2a_{\mathrm{i-j}}^2} \ , \tag{4.9}$$

which can be written as

$$A_1\, q_{\mathrm{i-j}}^2 + A_2\, q_{\mathrm{i-j}} + A_3 = 0 \tag{4.10}$$

where

$$A_1 = (K_{\mathrm{e}} + K_{\mathrm{c}}) \frac{\rho}{2a_{\mathrm{i-j}}^2}\,,\ A_2 = \left[\frac{L_{\mathrm{i-j,tot}}}{g_{\mathrm{i-j,tot}}}\right],\ A_3 = -\,\Delta P_{\mathrm{i-j}}^{\mathrm{tot}}.$$

For the laminar Darcy flow regime, the inertial forces due to expansion and contraction are neglected, i.e. the term $\left[A_1\, q_{\mathrm{i-j}}^2\right]$ in Equation 4.10 is neglected.

4.2.1.3 Solving the final system of equations

For each pore body i, considering incompressible steady flow, the mass conservation can be expressed as

$$\sum_{\mathrm{j}\in N_{\mathrm{i}}} q_{\mathrm{i-j}} = 0 \tag{4.11}$$

where N_{i} is the coordination number of pore body i.

For Darcy flow, the pressure losses due to expansion and contraction are neglected and, for the whole pore-network, Equation 4.5 is applied for each pore throat and Equation 4.11 is invoked at each pore body. This process results in a system of N_{PB} linear algebraic equations, where N_{PB} is the total number of pore bodies in the pore-network. Following Babaei and Joekar-Niasar (2016), the resulting system of linear equations is arranged in matrix

form $\left(\bar{\bar{K}}\bar{P} = \bar{B}\right)$, where $\bar{\bar{K}}$ is the coefficient matrix which is a symmetric, sparse, diagonal matrix that contains the values of $K_{\mathrm{i-j,tot}}$ (Equation 4.5) and has the dimension of $N_{\mathrm{PB}} \times N_{\mathrm{PB}}$, $\bar{P}$ is the unknown pressure vector and $\bar{B}$ is the right hand side vector which contains zero values except for the pores located at the inlet and outlet where the pressure is initially assigned. Then, solving this system of equations, the pressure value at each pore body can be obtained and by applying Equation 4.5, the discharge through each pore throat can be estimated. Finally, the overall Darcy permeability, K_D (mm^2), of the pore-network can be obtained by applying Darcy's law (Equation 2.1) for the whole pore-network.

For non-Darcy flow, for the whole pore-network, Equation 4.10 is applied for each pore throat and Equation 4.11 is invoked at each pore body. To apply the continuity equation at each pore body, Equation 4.10 is rewritten in the form of a simple quadratic equation (Equation 4.10), and because A_1 and A_2 are always positive, then its positive root is equal to $q_{i-j} = \frac{-A_2+\sqrt{{A_2}^2-4A_1A_3}}{2A_1}$. This process results in an N_{PB} system of non-linear algebraic equations. A FORTRAN code (Appendix A-4) has been developed with the use of HSL NS23 routine (HSL, 2013) to solve the resulting system of equations. The HSL NS23 routine uses the Marquardt algorithm (Marquardt, 1963) for solving the nonlinear system of algebraic equations. The initial guess of the pressure values at each pore body is provided from the Darcy flow case, then the HSL NS23 routine iterates until the final solution is achieved within an acceptable predefined error criterion (i.e. until the sum of squares of the residuals is less than 10^{-10}). By solving this nonlinear system of algebraic equations, the pressure value at each pore body can be obtained and by applying Equation 4.9 the discharge through each pore throat can be obtained. Finally, the non-Darcy coefficient, β (1/mm), and Forchheimer permeability, K_{F} (mm^2), can be obtained using a Forchheimer plot (Equation 2.3).

In all simulations, no-flow boundary condition is applied for all pore-network outer boundaries except the inlet and outlet boundaries where

constant pressure values are applied. Water is considered as the working fluid with viscosity μ = 0.001 kg/m·s and density ρ = 1000 kg/m^3. The overall volumetric fluid discharge, q (mm^3/s), is obtained by summing up all pore throat discharges either at the inlet or at the outlet of the pore-network, while the flow superficial velocity, v (mm/s), is estimated as $v = \frac{q}{A}$, where A (mm^2) is the whole cross-sectional area perpendicular to the flow direction. However, for highly heterogeneous media such as Estaillades carbonate rocks, the pore's cross-sectional area may differ significantly from one location to another, so using the whole cross-sectional area might cause uncertainties in v and K_D values. For that reason, for heterogeneous porous media, the average pore velocity is estimated through each pore throat (as a length harmonic average velocity, Equation 4.12), then the superficial velocity, v (mm/s), is derived as the average pore velocity times the medium porosity (ϕ):

$$\frac{L_{i-j,tot}}{u_{i-j,tot}} = \frac{L_i}{u_i} + \frac{L_{i-j}}{u_{i-j}} + \frac{L_j}{u_j} \qquad 4.12$$

where $u_{i\text{-}j}$ (mm/s) is the flow velocity through the pore throat that connects the two pore bodies i and j, and u_i (mm/s) and u_j (mm/s) are the fluid velocities through the pore bodies i and j.

Appendix A provides the algorithm and details of solving the nonlinear system of equations for the non-Darcy PNM flow simulation code.

4.3 Verification, results and discussion

4.3.1 Extracted pore-networks from the CT-images

The properties of the five CT-images used in this chapter are shown in Table 4-1 and Figure 4-2. The 300×300×300 voxels beadpack CT-image (Figure 4-2a) represents a random packing of uniform spheres. The beadpack image was created by Prodanović and Bryant (2006) to represent the experimental measurements of the sphere centres obtained by Finney (1970). The only available CT-image of the Bentheimer sandstone sample is a 1000×1000×1000 voxels image. I did not manage to get the 500×500×500 voxels cropped Bentheimer image used by Muljadi et al. (2015). I have tried to crop that large image into a 500×500×500 voxels image at some arbitrary

locations, but this results in different properties other than the properties mentioned by Muljadi et al. (2015). To cope with that, I arbitrary cropped the first 500 voxels in the *x*, *y* and *z* directions of the large image (1000×1000×1000 voxels), then I extracted the pore-network from that cropped image, but this process may result in some uncertainties with respect to the results obtained for the Bentheimer sandstone sample. Similarly, Mostaghimi et al. (2012) used a 300×300×300 voxels crop of the Berea sandstone sample, while in this work the whole 400×400×400 voxels CT-image has been used. Investigations on pore-scale flow behaviour and the morphological characteristics of Bentheimer sandstone and Estaillades carbonate, have revealed that Estaillades is more heterogeneous than Bentheimer (Bijeljic et al., 2013a; Bijeljic et al., 2013b; Guadagnini et al., 2014; Muljadi et al., 2015). This is also confirmed by plotting the semi-variograms of pore body radii and coordination numbers of each sample (Figure 2A and 3A in Appendix A). The properties of the extracted pore-networks of the beadpack, Bentheimer sandstone, Estaillades carbonate, REV of the packed spheres (d_m = 1.84 mm) and Berea sandstone samples are shown in Table 4-2 and Figure 4-2(f-k). The histograms of the inscribed pore body and pore throat radii for the five samples are shown in Figure 4-3.

Table 4-1 The properties and characteristic lengths of the beadpack, Bentheimer, Estaillades, packed spheres and Berea samples*.

Sample	*Resolution (μm)*	*Porosity, ϕ*	*Characteristic length, L_{charc} (μm)*	*Total voxels*	*Pore voxels*	*K_D ×10^{-12} (m^2)*	
Beadpack	2.0	0.359	100	300×300×300	9,700,082	Muljadi et al. (2015)	5.57
Bentheimer	3.0035	0.211	139.9	500×500×500	26,413,875		3.50
Estaillades	3.3113	0.108	253.2	500×500×500	13,522,500		1.70
Packed spheres	65.99	0.364	1,837	758×758×758	124,612,700	Lab data	2250 ± 7%
Berea	5.345	0.197	131.13	400×400×400	12,572,994	Mostaghimi et al. (2012)	1.38

*For the first three samples, the characteristic length (L_{charc}) values are obtained from Muljadi et al. (2015); for the unconsolidated beadpack they chose L_{charc} = 100 µm, while for consolidate porous media (Bentheimer and Estaillades) they followed the methodology in Mostaghimi et al. (2012) to determine L_{charc} as a function in the specific surface area of the pore-grain interface (the surface area divided by the whole volume including pores and grains). For the packed spheres sample, the characteristic length (L_{charc}) is the beads' mean diameter (d_m = 1.84 mm). For the Berea sandstone, L_{charc} = 131.13 µm (Mostaghimi et al., 2012).

Table 4-2 The extracted pore-network properties for the beadpack, Bentheimer, Estaillades, packed spheres and Berea samples.

Sample	*Beadpack*	*Bentheimer (500×500×500 voxels)*	*Estaillades*	*Packed spheres*	*Berea (400×400×400 voxels)*
Number of PBs	347	1,033	954	10,315	2,822
Number of PThs	1,424	2,418	1,649	53,960	6,691
Average coordination number	7.9	4.5	3.4	10.4	4.6
Maximum coordination number	21	23	19	30	28
Maximum inscribed PB radius (mm)	0.0344	0.0862	0.0692	0.7673	0.0709
Average inscribed PB radius (mm)	0.0178	0.0231	0.0196	0.4103	0.0587
Minimum inscribed PB radius (mm)	0.0051	0.0058	0.0064	0.1408	0.0223
Maximum inscribed PTh radius (mm)	0.0287	0.0571	0.0575	0.6958	0.0116
Average inscribed PTh radius (mm)	0.0089	0.0122	0.0116	0.1952	0.0103
Minimum inscribed PTh radius (mm)	0.0009	0.0015	0.0016	0.0320	0.00261

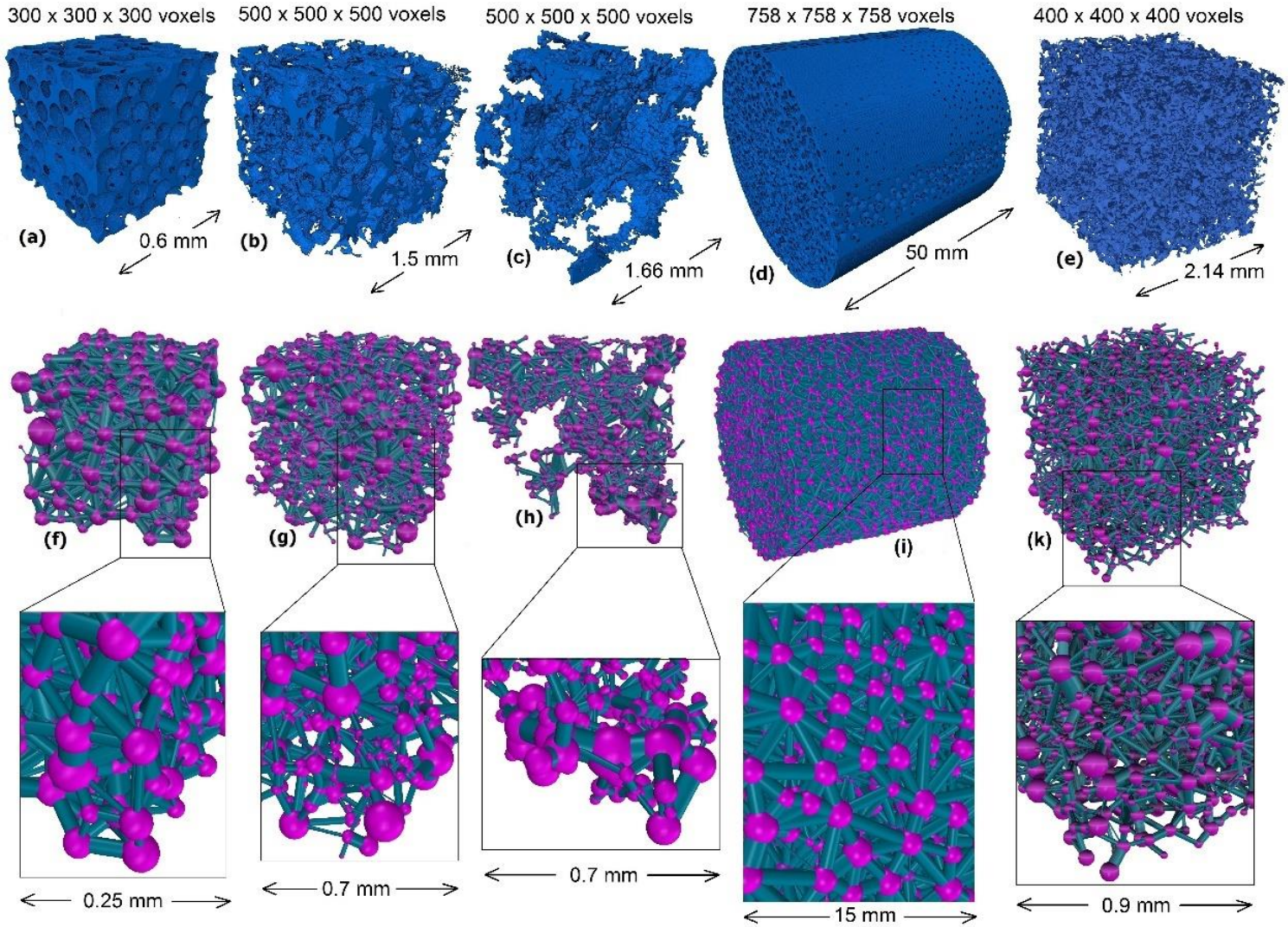

Figure 4-2 The pore spaces of the (a) beadpack, (b) Bentheimer, (c) Estaillades (d) packed spheres and (e) Berea samples, and their equivalent pore-networks (f-k).

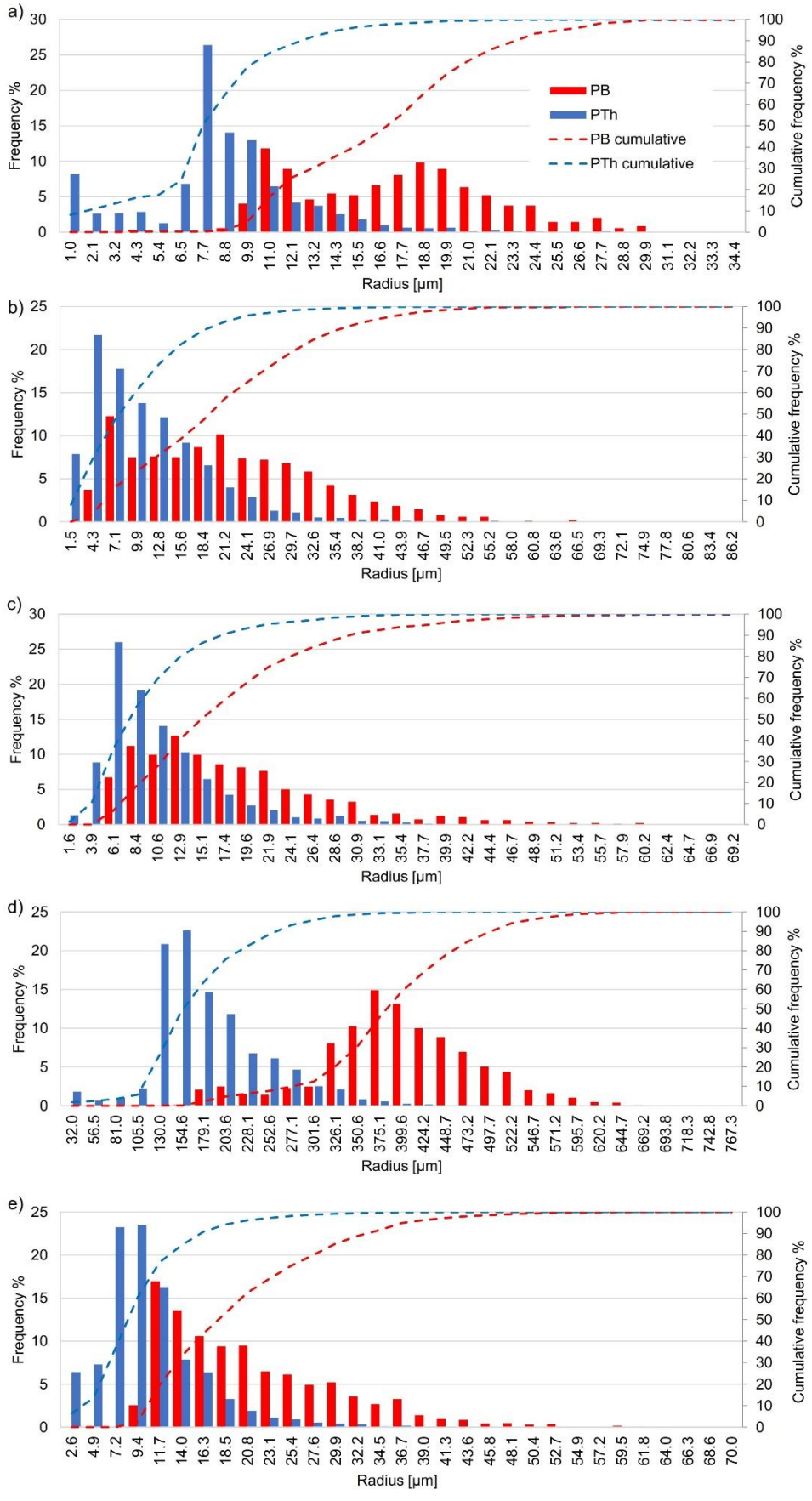
a)
Frequency %
Cumulative frequency %
PB
PTh
PB cumulative
PTh cumulative
Radius [µm]
b)
Frequency %
Cumulative frequency %
Radius [µm]
c)
Frequency %
Cumulative frequency %
Radius [µm]
d)
Frequency %
Cumulative frequency %
Radius [µm]
e)
Frequency %
Cumulative frequency %
Radius [µm]

Figure 4-3 Histograms of the inscribed pore body and pore throat radii for the a) beadpack, b) Bentheimer, c) Estaillades d) packed spheres and e) Berea samples.

4.3.2 The Darcy permeability (K_D) and non-Darcy coefficient (β)

The Darcy permeability (K_D) values obtained from PNM, by applying Darcy's law (Equation 2.1) while neglecting the inertial effects, are in a good agreement (varying less than 15.2%) with the corresponding values either in Muljadi et al. (2015), obtained from lab experiments or in Mostaghimi et al. (2012) as presented in Table 4-3. Relatively large discrepancies (14% and 15.2%) are observed for Bentheimer and the packed spheres (d_m = 1.84 mm) because the large Bentheimer image was cropped in an arbitrary location and because the packed spheres sample was scanned prior to experiments, so during experiments the position of some particles might have changed slightly under the effect of flow at large velocities. Another possible reason for these discrepancies is the geometry simplification inherently used in pore-networks. Also, the pore-network extraction code defines the parameters of the pore-network elements using single phase direct numerical simulation on the CT-image, these details can be found in Raeini et al. (2017) and Raeini et al. (2018). That is why the PNM simulations can accurately reproduce the results predicted with direct simulation (by Muljadi et al., 2015) and slightly differ from the results achieved by experiments.

Figure 4-4 shows a Forchheimer plot which is a plot of the inverse of apparent permeability $\left(\frac{1}{K_{app}}\right)$ versus $\left(\frac{\rho v}{\mu}\right)$ (Equation 2.3). The slope of each graph represents the non-Darcy coefficient (β) and it is equal to 1.49×10^5, 4.67×10^6, 2.82×10^8, 5.232×10^3 and 4.66×10^6 (1/m) for the Beadpack, Bentheimer, Estaillades, packed spheres and Berea samples, respectively. The corresponding β values obtained by Muljadi et al. (2015) and in the laboratory are 2.57×10^5, 2.07×10^6, 6.15×10^8 and $10.87\text{x}10^3$ (1/m), see Table 4-3. The study performed by Mostaghimi et al. (2012) was in the Darcy flow regime and they did not estimate β for the Berea sample. It is noticeable that the values of β achieved with PNM are in good agreement

(within the same order of magnitude and with a maximum variation of 54%) with the values obtained by Muljadi et al. (2015) except Bentheimer which has larger discrepancy (126%) because the cropped image used for PNM differs from the cropped image used by Muljadi et al. (2015). These discrepancies related to β values might be because of the simplifications of pore shapes during the pore-network extraction. In general, there is less good agreement for β compared to K_D when the obtained PNM results are compared to the results of Muljadi et al. (2015). This is because the value of β depends on the value of K_D, the pore geometries and the assumed shape for the velocity profile in each pore. Therefore, the potential error in the value of β is larger than the potential error in the K_D value which depends mainly on the pore geometries. In Figure 4-4, The shift in the horizontal part of each curve when comparing the obtained PNM results to those by Muljadi et al. (2015) or from lab experiments is due to the difference in K_D obtained from different methodologies, whilst the trend of each curve depends mainly on the pressure losses obtained at different velocities.

Table 4-4 shows some existing empirical equations for estimation of the non-Darcy coefficient (β). The estimated β values for the beadpack and packed spheres samples obtained by PNM agree well with values calculated using the equations proposed by Ergun (1952) and Macdonald et al. (1979) who used spherical beads in their experiments. A relatively larger deviation is observed for the packed spheres sample, which may be related to the effect of boundaries on the sample used in this study (Section 3.4.2). For Bentheimer and Berea sandstone, the obtained β values from PNM simulations are in good agreement with the values obtained from both Janicek and Katz (1955) and Li et al. (2001) who derived their equations after testing flow through sandstone, limestone and dolomite. However, the estimated β value from PNM for Bentheimer sandstone is significantly different from the values calculated by the equations proposed by Geertsma (1974), Coles and Hartman (1998) and Jones (1987) who used sandstone samples. Such a discrepancy in the predicted values of β was observed by Muljadi et al. (2015) as well. This may be related to the different degrees of heterogeneity that can be observed for different sandstone samples, concluding significant sensitivity of β to macro-sale heterogeneity of porous

media. The estimated β value for Estaillades carbonate agrees well with Janicek and Katz (1955) who performed their experiments on sandstone, limestone and dolomite. In the literature, there is a scarcity of studies that have provided β values for carbonate samples. It is noticed that the equation proposed by Friedel and Voigt (2006) provides accurate estimation for Bentheimer, Berea sandstone and Estaillades as well.

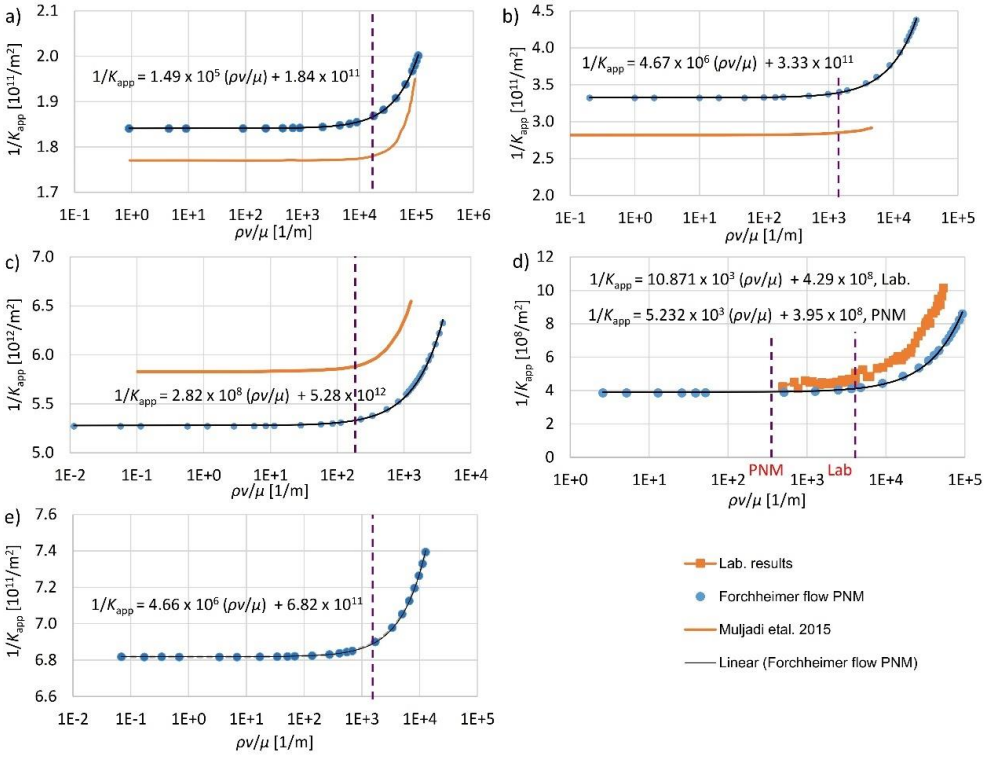

Figure 4-4 Forchheimer plots for a) Beadpack, b) Bentheimer, c) Estaillades, d) packed spheres and e) Berea. The vertical dashed lines represent the onset of non-Darcy flow.

Table 4-3 The permeability (K_D) and Forchheimer coefficient (β) for the three samples compared to those obtained by Muljadi et al. (2015).

Sample	*Image total voxels*	$K_D \times 10^{-12}$ *(m^2), PNM*	$K_D \times 10^{-12}$ *(m^2)*		ΔK_D *(%)*	$\beta \times 10^5$ *(1/m), PNM*	$\beta \times 10^5$ *(1/m)*		$\Delta\beta$ *(%)*
Beadpack	300×300×300	5.43	Muljadi et al. (2015)	5.57	2.5	1.49	Muljadi et al. (2015)	2.57	42
Bentheimer	500×500×500	3.01		3.50	14.0	46.7		20.7	126
Estaillades	500×500×500	0.19		0.170	11.8	2820		6150	54
Packed spheres	758×758×758	2593	Lab	2250 ± 7%	15.2	0.0523	Lab	0.1087 ± 11%	52
Berea	400×400×400	1.47	Mostaghii et al. (2012)	1.38	6.5	46.6	Mostaghimi et al. (2012)	NA	NA

Table 4-4 The non-Darcy coefficient (β) estimated using empirical equations, modified from Wang et al. (2014).

Reference	*β empirical equations*	*Investigation method*	*Bead pack, β (10^5/m)*	*Bentheimer, β (10^5/m)*	*Estaillades, β (10^5/m)*	*Packed spheres, β (10^5/m)*	*Berea, β (10^5/m)*
Ergun (1952)	$\beta = \frac{14.28 \times 10^4}{\sqrt{K_D \times 10^{-3}}\,\phi^{1.5}}$	Flow through various sizes of spheres, sands, and pulverized coke.	2.85	8.49	92.30	0.13	13.47
Janicek and Katz (1955)	$\beta = \frac{1.82 \times 10^{10}}{{K_D}^{1.25}\,\phi^{0.75}}$	Flow through sandstone, limestone and dolomite.	8.42	26.22	1,369.50	0.004	67.62
Geertsma (1974)	$\beta = \frac{1.59 \times 10^5}{{K_D}^{0.5}\,\phi^{5.5}}$	Both consolidated and unconsolidated sandstone, limestone and dolomite.	6.04	150.86	23,888.54	0.26	314.90

Macdonald et al. (1979) as reported by Wang et al. (2014)	$\beta = \frac{100}{\phi}\sqrt{\frac{245 \times 10^8}{12\,K_D\,\phi}}$	Experimental data from previous work, including spherical glass beads, cylindrical fibre beds and consolidated media.	2.85	8.50	29.21	0.13	13.48
Jones (1987)	$\beta = \frac{2.018 \times 10^{11}}{{K_D}^{1.55}}$	Experiments of vuggy limestone, crystalline limestone and fine-grained sandstone.	3.28	8.19	592.72	2×10^{-4}	24.86
Coles and Hartman (1998)	$\beta = \frac{3.51 \times 10^{12}\,\phi^{0.44}}{{K_D}^{1.88}}$	Sandstone and limestone samples for flow testing using the same porosity method.	2.11	5.04	671.83	2×10^{-5}	18.79
Li et al. (2001)	$\beta = \frac{1.15 \times 10^9}{K_D\,\phi}$	Numerical simulation of N_2 flowing at various rates through wafer-shaped Berea Sandstone.	5.90	18.11	560.43	0.01	39.71
Friedel and Voigt (2006)	$\beta = \frac{4.1 \times 10^{11}}{{K_D}^{1.5}}$	Experimental data from previous studies.	10.25	24.83	1565.50	0.001	72.75

*For all empirical equations, K_D is in mD ($\approx 10^{-3}\mu m^2$) and β in m^{-1}.

4.3.3 Onset of non-Darcy flow

Following Muljadi et al. (2015), the onset of non-Darcy flow is the point at which the pressure loss due to the linear term becomes less than 99% of the total pressure loss. Figure 4-5 shows the pressure gradient versus superficial velocity at different Reynold's numbers, the onset of non-Darcy flow is also indicated by a vertical dashed line. According to the Forchheimer equation, the pressure gradient is a function of two parameters (K_D and β) where their values are dependent on the geometry of the porous samples. The figure

shows a good match with the previous results obtained by Muljadi et al. (2015) for Beadpack, Bentheimer and Estaillades while there are relatively larger discrepancies between PNM and laboratory results. A main cause of these larger discrepancies between PNM and laboratory results is that the pores of the packed spheres sample used in the experiments are significantly larger than the pores in the other four samples. For that reason, the flow in the majority of pores in the packed spheres sample is a developing flow, i.e. the pores are not long enough for a fully developed flow to be achieved, which causes underestimation of the friction factor of each pore in the sample if the Hagen–Poiseuille equation is used (Section 2.3.1). This explains why the pressure losses obtained by PNM are less than those obtained in the lab (Figure 4-5d).

Following Section 2.3.1, and using Equation 2.9, the average values of the entrance region ($L_{\text{h, laminar}}$) for all pore throats in the five samples have been estimated within the applied ranges of pressure gradients. It has been found that $L_{\text{h, laminar}}$ increases when the applied pressure gradient increases. At the maximum applied pressure gradients, the average values for $L_{\text{h, laminar}}$ as a percentage of the average pore throats length was equal to 29%, 11%, 3% and 5% for the Beadpack, Bentheimer, Estaillades and Berea samples, respectively. For the packed spheres sample, at the maximum applied pressure gradients, the average value of $L_{\text{h, laminar}}$ as a percentage of the average pore throats' length reached 374%, which means that the pore lengths are very short and even shorter than $L_{\text{h, laminar.}}$ This demonstrates that the PNM approach has some limitations and the proposed set of equations cannot be applied for coarse media with large pores.

Another possible reason for the discrepancy between the predicted PNM results and those achieved in the laboratory or through direct numerical simulations presented by Muljadi et al. (2015) is the simplifications that were implemented by the pore-network method to describe the geometry of the samples. Also, the mesh size used by Muljadi et al. (2015) may have effects on the accuracy of their results.

The superficial velocities calculated using PNM at the onset of non-Darcy flow are 0.018, 0.001, 0.0001 and 0.0005 (m/s) for the Beadpack, Bentheimer, Estaillades and packed spheres samples, respectively, while the corresponding values presented in Muljadi et al. (2015) and measured in the lab are 0.0279, 0.0014, 0.000227 and 0.004 (m/s), see Table 4-5. It is noticeable that the onset of non-Darcy flow obtained by PNM is in good agreement with that obtained by Muljadi et al. (2015), but one order of magnitude lower than the values obtained from the experimental measurements which is attributed to the large pore sizes for the packed spheres sample and the large entrance length of its pores as explained earlier. In general, it is noticeable that the onset of non-Darcy flow occurs earlier, at a lower Reynold's number, when the medium has a higher degree of heterogeneity. This is due to a reduction in the effective area (area of interconnected pores) for the fluid flow in heterogeneous media (see Section 4.3.5).

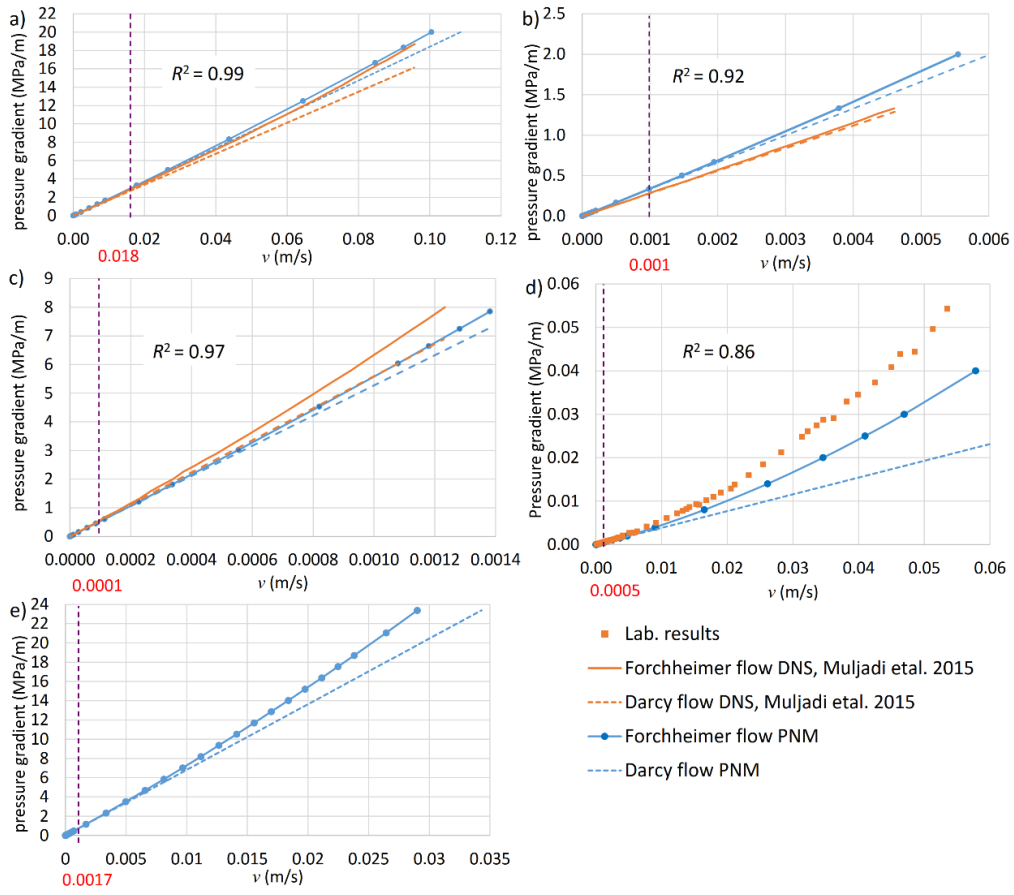

Figure 4-5 The pressure gradient versus superficial velocity for both linear Darcy flow and nonlinear Forchheimer flow compared to the results by Muljadi et al. (2015) and laboratory measurements; a) Beadpack, b) Bentheimer, c) Estaillades, d) packed spheres and e) Berea. The coefficient of determination (R^2) shows the goodness of fit for the Forchheimer flow case and the corresponding values obtained either by Muljadi et al. (2015) or via experimental measurements.

Considering the dimensionless apparent permeability (K^*) as

$$K^* = \frac{K_{app}}{K_D} \tag{4.13}$$

and following the same definition for the onset of non-Darcy flow, from equations 2.1 and 2.3, the onset of non-Darcy flow can be determined when K^* is equal to 0.99 in Figure 4-6, Figure 4-7 and Figure 4-8. The predicted superficial velocities and Reynold's number values for the onset of non-Darcy flow and the corresponding values obtained either in the work of Muljadi et al. (2015) or in the laboratory are shown in Table 4-5.

In Figure 4-6 and Figure 4-7, the dimensionless apparent permeability (K^*) is plotted against Re_K and Re (Section 2.4) while using the same characteristic lengths (L_{charc}) shown in Table 4-1. The PNM curves in Figure 4-6 and Figure 4-7 have similar trends to those results presented in Muljadi et al. (2015) and in the laboratory, but with some discrepancies. A better match is obtained, especially for Estaillades, in Figure 4-6 when Re_K is used instead of Re. According to equations 2.3, 2.12, 2.16 and 4.13 these discrepancies are attributed either to the change in superficial velocities or pressure losses in PNM results compared to the results of other studies. Figure 4-6 and Figure 4-7 also confirm that the onset of non-Darcy flow occurs earlier in highly heterogenous media as in the case of Estaillades carbonate.

When the dimensionless apparent permeability (K^*) is plotted versus the Forchheimer number $\left(F_o = \frac{K_D \beta \rho v}{\mu}\right)$, (Equation 2.18), in Figure 4-8, the curves of all of the samples coincide. This unique relationship can be derived mathematically from the Forchheimer Equation (Ruth & Ma, 1992;

Ruth & Ma, 1993). In petrophysics, the relationship shown in Figure 4-8 can be used to predict the apparent permeability for media with known K_D and β, without the need to perform laboratory experiments at different flow rates. K_D and β can be determined using literature data or empirical relationships such as those proposed by Kozeny (1927), Carman (1937), Ergun (1952), and Janicek and Katz (1955). In Figure 4-8, the onset of non-Darcy flow occurs when $K^* = 0.99$, and this corresponds to $F_o \approx 0.01$ for all PNM simulations and $F_o = 0.1$ for the experimental results. These F_o values at the onset of non-Darcy flow are in agreement with the range (0.01-0.1) proposed by Andrade et al. (1999).

Table 4-6 shows the onset of non-Darcy flow reported by some other authors and their criteria used for obtaining the onset of non-Darcy flow. For beadpack and packed spheres samples, the onset of non-Darcy flow agrees, within less than one order of magnitude, with most of the criteria shown in the Table 4-6 except the formulas proposed by Chilton and Colburn (1931), who used various types of packed particles, Blick and Civan (1988), who used a capillary-orifice model, Green and Duwez (1951), who performed an N_2 flow experiment through different porous media and Ma and Ruth (1993) who used a diverging-converging model. This shows that the obtained PNM results for these two samples agree well with previous studies that used similar methodology, fluid and porous medium. For Bentheimer and Berea sandstone samples, the obtained value for the onset of non-Darcy flow by PNM agrees well with the values obtained by Fancher and Lewis (1933) for loosely consolidated sand and Chukwudozie et al. (2012) for a 3D CT sandstone image. The onset of non-Darcy flow for Estaillades only agrees with the values proposed by Andrade et al. (1999) and Chukwudozie et al. (2012) who used the Forchheimer number in their analysis. This confirms the importance of using β for determining the onset of non-Darcy flow, especially for highly heterogenous media such as carbonate. It is worth mentioning that, in agreement with Muljadi et al. (2015), none of the studies in the Table 4-6 were performed on a highly heterogenous natural medium such as carbonate.

It is important to take into consideration the non-Darcy coefficient (β) when determining the onset on non-Darcy flow for different media. For that reason, in Figure 4-9, the pressure gradient is plotted versus the Forchheimer number, as this is a better comparison tool for follow up studies, instead of using velocities or Reynolds number as a criterion. The resulting curves are straight lines as expected according to the Forchheimer equation (Equation 2.2). The onset of non-Darcy flow shown in the figure is determined using the superficial velocity at $K^* = 0.99$.

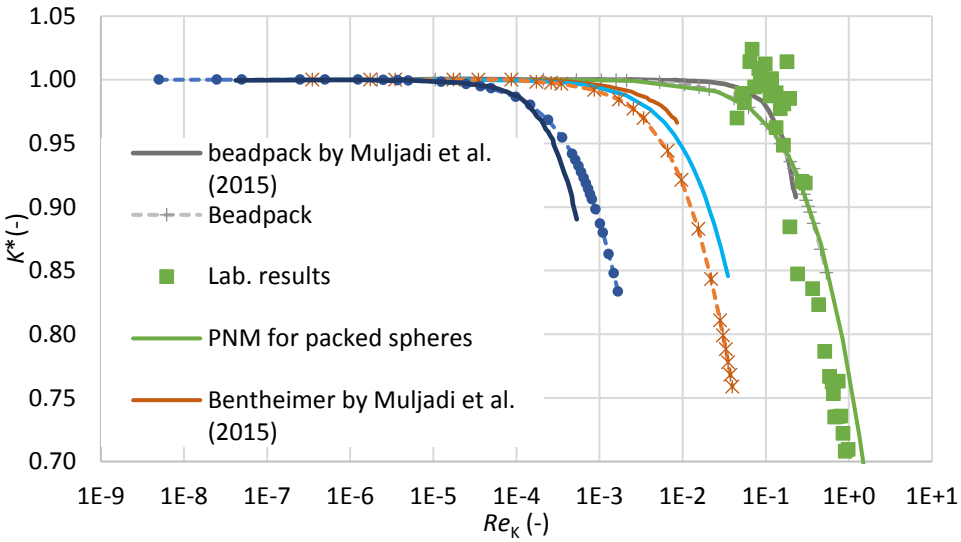

Figure 4-6 The dimensionless apparent permeability K^* versus Re_K (Equation 2.16), compared to the results by Muljadi et al. (2015).

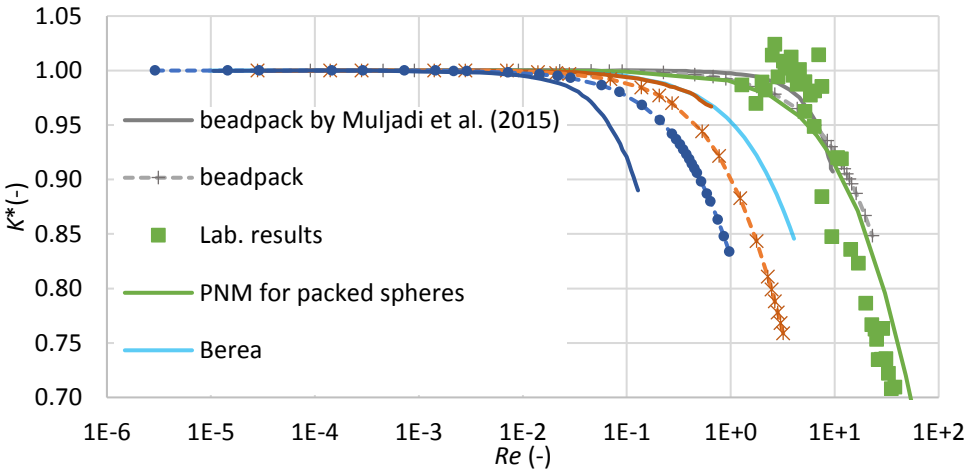

Figure 4-7 The dimensionless apparent permeability K^* versus Re (Equation 2.12), compared to the results by Muljadi et al. (2015).

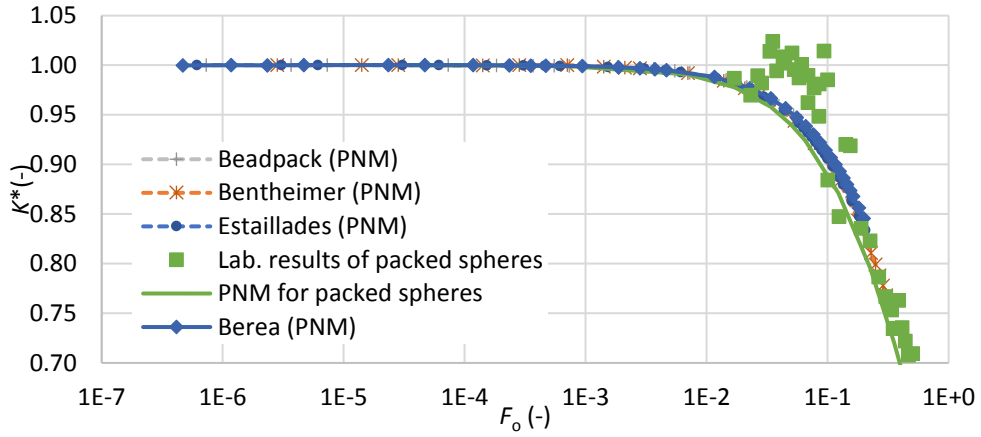

Figure 4-8 The dimensionless apparent permeability K^* versus F_o (Equation 2.18), compared to the results from experiments.

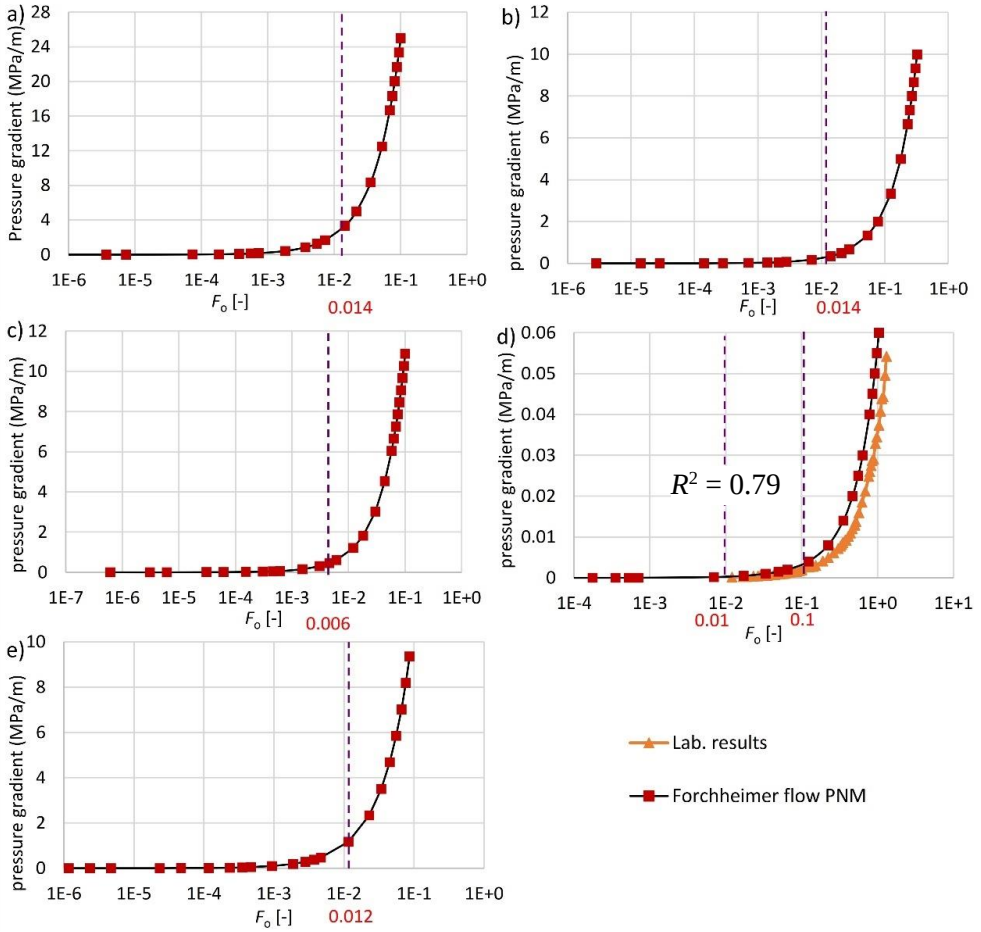

Figure 4-9 The pressure gradient versus Forchheimer number (F_o), Equation 2.18 , for; a) Beadpack, b) Bentheimer, c) Estaillades, d) packed spheres and e) Berea.

Table 4-5 Reynold's number and superficial velocity values for the onset of non-Darcy flow.

Sample	*Onset of non-Darcy flow (PNM)*			*Onset of non-Darcy flow*				*Difference (%)*		
	v (mm/s)	Re_K	*Re*	ref.	*v* (mm/s)	Re_K	*Re*	*v* (mm/s)	Re_K	*Re*
Beadpack	17.83	4.15×10^{-2}	1.78	Muljadi et al. (2015)	27.90	6.64×10^{-2}	2.79	36	38	36
Bentheimer	0.99	1.72×10^{-3}	0.14		1.40	2.64×10^{-3}	0.20	29	3	29
Estaillades	0.11	4.79×10^{-5}	0.03		0.23	9.40×10^{-5}	0.02	52	5	22
Packed spheres	0.51	2.60×10^{-2}	0.94	Lab	4.09 ± 3%	1.94×10^{-1} ± 7%	7.54 ± 3%	88	87	88
Berea	1.70	2.05×10^{-3}	0.22	Mostaghimi et al. (2012)	NA	NA	NA	NA	NA	NA

Table 4-6 The onset of non-Darcy flow reported by some other authors, modified after Wang et al. (2014).

Criterion	*Reference*	*Onset of non-Darcy flow*	*Method*	*The onset calculated using the criteria in the first column and the superficial velocity at K* = 0.99, and L_{charc} in Table 4-1.*				
				Beadpack	Bentheimer	Estaillades	Packed spheres	Berea
$Re = \frac{\rho\, d_m\, v}{\mu}$ *where* d_m *is the average diameter of particles.*	Chilton and Colburn (1931)	40-80	Experiments on various types of packed particles	1.78	0.14	0.03	0.94	0.22
	Fancher and Lewis (1933)	10–1000 for unconsolidated sand, 0.4–3 for loosely consolidated sand	Crude oil, water and air through consolidated sandstones and unconsolidated sands					
	Tek (1957)	1.0	Air, water flow through Woodbine, Wilcox, Warren and 3rd Venango sands					
	Bear (1972)	3–10	Review and analysis					
	Scheidegger (1974)	0.1–75	Review and analysis					
	Dybbs and Edwards (1984)	1–10	Experiments in fixed beds of arranged spheres					

			and rods					
	Blick and Civan (1988)	100	Simulation of capillary-orifice model					
	Du Plessis and Masliyah (1988)	3.4–17.1	Representative unit cell simulation					
	Hassanizadeh and Gray (1987)	1-15	Various previous experiments					
$Fo = \frac{K_D \beta \rho v}{\mu}$	Green and Duwez (1951) as mentioned in Zeng and Grigg (2006)	0.1-0.2	N_2 flow experiments through four different porous metal samples	0.01	0.01	0.01	0.01	0.01
	Andrade et al. (1999)	0.01-0.1	Simulation in 2D disordered porous media					
	Chukwudozie et al. (2012)	0.02-0.08	Lattice Boltzmann simulation of 3D CT sandstone image					
$Re = \frac{\rho d_m v}{\mu (1-\emptyset)}$	Ergun (1952) as mentioned in Wang et al. (2014)	3–10	Gas flow experiments through packed particles	2.78	0.18	0.03	1.47	0.28
$Re = \frac{\rho d_{PTh} u}{\mu}$, d_{PTh} *is the throat diameter*	Ma and Ruth (1993)	3–10	Diverging-converging model simulation	0.442	0.057	0.012	0.274	0.089
$Re = \frac{\rho r_{PTh} v}{\mu}$, r_{PTh} *is the average throat radius*	Thauvin and Mohanty (1998)	0.11	Simulation of a pore-network model	0.221	0.029	0.006	0.137	0.044

4.3.4 Friction factor

Similar to the Hagen–Poiseuille equation (Hagen, 1839; Poiseuille, 1841) for laminar flow through pipes, the Moody chart, Figure 2-4, (Moody, 1944) is the most widely used chart for designing flow through pipes in all flow regimes. It is used to estimate the dimensionless friction factor, f (-), of a pipe at a specific Reynold's number, and from this friction factor, the pressure needed to pass the flow at specific rate through the pipe can be determined. Thinking of porous media as a group of connected pipes, Carman (1937) developed a similar chart that relates the dimensionless friction factor to the Reynold's number for porous media in all possible

flow regimes (Holdich, 2002). This friction factor can be used to evaluate the medium resistance to flow, or in other words, it can be used to estimate the pressure needed to pass flow at a specific rate through the porous medium within any flow regime (Hlushkou & Tallarek, 2006).

The friction factor (*f*) in porous media can be determined by neglecting the small difference between K_D and K_F, then Equation 2.2 can be rewritten as $f = \frac{1}{F_o} + 1$, where $f = \frac{\Delta P}{L\beta\rho v^2}$ (-) and $F_o = \frac{K_D\beta\rho v}{\mu}$ (-) (Macdonald et al., 1979; Macedo et al., 2001; Pamuk & Özdemir, 2012). Figure 4-10 to Figure 4-12 show that the friction between the medium particles and the fluid decreases when the fluid velocity increases. Figure 4-10 and Figure 4-11 show that higher head loss due to friction occurs earlier, i.e. at low Reynold's numbers, for media with high degree of heterogeneity. The friction factor and Forchheimer number predictions for all samples are in excellent agreement with each other and in agreement with the experimentally measured values (Figure 4-12). This agreement is because all the parameters (*f*, K_D and β) used to develop the figure are predicted from the Forchheimer equation. However, this is not the case when the friction factor is plotted versus the Reynold's number (Figure 4-10 and Figure 4-11), and this shows that Forchheimer number is a better dimensionless parameter that can be used to describe the flow through porous media. The resulting friction factor versus Forchheimer number curve is a unique relationship that agrees very well with the results presented by Geertsma (1974) and can be used for all samples regardless of its degree of heterogeneity.

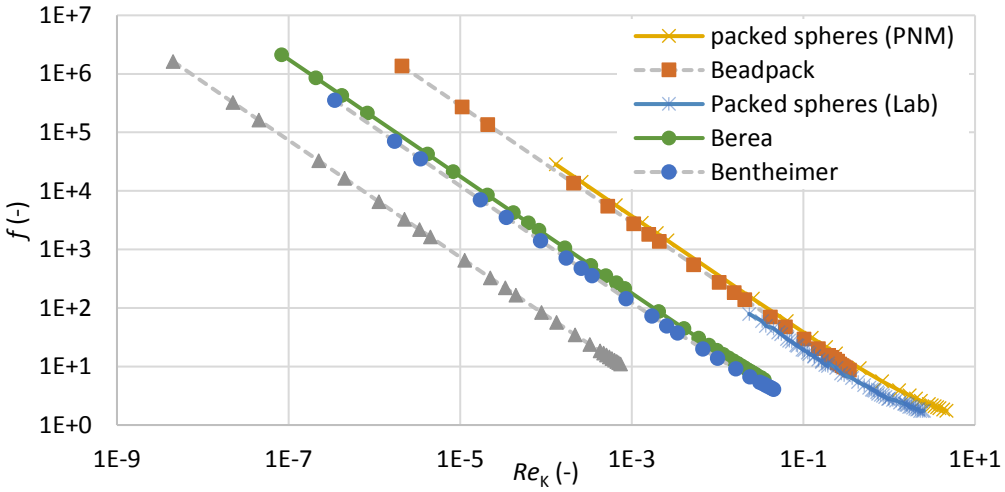

Figure 4-10 The medium friction factor (f) versus permeability-based Reynold's number (Re_K), Equation 2.16.

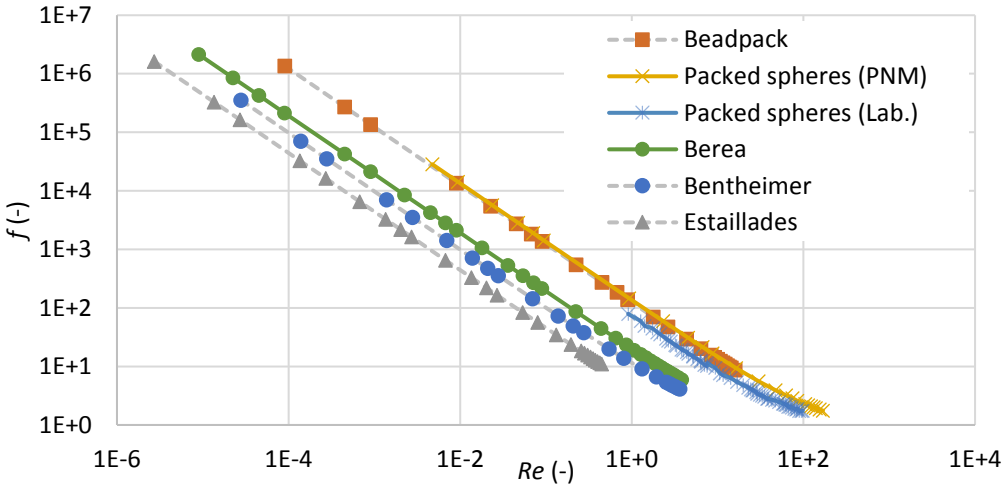

Figure 4-11 The medium friction factor (f) versus Reynold's number (Re), Equation 2.12.

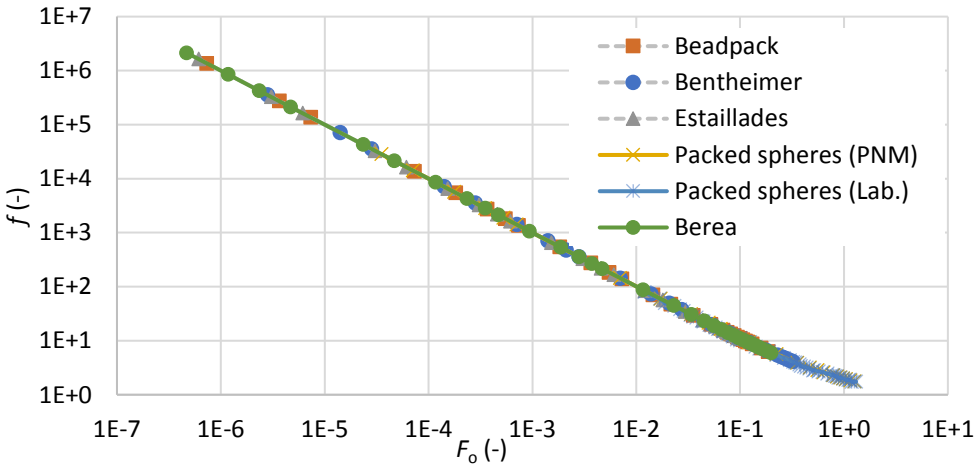

Figure 4-12 The medium friction factor (f) versus Forchheimer number (F_o), Equation 2.18.

4.3.5 Pressure distribution

One of the advantages of pore-network modelling approach is that it provides a detailed overview of the pressure field at the pore-scale as presented in Figure 4-13. Figure 4-13 shows the pressure value at each pore body versus distance (x) along the flow direction when applying a 10,000 Pa pressure drop. The 3D pressure distribution at each pore body is shown at the top right corner for each sub-figure. The dotted black curve represents the average pressure value at any cross-section perpendicular to the flow direction. Inspection of Figure 4-13 shows that for the media with low degree of heterogeneity, i.e. beadpack, packed spheres, Bentheimer and Berea there is a regular change of pressure over distance. At any vertical cross-section perpendicular to the flow direction, the maximum pressure variation between pores remains within 25% of the overall pressure drop in the case of beadpack, 10% in the packed spheres, 45% in the Bentheimer and 37% in the Berea. Nevertheless, for highly heterogeneous media (Estaillades) the pressure variation between pores at one cross-section may extend up to 98% of the overall pressure drop. This is mainly caused by the medium's heterogeneity that creates some stagnant zones with low pressure values next to the zones with high pressure. The pressure distribution in Figure 4-13c shows that the sample is composed of several zones, poorly connected to each other. Therefore, the pressure values within each zone are nearly equal and are significantly different from the pressure values of other zones. Consequently, the velocity distribution within the sample ranges from low in stagnant zones to high at the connection between zones where the inertial effects can be observed even at low pressure gradients. The pressure distribution along the flow direction in the beadpack (Bentheimer) packed spheres and Berea samples can be approximated by a linear relationship (the dotted black curve in Figure 4-13), however, this is not the case for the Estaillades sample where a nonlinear relationship would be more appropriate.

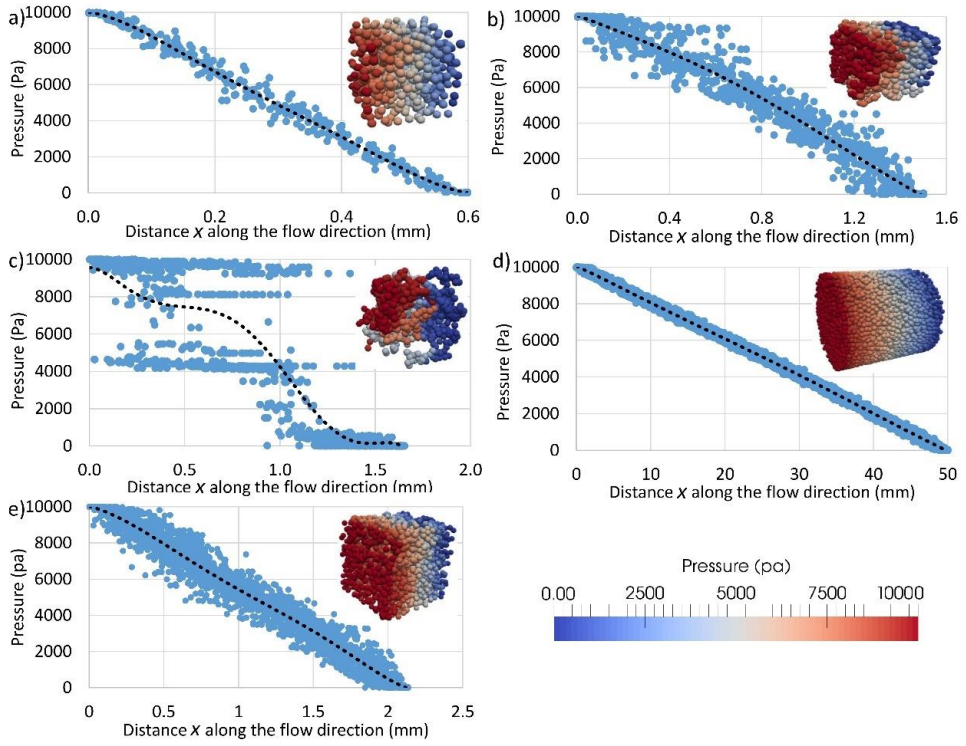

Figure 4-13 Pressure values at each pore body vs. distance (x) along the flow direction when applying 10,000 Pa pressure drop; a) Beadpack, b) Bentheimer, c) Estaillades, d) packed spheres and e) Berea. The 3D pressure distribution at each pore body is shown at the top right corner of each sub-figure. The dotted black curve represents the average pressure value at any cross-section perpendicular to the flow direction. The flow direction is from left to right.

4.3.6 Tortuosity

Wang et al. (1999) defined tortuosity, τ (-), in isotropic media as

$$\tau = \frac{\hat{L}}{\tilde{L}_e} \qquad 4.14$$

where $\hat{L}$ (mm) is the average streamwise flow path or the actual distance including any encountered curves between two points and $\tilde{L}_e$ (mm) is the straight distance between these two points. Some other authors define tortuosity as the square of this ratio (Dullien, 1992). Thauvin and Mohanty (1998) and Wang et al. (1999) investigated the effect of tortuosity on the non-Darcy coefficient and concluded that its effect (< 2%) is tiny and negligible. As it is difficult to obtain tortuosity either experimentally or numerically, Muljadi et al. (2015) used the method proposed by Duda et al.

(2011) and Koponen et al. (1996) to obtain tortuosity from the fluid velocity field without the need to determine flow paths as follows:

$$\tau = \frac{\langle |u_{avg}| \rangle}{\langle u_{\mathrm{x}} \rangle} \geq 1 \qquad 4.15$$

where $\langle |u_{\mathrm{avg}}| \rangle$ (mm/s) is the average magnitude of the interstitial velocity over the entire volume and $\langle u_{\mathrm{x}} \rangle$ (mm/s) is the volumetric average of its component along the macroscopic flow direction.

In the proposed PN model, the discharge through each pore throat can be easily determined after solving the pressure value at each pore body, then the velocity of flow in each pore throat can be determined by dividing the discharge value in each pore throat by the cross-sectional area of that pore throat. The velocity through the connected pore bodies can be determined by dividing the pore throat discharge by the cross-sectional area of the pore body as well. Then the overall average fluid velocity through the pore throat and the two connected pore bodies can be estimated as the length harmonic average of the velocities (Equation 4.12).

Finally, the volumetric average interstitial velocity $\langle |u_{\mathrm{avg}}| \rangle$ (mm/s) can be obtained as

$$\langle |u_{avg}| \rangle = \frac{\sum u_{\mathrm{i-j,tot}}\, a_{\mathrm{i-j}}}{\sum a_{\mathrm{i-j}}} \qquad 4.16$$

Similarly, u_x (mm/s) for each pore throat can be estimated as the *x*-component, along the macroscopic flow direction, corresponding to each $u_{i-j,tot}$ (mm/s). Then, $\langle u_x \rangle$ (mm/s) can be obtained by replacing $u_{i-j,tot}$ by u_x in Equation 4.16.

Figure 4-14 shows that tortuosity increases slightly when the Reynold's number increases, this is due to the increase in velocities and the possible occurrence of some eddies as a result of inertial effects. The PNM results for all samples in Figure 4-14 have a trend similar to that obtained by Muljadi et al. (2015) and Chukwudozie et al. (2012), and they are in agreement (varying within less than 8%) with the values obtained by Muljadi et al. (2015). It is noticeable that in Figure 4-14c, the increasing trend of τ is delayed compared to the results by Muljadi et al. (2015), this is attributed to some discrepancies in predicting the flow velocities and pressure losses (as in Figure 4-5c) for Estaillades sample. Due to the high

heterogeneity level of Estaillades sample, its tortuosity is larger than other samples. This is due to the poor connectivity between different zones in the sample, as in Section 4.3.5, so each fluid particle may need to travel a longer path.

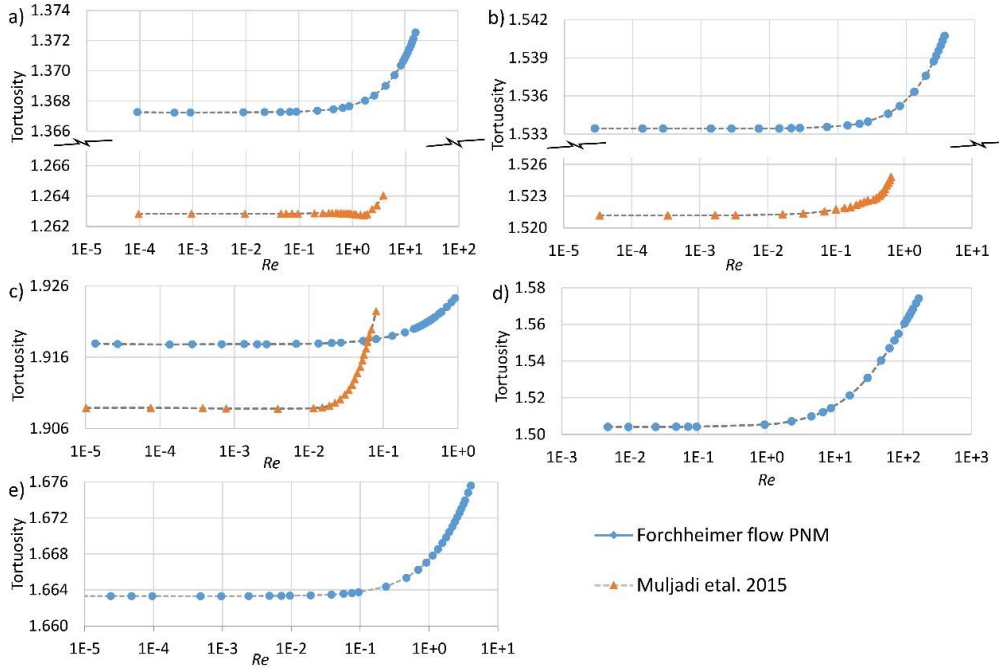

Figure 4-14 Tortuosity versus *Re* for; a) Bead pack, b) Bentheimer, c) Estaillades d) packed spheres, and e) Berea samples.

4.4 Conclusion

In this chapter, Darcy permeability, apparent permeability, the non-Darcy coefficient and tortuosity were estimated for five porous samples (Beadpack, Bentheimer sandstone, Estaillades carbonate, packed spheres and Berea sandstone) with different degrees of heterogeneity using pore-network modelling and applying the Forchheimer Equation. The proposed model overcomes most of the limitations in all previous studies that used pore-network modelling to simulate non-Darcy flow; i.e. limited coordination number, 2D simulations only, inaccuracy of some equations, limitations regarding the use of regular structured networks only and lack of calibration. In addition, the onset of non-Darcy flow was fully investigated in detail for all samples.

Based on the findings of this research, it is concluded that the Forchheimer number (F_o), instead of the permeability-based Reynold's number (Re_K) or

standard Reynold's number (*Re*), is recommended as a criterion to determine the onset of non-Darcy flow. This is because the Forchheimer number accounts for Darcy permeability, the Forchheimer coefficient and the medium degree of heterogeneity. The onset of non-Darcy flow, determined at, the dimensionless apparent permeability, $K^* = 0.99$ and using Re_K, is highly dependent on the medium's degree of heterogeneity. For Bentheimer sandstone the onset of non-Darcy flow is one order of magnitude smaller than in the case of beadpack, and for Estaillades the onset of non-Darcy flow is three orders of magnitudes smaller than that in the case of beadpack. Nevertheless, the Forchheimer number values for the onset of non-Darcy flow for the five samples ranged from 0.01 to 0.1 and this is in agreement with Andrade et al. (1999).

The Darcy Permeabilities (K_D) and Forchheimer coefficients (β) for all samples are in good agreement (varying within 15.2% and 54% respectively) with the values obtained either in the laboratory, by Muljadi et al. (2015) or by Mostaghimi et al. (2012) for the same samples, except in the case of Bentheimer, where its β value varied by 126%.

The medium friction factor is a good feature that can be used to calculate the pressure gradient at different velocities for different flow regimes, regardless of the heterogeneity of the medium, if the Darcy permeability and Forchheimer coefficient are known. It was found that the medium friction coefficient decreases when the fluid velocity increases. Following the Forchheimer equation, the medium friction factor versus the Forchheimer number curve is identical for all media regardless of their degree of heterogeneity. Tortuosity was found to increase slightly when the flow velocity increases, in all samples.

For highly heterogeneous media, i.e. Estaillades, the pressure variation between pores at one cross-section, perpendicular to the flow direction, may extend to up to 98% of the overall pressure drop. This is mainly caused by the medium's heterogeneity that creates some stagnant zones with low pressure values next to other zones with high pressure values.

The pore-network modelling approach has been shown to be computationally more efficient in comparison to direct flow simulations and could dramatically reduce the running time from a few hours (3 hours and 37 minutes for the Estaillades model in Muljadi et al. (2015) work) using 16 parallel computer nodes to less than one minute using a standard PC, but it is still relatively memory demanding when a large number of pore bodies are used, especially for non-linear flow simulations. For instance, a pore-network with 120,000 pore bodies requires 185 GB Ram. Nevertheless, in terms of pore geometries, direct numerical simulation is believed to be more accurate than pore-network modelling which simplifies the irregular pore shapes into pores with simple geometries for which the analytical flow equations can be applied.

Chapter 5

Pore-network modelling of Darcy, Forchheimer and turbulent flow

In this chapter, a PNM algorithm for modelling all flow regimes in porous media is developed. The limits of different flow regimes are predefined at the pore-scale for each pore body and pore throat (see Figure 5-1), then the boundaries between macro-scale flow regimes are detected from the results (as shown in Figure 5-5). The proposed model has been applied to two porous media; the packed spheres (d_m = 1.84 mm) sample used in the experimental work explained in Chapter 3 and another regularly structured packing of 5 mm uniform beads. The experiments done on the second medium were performed by an undergraduate student (Richardson, 2019). The pore-network of the randomly packed spheres has been extracted from the available CT-images as explained before in Section 3.4.2 and Section 4.3.1, while another method (the developed code and algorithm are explained in Appendix C) is applied to generate a pore-network equivalent to the 5 mm beads sample. The 5 mm beads sample has been used because, to my knowledge, no previous work has been done on simulating turbulent flow through porous media using a 3D CT-image that can be used as an additional case for verifying the proposed model. Also, the pore-network extraction process may affect the simulation results due to the simplifications made while converting from the irregular complex shape of a medium to its equivalent simplified pore-network. Therefore, a regularly structured medium can be used for the laboratory experiments (Richardson, 2019), then its equivalent pore-network will be used to verify the proposed model against the experimental results. This will reduce the uncertainties associated with the pore-network extraction process as such regular structured medium has known pore locations and dimensions.

In the experimental work of Richardson (2019), the same test rig and an experimental setup similar to that described in Section 3.2 were used. The sample used is composed of 5 mm uniform beads arranged in a regular

structured order (see Figure 5-2a). The sample length is 200 mm and the sample cross-section is square with 50 mm side length. Water was used as the working fluid at different discharge rates ranging from ~0.01 to 0.16 l/s, and for each run, the discharge rate was measured using the provided digital flowmeter (Siemens Sitrans FM Magflo MAG 5100W flowmeter). The head loss measurements were done using two manometer tubes located 25 mm after the sample inlet and before the sample outlet to eliminate the effect of boundaries on the flow, i.e. the head loss was measured through a distance of 150 mm in the porous medium. The experiment was aimed at estimating the medium parameters (K_D, β, and $\beta`$) and defining the onset of non-Darcy and turbulent flow regimes for a medium with known structure. Unfortunately, the error in the experimental work of Richardson (2019) cannot be quantified. For instance, the error resulting from using the flowmeter without calibration cannot be quantified.

5.1 Introduction

Turbulent flow in porous media has been the focus of many researchers due to the large number of engineering applications in which turbulent flow permeates through a porous medium. The spreading of contaminants through underground reservoirs, fluidised bed combustors, chemical catalytic reactors, accelerating flow near oil wells, movement of natural gas through sand, flow through the hyporheic zone (the zone beneath a stream bed where there is an exchange between shallow groundwater and surface water) and flow through porous media composed of coarse particles are such examples of turbulent flow through porous media (Carman, 1937; Pedras & de Lemos, 2000, 2001; Packman et al., 2004). For such applications pore-scale models, such as PNM, provide more details and help us to understand phenomena and mechanisms that cannot be understood using macro-scale models. Moreover, turbulent flow has a chaotic nature and is difficult to predict analytically. For such a case, numerical models provide an alternative affordable solution for the flow.

As mentioned in Section 2.3.3, the only work that has been done to model turbulent flow using PNM is that presented by Martins et al. (2007), but this

work was performed with many assumptions which restrict its application to other cases. For example, they assumed fixed boundaries between laminar and transition flow (when Re_{pore} = 2300), Equation 2.12, and between transition and turbulent flow (when Re_{pore} = 5000) in each pore throat. However, these values were obtained from studying flow through macro-scale commercial pipes with very large dimensions compared to the dimensions of voids in real porous media and do not represent the boundaries between flow regimes in porous media (Dybbs & Edwards, 1984; Fand et al., 1987; Kececioglu & Jiang, 1994; Horton & Pokrajac, 2009). They assumed a constant factor of 1.5 as the summation of the sudden expansion and sudden contraction coefficients (Section 4.2.1.2), despite the fact that these coefficients are dependent on the pore throat and pore body dimensions. Additionally, they assumed fully developed flow in each pore (Section 2.3.1) without checking the validity of this assumption. Also, the model proposed by Martins et al. (2007) was not verified or applied to the modelling of flow through any real porous media.

The main objective of this chapter is to develop a pore-network model capable of overcoming the aforementioned limitations, which can represent the flow characteristics and predict the properties of the porous media within all flow regimes including the turbulent flow regime.

5.2 Method

Bearing in mind that any porous medium is composed of pores with various dimensions and geometries, then, while applying a constant pressure drop across a single porous medium, the flow regime may vary from one pore to another. At the pore-scale, some pores may exhibit laminar flow, while the flow in other pores may be transitional or turbulent. To model the flow behaviour under all these possible flow regimes, the following strategy is followed.

- First, the non-Darcy flow model (presented in Chapter 4) is applied to the pore-network and this provides an initial guess of the pressure value and velocity in each pore, then the Reynold's number of each pore is estimated.

- Following the method proposed by Martins et al. (2007), and based on the Reynold's number (Equation 2.12) value in each pore, the flow regime at the pore-scale (for each pore body and pore throat) is determined using the predefined limits discussed in Section 2.4 (laminar when $Re_{\text{pore}} < 150$, transition when $150 \leq Re_{\text{pore}} \leq 300$, and turbulent when $Re_{\text{pore}} > 300$).
- Then, the friction factor of each pore (f_{pore}) is recalculated depending on the new defined flow regime in the pore (see Figure 5-1). The transition and turbulent flow regimes were found to initiate locally in each pore in a porous medium at the Reynold's number values of 150 and 300, see Section 2.4, (Dybbs and Edwards, 1984; Horton and Pokrajac, 2009).
- Then, the proposed set of equations (Equations 5.1 to 5.7) shown below are applied to the whole pore-network. The proposed solution requires few iterations before f_{pore} reaches a constant value in each pore.
- Finally, the medium parameters (e.g. K_D and β), Equation 2.3, can be obtained and the limits between the flow regimes at the macro-scale can be determined. For instance, the onset of non-Darcy and turbulent flow regimes can be obtained by plotting the results in the form of normalized dimensionless pressure $\left(\frac{\Delta P\, K_D}{L\, \mu\, v}\right)$ versus Reynold's number, and a change in the slope of the results represents the different flow regimes (Section 5.3.3).

5.2.1 Flow modelling

5.2.1.1 Pressure loss due to friction at the pore-scale

The average velocity through any pore, u_{pore} (mm/s), can be related to the pressure loss using the Darcy-Weisbach equation (Weisbach, 1845; Darcy, 1857), Equation 2.8 $\left(\Delta h_{pore} = \frac{\Delta P_{\text{pore}}}{\gamma} = f_{\text{pore}} \frac{L_{\text{pore}}}{2\, r_{\text{pore}}} \frac{u_{\text{pore}}^2}{2g}\right)$. For fully developed laminar flow, the pore friction factor, f_{pore} (-), is a function of the Reynold's number, Re_{pore} (-), only, and it can be estimated using Equation 5.1 (Çengel & Cimbala, 2006):

$$f_{\text{pore (laminar)}} = \frac{32}{k\, Re_{\text{pore}}} \quad 5.1$$

where $Re_{\text{pore}} = \frac{\rho\, u_{\text{pore}}\, (2\, r_{\text{pore}})}{\mu}$, is the pore Reynold's number, and k (-) is a constant that depends on the cross-sectional shape of the pore, which is equal to 1/2, 3/5, and 0.5623 for circular, triangular and square cross-sections, respectively (Çengel & Cimbala, 2006). Substituting Equation 5.1 into Equation 2.8 leads to the Hagen–Poiseuille equation (Hagen, 1839; Poiseuille, 1841), Equation 4.1, for laminar flow.

In the turbulent flow regime, unlike laminar flow and due to the complexity caused by the randomness and fluctuations in the fluid particle movements, the expressions for velocity and pressure loss are based on both analysis and experimental measurements, therefore, they are considered semi-empirical and may have some constants obtained from experimental data (Çengel & Cimbala, 2006). For fully developed turbulent flow, f_{pore} is a function of the Reynold's number and the average internal surface roughness of the pore, ε (mm), and it can be expressed implicitly using Equation 5.2 (Colebrook & White, 1937), by:

$$f_{\text{pore (turbulent)}} = \left[2\, log_{10}\left(\frac{2.51}{Re_{\text{pore}}\sqrt{f_{\text{pore(turbulent)}}}} + \frac{\varepsilon}{3.7\, D_{\text{pore}}}\right)\right]^{-2} \quad 5.2$$

where D_{pore} (mm) is the diameter of the maximum inscribed circle inside the pore and the ratio $\varepsilon/D_{\text{pore}}$ (-) is the relative roughness of the pore. For the case of smooth pores, the relative roughness term $\left(\frac{\varepsilon}{3.7\, D_{pore}}\right)$ in Equation 5.2 can be neglected (Çengel & Cimbala, 2006; Rennels & Hudson, 2012), which is the case for the media composed of glass beads with smooth surface used. In the proposed model, $f_{\text{pore (turbulent)}}$ is estimated at a constant Re_{pore}, using Equation 5.2, by iterations. The iterations continue until the relative error between $\left(\Delta f_{\text{pore}}\% = \frac{|f_{\text{pore}}(n+1) - f_{\text{pore}}(n)|}{f_{\text{pore}}(n+1)} \times 100\right)$ between the last two successive values of $f_{\text{pore (turbulent)}}$ is less than 1%.

For transitional flow, when $150 \leq Re_{\text{pore}} \leq 300$, following the method proposed by Martins et al. (2007), $f_{\text{pore (transition)}}$ is calculated by interpolation, i.e. $f_{\text{pore (laminar)}}$ is estimated using Equation 5.1 at $Re_{\text{pore}} =$

150, and $f_{\text{pore (turbulent)}}$ is estimated using Equation 5.3 at $Re_{\text{pore}} = 300$, then $f_{\text{pore (transition)}}$ is calculated at Re_{pore} using interpolation between these two values.

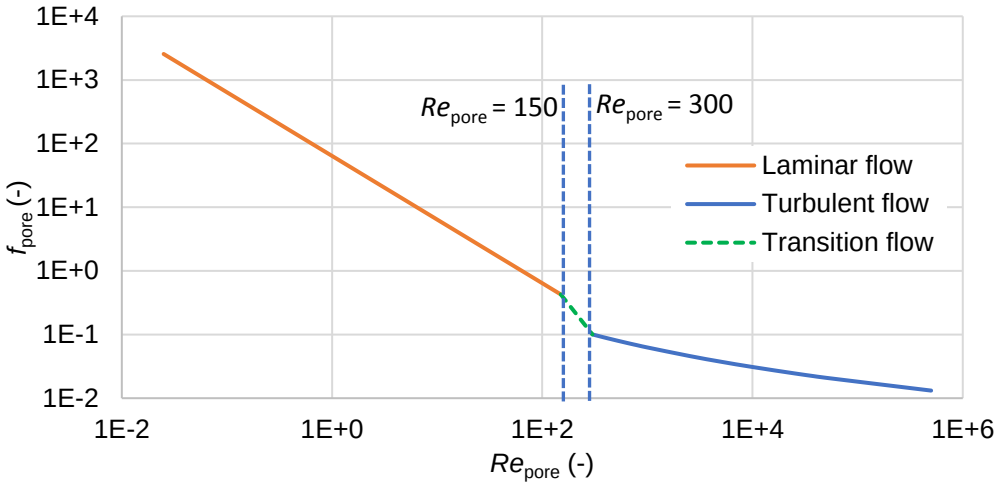

Figure 5-1 The pore friction coefficient (f_{pore}) vs. pore Reynold's number (Re_{pore}) for a 0.5 mm radius circular tube, following Equation 5.1 for laminar flow and Equation 5.2 for turbulent flow, while f_{pore} for transition flow is obtained by linear interpolation between the two values obtained at Re_{pore} =150 and Re_{pore} =300.

The Darcy-Weisbach equation, Equation 2.8, can be rewritten as,

$$q_{\text{pore}}^2 = \frac{g_{\text{pore}}^f}{L_{\text{pore}}} \Delta P_{\text{pore}}^f \qquad 5.3$$

where ΔP_{pore}^f (Pa) represents the pressure loss due to friction (between fluid particles, and between the fluid and the pore internal surface) through the pore, and the conductance, g_{pore}^f (mm^4/Pa·s), of any pore cross-section, is given by

$$g_{\text{pore}}^f = \frac{4\, r_{\text{pore}}\, a^2}{f_{\text{pore}}\, \rho}. \qquad 5.4$$

From Equation 5.3 and using the same harmonic mean concept of Equation 4.4, the friction pressure loss, $\Delta P_{\text{i-j,tot}}^{\text{f}}$ (Pa), between any two pore bodies (i and j) can be related to the discharge as

$$q_{\text{i-j}}^2 = \frac{g_{\text{i-j,tot}}^f}{L_{\text{i-j,tot}}} \Delta P_{\text{i-j,tot}}^{\text{f}} \qquad 5.5$$

where $L_{\mathrm{i-j,tot}}$ (mm) is the length between the centres of the two pore bodies (i and j) and $\frac{g^{f}_{\mathrm{i-j,tot}}}{L_{\mathrm{i-j,tot}}} = \frac{1}{\frac{L_{\mathrm{i}}}{g_{\mathrm{i}}}+\frac{L_{\mathrm{i-j}}}{g_{\mathrm{i-j}}}+\frac{L_{\mathrm{j}}}{g_{\mathrm{j}}}}$, see Figure 4-1 and Equation 4.4.

5.2.1.2 Pressure loss due to inertial effects at the pore-scale

The inertial effects due to expansion, i.e. when flow moves from a pore throat to a connected pore body, and contraction, i.e. when flow moves from a pore body to a connected pore throat, can be calculated across each pore throat using equations 4.6 and 4.7 (Crane, 1942; Bird et al., 1960). Then, the total pressure loss for any pore throat in the network is the summation of the pressure losses due to friction, expansion and contraction, and can be estimated according to Equation 5.6 as follows:

$$\Delta P^{\mathrm{tot}}_{\mathrm{i-j}} = \Delta P^{\mathrm{f}}_{\mathrm{i-j,tot}} + \Delta P^{\mathrm{exp}}_{\mathrm{i-j}} + \Delta P^{\mathrm{cont}}_{\mathrm{i-j}} = \left[\frac{L_{\mathrm{i-j,tot}}}{g^{f}_{\mathrm{i-j,tot}}}\right] q^{2}_{\mathrm{i-j}} + K_{\mathrm{e}}\frac{\rho q^{2}_{\mathrm{i-j}}}{2a^{2}_{\mathrm{i-j}}} + K_{c}\frac{\rho q^{2}_{\mathrm{i-j}}}{2a^{2}_{\mathrm{i-j}}} \qquad 5.6$$

where K_{e} (-) and K_{c} (-) were previously defined in Section 4.2.1.2 as the expansion and contraction coefficients.

Equation 5.6 can then be rewritten as,

$$q_{\mathrm{i-j}} = \sqrt{\frac{\Delta P^{\mathrm{tot}}_{\mathrm{i-j}}}{\left[\frac{L_{\mathrm{i-j,tot}}}{g^{f}_{\mathrm{i-j,tot}}}\right] + K_{\mathrm{e}}\frac{\rho}{2a^{2}_{\mathrm{i-j}}} + K_{\mathrm{c}}\frac{\rho}{2a^{2}_{\mathrm{i-j}}}}} \; . \qquad 5.7$$

5.2.1.3 Solving the final system of equations

For the whole pore-network, Equation 5.7 is applied for each pore throat and the continuity equation (i.e. Equation 4.11) is invoked at each pore body. This process results in a system of N_{PB} non-linear equations, where N_{PB} is the total number of pore bodies in the pore-network. The resulting system of equations is solved for pressure using a developed FORTRAN code with the use of the HSL NS23 routine (HSL, 2013). The initial guess of the pressure values at each pore body is provided, as input, from the non-Darcy flow case (presented in Chapter 4). Then, the HSL NS23 routine iterates until the sum of the squares of the residuals is less than the predefined value of 10^{-10}. It is worth mentioning that the resulting system of equations is implicit, which means that the equations are solved to obtain the pressure value at each pore body, while the friction factor $\left(f_{\mathrm{pore}}\right)$ used

to obtain the conductance $\left(g^{f}_{\mathrm{i-j,tot}}\right)$ between any two pore bodies (in Equation 5.7) is a function of velocity which depends on the pressure values. This requires another iterative process until a constant value of f_{pore} is obtained for each pore. The following steps summarise the procedures followed to achieve a final solution of the nonlinear system of equations:

1. Using the non-Darcy flow case (presented in the Chapter 4) as an initial guess for the pressure value at each pore body, the velocity (u_{pore}), Equation 4.1, and Reynold's number (Re_{pore}), Equation 2.12, for each pore can be estimated. Then, the friction factor $\left(f_{\mathrm{pore}}\right)$ and conductance (g^{f}_{pore}) for each pore in the pore-network are initially estimated using equations 5.1, 5.2 and5.4.
2. Using Equation 4.4, an initial value for $g^{f}_{\mathrm{i-j,tot}}$ is obtained for each pore throat and invoked in Equation 5.7. After that, the continuity equation is applied at each pore body to generate a system of non-linear algebraic equations.
3. The HSL NS23 subroutine (HSL, 2013) is called to solve the proposed system of equations and to provide an updated pressure value at each pore body.
4. The updated pressure values are used to recalculate the velocity (u_{pore}), Reynold's number (Re_{pore}), friction factor $\left(f_{\mathrm{pore}}\right)$ and conductance (g^{f}_{pore}) for each pore in the pore-network.
5. The steps 2 to 4 are repeated iteratively. At each iteration, the Reynold's number of each pore $\left(Re_{\mathrm{pore}}\right)$ from the current iteration (iteration number n+1) is compared to the value from the previous iteration (iteration number n). If the relative error between the two values $\left(\Delta Re_{\mathrm{pore}}\% = \frac{|Re_{\mathrm{pore}}(n+1) - Re_{\mathrm{pore}}(n)|}{Re_{\mathrm{pore}}(n+1)} \times 100\right)$ for any single pore is larger than a predefined relative error of 1%, then the code continues iterating. The iterations stop if the relative error $\left(\Delta Re_{\mathrm{pore}}\%\right)$ for all pores in the pore-network is less than 1%, or if the relative error of the overall discharge through the medium is less than 1% as well.

By solving this nonlinear system of algebraic equations, the final pressure value at each pore body is obtained, then Equation 5.7 is used to determine the discharge through each pore throat. Finally, at the macro-scale and after the onset of turbulence, the Forchheimer equation can be applied to describe the turbulent flow behaviour with modified values of the Forchheimer coefficient ($\beta`$) and the Forchheimer permeability ($K_{\mathrm{F}}^{`}$) that can be obtained using a Forchheimer plot (See Equation 2.3).

In all simulations, a no-flow boundary condition is applied to all pore-network boundaries except the inlet and outlet boundaries where constant pressure values are applied. The same fluid properties used for modelling the non-Darcy flow regime are applied, i.e. μ = 0.001 kg/ms and ρ = 1000 kg/m^3. The overall volumetric fluid discharge (q) is obtained by summing up all the pore throat discharges either at the inlet or the outlet of the pore-network, while the flow superficial velocity (v) is estimated as the volumetric fluid discharge (q) divided by the whole cross-sectional area (A) perpendicular to the flow direction.

The algorithm and details of the approach used for solving the resulting nonlinear system of algebraic equations for the proposed pore-network model are shown in Appendix B.

5.2.2 Numerical instability

An instability problem was discovered during the development of the pore-network flow code developed in this chapter. This problem happens when either the velocity through any pore throat, in the pore-network, is equal to zero or the pressure values of two connected pore bodies are exactly the same. If the velocity through a pore throat is equal to zero, the Reynold's number for this pore throat is equal to zero as well, and the value of the friction factor for this pore throat, which is calculated either from Equation 5.1 or Equation 5.2, goes to infinity due to the division by zero. Also, during the iterative processes, explained in the Section 5.2.1.3, the pressure values of any two connected pore bodies (i and j) can be the same, then any derivative value that contains $\Delta P_{\mathrm{i-j}}^{\mathrm{tot}}$ will be equal to infinity due to the division by zero as shown in Appendix B.

To resolve this instability problem, the code was designed to check the velocity through each pore throat and the pressure values of each two connected pore bodies before each iteration. Then, if any of the two cases that cause instability are identified for any pore throat, then the pore throat is marked and excluded from the calculations (during the current iteration only). The final system of equations and the Jacobian matrix that contains the nonzero derivatives are updated and the iterations continue as normal.

5.3 Verification, Results and Discussion

5.3.1 Extracted pore-networks

The same extracted pore-network for the REV selected from the packed spheres (d_m = 1.84 mm) sample which was used in the experimental work (Chapter 3) has been used to verify the code developed for the turbulent flow regime. The properties of this extracted pore-network together with the pore-network equivalent to the regularly structured uniform beads (d_m = 5 mm) sample are shown in Table 5-1 and Figure 5-2.

Table 5-1 Properties and characteristics length of the packed spheres (d_m = 1.84 mm) and regularly structured uniform beads (d_m = 5 mm) samples.

Sample	*Resolution (μm)*	*Porosity, ϕ*	*Characteristic length, L_{charc} (mm)*	*Sample size*	*Pore voxels*	*K_D ×10^{-9} (m^2), Lab.*
Packed spheres (d_m = 1.84 mm)	65.99	0.364	1.837	758×758×758 voxels	124,612,700	2.25 ± 7%
Regularly structured uniform beads (d_m = 5 mm)	NA	0.48	5.0	50×50×100 mm^3	NA	29.70

Table 5-2 The properties of the pore-networks equivalent to the packed spheres (d_m = 1.84 mm) and regularly structured uniform beads (d_m = 5 mm) samples.

Sample	*No. of PBs*	*No. of PThs*	*Average coordination number*	*Maximum coordination number*
Packed spheres (d_m = 1.84 mm)	10,315	53,960	10.4	30
Regularly structured uniform beads (d_m = 5 mm)	2,299	6,600	5.6	6

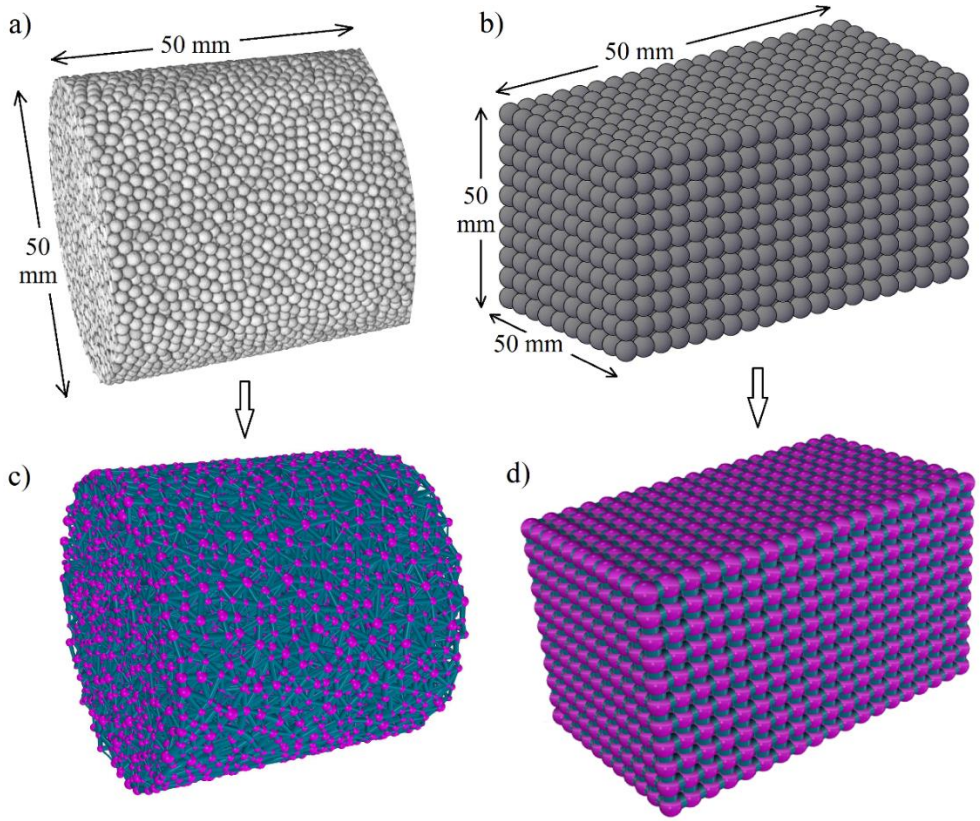

Figure 5-2 The porous media used in the laboratory and their equivalent pore-networks; a) the REV of the randomly packed spheres (d_m = 1.84 mm), and b) is 5 mm diameter uniform beads, packed regularly in a 50 mm × 50 mm × 100 mm Perspex duct.

5.3.2 Flow behaviour

PNM has been used in the literature for small samples and narrow pores compared to the two samples used in this chapter. Most of the previous work done using PNM was performed in the Darcy laminar flow regime, while only five studies were done in the laminar non-Darcy flow regime (Section 4.1). The sizes of the pores used in most of these studies ranged from 1 nm to 0.1 mm in terms of pore diameters (Dong et al., 2007; Lawrence & Jiang, 2017) and the length of each pore ranged from less than the pore diameter up to ~40 times the pore diameter. Within this range of pore dimensions, the Reynold's number in each pore is small and the pore entrance length (L_h), see Section 2.3.1, is small compared to the whole length of the pore, so the assumption of the fully developed flow is valid. Meanwhile, the pore diameters in the packed spheres' (d_m = 1.84 mm) sample ranged from 0.06 mm to 1.4 mm. In the regularly structured uniform (d_m = 5 mm) beads, the pore body and pore throat diameters are fixed, and they are equal to 4.25 mm and 2.34 mm, respectively. As mentioned in Chapter 4, for the Forchheimer flow regime in the packed spheres' (d_m = 1.84 mm) sample, the Reynold's number in each pore is relatively high, and the flow in most pores is a developing flow, i.e. within these relatively large pores, the pores are not long enough for a fully developed flow to be achieved. In such cases, if the flow is assumed to be fully developed in each pore, this causes underestimation of the friction factor for each pore in the sample and consequently underestimation of the pressure loss through the pore.

For the turbulent flow regime, by checking the entrance length ($L_{h,turbulent}$) for both samples using either Equation 2.10 or 2.11, it has been found that the flow in both samples is also a developing flow. Even for samples that have a small pore such as the Bentheimer and Estaillades samples used in Chapter 4, using Equation 2.11, it has been found that the flow cannot achieve a fully developed state in each pore. Unfortunately, this conclusion could not have been achieved before proposing and checking the results of the pore-network turbulent flow model that assumed fully developed turbulent flow in all pores. The only previous study that modelled turbulent

flow using PNM (by Martins et al., 2007) assumed a fully developed flow in each pore and they did not find that the flow is a developing flow in most of the pores.

From the literature related to previous studies that modelled developing turbulent flow through pipes, it has been found that there is scarcity in such studies. To my knowledge, there is only one study presented by Bhatti and Shah (1987) that determines the friction coefficient through short pipes within the developing turbulent flow regime, but this study has some limitations in terms of the entrance length and the range of Reynold's number for which their proposed solution is valid. Nevertheless, the analysis of the proposed model results, that do not fully agree with the experimental results, are done based on the current model that assumed fully developed flow in each pore.

The proposed PNM code developed in this chapter is capable of simulating flow through the laminar, Forchheimer and turbulent flow regimes, however, in the following discussion, this code will be referred to, in short, as the "turbulent flow code". Figure 5-3 shows the pressure gradient ($\Delta P/L$) versus superficial velocity (v) obtained by PNM for both non-Darcy Forchheimer flow and turbulent flow compared to the experimental results. As shown in Chapter 3, the packed spheres sample (d_m = 1.84 mm) was designed to achieve flow measurements in the three flow regimes (Darcy, Forchheimer and turbulent flow regimes) within the laboratory capacity. It can be seen from Figure 5-3a that neither the Forchheimer flow model (presented in Chapter 4) nor the turbulent flow model can predict the experimental results, except at very low velocities (when v < 0.01 m/s). At any specific velocity larger than 0.01 (m/s), the pressure loss predicted by PNM is less than the measured value in the laboratory. This is because PNM assumes fully developed flow in all pore throat, which leads to underestimation of the friction factor and the pressure loss in all pores and, consequently, less pressure loss in the whole medium (El-Zehairy et al., 2019). On the other hand, Figure 5-3b shows a good match with the experimental results when v < 0.045 (m/s). Also, the results of the non-Darcy flow model and the turbulent flow model are close to each other. This

is because in such a medium (5 mm beads) with large pores, the flow behaviour is dominated by the inertial effects due to expansion and contraction, while the pressure loss due to friction in each pore may be neglected as shown in Section 5.3.5. In Figure 5-3b, when $v > 0.045$, there is a mismatch between the PNM and the experimental results which might be due to some uncertainties related to using the digital flowmeter, in the test rig, used to estimate the discharge for the 5 mm beads sample, while the discharge rates for the 1.84 mm beads sample was measured manually for each run.

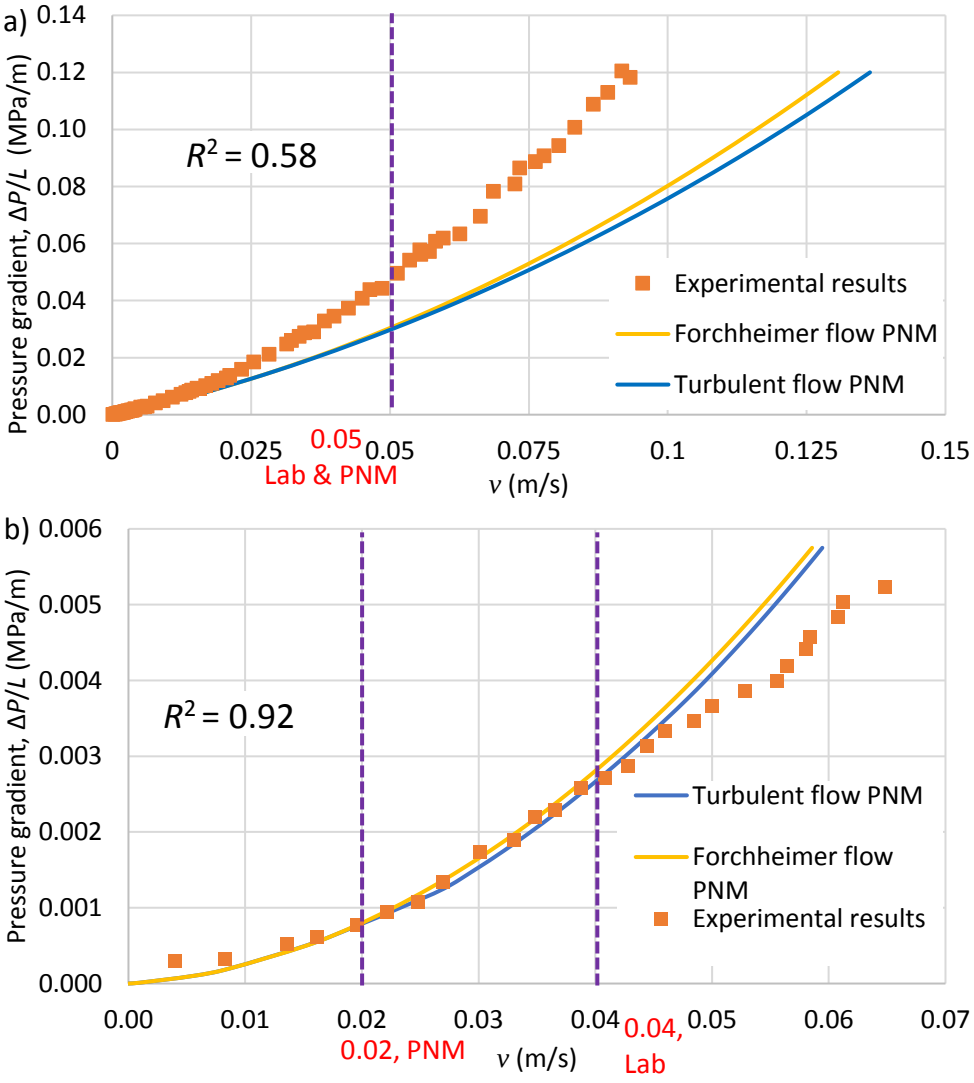

Figure 5-3 The pressure gradient ($\Delta P/L$) versus superficial velocity (v) for both non-Darcy Forchheimer flow and turbulent flow compared to the experimental results; a) is for the 1.84 mm diameter randomly packed spheres, and b) is for the 5 mm diameter regularly packed beads. The

vertical dashed lines represent the onset of turbulence determined according to Section 5.3.3.

5.3.3 Onset of turbulent flow

The results for both samples used in the experimental work (Figure 5-5) and the majority of the previous experimental work carried out through different porous media (Fand et al., 1987; Kececioglu & Jiang, 1994; Bağcı et al., 2014) showed that the rate of pressure loss, or pressure gradient, within the turbulent flow regime decreases compared to the pressure loss rate in the Forchheimer regime. The fact that turbulent flow is characterised by flow fluctuations and eddies, i.e. larger pressure losses, made this phenomenon strange and difficult to understand. On the other hand, the experiments performed by Lage et al. (1997) using air flow through three different aluminium blocks (layers) showed a different behaviour; the rate of pressure loss within the turbulent flow regime increases compared to the pressure loss rate in the Forchheimer flow regime. Lage et al. (1997) attributed this different behaviour to the medium morphology.

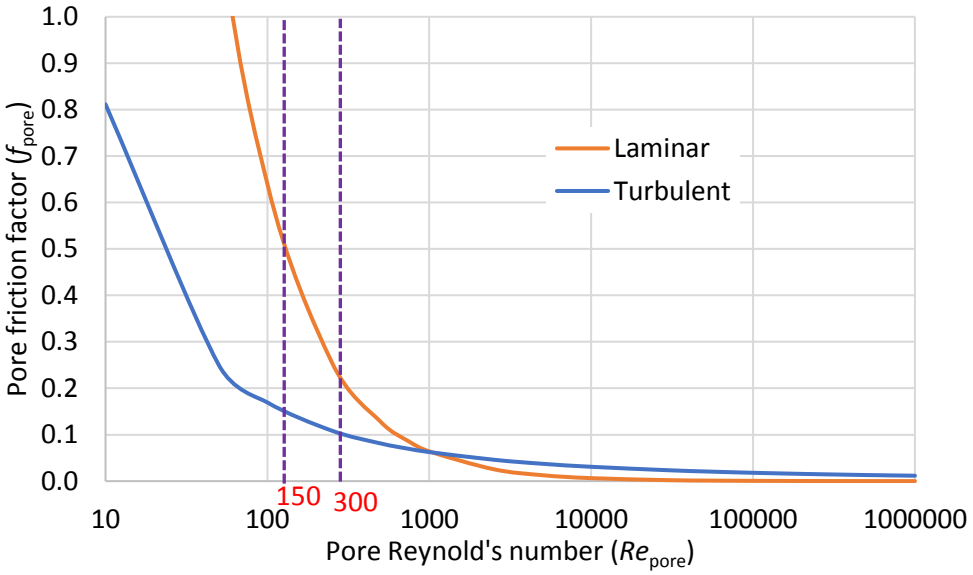

Figure 5-4 The friction factor for a single pore with 0.5 mm radius assuming laminar flow (Equation 5.1) and turbulent flow (Equation 5.2). The vertical lines represent the onset of the transition (Re_{pore} = 150) and turbulent (Re_{pore} = 300) flow regimes.

In PNM, any porous medium can be simplified into a group of single pores (tubes) connected to each other. While the friction factor in each pore is obtained using equations equivalent to Moody's Diagram (Figure 2-4). However, in Moody's Diagram, the laminar friction factor is not shown at high Reynold's number (i.e. in the turbulent flow regime). Additionally, Moody's Diagram is specific for large tubes and not micro-tubes. Therefore, Equation 5.1 and Equation 5.2 were used to developed Figure 5-4 for a single capillary tube with 0.5 mm radius. Different pore diameters (other than 0.5 mm) were tested as well and the intersection point of the two curves in Figure 5-4 is always around Re = 1000. From Figure 5-4, it is shown that when the pore Reynold's number is less than 1000, at any specific velocity, the turbulent flow friction factor is less than the laminar flow friction factor. According to Equation 2.8, at any constant velocity, the pressure loss through any pore increases when the pore friction factor increases. From the Forchheimer and turbulent flow PNM results, for both of the porous media used in the experiments (1.84 mm and 5 mm beads), within the maximum applied pressure drop through the media, the Reynold's number in most of the pores did not exceed 1000. Therefore, the pore friction factors within the turbulent flow regime are always less than the pore friction factors when laminar flow is assumed. This leads to less pressure loss through the porous medium within the turbulent flow regime compared to the pressure loss if a Forchheimer flow regime is assumed (at any constant velocity after the onset of turbulence).

From Moody's diagram (Figure 2-4), it can be seen that the friction factor in a single tube depends on its relative roughness. For smooth tubes, the friction factor of the tube is the lowest, while the tube friction factor increases when the relative roughness of the tube increases. Therefore, all porous media composed of beads with smooth surface (Fand et al., 1987; Kececioglu & Jiang, 1994; Bağcı et al., 2014) exhibited a lower pressure loss rate in the turbulent flow regime, while the medium with high relative roughness used by Lage et al. (1997) exhibited a higher pressure loss rate in the turbulent flow regime compared to the pressure loss rate in the

Forchheimer flow regime. This means that the flow behaviour depends on the medium's morphology as concluded by Lage et al. (1997).

The onset of turbulent flow can be determined when the pressure gradient results are plotted in the form of normalised dimensionless pressure $\left(\frac{\Delta P\, K_D}{L\, \mu\, v}\right)$ versus Reynold's number (Equation 2.12), as shown in Figure 5-5, and the change in the slope of the results represents the different flow regimes. Table 5-4 shows the onset of non-Darcy flow, determined according to Section 4.3.3, and the onset of turbulence for the two porous media used in this chapter compared to some results in the literature. For the results presented in Figure 5-5a, it is noticed that the onset of turbulent flow obtained by PNM (when *Re* = 92.7) is in good agreement with the onset obtained from experiments (when *Re* = 98) and obtained by Fand et al. (1987) for the 2.098 mm mean diameter packed spheres (*Re* = 80-120). However, in Figure 5-5b, the onset of turbulent flow obtained by PNM (when *Re* = 116), does not agree with the onset obtained from experiments (when *Re* = 204). This could be because of some uncertainties in the discharge measurements for the 5 mm beads sample which was done using a digital flowmeter (without calibration). Nevertheless, for the 5 mm beads, when Re_K (2.16) is used instead of *Re* (2.12) to determine the onset of turbulence, a good match between the PNM results (Re_K = 7.42) and the experimental results (Re_K = 6.56) is obtained.

In Table 5-3, different porous media with different properties are presented, therefore, the presented Darcy permeability (K_D) and Reynold's number values are not expected to match with each other. For instance, when the average bead diameter of the sample increases, the permeability (K_D) increases as it is easier for the flow to move through the medium. Moreover, in general, it is noticed that the onset of non-Darcy flow and the onset of turbulent flow occur earlier (at lower Reynold's number) in fine media compared to media composed of coarse particles. This is because media composed of fine particles have a more complex pore structure compared to media composed of coarse particles.

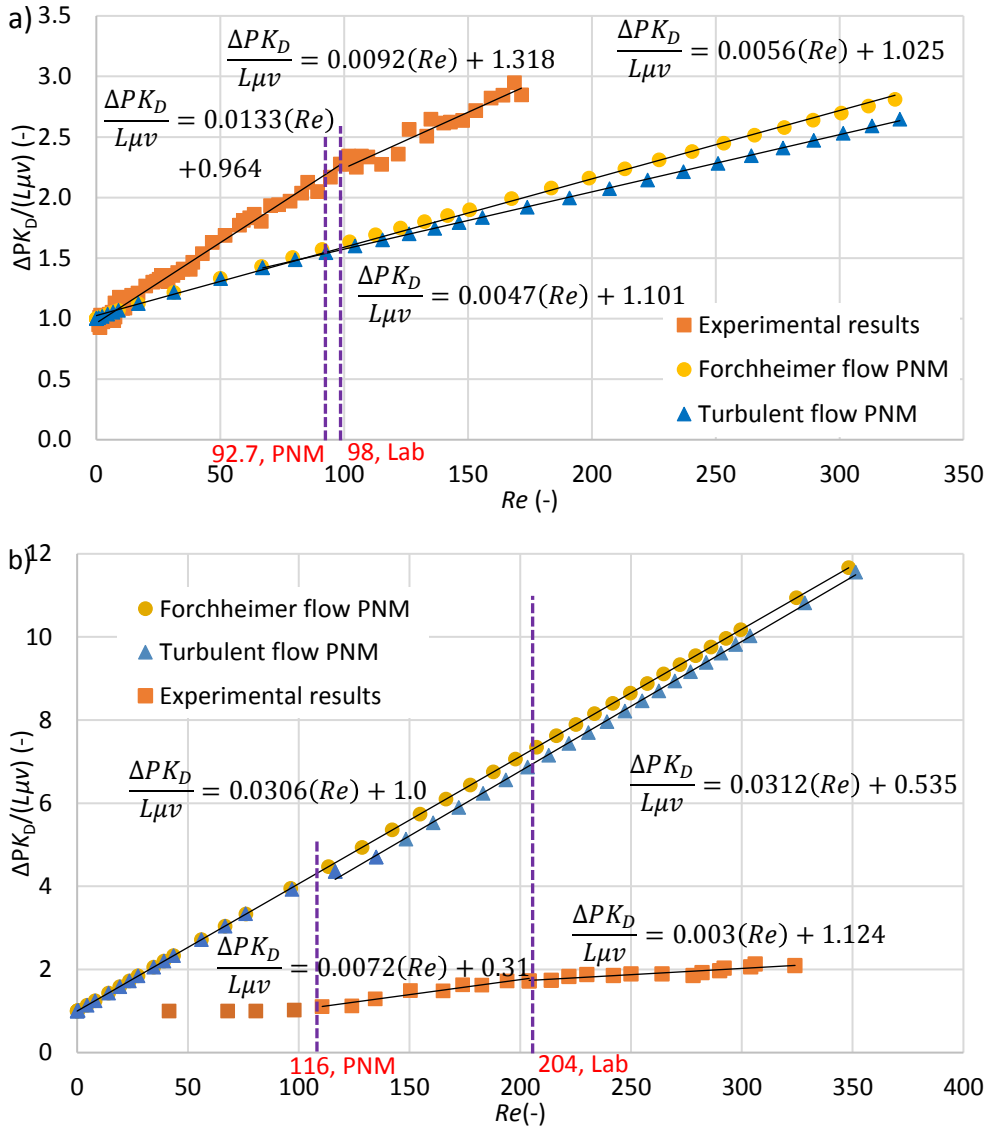

Figure 5-5 The normalised dimensionless pressure ($\Delta PK_D/L\mu v$) versus Reynold's number, *Re*, (Equation 2.12) for a) the 1.84 mm diameter randomly packed spheres, and b) the 5 mm diameter regular packed beads.

Table 5-4 The onset of non-Darcy flow, determined according to Section 4.3.3, and the onset of turbulence for the two porous media used in this chapter compared to some results in the literature.

sample	$K_D \times 10^{-9}$ *(m^2)*	*Onset velocity, v (mm/s)*		*Onset of non-Darcy flow*		*Onset of turbulent flow*		
		Non-Darcy	*turbulence*	*Re*	Re_K	*Re*	Re_K	F_o
Lab results, d_m = 1.84 mm	2.25 ± 7%	4.1 ± 3%	53.5 ± 4%	7.50 ± 3%	0.19 ± 7%	98.0 ± 4%	2.54 ± 7%	1.20 ± 21%
PNM, d_m = 1.84 mm	2.59	0.51	50.4	0.94	0.03	92.7	2.56	0.43
Fand et al. (1987), d_m = 2.098 mm	3.89	1.74	47.7	2.30-5.0	0.068-0.15	80.0-120.0	2.37-3.57	1.84
Kundu et al. (2016), d_m = 2.5 mm	5.49	7.24	N.A.	18.10	0.20	N.A.	N.A.	N.A.
Bağcı et al. (2014), d_m = 3 mm	6.42	7.5	77.5	22.45	0.59	232.5	6.21	2.85
Lab results, d_m=5 mm	29.7	19.6	40.8	98	3.15	204.0	6.56	0.61
PNM, d_m = 5 mm	101.53	0.1	23.3	0.5	0.03	116.5	7.42	3.62

5.3.4 Forchheimer plots

The Forchheimer equation (i.e. Equation 2.2) can be used to describe the flow behaviour in the turbulent flow regime in a similar way to how it was used to describe the flow in the Forchheimer flow regime, but it requires adjustments to the values of β and K_F. In the turbulent flow regime, the non-Darcy coefficient (β) is denoted by $\beta`$ and the Forchheimer permeability ($K_F$) is denoted by $K_F^`$. In Figure 5-6, the slope of each line in the turbulent flow regime represents the modified non-Darcy coefficient ($\beta`$) and its intercept is $1/K_F^`$ (Equation 2.3).

The β` values predicted by PNM for the packed spheres (d_m = 1.84 mm) and the 5 mm regular packed beads in the turbulent flow regime are 3.30×10^3 (1/m) and 1.53×10^3 (1/m), respectively. The corresponding values measured in the experiments are 7.57×10^3 and 0.58×10^3 (1/m) as presented in Table 5-5. For the packed spheres (d_m = 1.84 mm), there is a good match between β` obtained from PNM and the experimental results, this can be confirmed from Figure 5-6a as the two curves are almost parallel to each other, i.e. they have a similar trend. While for the regular packed beads, the difference between $\beta$` obtained by PNM and the corresponding experimental value is ~164%, which is associated with the aforementioned uncertainties related to the discharge measurements done using the digital flowmeter without calibration and also due to the difference between the Darcy permeability value obtain by PNM (101.5×10^{-9} m^2) and in the lab (29.7×10^{-9} m^2) as β` depends on Darcy permeability. The difference in the Darcy permeability could be due to two reasons. The first reason is the assumption of fully developed flow in each pore, which causes underestimation of the pore friction factors and this leads to less resistance to the flow's motion and higher permeability obtained by PNM. The second reason is due to the high potential error related to the experimental measurements at low discharges, because at low discharges the difference between the manometer readings is small and the potential error is high.

The predicted $K_F^{`}$ value, by PNM, for the packed spheres (d_m = 1.84 mm) and the 5 mm regular packed beads in the turbulent flow regime are 2.33×10^{-9} (m^2) and 181.8×10^{-9} (m^2), respectively. The corresponding values obtained from the experimental results are 1.7×10^{-9} and 23.26×10^{-9} (m^2), Table 5-5. For the packed spheres (d_m = 1.84 mm), there is a good match for the $K_F^{`}$ values obtained by PNM and by experiments, while for the 5 mm beads sample there is about one order of magnitude difference. There are a few reasons that may cause this mismatch for the 5 mm beads. First, permeability depends on the flow velocity and the corresponding pressure loss at low velocities, and the flowmeter is more likely to give inaccurate measurements at very low velocity, i.e. the flowmeter reading keeps fluctuating with a high degree of inaccuracy. Second, as explained in

sections 5.3.2 and 2.3.1, the entrance length of a pore (where the flow is developing) increases when the size of the pore increases, i.e. the flow is developing in each pore and it is far away from the assumption that the flow is fully developed. This is why the mismatch between the experimental results and the PNM results for the 5 mm beads is larger than the mismatch for the 1.84 m packed spheres sample.

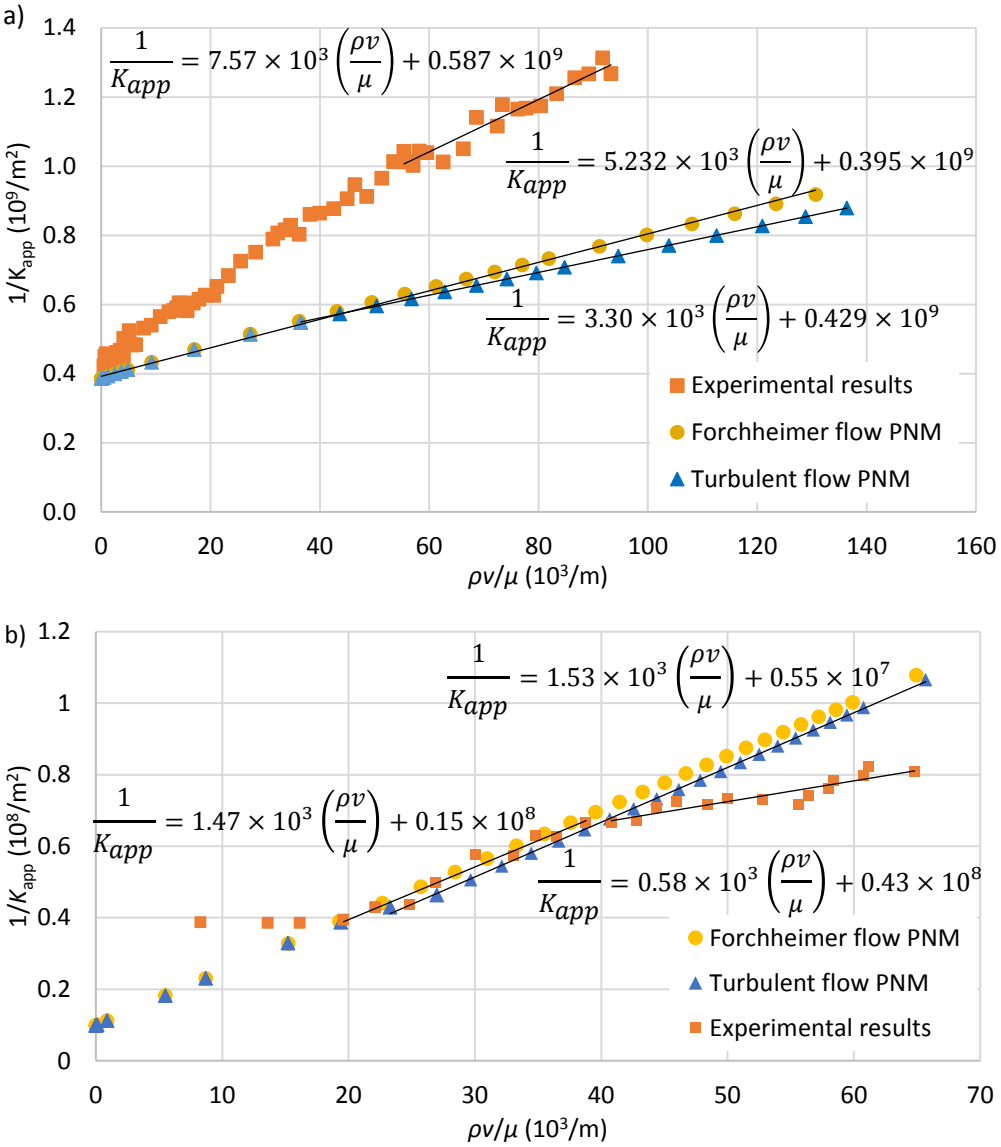

Figure 5-6 Forchheimer plot for a) packed spheres (d_m = 1.84 mm) and b) regularly structured uniform beads (d_m = 5 mm).

Table 5-5 The Darcy permeability (K_D), Equation 2.1, modified Forchheimer permeability (K_F`) and modified Forchheimer coefficient ($\beta$`), Equation 2.3, for the two samples (d_m = 1.84 mm and d_m = 5 mm).

Sample	ΔK_D ($10^{-9}\times m^2$)		ΔK_D [%]	K_F` ($10^{-9}\times m^2$)		ΔK_F` [%]	β` ($10^3/m$)		$\Delta\beta$` [%]
	Lab	PNM		Lab	PNM		Lab	PNM	
d_m = *1.84 mm*	2.25± 7%	2.59	15.2	1.70± 7%	2.33	37	7.57± 11%	3.30	56.4
d_m = *5 mm*	29.70	101.53	243.4	23.26	181.80	681	0.58	1.53	163.8

5.3.5 Decoupling inertial effects from friction losses

The proposed pore-network model was adjusted to decouple the pressure loss due to inertial effects (expansion and contraction) from the pressure loss due to friction in each pore, and the results are presented in Figure 5-7. In Figure 5-7a, both the inertial effects and the friction in each pore affect the flow behaviour. However, at higher velocities, when v > 0.075 (m/s), the pressure loss due to inertial effects is larger than the pressure loss due to friction. Another behaviour can be observed for the 5 mm beads sample, in Figure 5-7b, due to the large pore sizes in the 5 mm beads sample. In Figure 5-7b, the inertial effects dominate the flow behaviour except at very low velocities (when v < 0.1 mm/s) which is difficult to measure experimentally using the current laboratory capabilities.

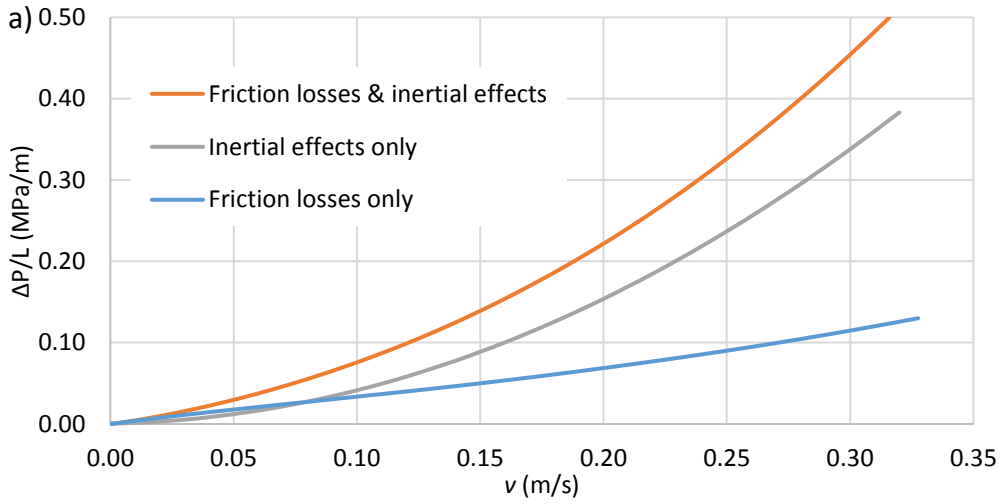

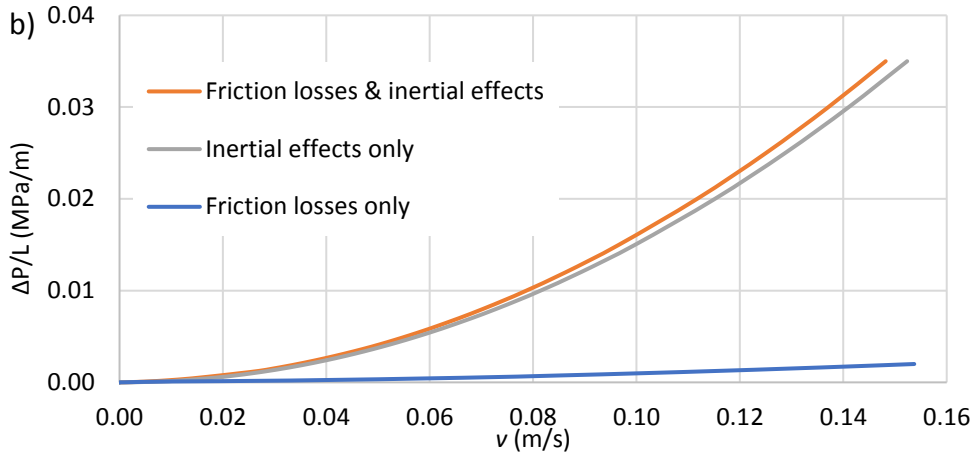

Figure 5-7 Decoupling the inertial effects from friction losses for a) the packed spheres (d_m = 1.84 mm) and b) the regularly structured uniform beads (d_m = 5 mm).

5.3.6 Friction factor

As in Section 4.3.4, according to the Forchheimer equation, the friction factor, f (-), can be related to the pressure loss as $f = \frac{1}{F_o} + 1$, but here, for the turbulent flow regime, $f = \frac{\Delta P}{L\beta`\rho v^2}$ (-), and $F_o = \frac{K_D \beta` \rho v}{\mu}$ (-), i.e. β is replaced by $\beta`$. Figure 5-8 shows the dimensionless friction factor (f), between the medium particles and the fluid, plotted versus the Forchheimer number (F_o), Equation 2.18. In agreement with Section 4.3.4, it is shown that the friction factor decreases when the fluid velocity increases. In Figure 5-8a, the friction factor predictions achieved using PNM in the turbulent flow regime agree well with the experimental results. In Figure 5-8a, when F_o > 1, it is noticed that the friction factor obtained by PNM for the Forchheimer flow is slightly less than the friction factor obtained by PNM for turbulent flow, while, in principle, according to Figure 5-4, the friction factor for the turbulent flow regime should be less than the friction factor for the Forchheimer flow regime. This is attributed to the difference between β and $\beta`$ values used to estimate f and F_o in each of these two cases. In Figure 5-8b, there is agreement between the PNM results and the experimental results after the onset of turbulent flow obtained in the lab, i.e. when F_o > 0.6. However, the onset of turbulence obtained in the lab (F_o = 0.6) is earlier compared to the onset of turbulence obtained by PNM (F_o =

3.6). In Table 5-4, all previous experimental results, by Fand et al. (1987), Bağcı et al. (2014) and also for the 1.84 mm packed spheres, obtained the onset of turbulence when F_o > 1.20. Therefore, the onset of turbulence obtained for the 5 mm beads in the lab (at F_o=0.6) is attributed to some uncertainties in the experimental measurements for this sample as discussed earlier.

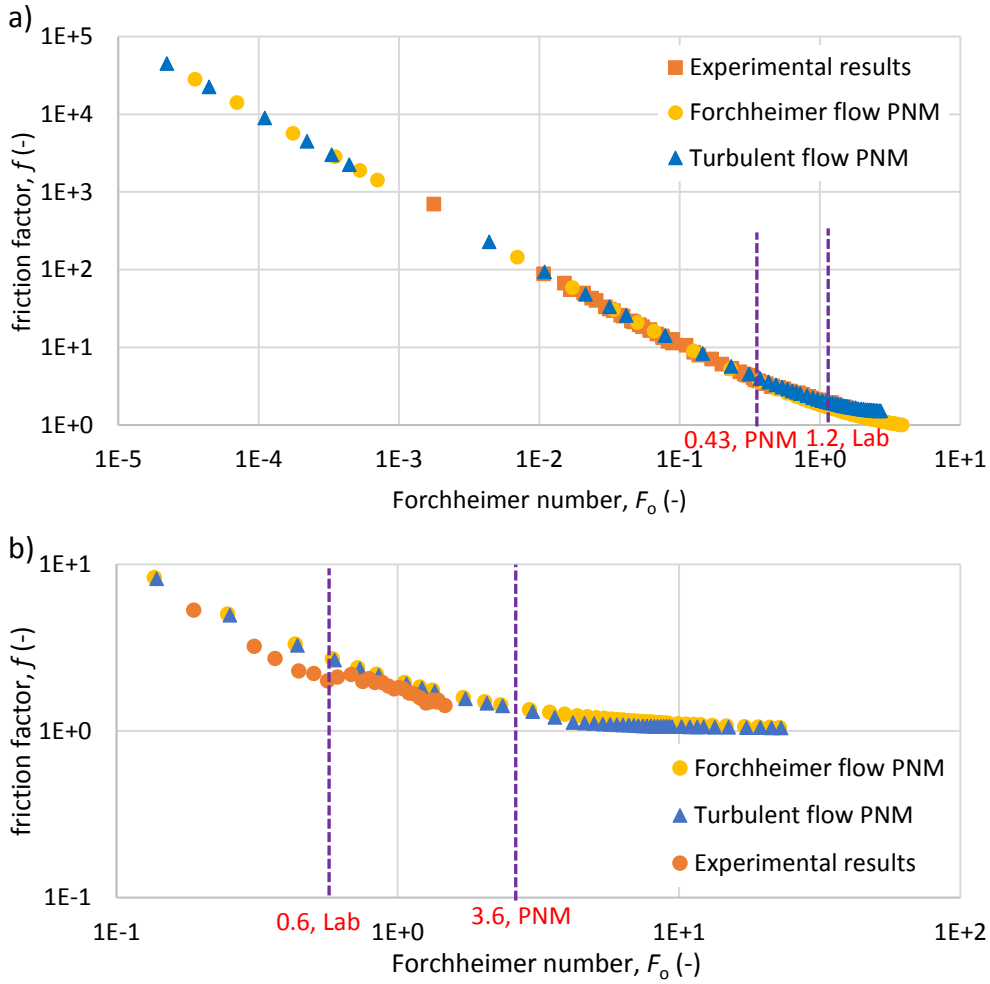

Figure 5-8 The medium friction factor (f) versus Forchheimer number (F_o), Equation 2.18, for a) the packed spheres (d_m = 1.84 mm) and b) the regularly structured uniform beads (d_m = 5 mm). The vertical dashed lines represent the onset of turbulent flow.

5.4 Conclusion

In this chapter, macro-scale (50-200 mm) flow behaviour was modelled within the Darcy, Forchheimer and turbulent flow regimes. The Darcy-Weisbach equation and Borda-Carnot equations (Equations 2.8, 4.6 and 4.7)

were used to estimate the pressure losses due to friction and inertial effects at the pore-scale. At the pore-scale, the limits between different flow regimes (laminar, transition and turbulent) were predefined using the Reynold's number limits obtained by Dybbs and Edwards (1984) and Horton and Pokrajac (2009) who experimentally measured the onset of transition and turbulent flow inside the pores of different porous media (laminar when $Re_{\text{pore}} < 150$, transition when $150 \leq Re_{\text{pore}} \leq 300$, and turbulent when $Re_{\text{pore}} > 300$). Assuming fully developed flow in each pore, the pore friction factor was estimated based on the flow regime. The model was verified against the experimental results obtained for two different samples. There were some discrepancies between the PNM results and the experimental measurements because the assumption of fully developed flow in each pore is not valid.

At the macro-scale, the Forchheimer equation was used to describe the turbulent flow behaviour with modified values for the Forchheimer coefficient ($\beta`$) and the Forchheimer permeability ($K_{\text{F}}`$) that can be obtained using a Forchheimer plot. When the size of the pores is large, the inertial effects dominated the flow behaviour and the friction loss in each pore is negligible (as concluded for the 5 mm uniform beads sample).

At the macro-scale, the onset of the turbulent flow regime was obtained using the conventional Reynold's number (*Re*), the permeability-based Reynold's number (Re_{K}) and the Forchheimer number (F_o). The onset of the turbulent flow obtained by the conventional Reynold's number (*Re*), for the tested samples, had a wide range of values (93-204) depending on the medium characteristic length and size of the pores, this is due to the ambiguity in defining the characteristic length and because a conventional Reynold's number does not account for the medium's degree of heterogeneity. Nevertheless, the onset of turbulent flow obtained using Re_{K} ranged from 2.5 to 7.4, and the onset of turbulent was flow obtained where F_o ranged from 0.4 to 3.6.

The medium friction factor decreases when the fluid velocity increases. The relationship between the medium friction factor (*f*) and the Forchheimer

number (F_o) is unique for all media, and it can be derived from the Forchheimer equation.

To obtain better results from PNM within the turbulent flow regime, it is recommended to modify or replace the equations used to estimate the pore friction factor by other equations capable of estimating the pore friction factor for developing flow.

Chapter 6

Pore-network modelling of solute transport for Darcy and Non-Darcy flow

This chapter contains an introduction in which some commonly used terminologies and principles are explained, then the developed PNM algorithm for modelling solute transport within the Darcy and non-Darcy flow regimes in porous media is explained. According to my knowledge, all previous studies that modelled solute transport using PNM were limited to the Darcy flow regime only. The proposed solute transport pore-network model is the first model which can be applied to both Darcy and non-Darcy flow regimes. For verification, the proposed model has been applied to two porous media; Berea Sandstone and packed spheres (d_m = 1.84 mm) samples used in Chapter 4. The pore-networks of the Berea sandstone and packed spheres have been extracted from available CT-images using the same method explained before in Chapter 4. The results of each sample are presented, discussed and compared with related results existing in the literature.

6.1 Introduction

Modelling solute transport in porous media is essential for designing many engineering processes such as tracking contaminants in groundwater (Buselli & Lu, 2001), remediation of contaminated groundwater (Hashim et al., 2011), enhanced oil recovery (Ju et al., 2006), geological carbon storage (Andrew et al., 2013) and the fate of nuclear waste repositories in the long-term (Kumblad et al., 2006). The transport process through porous media is controlled by the geometry of the pore space and flow conditions. Considering that pore-network models are simplified representations of complex pore geometries, by changing the geometrical characteristics of pore-networks or by using porous media with different characteristics and estimating the associated effects on flow and solute transport, our understanding of the relationship between a porous media structure and

transport properties can be improved (Vogel & Roth, 2001). Moreover, PNM can be used to predict averaged macroscopic flow and transport parameters for porous media which are difficult to obtain experimentally (Mostaghimi, 2012). The focus of this chapter is on dissolved conservative solutes, which spread within water under the processes of advection and hydrodynamic dispersion. Hydrodynamic dispersion is a result of two processes; molecular diffusion and mechanical dispersion. Molecular diffusion results from the random molecular movement of solute molecules. Mechanical dispersion is caused by tortuosity (specified by streamlines distributions) and nonuniform velocity in each pore (Figure 6-1) which causes shear stress between fluid layers (Gaganis et al., 2005).

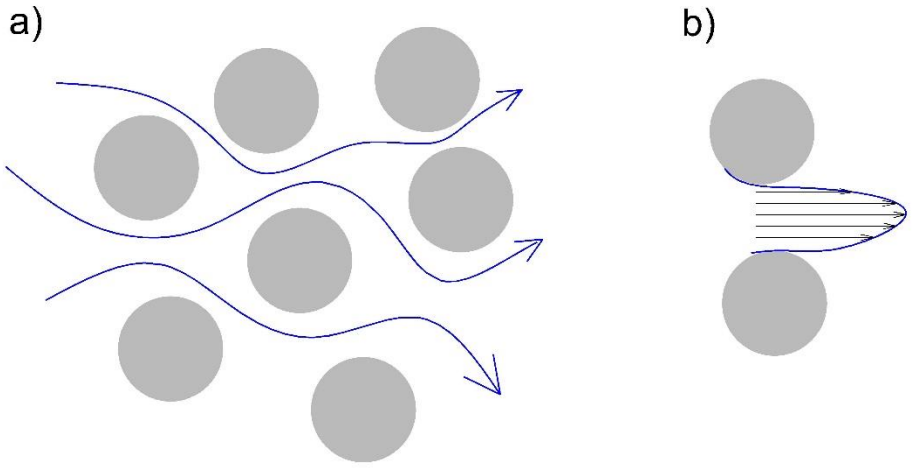

Figure 6-1 The two processes that cause mechanical dispersion in porous media; a) tortuosity, and b) the nonuniform velocity profile in each pore, where grey spheres represent the soil particles, after Mostaghimi (2012).

Figure 6-2 shows the propagation of a pulse of solute injected into a 2D (3 mm × 30 mm) regular structured pore-network equivalent to a regular packing of uniform beads with 0.3 mm diameter. The concentration decays with time and its distribution can be treated as a Gaussian distribution according to the 1D ADE. After ~3.4 s, the variance , σ^2 (mm^2), of the Gaussian distribution increases linearly with time (Figure 6-3), the "asymptotic Fickian" regime is reached and the longitudinal dispersion coefficient reaches a constant value over time (Jha et al., 2011; Mostaghimi, 2012).

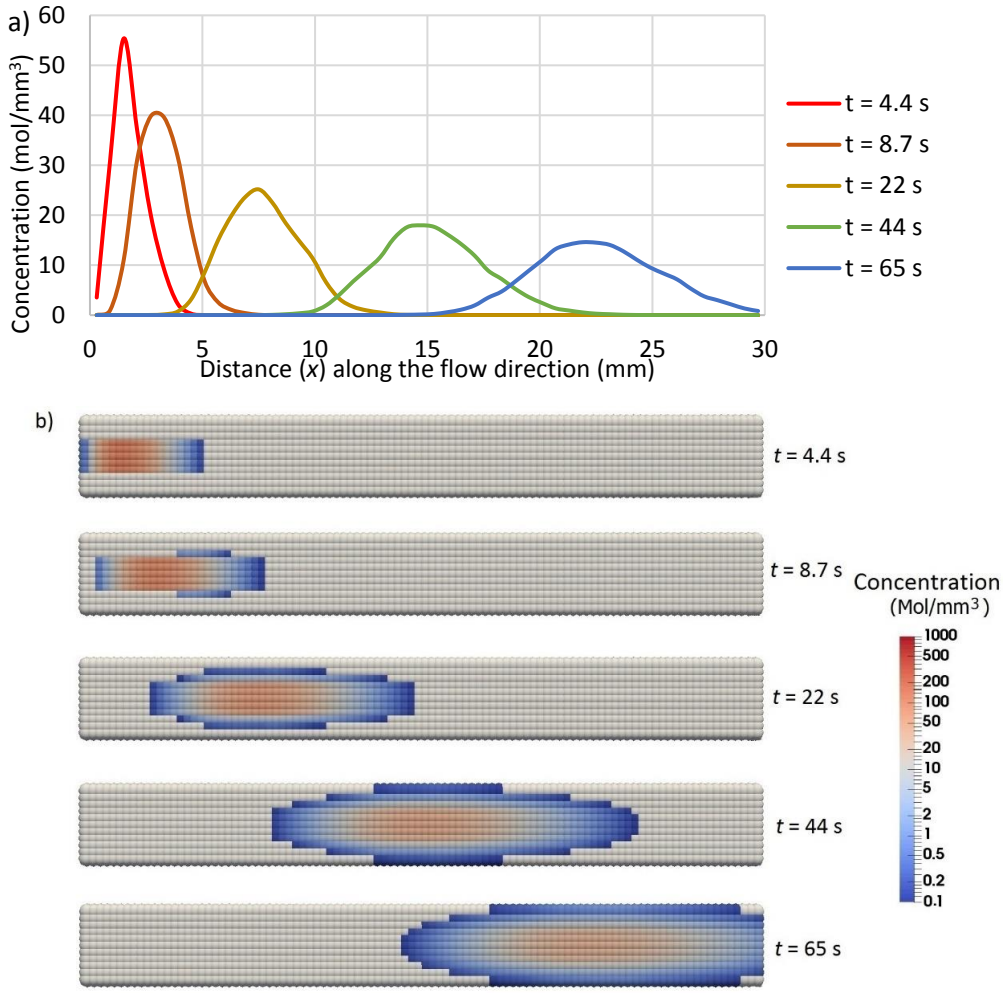

Figure 6-2 The concentration decays of a pulse of solute injected into a 2D (3 mm × 30 mm) pore-network equivalent to 0.3 mm diameter beads arranged in a regular structured order, a) is the average cross-sectional concentration distribution at different times, and b) is visualisation of the solute propagation through the medium.

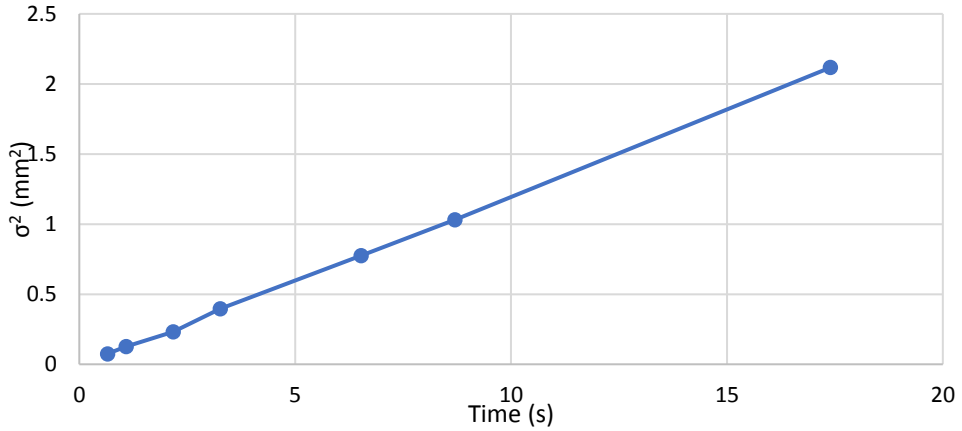

Figure 6-3 The variance grows over time for the system shown in Figure 6-2. The variance starts to grow linearly after ~3.4 seconds.

6.2 The Mixed Cell Method (MCM)

The first step before modelling solute transport in porous media is modelling the fluid flow and solving the flow and pressure fields everywhere in the medium. Then, the transport equations can be applied. The details of modelling Darcy and non-Darcy flow using PNM were explained before in Chapter 4, therefore, this chapter focuses on the solute transport equations only.

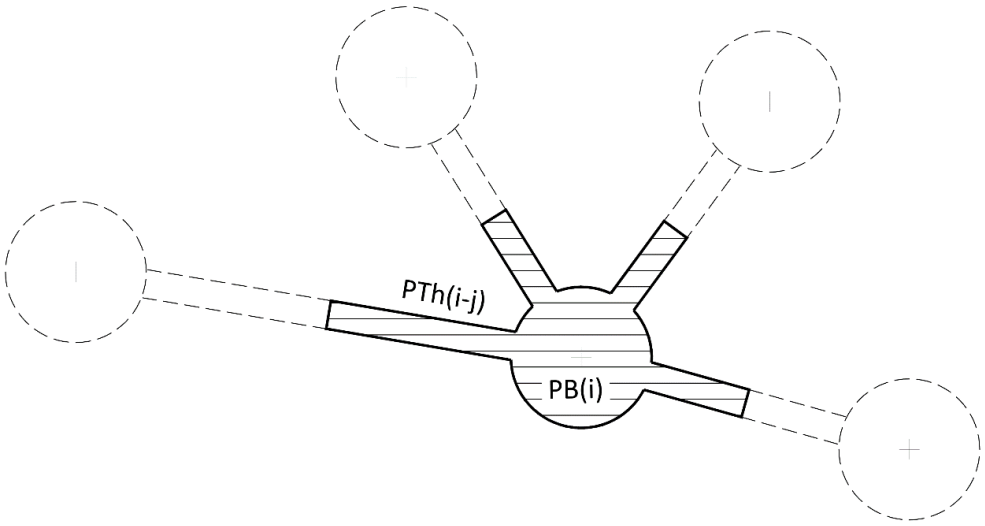

Figure 6-4 A 2D schematic diagram of a pore-unit (PU). The hatched area represents a pore-unit which is a pore body and half of all pore throats connected to it.

In the MCM, dispersion is assumed to occur mainly in pore throats and perfectly mixed conditions are assumed at each pore, i.e. the concentration is assumed to be constant in each pore body. Following Acharya et al. (2005) and Köhne et al. (2011), the transport equation for any pore-unit i, PU(i), defined as a pore body and half of all pore throats connected to it (Figure 6-4), in the pore-network is given by

$$V_{\mathrm{i}}\frac{C_{\mathrm{i}}(t+dt)-C_{\mathrm{i}}(t)}{dt}=\sum_{q_{\mathrm{i-j}}<0}q_{\mathrm{i-j}}C_{\mathrm{i}}(t)+\sum_{q_{\mathrm{i-j}}>0}q_{\mathrm{i-j}}C_{\mathrm{j}}(t)+\sum_{\mathrm{j}\in N_{\mathrm{i}}}a_{\mathrm{i-j}}D_{\mathrm{i-j}}^{\mathrm{eff}}\frac{C_{\mathrm{j}}(t)-C_{\mathrm{i}}(t)}{L_{\mathrm{i-j}}} \quad 6.1$$

which can be written as

$$C_{\mathrm{i}}(t+dt) = C_{\mathrm{i}}(t) + \frac{dt}{V_{\mathrm{i}}}\left(\sum_{q_{\mathrm{i-j}}<0} q_{\mathrm{i-j}} C_{\mathrm{i}}(t) + \sum_{q_{\mathrm{i-j}}>0} q_{\mathrm{i-j}} C_{\mathrm{j}}(t) + \sum_{j\in N_{\mathrm{i}}} a_{\mathrm{i-j}} D_{\mathrm{i-j}}^{\mathrm{eff}} \frac{C_{\mathrm{j}}(t)-C_{\mathrm{i}}(t)}{L_{\mathrm{i-j}}}\right) \quad 6.2$$

where the subscript i denotes the index of the pore body (pore-unit) for which the mass balance is calculated and j is a neighbouring pore body, V_{i} (mm^3) is the volume of pore-unit i, dt (s) is the time step, $C_{\mathrm{i}}(t)$ is the solute concentration of PU(i) at time t in $\mathrm{mol/mm}^3$, $D_{\mathrm{i-j}}^{\mathrm{eff}}$ (mm^2/s) is the pore throat effective diffusion coefficient. According to Section 2.6.1, all previous studies, that used PNM and applied the Taylor-Aris solution $\left(D_{\mathrm{i-j}}^{\mathrm{eff}} = D_m + \frac{u^2 r^2}{48\, D_m}\right)$ in each pore throat, did not check the residence time needed to reach an asymptomatic state in each pore throat in the pore-network. However, in the proposed solution, $D_{\mathrm{i-j}}^{\mathrm{eff}}$ depends on the residence time in each pore throat and is given by the following equation proposed by Lee (2004):

$$D_{\mathrm{i-j}}^{\mathrm{eff}} = D_{\mathrm{m}} + \kappa_o D_{\mathrm{m}} Pe_{\mathrm{i-j}}^2 \left[1 - exp\left(-\frac{t}{\tau_o}\right)\right] \quad 6.3$$

where t (s) is the solute residence time in the pore throat that connects the two pore bodies i and j, τ_o is the Lagrangian time scale reflecting molocular diffusivity across the pipe radius and it is given by: $\tau_o = \frac{r_{i-j}^2}{16\, D_{\mathrm{m}}}$ (s), $r_{\mathrm{i-j}}$ is the average radius of the inscribed circle inside the pore throat, D_{m} (mm^2/s) is the molecular diffusion coefficient, κ_o (-) is a factor that can be determined analytically and it is approximately equal to 0.0208, 0.0342 and 0.019 for circular, square and triangular cross-sectional pores (Bijeljic et al., 2004), respectively, and $Pe_{\mathrm{i-j}}$ (-) is the pore throat Péclet number. The factor κ_o indicates higher dispersion in the throats with higher cross-sectional irregularity; κ_o is higher for square cross-section because the higher number of corners causes nonuniformity in the velocity field (Bijeljic et al., 2004). Different characteristic lengths were used in the literature to calculate the Péclet number (Huysmans & Dassargues, 2005). If the pore throat inscribed radius, $r_{\mathrm{i-j}}$ (mm), is consider as the characteristic length, then following Bruderer and Bernabé (2001) and Babaei and Joekar-Niasar (2016), the pore throat Péclet number can be calculated as

$$Pe_{\mathrm{i-j}} = \frac{u_{\mathrm{i-j}} r_{\mathrm{i-j}}}{D_{\mathrm{m}}}\,. \qquad 6.4$$

In Equation 6.1, dispersion due to flow field heterogeneity, as a result of tortuosity and change of flow-paths, is represented by $\sum_{q_{\mathrm{i-j}<0}} q_{\mathrm{i-j}} C_{\mathrm{i}}(t) + \sum_{q_{\mathrm{i-j}>0}} q_{\mathrm{i-j}} C_{\mathrm{j}}(t)$, while dispersion through each pore throat is represented by $\sum_{j \in N_{\mathrm{i}}} a_{\mathrm{i-j}} D_{\mathrm{i-j}}^{\mathrm{eff}} \frac{C_{\mathrm{j}}(t) - C_{\mathrm{i}}(t)}{L_{\mathrm{i-j}}}$. Equation 6.3 is applied when the pore throat dimensionless residence time $\left(T = \frac{D_m}{r_{i-j}^2\, t}\right)$ is larger than 0.01. The investigations of Bailey & Gogarty (1962) and Ananthakrishnan et al. (1965) have proven that the transport regime in a pore throat is purely advective and $D_{\mathrm{i-j}}^{\mathrm{eff}} = 0.0$ when $T \leq 0.01$. Moreover, Romero-Gomez and Choi (2011) concluded that Equation 6.3 overestimates the effective diffusion coefficient by 25% when $T \leq 0.01$ (Hart et al., 2016). In Equation 6.3, if the solute residence time *t* is a few times larger than τ_o, the equation leads to the well-known Taylor-Aris effective diffusion coefficient in the asymptotic Fickian regime (Figure 2-9).

While using the mixed cell method (MCM), the solution stability depends mainly on the selected time step (*dt*). Acharya et al. (2007) who used a similar methodology, but neglected dispersion in pore throats, proposed that the time step (*dt*) should be selected based on the minimum value of the residence time either in each pore-unit or in each single pore throat as per equations 6.5 and 6.6 (Acharya et al., 2007), namely

$$0 < dt \leq min\{\boldsymbol{t}_{\mathrm{PU}}\} = min\left\{\frac{\boldsymbol{V}_{\mathrm{PU}}}{\boldsymbol{q}_{\mathrm{PU}}}\right\}, \qquad 6.5$$

and

$$0 < dt \leq min\{\boldsymbol{t}_{\mathrm{PTh}}\} = min\left\{\frac{\boldsymbol{L}_{\mathrm{PTh}}}{\boldsymbol{u}_{\mathrm{PTh}}}\right\} = min\left\{\frac{\boldsymbol{V}_{\mathrm{PTh}}}{\boldsymbol{q}_{\mathrm{PTh}}}\right\}, \qquad 6.6$$

where $\boldsymbol{V}_{\mathrm{PU}}$ (mm^3) and $\boldsymbol{q}_{\mathrm{PU}}$ (mm^3/s) are the vectors of the pore-unit volumes and total absolute discharges either from or into the pore-units, respectively, and $\boldsymbol{t}_{\mathrm{PU}}$ (s) is the vector of pore-unit residence times. $\boldsymbol{q}_{\mathrm{PTh}}$ (mm^3/s) and $\boldsymbol{u}_{\mathrm{PTh}}$ (mm/s) are the vectors of discharges and average velocities through the pore throats, and $\boldsymbol{V}_{\mathrm{PTh}}$ (mm^3) and $\boldsymbol{L}_{\mathrm{PTh}}$ (mm) are the vectors of the pore throat volumes and lengths.

Additionally, because dispersion is considered in each pore throat, the following case is proposed (Equation 6.7),

$$0 < dt \leq min\{\grave{\boldsymbol{t}}_{\mathrm{PTh}}\} = min\left\{\frac{\boldsymbol{L}_{\mathrm{PTh}}^{2}}{\boldsymbol{D}_{\mathrm{PTh}}^{\mathrm{eff}}}\right\} \quad 6.7$$

where $\boldsymbol{L}_{\mathrm{PTh}}^{2}$ (mm^2) and $\boldsymbol{D}_{\mathrm{PTh}}^{\mathrm{eff}}$ (mm^2/s) are the vectors of the squared pore throat lengths and the pore throat effective diffusion coefficients. Because Equation 6.6 is derived from the advection rate of each pore throat in Equation 6.1, similarly, Equation 6.7 is derived from the dispersion rate of each pore throat in Equation 6.1. Finally, *dt* (s) should be selected less than or equal to the minimum value of the components of the three vectors $\boldsymbol{t}_{\mathrm{PU}}, \boldsymbol{t}_{\mathrm{PTh}}, \grave{\boldsymbol{t}}_{\mathrm{PTh}}$. Using a larger time step results in instability in the numerical solution (Section 6.3.1).

After solving the pressure and flow fields in the pore-network, Equation 6.1 is solved explicitly for each time step as per Equation 6.2. Appendix D shows the flow chart, algorithm and details of the proposed pore-network transport model.

Then, based on averaging, the overall average concentration, $\bar{C}$ (mol/mm^3), at each time step and the medium average Péclet number, $\overline{Pe}$ (-), can be estimated according to equations 6.8 (Babaei & Joekar-Niasar, 2016) and 6.9,

$$\bar{C} = \frac{\sum V_i C_i}{\sum V_i}, \quad 6.8$$

$$\overline{Pe} = \frac{u_{avg}\, L_{charc}}{D_m}, \quad 6.9$$

where u_{avg} (mm/s) is the average value of the fluid velocities through all pore throats (Equation 4.16) and L_{charc} (mm) is the medium characteristic length, which is equal to the average bead diameter (1.84 mm) in the case of the packed spheres sample and 131.13 μm for the Berea Sandstone sample used (Mostaghimi et al., 2012).

6.3 Verification, results and discussion

In this section, because the proposed pore-network flow model overestimates the velocities in the packed spheres sample due to its

relatively large size of pores (as mentioned in Section 4.3.3), more detail will be given for the Berea Sandstone sample results while less discussion and results will be shown for the packed spheres sample.

For all simulations, the coefficient of molecular diffusion (D_m) is considered equal to 10^{-9} m^2s^{-1} (Bijeljic et al., 2004; Babaei & Joekar-Niasar, 2016). Dirichlet boundary conditions are applied at the inlet, i.e. the conservative solute is injected continuously at the inlet boundary with constant concentration (C_o) equal 1 mol/mm^3. The simulation continues until the concentration of the solute is nearly equal to 1 mol/mm^3 at every pore-unit. Using continuously injected solute is better than a pulse injection because by the end of the simulation, the final concentration values at each PU are expected to be equal to C_o, and the effect of dead ends and stagnant zones can be easily detected and visualised. A wide range of pressure drops (1×10^{-5} to 80,000 Pa) across the pore-network were applied. For flow simulation, the same fluid properties and boundary conditions explained in Section 4.2.1.3 are used.

For each run, i.e. for each applied pressure drop across the pore-network, the longitudinal dispersion coefficient is determined by fitting the analytical solution of the 1D ADE (Ogata & Banks, 1961) to the breakthrough curve (BTC) obtained from pore-network simulation by using the CXTFIT computational software (Toride et al., 1995). The BTC for each run is measured at the middle of the sample, i.e. where $x = L/2$, where L is the length of the pore-network along the flow direction, then the concentration values over time (i.e. the BTC) are used as inputs to CXTFIT. These concentrations and time values are fitted to the analytical solution of the 1D ADE (Equation 2.20) to obtain the D_L estimate and the average pore velocity (u_{avg}) values.

6.3.1 The effect of time step on the solution's stability

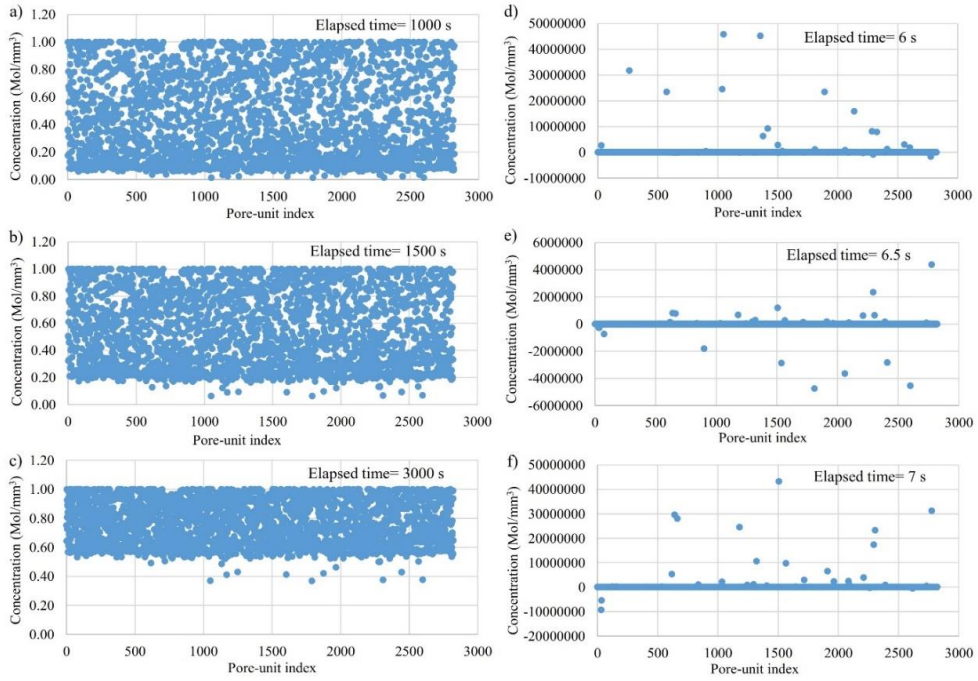

Figure 6-5 The pore-unit concentration values for the Berea sandstone sample at different times when a conservative solute with concentration (C_o) equal 1 mol/mm^3 is injected continuously at the inlet boundary; a), b) and c) are for the stable case when dt = 0.00356 s, while d), e) and f) are for the unstable case when dt = 0.356 s.

The stability of the proposed numerical solution depends mainly on the time step (dt). Using a larger time step other than dt defined by equations 6.5, 6.6 and 6.7 results in some pore-units having concentration values larger than the concentration of the injected solute (C_o), and in addition, there may be other pore-units with negative concentration values. Figure 6-5 shows a comparison between a stable case (Figure 6-5(a-c) when dt is selected based on equations 6.5, 6.6 and 6.7, and the unstable case (Figure 6-5(d-f)) when a larger dt value is used.

6.3.2 Breakthrough curves and the longitudinal dispersion coefficients

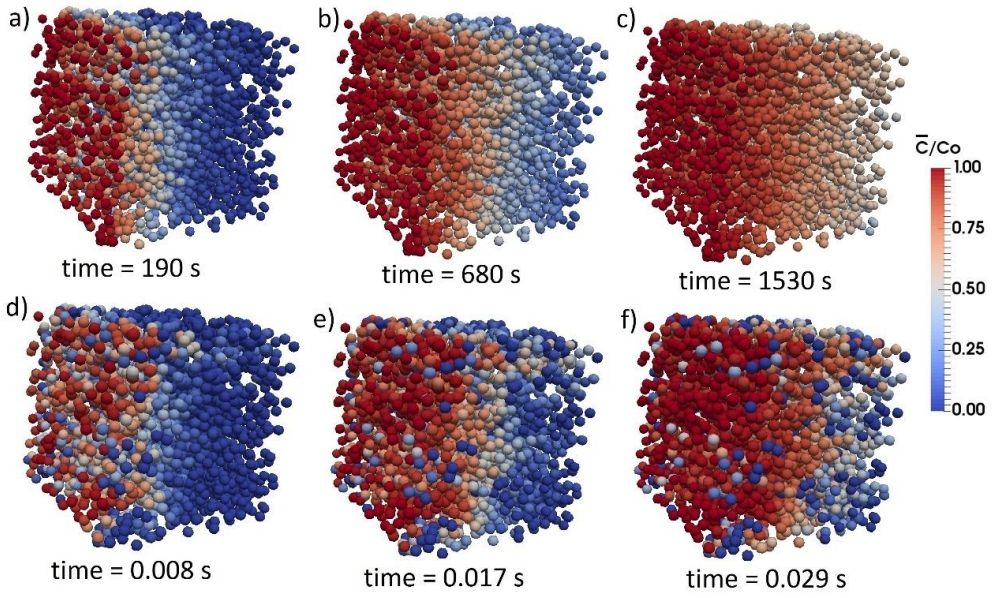

Figure 6-6 Snapshots of the concentration distribution for the Berea Sandstone sample at a) $\bar{C}/C_o = 0.25$, b) $\bar{C}/C_o = 0.50$, c) $\bar{C}/C_o = 0.75$ when ΔP = 0.1 Pa and $\overline{Pe}$ = 0.1; d) $\bar{C}/C_o = 0.25$, e) $\bar{C}/C_o = 0.50$, f) $\bar{C}/C_o = 0.75$ when ΔP = 10,000 Pa and $\overline{Pe}$ = 9933. The flow direction is from left to right.

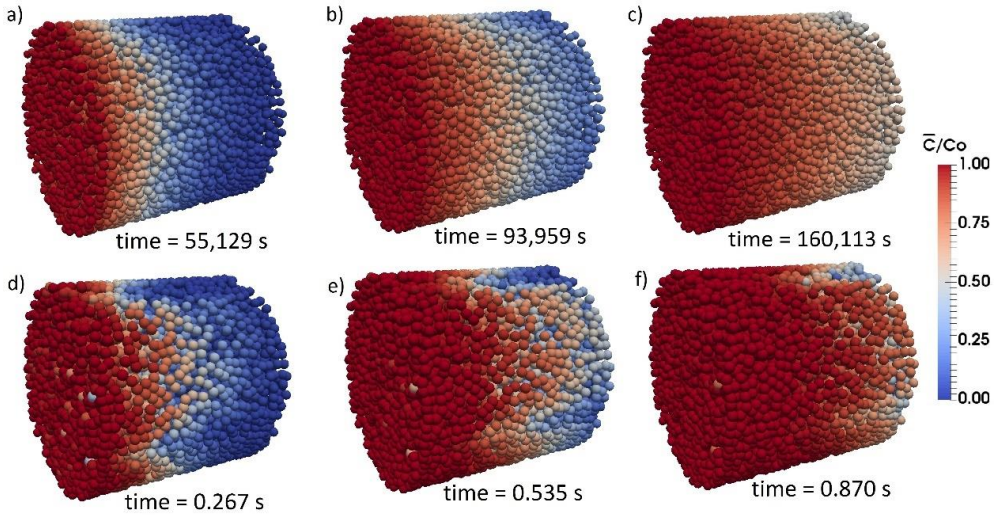

Figure 6-7 Snapshots of the concentration distribution for the packed spheres sample; a) $\bar{C}/C_o = 0.25$, b) $\bar{C}/C_o = 0.50$, c) $\bar{C}/C_o = 0.75$ when ΔP = 0.001 Pa and $\overline{Pe}$ = 0.31; d) $\bar{C}/C_o = 0.25$, e) $\bar{C}/C_o = 0.50$, f) $\bar{C}/C_o = 0.75$ when ΔP = 400 Pa and $\overline{Pe}$ = 103,064. The flow direction is from left to right.

Figure 6-6 shows snapshots of the solute transport simulations at different times for the Berea Sandstone sample; a), b) and c) are for Darcy flow when ΔP = 0.1 Pa and $\overline{Pe} = 0.1$, while d), e), and f) are for non-Darcy flow when ΔP = 10,000 Pa and $\overline{Pe} = 9{,}933$. Figure 6-6(a-c), represent a diffusion dominated transport case, when the concentration front moves regularly over time in the longitudinal direction. In this case, the residence time in each pore throat is long and the effective diffusion coefficient for each pore throat is a maximum and equal to the Taylor-Aris effective diffusion coefficient. Moreover, the advection through each pore throat is negligible and solute particles are allowed to move freely through each pore throat depending on the concentration gradient between the two ends of the pore throat (as per the RHS of Equation 6.1). This allows all solute particles to move from high concentration to low concentration resulting in a nearly uniform distribution of the solute over any cross-section perpendicular to the longitudinal flow direction. As explained by Bruderer and Bernabé (2001), molecular diffusion acts in the transverse direction and works against the increasing longitudinal dispersion, which allows the solute particles to encounter a wide range of velocities and results in a uniform or semi-uniform distribution of solute concentrations. While in Figure 6-6(d-f), when the fluid moves with higher speed, the effect of advection increases, and the concentration front extends over a larger length depending on the velocity value in each pore. The final concentration distribution for the case shown in Figure 6-6(d-f) is controlled by the amount of discharge entering or leaving each pore-unit. If the pore-unit receives high discharge, this leads to a high concentration, while a low discharge is associated to a relatively lower concentration because this case represents an advection dominated transport regime.

Comparing both cases (ΔP = 0.1 Pa and ΔP = 10,000 Pa) in Figure 6-6, the existence of a few pores with low concentration (blue colour) within the zones with high concentration (red colour), when ΔP = 10,000 Pa, can be noticed. But these low concentration pores do not exist in the diffusion dominated case. These blue pores represent pore-units with low discharge or dead-ends where the flow velocity is zero and the solute spreads by

diffusion only. A similar behaviour can be observed in highly heterogenous media (not Berea Sandstone) due to the existence of some stagnant zones in the medium. This phenomenon is referred to as “hold-up dispersion” (Koch & Brady, 1985; Bijeljic et al., 2004). Such pores with low concentration require a long time to gain the concentration value of C_o. The total simulation time in the first case, when ΔP = 0.1 Pa, is longer (~2,400 s) than the total simulation time (0.12 s) of the second case when ΔP = 10,000 Pa. The long simulation time in the first case allows these pores to gain concentration by diffusion, but the short simulation time in the second case allows only the effect of advection to occur.

The packed spheres sample, in Figure 6-7, shows a behaviour similar to that in Figure 6-6, but without the existence of dead ends because the packed sphere sample has a more homogenous structure compared to Berea Sandstone. In Figure 6-7(d-f), it is noticed that the solute concentration in most of the pore-units located at the boundary of the sample (close to the external containing circular pipe) have a higher concentration compared to the inner pore-units. This is because the sample boundary has a high effect on the overall porosity (see Section 3.4.2) and the pores located at the boundary have a relatively larger size and higher discharges compared to the inner pores.

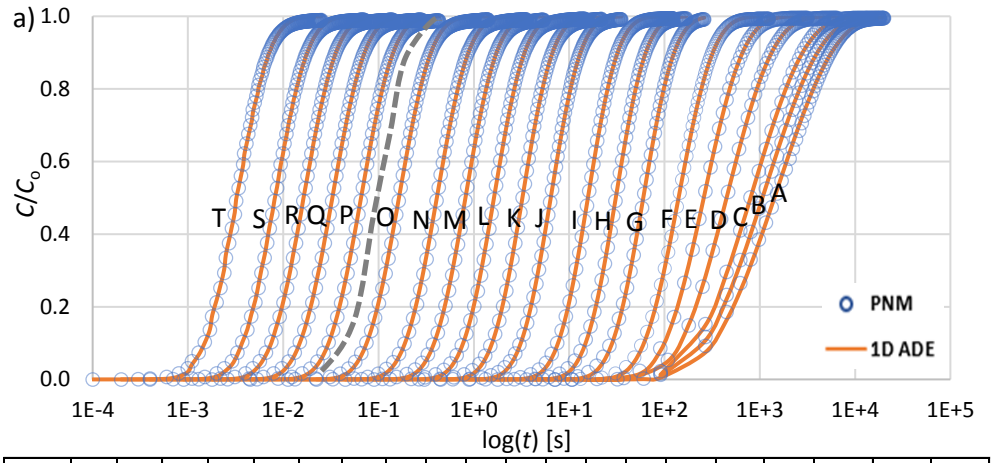

	A	B	C	D	E	F	G	H	I	J	K	L	M	N	O	P	Q	R	S	T
ΔP (pa)	0.01	0.05	0.10	0.25	0.50	1.00	2.50	5.0	10	25	50	100	200	400	1000	2500	5000	10000	20000	50000
Pe	0.01	0.05	0.10	0.26	0.52	1.03	2.59	5.2	10	26	52	103	207	414	1034	2586	5171	10342	20685	51712

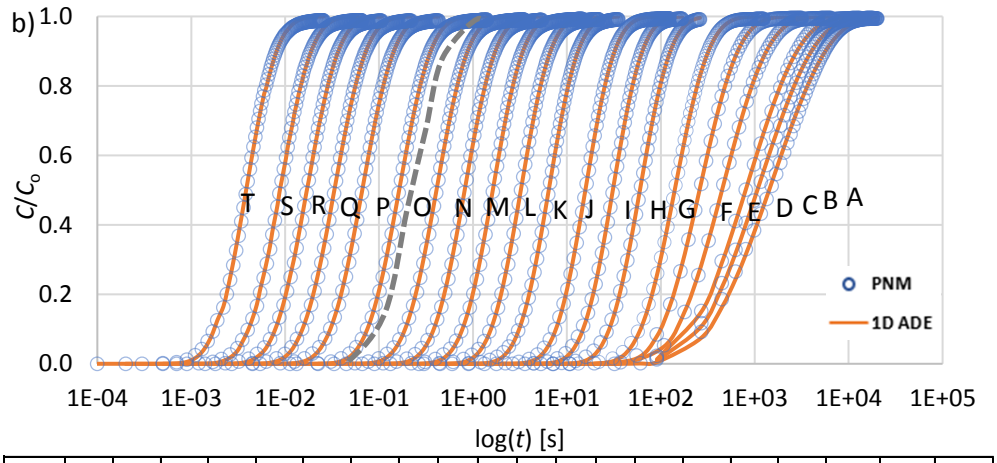

	A	B	C	D	E	F	G	H	I	J	K	L	M	N	O	P	Q	R	S	T
ΔP (pa)	0.01	0.05	0.10	0.25	0.50	1.00	2.50	5.0	10	25	50	100	200	400	1000	2500	5000	10000	20000	50000
$\overline{Pe}$	0.01	0.05	0.10	0.26	0.52	1.03	2.59	5.2	10	26	52	103	207	414	1030	2558	5063	9933	19201	44294

Figure 6-8 The Berea Sandstone breakthrough curves at different Péclet numbers, fitted to the analytical solution of the 1D ADE (Equation 2.20), the concentration C is obtained at the middle ($x = L/2$) of the sample under a) Darcy flow and b) Forchheimer flow conditions. The grey dashed curves represent the onset of non-Darcy flow, when $\overline{Pe}$ = 2,570, determined using Equation 6.9 and the average pore velocity at the onset of non-Darcy flow.

The breakthrough curves shown in Figure 6-8 show a very good match with the analytical solution of the 1D ADE (Equation 2.20) obtained using the CXTFIT software. This is due to the well-defined effective diffusion coefficient $\left[D_{i-j}^{eff}\right]$ for each pore throat (Equation 6.3) which is based on the pore throat transport regimes including; the asymptotic Fickian regime, the

pre-asymptotic time dependent regime and the pure advection regime (see Figure 2-9). In Figure 6-8, it is shown that for $\overline{Pe} > \sim 2{,}570$, if the inertial forces are ignored (as in Figure 6-8a) and the flow is assumed to be within the Darcy flow regime, then the solute spreads faster through the medium and the predicted velocity is higher compared to the non-Darcy case at the same applied pressure drop. This results in overestimation of the overall Péclet numbers and the longitudinal dispersion coefficients. Therefore, it is concluded that the flow inertial effects reduce the fluid velocity and consequently cause a time delay for solute dispersion.

Figure 6-9 shows the longitudinal dispersion coefficient (D_L) scaled by the molecular diffusion (D_m) versus Péclet number ($\overline{Pe}$). The figure shows the obtained PNM results compared to various results from the literature, i.e. experimental data for graded sands and other single-grained materials (Pfannkuch, 1963), for packed spheres (Ding & Candela, 1996; Seymour & Callaghan, 1997; Kandhai et al., 2002), for Latex spheres (Khrapitchev & Callaghan, 2003), for silica grains with many sharp edges and spherical plexiglass (Stöhr, 2003), in addition to numerical and experimental measurements for artificial glass-etched 2D pore-network (Theodoropoulou, 2007), PNM for Berea Sandstone (Bijeljic et al., 2004), and DNS for Berea Sandstone (Mostaghimi et al., 2012). From Figure 6-9, it can be seen that the results of the proposed model, for Berea Sandstone, match well with Pfannkuch's (1963) results for graded sands and other single-grained materials when $log(\overline{Pe}) < 3.0$, i.e. before the onset of non-Darcy flow. Also, they match with the results achieved by Theodoropoulou (2007) for the artificial pore-network. After the onset of non-Darcy flow, the proposed model underestimates D_L compared to the results by Pfannkuch (1963) and Stöhr (2003), this is because the proposed model assumed laminar flow and neglected the effect of turbulent diffusion on the transport process (more details are given in Chapter 7), and the results obtained by Pfannkuch (1963) and Stöhr (2003) are more likely to be in the turbulent flow regime when $log(\overline{Pe}) > 3.0$.

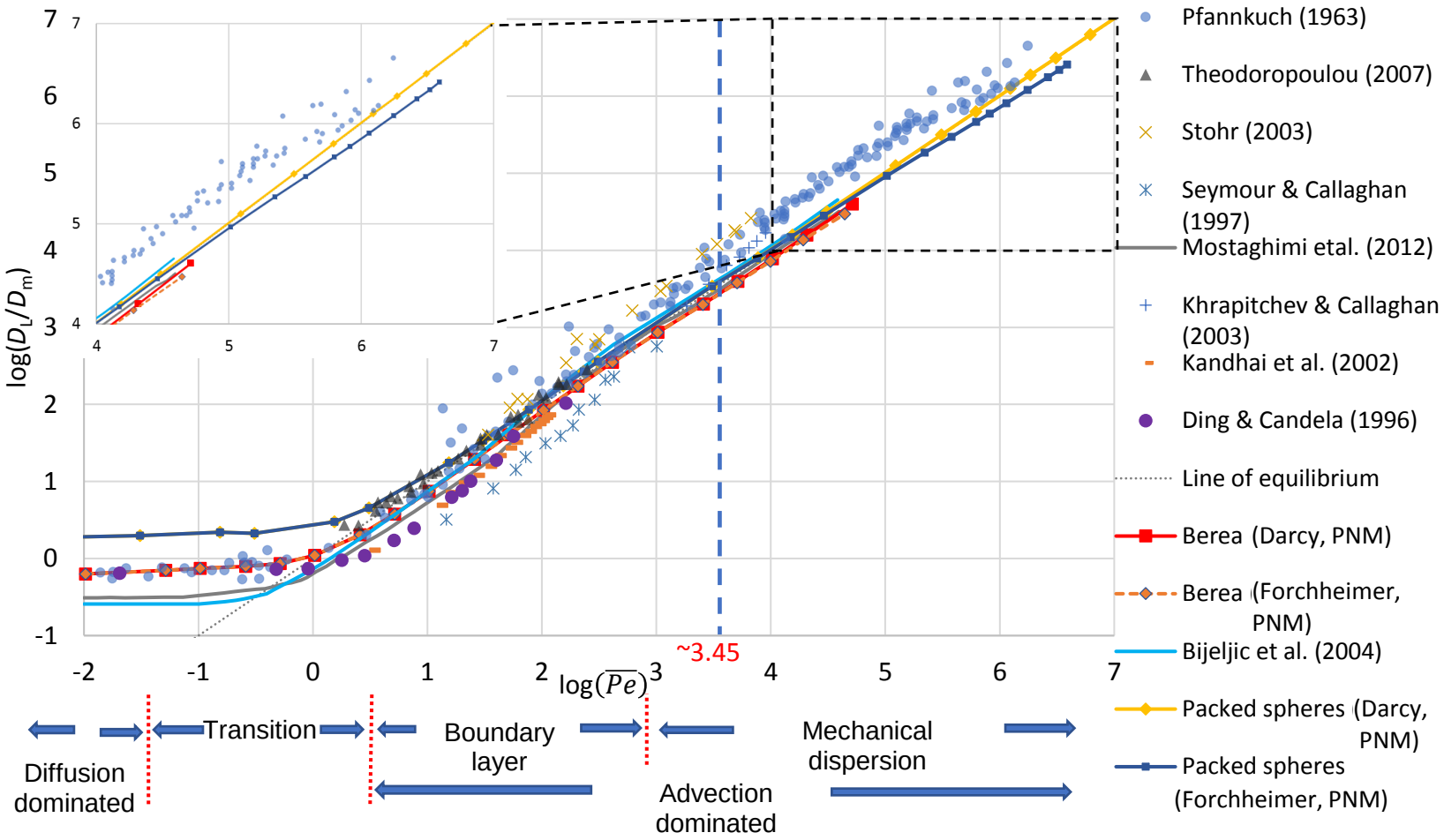

Figure 6-9 The longitudinal dispersion coefficient (D_L) scaled by molecular diffusion (D_m) vs. Péclet number ($\overline{Pe}$) compared with previous experimental and numerical data. The blue vertical dashed line represents the onset of non-Darcy flow, when $\overline{Pe}$ ≈3,000.

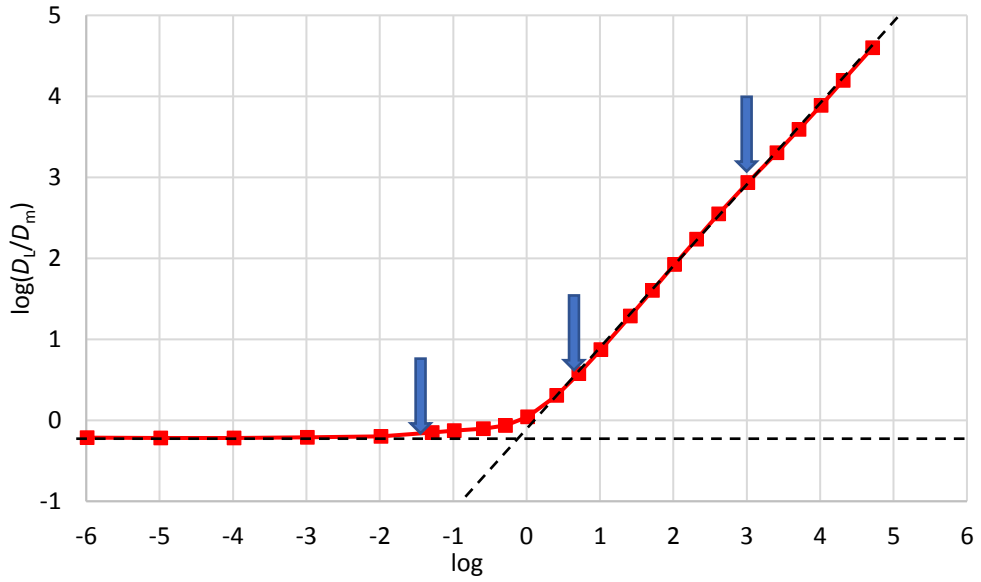

Figure 6-10 Detecting different transport regimes for the Berea Sandstone sample results in the Darcy flow regime by using construction lines.

Comparing the results achieved using the proposed model for Berea Sandstone with the previous results obtained for a similar Berea Sandstone sample by Bijeljic et al. (2004) and Mostaghimi et al. (2012), a good match can be detected, however, both the results of Bijeljic et al. (2004) and Mostaghimi et al. (2012) underestimate D_L in the diffusion dominated regime, by ~170%, when $log(\overline{Pe}) < 0.5$, and they attributed this underestimation to the existence of the solid matrix which works as a barrier to molecules resulting in $D_L < D_m$.

For the packed spheres sample, the proposed model overestimates D_L, by ~200%, at low Péclet numbers, when $log(\overline{Pe}) < 0.5$. This is because the packed spheres sample has pores with relatively large size and it was assumed that dispersion occurs over the pore throat length only (see the last term in the RHS of Equation 6.1), and the lengths of the pore bodies connect to both ends of the pore throats were neglected. So, using shorter lengths resulted in higher dispersion rates especially at low flow velocities when the effect of advection is negligible compared to the effective diffusion at the pore throats.

Three different transport regimes can be detected from the Berea Sandstone results shown in Figure 6-9, depending on the change of the curvature of the

obtained results as explained in Figure 6-10, following the method proposed by Babaei and Joekar-Niasar (2016). First, the diffusion dominated regime is detected by a horizontal line, when $log(\overline{Pe}) < -1.5$, this is in agreement with Bijeljic et al. (2004) who found that diffusion dominates when $log(\overline{Pe}) < -1.0$ for Berea Sandstone. The small deviation between the two values (-1.5 and -1.0) is because Bijeljic et al. (2004) underestimated D_L in the diffusion dominated regime and because the proposed model neglects dispersion in the pore bodies. Second, the transition regime is the region between the horizontal dashed line and the 45-degree dashed line in Figure 6-10, where both advection and diffusion affect the transport process. This regime is observed when $-1.5 < log(\overline{Pe}) < 0.5$, compared to the range of $-1 < log(\overline{Pe}) < 1$ by Bijeljic et al. (2004). Third, the advection dominates when $log(\overline{Pe}) > 0.5$, and this zone can be further divided into two zones. The first zone in the advection dominated regime ($0.5 < log(\overline{Pe}) < 3.0$) is referred to as the boundary-layer dispersion regime, when advection dominates the mixing process, but the dimensionless residence time (T) in most of the pore throats is still > 0.01, i.e. there is small effect of dispersion through the pore throats, more details are given in Section 6.3.3. In this zone, the power law according to the obtained PNM results obeys the relation $\frac{D_L}{D_m} = 0.65\ P_e^{1.05}$, this is in agreement with the power (δ = 1.02-1.13) obtained by Sorbie et al. (1987) and Gist et al. (1990) for various Sandstones, and still close to the value of δ = 1.19 obtained by Bijeljic et al. (2004) for Berea Sandstone. The second zone is referred to as the mechanical dispersion zone, when $log(\overline{Pe}) > 3.0$, which is a purely advective regime and the dimensionless residence time (T) in most of the pore throats is < 0.01. In this zone D_L is directly proportional to $\overline{Pe}$.

Even though in Figure 6-6 there is evidence of hold-up dispersion, the number of dead-ends did not exceed 7 % of the total number of pore bodies in the Berea pore-network and this did not affect the dispersion or showed evidence that D_L in this zone scales with $\overline{Pe}^2$ as proposed by Bijeljic et al. (2004) and Sahimi (2011b). In the advection dominated regime, D_L is directly proportional to $\overline{Pe}$. Moreover, Bijeljic et al. (2004) confirmed that

hold-up dispersion does not exist at a small-scale (few centimetres) in Berea sandstone.

In Figure 6-9, when $log(\overline{Pe}) > 3.45$, neglecting the inertial force in the flow, i.e. assuming Darcy flow, causes an overestimation of both the Péclet number and the longitudinal dispersion coefficient. This is also observed for the packed spheres sample and is further shown in Figure 6-11.

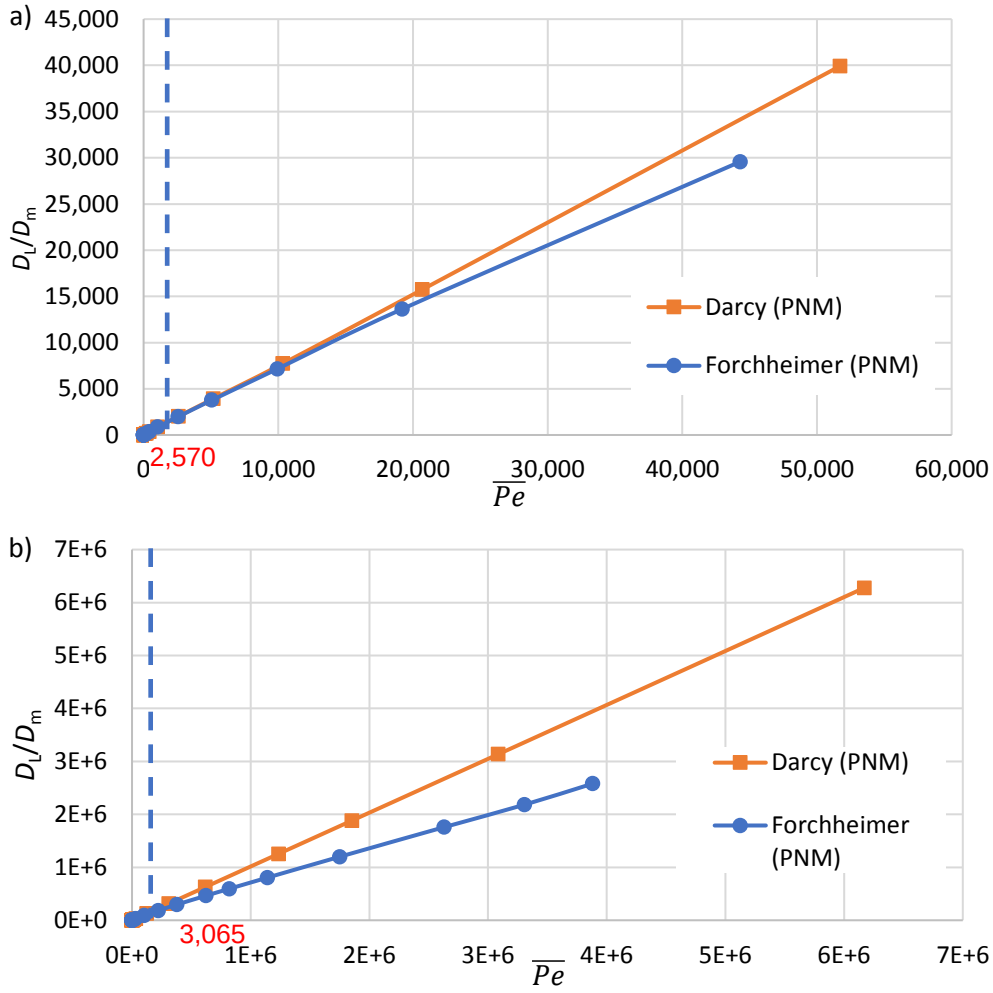

Figure 6-11 The longitudinal dispersion coefficient (D_L) scaled by molecular diffusion (D_m) vs. Péclet number ($\overline{Pe}$) for a) Berea Sandstone and b) packed spheres. The vertical blue dashed line represents the onset of non-Darcy flow.

To further explain the inertial effects on the longitudinal dispersion, the longitudinal dispersion coefficient (D_L) scaled by molecular diffusion (D_m) versus Péclet number ($\overline{Pe}$) is replotted on a normal scale (not a log-log scale as in Figure 6-9). In Figure 6-11, after the onset of non-Darcy flow,

the longitudinal dispersion coefficient is directly proportional to the Péclet number and it increases when the fluid velocity increases. If the inertial forces are not accounted for, i.e. assuming Darcy flow, this causes overestimation in the longitudinal dispersion coefficient and the Péclet number. In Figure 6-11a, for Berea Sandstone at the maximum applied pressure drop, the Péclet number for the Darcy flow case is 1.17 times higher than the non-Darcy flow case, while D_L is 1.35 times higher compared to the non-Darcy flow case. However, these factors may differ for other media and for different ranges of velocities. For instance, the onset of non-Darcy flow occurs much earlier in heterogenous media such as Carbonate compared to less heterogenous media such as packed beads or Sandstone (El-Zehairy et al., 2019). For the case of heterogeneous media, *Pe* and D_L values for non-Darcy flow are expected to differ significantly from the values obtained when Darcy flow is assumed. In Figure 6-11b, at the maximum applied pressure drop for Packed spheres, the Péclet number for the Darcy flow case (not shown in the figure) is 6.36 times higher than the non-Darcy case, while D_L is 9.7 times higher compared to the non-Darcy case.

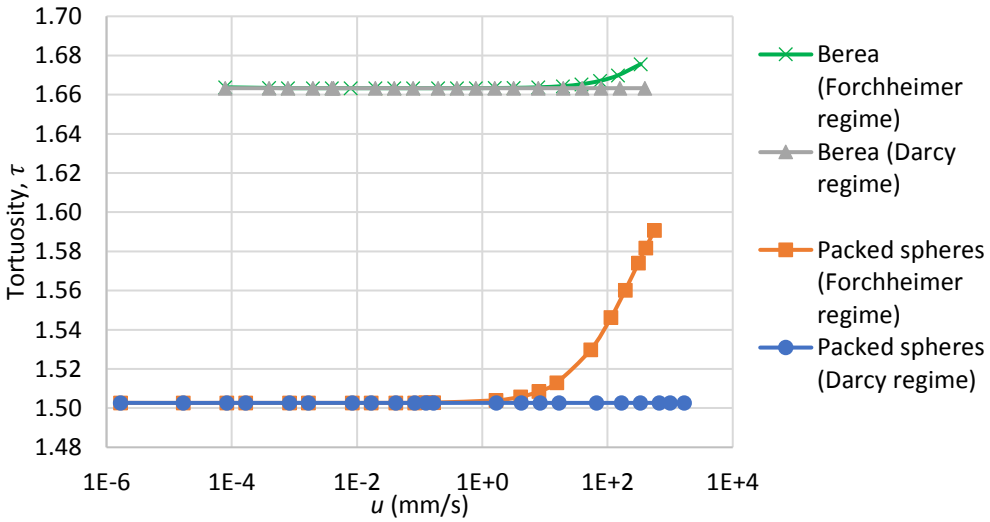

Figure 6-12 Tortuosity (τ), Equation 4.15, versus average pore velocity (u) for the Berea sandstone and packed spheres samples. The onset of non-Darcy flow occurs when u = 20 mm/s and u = 1.7 mm/s for the Berea and packed spheres samples, respectively.

In Figure 6-9 and Figure 6-11, after the onset of non-Darcy flow, the curve that represents the relationship between D_L/D_m versus $\overline{Pe}$ for non-Darcy flow deviates from the same relationship for Darcy flow for the same medium. This is because when the inertial effects are taken into account, after solving the flow and pressure field at each pore body in the medium, the pressure values at each pore body for the non-Darcy flow case are not the same as the pressure values for the Darcy flow case (even when the discharge or average pore velocity is the same in both cases; Darcy and non-Darcy flow). Consequently, at the same average pore velocity, the tortuosity value (Equation 4.15) for the non-Darcy case is not the same as the tortuosity values for the Darcy flow case according to Figure 6-12. In Figure 6-12, for the Berea sandstone and packed spheres samples, within the Darcy flow regime, tortuosity is almost constant at any velocity. While in the non-Darcy flow regime, tortuosity increases when pore velocity increases. This change in tortuosity for the same medium indicates that, after the onset of non-Darcy flow, for a constant value of velocity or discharge through the medium, the longitudinal dispersion coefficient (D_L) is not the same within the Darcy and the non-Darcy flow regimes.

6.3.3 Decoupling pore-scale dispersion from dispersion due to flow field heterogeneity

The right-hand side of Equation 6.1 represents two different processes; dispersion due to flow field heterogeneity which results from tortuosity and change of flow-paths $\left[\sum_{q_{i-j<0}} q_{i-j} C_i(t) + \sum_{q_{i-j>0}} q_{i-j} C_j(t)\right]$ and (time-dependent Taylor-Aris) dispersion through each pore throats $\left[\sum_{j\in N_i} a_{i-j} D_{i-j}^{eff} \frac{C_j(t)-C_i(t)}{L_{i-j}}\right]$. In this section, each model run was repeated, while the effects of dispersion due to flow field heterogeneity, $D_{L,\,hetero}$, and (time-dependent Taylor-Aris) dispersion, $D_{L,\,T\text{-}A}$, were decoupled from each other. The results of both cases are shown in Figure 6-13 for the Berea sandstone sample.

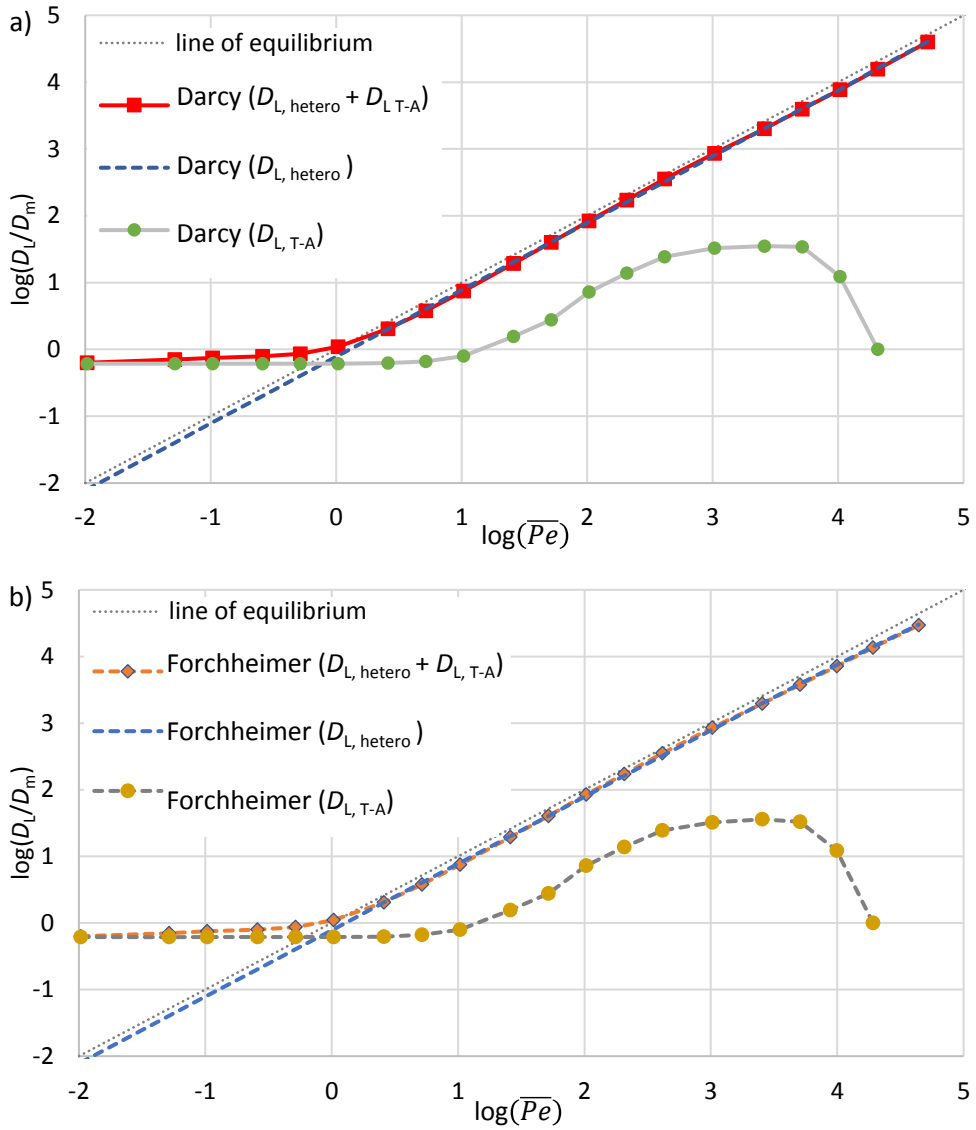

Figure 6-13 The longitudinal dispersion coefficient due to flow field heterogeneity, pore-scale (time-dependent Taylor-Aris) dispersion and both processes scaled by molecular diffusion vs. Péclet number for the Berea sandstone sample; a) Darcy flow and b) Forchheimer flow.

Figure 6-13 shows that the longitudinal dispersion coefficient due to flow field heterogeneity only, $D_{L, hetero}$, while neglecting the effect of pore-scale dispersion, is directly proportional to the average pore velocity. The relationship between $D_{L, hetero}$ and u (or $\overline{Pe}$), is linear within the Darcy flow regime, then it becomes nonlinear in the Forchheimer flow regime. The longitudinal dispersion coefficient due to pore-scale dispersion only, $D_{L, T-A}$, while neglecting the effect of $D_{L, hetero}$, shows a different behaviour. In the diffusion dominated regime and in the first part of the transition regime, $D_{L,}$

$_{T\text{-}A}$ is constant because the average pore velocity and the pore throat Péclet number are small, and molecular diffusion dominates the transport process in each pore throat as per Equation 6.3. Then, $D_{L,\,T\text{-}A}$ increases gradually in the transition regime and in the boundary-layer dispersion regime because when pore velocity increases, the Péclet number increases and the effective diffusion coefficient for each pore throat $\left(D_{i-j}^{eff}\right)$ increases as per Equation 6.3. After that, in the mechanical dispersion regime, when pore velocity increases, the residence time in each pore throat decreases and, as a result, $D_{L,\,T\text{-}A}$ decreases gradually.

6.4 Conclusion

Solute transport has been modelled within the laminar Darcy and non-Darcy flow regimes using a pore-network modelling approach and applying the 1D Advection-Dispersion Equation (ADE). Berea Sandstone and packed spheres samples were used to investigate the effect of non-Darcy flow on solute transport for a wide range of Péclet number ($\overline{Pe}$ = 0.003- 24×10^6).

When applying Dirichlet boundary conditions, at low flow velocities within the Darcy flow regime, the concentration front moves regularly over time in the longitudinal direction. While at higher velocities, within the non-Darcy flow regime, the effect of advection increases, and the concentration front extends over a larger length.

Based on the solute residence time in each pore throat, three cases have been defined to calculate the effective diffusion coefficient for each pore throat; an asymptotic Fickian regime, a pre-asymptotic time dependent regime and a pure advection regime, and consequently the breakthrough curves show a very good match with the analytical solution of the 1D ADE.

When the longitudinal dispersion coefficient (D_L) scaled by the molecular diffusion (D_m) is plotted versus the Péclet number ($\overline{Pe}$), a good match between the proposed model results and the previous results found in the literature has been observed, except at low velocities in the packed spheres sample where relatively higher values for the longitudinal dispersion coefficient were obtained. This has been attributed to the large size of the

pores in the packed spheres sample and to the assumption that dispersion occurs over the pore throat length only, neglecting the length of pore bodies connected to both ends of the pore throat.

At higher flow velocities, i.e. after the onset of non-Darcy flow, the longitudinal dispersion coefficient is directly proportional to the fluid velocity. After the onset of non-Darcy flow, if the inertial forces are not accounted, i.e. assuming Darcy flow, this causes overestimation in the Péclet number and in the longitudinal dispersion coefficient, which may be up to ~10 times higher than the true value obtained under Forchheimer flow conditions. However, this depends mainly on the degree of heterogeneity of the medium, and the factor of 10 might differ for other media.

By decoupling the effects of dispersion due to flow field heterogeneity from pore-scale dispersion, it was found that pore-scale dispersion is constant in the macro-scale diffusion dominated regime and in the first part of the transition regime, because the average pore velocity is very small and molecular diffusion dominates the transport process. Then, the effect of pore-scale dispersion increases gradually in the macro-scale transition regime and in the boundary-layer dispersion regime. After that, the effect of pore-scale dispersion decreases gradually in all of the macro-scale mechanical dispersion regime before it vanishes. Meanwhile, in all macro-scale transport regimes, dispersion due to flow field heterogeneity is directly proportional to the average pore velocity.

Chapter 7

Pore-network modelling of solute transport for turbulent flow

This chapter contains a short introduction about the effect of turbulence on solute transport, then the developed PNM algorithm for modelling solute transport within all flow regimes (Darcy, Forchheimer and turbulent) in porous media is explained. According to my knowledge, solute transport within the turbulent flow regime has never been investigated before using PNM. The proposed model has been applied on the packed spheres (d_m = 1.84 mm) sample used in the experimental work. The results are presented, discussed and compared to related results existing in the literature and to the observed experimental results.

7.1 Introduction

Turbulent flow differs from Darcy and Forchheimer flow because it is characterised by high levels of velocity fluctuations and random motion which lead to rapid diffusivity and kinetic energy dissipation. Such characteristics enhance the process of solute mixing and results in higher values of D_L. In Darcy and Forchheimer flow through porous media, solute transport occurs due to molecular diffusion and mechanical dispersion (see Section 6.1). In turbulent flow, in addition to the previously mentioned two mechanisms, there is an additional process called turbulent diffusion which results from the chaotic movements of fluid particles and velocity fluctuations. Turbulent diffusion causes rapid solute mixing and its effect is much higher than the effect of molecular diffusion within the turbulent flow regime (Shen et al., 2002).

7.2 The Mixed Cell Method

Following the methodology introduced in Section 6.2 and by dividing the pore-network into pore-units, the transport equation for any pore-unit, PU(i), in the pore-network is given by Equation 6.2. However, for turbulent

flow, the pore throat effective diffusion coefficient, $D_{\mathrm{i-j}}^{\mathrm{eff}}$ (mm^2/s), is given by Equation 7.1 (Taylor, 1954b):

$$D_{\mathrm{i-j}}^{\mathrm{eff}} = 10.1\, r_{\mathrm{i-j}}\, u_{*\mathrm{i-j}} = 10.1\, r_{\mathrm{i-j}} \sqrt{\frac{a_{\mathrm{i-j}}\, \Delta P_{\mathrm{i-j}}^{\mathrm{tot}}}{\rho\, p_{\mathrm{i-j}}\, L_{\mathrm{i-j}}}} \qquad 7.1$$

where $u_{*\mathrm{i-j}}$ (mm/s) is the pore throat shear velocity which depends on the friction between the fluid and the pore throat walls, and $p_{\mathrm{i-j}}$ (mm) is the pore throat average perimeter. For each pore throat in the pore-network, $D_{\mathrm{i-j}}^{\mathrm{eff}}$ is estimated using Equation 7.1, then the mass balance equation (Equation 6.2) is invoked at each pore body in the pore-network. Equation 7.1 can be applied without any restrictions regarding the pore throat length or the solute residence time as far as the flow is fully developed (Sittel et al., 1968) and the solute is fully mixed with water (Hart et al., 2016) which agrees with the definition of the MCM that assumes fully mixed conditions in each pore body.

Recalling that any porous medium is composed of pores with various geometries, so at the pore-scale, the flow regime may vary from one pore to another, i.e. some pores may exhibit laminar flow, while the flow in other pores may be transitional or turbulent. Then, based on the Reynold's number (Equation 2.12) value at each pore throat, the flow regime at the pore-scale is determined using the predefined limits discussed in Section 2.4 (laminar when $Re_{\mathrm{pore}} < 150$, transitional when $150 \leq Re_{\mathrm{pore}} \leq 300$, and turbulent when $Re_{\mathrm{pore}} > 300$). In the literature, there is a scarcity of studies that have determined the effective diffusion coefficient for tubes under transitional flow conditions. Most of these studies determined the effective diffusion coefficient using empirical equations or by regression analysis of experimental measurements. However, these studies were performed on macro-scale tubes and their equations were derived only for a high range of Reynold's number values (> 2,000), which is much higher than the range of Reynold's number values in porous media. Moreover, in the transitional flow regime, i.e. when $150 \leq Re_{\mathrm{pore}} \leq 300$, it is inappropriate to determine the effective diffusion coefficient by interpolation, in a way similar to that used in Chapter 5 to determine the pore friction factor in the

transitional flow regime, because the effective diffusion coefficient is not directly related to the Reynold's number. Therefore, in the proposed model, if $Re_{\text{pore}} \leq 300$, the effective diffusion coefficient is calculated using Equation 6.3, while if $Re_{\text{pore}} > 300$, the effective diffusion coefficient is calculated using Equation 7.1. Equations 6.8 and 6.9 are used to estimate the overall average concentration ($\bar{C}$) at each time step and the overall medium average Péclet number ($\overline{Pe}$), Equation 6.9.

The algorithm and details of the proposed pore-network transport model are very similar to the details of the algorithm developed for modelling solute transport within the non-Darcy flow regime which are presented in Appendix D.

7.3 Verification, results and discussion

The properties of the extracted pore-network for the packed spheres sample were presented in Section 4.3.1. A wide range of pressure drops (ΔP) ranging from 0.00001 to 80,000 Pa was applied for each run to obtain all possible flow conditions including the turbulent flow regime, and this corresponded to average Péclet numbers ($\overline{Pe}$) ranging from 0.003 to 3.88×10^{6} (Equation 6.9). For each run, a fixed pressure drop across the pore-network is applied. After solving the flow equations and predicting the pressure and flow fields in the pore-network (the simulation results were presented in Chapter 5), Equation 6.2 is solved explicitly at each time step. For all simulations, following Bijeljic et al. (2004) and Babaei & Joekar-Niasar (2016), the coefficient of molecular diffusion (D_{m}) is considered equal to 10^{-9} m^2s^{-1} and Dirichlet boundary conditions are applied, i.e. a conservative solute is injected continuously at the inlet boundary maintaining a constant concentration (C_{o}) equal to 1 mol/mm^3. Water is considered as the working fluid with viscosity μ = 0.001 kg/m·s and density ρ = 1000 kg/m^3. The simulation continues until the concentration of the solute is nearly equal to 1 mol/mm^3 at every pore-unit. For each run, the longitudinal dispersion coefficient is determined by fitting the analytical solution of the 1D ADE (Ogata & Banks, 1961), Equation 2.20, to the breakthrough curve (BTC) obtained from pore-network simulation by using

the CXTFIT computational software (Toride et al., 1995). The BTC for each run is measured at the middle of the sample, i.e. when $x = L/2$, where x is the longitudinal flow direction, then the concentration values over time (BTC) are used as inputs to CXTFIT. These concentration and time values are fitted to the analytical solution of the 1D ADE (Equation 2.20) to obtain the D_L and the average pore velocity (u_{avg}) values.

7.3.1 Solute concentration distribution and breakthrough curves

Figure 7-1 shows snapshots of a solute transport simulation when ΔP = 10,000 Pa across the pore-network and $\overline{Pe} = 1.19\times10^6$. In this run, only 29% of the pore throats exhibit turbulent flow conditions while flow in the remaining pore throats is either laminar or transitional. The figure represents an advection dominated regime, similar to the non-Darcy flow case shown in Figure 6-7(d-f). Very few pore-units with low concentration values can be observed in the dark red zone which represents a high concentration value in Figure 7-1. These few pore-units represent dead ends, i.e. a pore body connected to a single pore throat and this pore body gains concentration as a result only of effective diffusion. Such pore bodies can gain higher concentrations after a long time, compared to other pore bodies where the effect of advection causes a faster increase in concentration.

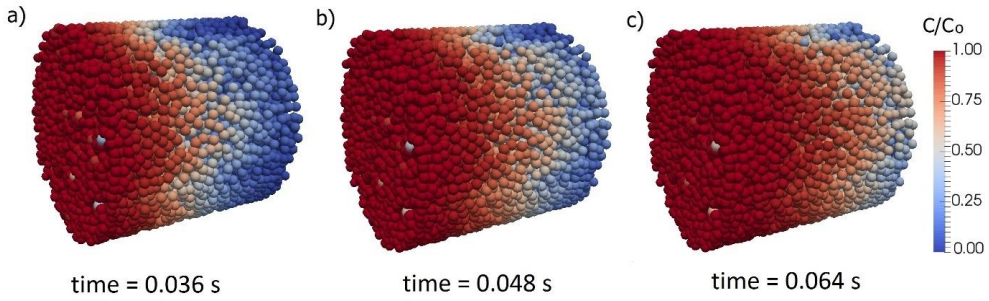

Figure 7-1 Snapshots of the concentration distribution at three different time steps for the packed spheres sample; a) $\bar{C}/C_o = 0.25$, b) $\bar{C}/C_o = 0.50$, c) $\bar{C}/C_o = 0.75$ when ΔP = 10,000 Pa. The flow direction is from left to right.

Figure 7-2 shows the breakthrough curves, at different Péclet numbers, fitted to the 1D ADE analytical solution. There is a good match between the results obtained using PNM and the analytical solution of the 1D ADE

(Equation 2.20). The figure demonstrates that the breakthrough curves, within the turbulent flow regime, can be developed within a very short time ranging from ~0.06 seconds for the largest Péclet number, and up to ~1 second for the lowest Péclet number. This is because turbulent flow is characterised by high velocities compared to the Darcy and Forchheimer flow regimes, and also due to the effect of turbulent diffusion which enhances the solute mixing.

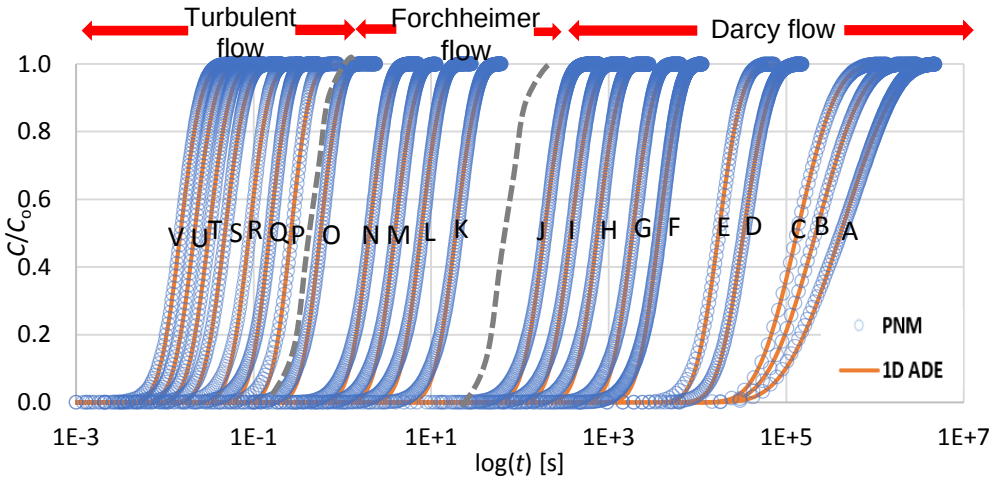

Curve	A	B	C	D	E	F	G	H	I	J	K
ΔP (Pa)	0.0001	0.0005	0.001	0.005	0.01	0.05	0.1	0.25	0.5	1	10
$\overline{Pe}$	0.031	0.154	0.309	1.543	3.085	15.43	30.85	77.13	154.3	308.3	3064.5
Curve	L	M	N	O	P	Q	R	S	T	U	V
ΔP (Pa)	25	50	100	400	1000	2000	4000	10000	20000	40000	80000
$\overline{Pe}$	7586.8	14943.8	29075	103053	222854	386525	646306	1187188	1785630	2610495	3769888

Figure 7-2 The packed spheres breakthrough curves at different Péclet numbers fitted to the analytical solution of the 1D ADE (Equation 2.20). The concentration C is obtained at the middle ($x = L/2$) of the sample, where x is the longitudinal flow direction. The dashed grey curves represent the onset of non-Darcy flow and the onset of turbulence.

7.3.2 Verification against experimental measurements and data in the literature

The longitudinal dispersion coefficients (D_L) scaled by molecular diffusion (D_m) versus Péclet numbers ($\overline{Pe}$) are shown in Figure 7-3. The figure shows the obtained PNM results for Darcy, Forchheimer and turbulent flow regimes compared to the obtained experimental results and various results in the literature. There is a scarcity in the literature data at very high velocities that represent turbulent flow, also most previous work did not

investigate the effect of flow regime on the transport process but they investigated different transport regimes apart from the flow regime. To my knowledge, the only available data within the turbulent flow regime, i.e. at high Péclet numbers, are those obtained experimentally by Pfannkuch (1963) for graded sands and other single-grained materials, Carberry and Bretton (1958) for fixed packed spheres and rings, and Ebach and White (1958) for spherical glass beads, Porcelain Raschig rings, Berl saddles and Intalox saddles. From Figure 7-3, the results of the proposed PNM model, in the turbulent flow regime, show a reasonable match with all presented previous results and the obtained experimental results. However, in the turbulent flow regime, the obtained PNM results may underestimate D_L (by a factor of ~2 or less) when compared to the data by Pfannkuch (1963) and Ebach and White (1958), this might be attributed to the use of different characteristic length (used to calculate $\overline{Pe}$) or due to different degrees of heterogeneity of the samples they used. When $log(\overline{Pe})$>~3, i.e. after the onset of non-Darcy flow, there is a downward shift in the obtained PNM results compared to the results in the literature. A possible reason for this downward shift is that the data in the literature were analysed using Darcy's law, as Forchheimer's law was quite new and not well known at that time (1958, 1963). Analysing the data using Darcy's law causes overestimation of the D_L values as explained below. The obtained experimental results (shown in cyan coloured squares) are limited to a narrow range of $\overline{Pe}$ because for larger discharge values, the manometric tubes used to measure the pressure in the lab are flooded with water. Additionally, in the Darcy and Forchheimer flow regimes, the solute is not fully mixed with water (see Section 3.4.4) and the experimental setup used cannot provide accurate measurements for concentration. Moreover, these experimental results (shown in cyan coloured squares) show high variations among each other, at any specific $\overline{Pe}$, due to the possible large error in the measurements as explained in Section 3.4.4. It is noticed that all the results obtained using PNM for the turbulent flow regime are within the advection dominated (mechanical dispersion) transport regime due to high fluid velocities in the turbulent flow regime that dominate the transport process.

The results of the proposed model presented in this chapter (shown in light green) follow the Darcy flow PNM results (shown in yellow) from very low $\overline{Pe}$ values until the onset of non-Darcy flow at $log(\overline{Pe}) \approx 3.45$. After the onset of non-Darcy flow, it follows the Forchheimer flow PNM results (shown in dark blue) until the onset of turbulence at $log(\overline{Pe}) = 5.35$. After the onset of turbulence, D_L increases gradually due to the effect of turbulent diffusion, and this results in higher D_L values compared to the values obtained by PNM when Forchheimer flow is assumed at the same Péclet number. It is difficult to find a relationship between D_L and $\overline{Pe}$ in the turbulent flow regime, however in this region, D_L is directly proportional to $\overline{Pe}$. After the onset of turbulence, by comparing the two curves that represent Forchheimer and turbulent flow PNM modelling results, we notice that D_L values represented by turbulent flow are higher (by a factor up to 1.62) than D_L values represented by Forchheimer flow at the same Péclet number. This is attributed to the presence of turbulent diffusion, accounted for in Equation 7.1, which enhances the longitudinal dispersion process. In other words, in the turbulent flow regime, if the effect of turbulent diffusion is neglected, i.e. if the flow is assumed to be in the Forchheimer flow regime, this causes underestimation of D_L by a factor of 0.6.

If the flow inertial effects are neglected, i.e. if the flow is assumed to be Darcian even at very high velocities after the onset of turbulence, the resulting D_L and $\overline{Pe}$ values are much higher than D_L and $\overline{Pe}$ in the Forchheimer and turbulent flow regimes. For instance, at the maximum applied pressure drop across the sample (when ΔP = 80,000 Pa), D_L and $\overline{Pe}$ obtained when the inertial effected are neglected (assuming Darcy flow) are higher than the values obtain for Forchheimer flow by factors of 10 and 6, respectively. While in the same case (when ΔP = 80,000 Pa), D_L and $\overline{Pe}$ obtained when the inertial effects are neglected (assuming Darcy flow) are higher than the values obtained for turbulent flow by factors of 6 and 6.5, respectively. In conclusion, neglecting the inertial effects and assuming Darcy flow, after the onset of non-Darcy flow, causes up to one order of magnitude overestimation in the Péclet number and the longitudinal dispersion coefficient.

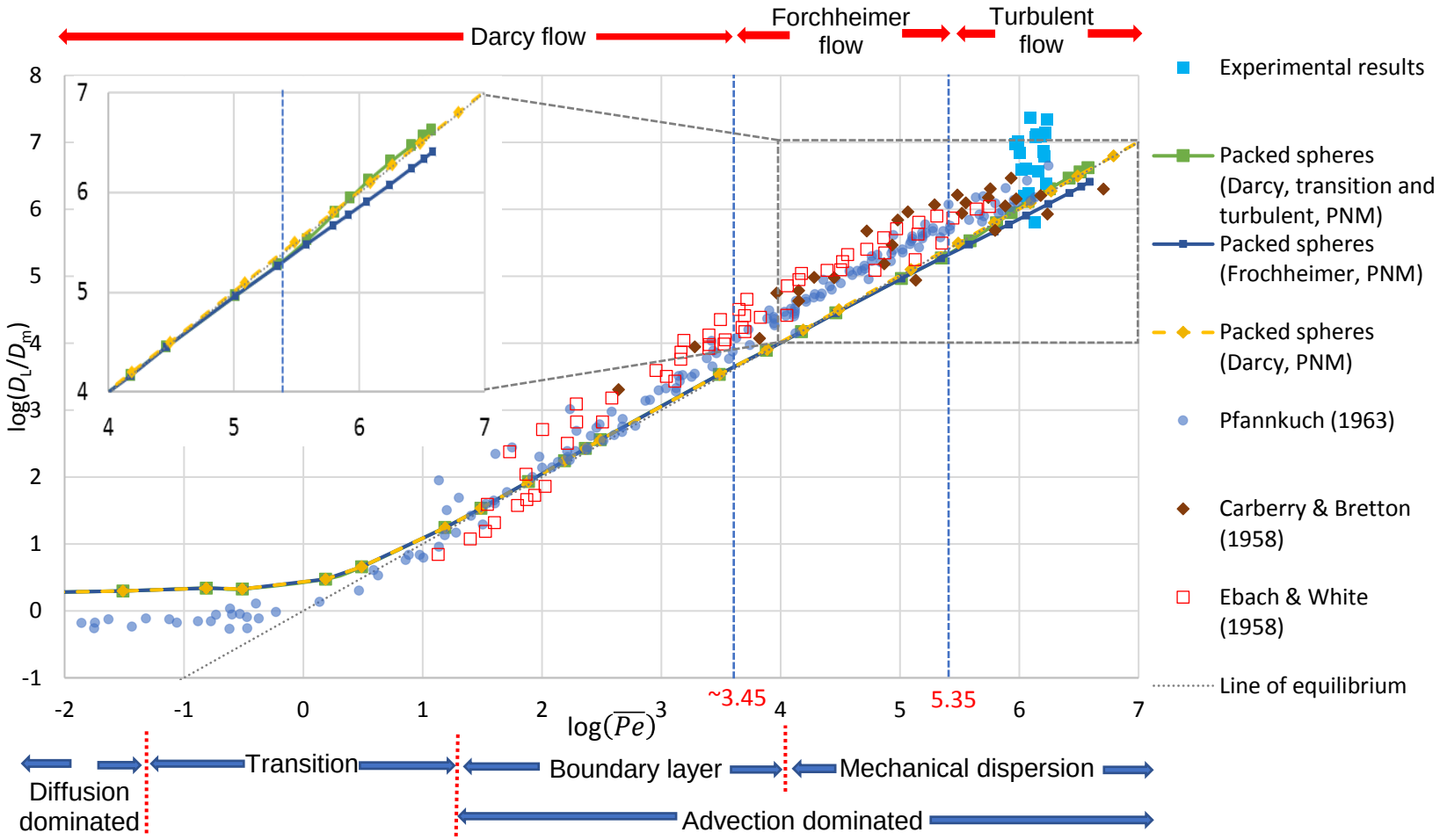

Figure 7-3 The longitudinal dispersion coefficients (D_L) scaled by molecular diffusion (D_m) vs. Péclet numbers ($\overline{Pe}$) compared to experimental measurements and data in the literature. The two blue dashed vertical lines represent the onset of non-Darcy and the onset of turbulent flow.

7.3.3 Decoupling pore-scale dispersion from dispersion due to flow field heterogeneity

We recall that the right-hand side of Equation 6.1 represents two different processes; dispersion due to flow field heterogeneity which results from tortuosity and change of flow-paths $\left[\sum_{q_{\mathrm{i-j}<0}} q_{\mathrm{i-j}} C_{\mathrm{i}}(t) + \sum_{q_{\mathrm{i-j}>0}} q_{\mathrm{i-j}} C_{\mathrm{j}}(t)\right]$ and Taylor-Aris dispersion through each pore throat $\left[\sum_{j\in N_{\mathrm{i}}} a_{\mathrm{i-j}} D_{\mathrm{i-j}}^{\mathrm{eff}} \frac{C_{\mathrm{j}}(t)-C_{\mathrm{i}}(t)}{L_{\mathrm{i-j}}}\right]$. Additional model runs were performed by dropping one of these two processes while considering the other and vice versa. Figure 7-4 shows the overall longitudinal dispersion coefficient ($D_{\mathrm{L,\ hetero}} + D_{\mathrm{L,\ T\text{-}A}}$) due to the combined actions of flow field heterogeneity and dispersion through each pore throat, due to flow field heterogeneity ($D_{\mathrm{L,\ hetero}}$) only, and due to dispersion through each pore throat ($D_{\mathrm{L,\ T\text{-}A}}$) only, at different Péclet numbers ($\overline{Pe}$). The figure demonstrates that $D_{\mathrm{L,\ hetero}}$ is directly proportional to the average pore velocity or Péclet number. The relationship between $D_{\mathrm{L,\ hetero}}$ and u (or $\overline{Pe}$), is linear within the Darcy flow regime, then it becomes nonlinear within the Forchheimer and turbulent flow regimes. The longitudinal dispersion coefficient due to pore-scale dispersion ($D_{\mathrm{L,\ T\text{-}A}}$) shows a different behaviour compared to $D_{\mathrm{L,\ hetero}}$. In the diffusion dominated regime, $D_{\mathrm{L,\ T\text{-}A}}$ is constant because the flow is Darcian, the average pore velocity and $\overline{Pe}$ values are very small and the coefficient of molecular diffusion (D_{m}) dominates the transport process in each pore throat as per Equation 6.3. In other words, due to the long residence time in each pore throat, the molecules jump from one streamline to another under the effect of molecular diffusion while the effect of velocity can be neglected. Then, $D_{\mathrm{L,\ T\text{-}A}}$ increases gradually in the boundary-layer transport regime because when pore velocity increases, the Péclet number increases and the effective diffusion coefficient of each pore throat $\left(D_{\mathrm{i-j}}^{\mathrm{eff}}\right)$ increases as a result of increased shear stress between the fluid layers (as per Equation 6.3). After that, in the mechanical dispersion regime, before the onset of turbulent flow, when the pore velocity increases, the residence time in each pore throat decreases and $D_{\mathrm{L,\ T\text{-}A}}$ decreases gradually, as long as the Reynold's number in most of the pore throats does not exceed the onset of

turbulence (Re_{pore}<300). The reason that $D_{L,\ T\text{-}A}$ decreases is the small residence time in the pore throats which is not long enough for molecules to move from one streamline to another, i.e. there is no dispersion in the pore throats. However, once the Reynold's number in any pore throat exceeds 300, i.e. the Reynold's number exceeds the predefined onset of turbulence for each pore throat, then the D_{i-j}^{eff} value increases due to the effect of turbulent diffusion (considered via Equation 7.1) and $D_{L,\ T\text{-}A}$ increases again. In the turbulent flow regime, the effect of flow field heterogeneity on dispersion is comparable to the pore-scale (Taylor-Aris) dispersion, and this confirms that turbulent diffusion enhances the longitudinal dispersion process.

In Figure 7-4, there is a gap in the curve that represents dispersion through each pore throat ($D_{L,\ T\text{-}A}$) within the turbulent flow regime. This is because within this range of Péclet numbers (when $log(\overline{Pe}) = 5.5 - 6.0$), the Reynold's number in most of the pore throats is less than 300 and only a few pore throats have Reynold's number > 300. In most of the pore throats that have Reynold's number < 300, $D_{i-j}^{eff} = 0.0$, because the dimensionless residence time in these pore throats is less than 0.01. In the meantime, only few pore throats have *Re* > 300 and $D_{i-j}^{eff} > 0.0$, and this causes the solute concentration to be trapped only in a few pore-units, while the concentration in the rest of the pore-units is zero. Therefore, it is difficult to obtain the BTC or D_L value for these cases.

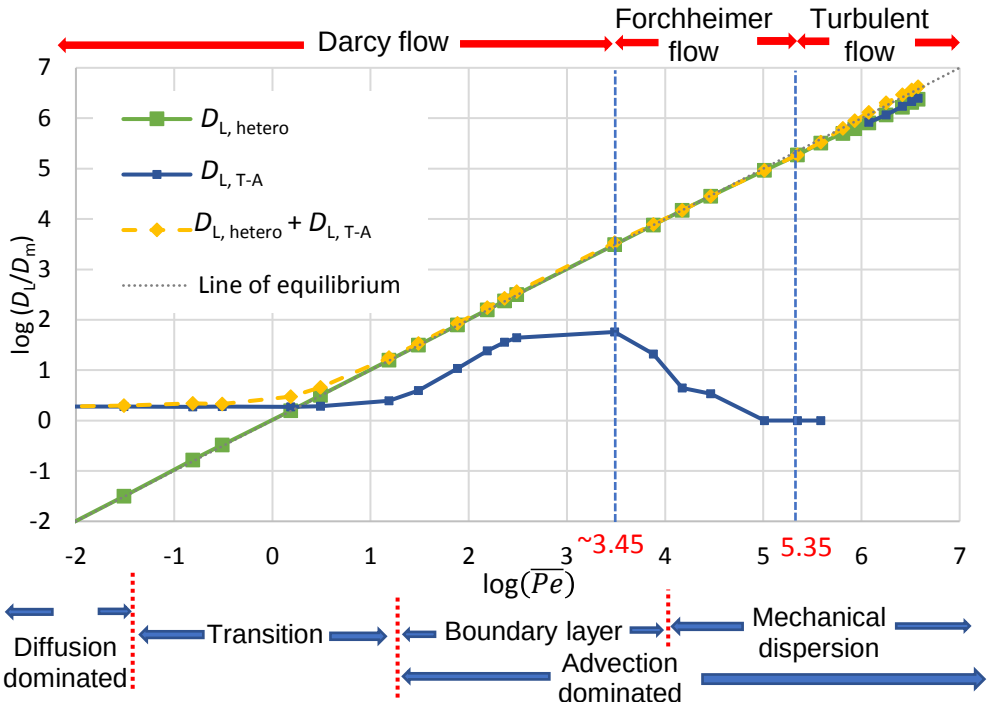

Figure 7-4 The longitudinal dispersion coefficients, due to flow field heterogeneity ($D_{L,\ hetero}$), pore-scale (Taylor-Aris) dispersion ($D_{L,\ T\text{-}A}$) and both processes ($D_{L,\ hetero} + D_{L,\ T\text{-}A}$), scaled by molecular diffusion (D_m) versus Péclet number ($\overline{Pe}$).

7.3.4 Conclusion

Solute transport within the Darcy, Forchheimer and turbulent flow regimes has been modelled using pore-network modelling for a wide range of Péclet numbers ($\overline{Pe}$), from $Pe = 3\times10^{-3}$ to 3.88×10^{6}. The model has been applied to the packed sphere sample and verified against the obtained experimental results for the same sample and previous data in the literature. The obtained turbulent flow results were found to be in the advection dominated transport regime where the longitudinal dispersion coefficient (D_L) is directly proportional to the Péclet number.

In the turbulent flow regime, the transport process is governed mainly by advection and turbulent diffusion. Turbulent diffusion results from velocity fluctuations and the chaotic movements of fluid particles. It causes the solute to be mixed rapidly and transversely through the sample and works against the longitudinal spread of the solute due to advection.

If Darcy flow is assumed at high flow velocities and inertial effects are neglected, then this causes overestimation of the Péclet number and the longitudinal dispersion coefficient by a factor up to 10. In the turbulent flow regime, if the effect of turbulent diffusion is neglected, the obtained value of D_L is less (by a factor up to 0.6) than the value obtained when Forchheimer flow is assumed at the same Péclet number.

When the longitudinal dispersion coefficient (D_L) scaled by the molecular diffusion (D_m) is plotted versus Péclet number ($\overline{Pe}$), a good match between the proposed model results and previous data in the literature has been obtained.

By investigating the effect of flow field heterogeneity and pore-scale dispersion separately, it has been found that dispersion due to flow field heterogeneity is directly proportional to the average pore velocity. In the turbulent flow regime, turbulent diffusion increases gradually when the average pore velocity increases. Consequently, pore-scale dispersion increased gradually, and was comparable to the effect of flow field heterogeneity. This confirms that in the turbulent flow regime, turbulent diffusion enhances the longitudinal dispersion process.

Chapter 8

Conclusion and future studies

8.1 Conclusion

In this work, flow and solute transport were modelled using pore-network modelling across two different scales; the micro (0.5-2.5 mm) and macro (50-200 mm) scales. At the micro-scale, the proposed models were applied on X-ray Computed Tomography (XCT) scans of beadpack, sandstone and carbonate samples, while at the macro-scale two samples composed of randomly packed and regularly structured uniform spheres were used. At the micro-scale, flow and solute transport were modelled within the Darcy and non-Darcy (Forchheimer) flow regimes, while at the macro-scale, all possible flow regimes, including the Darcy, Forchheimer and turbulent flow regimes, were modelled. When using pore-network modelling, any porous medium can be simplified into pore bodies, which represent large pores in the medium, connected to each other by pore throats, which represent narrow pores in the medium. Then, analytical or semi-analytical equations can be used to model the flow behaviour and the transport process through the medium. The simplifications made to the porous medium and the use of analytical equations reduce the computational resources needed for the simulations.

Three different approaches can be followed to generate a pore-network equivalent to a specific medium. The first approach is to directly map the porous media, e.g. from a CT-image, while the second method is to construct a representative pore-network using statistical distributions of basic morphological parameters. The third approach is called the grain-based model which is used to generate a pore-network equivalent to a packing of grains by considering information about the grain diameters and locations. To verify the proposed models, the equivalent pore-networks of the porous media used were generated using two different methods. First, the pore-network extraction code developed by Raeini et al. (2017) was used to extract the pore-networks equivalent to all samples, excluding the

regularly structured uniform spheres sample, from their CT-images. Second, to save time and effort in the CT-scanning process, another in-house pore-network generation code was developed to generate a regularly structured pore-network equivalent to the regularly structured uniform spheres sample used.

For non-Darcy flow, the Forchheimer equation was used to model the flow at the micro and macro scales, and the proposed model was able to predict the Darcy Permeability (K_D) and Forchheimer coefficient (β) for all tested samples to a reasonable degree of accuracy (with a maximum percentage of error of 15.2% and 54%, respectively). The onset of non-Darcy flow was dependent on the medium's degree of heterogeneity. The Reynold's number and superficial flow velocity at which the onset of non-Darcy flow occurs were two or three orders of magnitude lower for highly heterogenous media, while the obtained Forchheimer number values at the onset of non-Darcy flow for all of the tested samples ranged from 0.01 to 0.1. The medium friction coefficient decreased when the fluid velocity increased, and following the Forchheimer equation, the medium's friction factor versus Forchheimer number curve was identical for all media regardless of their degree of heterogeneity.

For turbulent flow, the Forchheimer equation was used to describe the flow behaviour at the macro-scale, but with modified parameters (Forchheimer Permeability, $K_F^{`}$, and Forchheimer coefficient, $\beta^{`}$). Because turbulent flow occurs at high velocities and through large pores, the assumption of a fully developed flow in each pore is not valid, and this caused some discrepancies between the obtained PNM results and the experimental measurements. For the macro-scale samples, the onset of turbulent flow obtained using the conventional Reynold's number (Re) ranged from 93 to 204, depending on the medium characteristic length and size of pores. While the onset of turbulent flow obtained using the permeability-based Reynold's number (Re_K) ranged from 2.5 to 7.4, and using the Forchheimer number (F_o), the onset of turbulent flow occurred when $F_o =$ 0.4-3.6. In the turbulent flow regime, if the medium's average size of particles increases ($\geq$ 5 mm), then

the pressure loss due to inertial effects dominates the flow behaviour, while the frictional pressure loss becomes negligible.

To model solute transport within the non-Darcy flow regime, the Taylor-Aris diffusion coefficient cannot be used for all pore throats because the residence time is less than the time required for the dye to be fully mixed cross-sectionally, i.e. to reach an asymptotic state. Therefore, three cases were defined to calculate the effective diffusion coefficient for each pore throat, depending on the residence time; asymptotic Fickian regime, pre-asymptotic time dependent regime and pure advection regime. Then, the mass balance equation was applied at each pore body. Consequently, the breakthrough curves showed a very good match with the analytical solution of the 1D Advection Dispersion Equation (ADE). In the diffusion dominated regime, the concentration front moved regularly over time in the longitudinal direction, in a way that the concentration at any cross-section perpendicular to the flow direction is almost constant. At higher velocities, in the non-Darcy flow regime, the effect of advection increased, and the concentration front extends over larger length. After the onset of non-Darcy flow, if the inertial forces are not accounted for, i.e. if Darcy flow is assumed, then this causes overestimation of the overall Péclet number and longitudinal dispersion coefficient (D_L), which may be up to 10 times higher than the true value.

In the macro-scale (50-200 mm) turbulent flow regime, depending on the pore throat geometries and the pressure distribution in the medium, the flow nature in the pore throats may be either laminar, transition or turbulent. For turbulent flow, the Taylor-Aris effective diffusion coefficient, which accounts for turbulent diffusion, was used and the mass balance equation was applied at each pore body. The transport process was governed mainly by advection and turbulent diffusion, i.e. the effect of molecular diffusion was negligible. Turbulent diffusion results from velocity fluctuations and the chaotic movements of fluid particles, it mixes the solute rapidly over the sample cross-sectional area and works against the longitudinal spread of solute due to advection. The effect of pore-scale (Taylor-Aris) dispersion, which accounts for turbulent diffusion, on the longitudinal dispersion

increased gradually when the average pore velocity increased. After the onset of turbulent flow, pore-scale dispersion was lower than dispersion due to flow field heterogeneity, then it increased gradually until it was equivalent to the effect of the flow field heterogeneity. This confirms that in the turbulent flow regime, turbulent diffusion enhances the longitudinal dispersion process. In the turbulent flow regime, if the effect of turbulent diffusion is neglected, by considering only dispersion due to flow field heterogeneity, then the obtained value of D_L was less (by a factor up to 0.6) than the value obtained when Forchheimer flow is assumed at the same Péclet number ($\overline{Pe}$).

The pore network modelling (PNM) approach has proved to be computationally more efficient in comparison to other pore-scale modelling techniques and could dramatically reduce the running time from few hours (3 hours and 37 minutes for the Estaillades model in Muljadi et al. (2015) work) using 16 parallel computer nodes to less than one minute using a standard PC.

8.2 The achieved aims and main contributions of the work

The following aims and contributions have been achieved:

- A pore-network model has been developed to simulate flow and solute transport through porous media within all possible flow regimes including the macro-scale Darcy, Forchheimer and turbulent flow regimes.
- The proposed model can determine the boundaries between different flow regimes, i.e. the onset of non-Darcy flow and the onset of turbulence after which Darcy's law loses its validity.
- An in-depth understanding of the flow behaviour and the pressure distribution in porous media, including heterogenous media, has been obtained.
- The effect of inertial forces and turbulence on the longitudinal solute transport process has been quantified.
- The different possible pore-scale transport processes through porous media have been quantified and understood separately.

8.3 Future work

Most of the previous work that modelled flow using pore-network modelling assumed fully developed flow in each pore, i.e. the velocity profile is assumed to be fully developed and the entrance length is small compared to the total pore length. This assumption is not valid for coarse porous media with wide pores and relatively large diameters. In the case of developing flow, the friction between the pore walls and the fluid is higher compared to fully developed flow, and the Hagen–Poiseuille equation is not valid. For more accurate results, more specific equations, such as those presented by Shah and Bhatti (1987) for laminar flow and by Bhatti and Shah (1987) for turbulent flow, can be used to predict the pore friction factor for developing flow, and this will provide more accurate results.

The focus of this thesis was on single phase flow, however, a next step is to further extend the models to include two phase or multiphase flow within the non-Darcy and turbulent flow regimes which is important for petroleum engineering applications. Nevertheless, the solute transport work may be further extended to model reactive transport and account for the chemical reactions that might occur through the porous medium.

The presented solute transport study was specific to Fickian transport. More work is needed to further extend this work for modelling non-Fickian transport in heterogenous porous media. Moreover, the inertial effects on transverse dispersion can be determined as well.

The solute transport laboratory experiments in the Darcy and Forchheimer flow regimes did not provide accurate results because the dye was not fully mixed with water at any cross-section perpendicular to the flow direction. Consequently, the Cyclops sensors did not provide accurate measurements. In the turbulent flow regime, the velocity fluctuations and eddies enhanced the process of rapid mixing and the dye was cross-sectionally fully mixed with the water. For the Darcy and Forchheimer flow regimes, better results can be achieved, following the study by Taylor (1954a), if a smaller diameter and larger length of the recirculating pipe is used, but in this case the head loss through the small recirculating pipe may exceed the maximum

head that the pump can deliver. Also, if a smaller diameter of the recirculating pipe is used, a smooth transition section is required to transfer from the small pipe diameter to the 50 mm diameter of the packed spheres sample to avoid disturbing the flow. Another option is to use a mixing chamber to mix the dye properly with water before it reaches the Cyclops sensors, but this requires a specific design for the mixing chamber dimensions, propeller size and motor horsepower. Nevertheless, the propeller motion may create some eddies and affect the flow.

To apply the proposed flow and solute transport models at larger scales, e.g. at the field scale, a suitable upscaling technique, such as the method of volume averaging (Whitaker, 1999), could be used.

The proposed models can be further extended to couple surface flow with subsurface flow and to account for the biogeochemical and contamination exchange processes that occur in the hyporheic zone.

References:

Abdelall, F. F., Hahn, G., Ghiaasiaan, S. M., Abdel-Khalik, S. I., Jeter, S. S., Yoda, M., & Sadowski, D. L. (2005). Pressure drop caused by abrupt flow area changes in small channels. *Experimental Thermal and Fluid Science, 29*(4), 425-434. doi:https://doi.org/10.1016/j.expthermflusci.2004.05.001

Acharya, R. C., Van der Zee, S. E. A. T. M., & Leijnse, A. (2005). Transport modeling of nonlinearly adsorbing solutes in physically heterogeneous pore networks. *Water Resources Research, 41*(2). doi:10.1029/2004WR003500

Acharya, R. C., Van der Zee, S. E. A. T. M., & Leijnse, A. (2007). Approaches for modeling longitudinal dispersion in pore-networks. *Advances in Water Resources, 30*(2), 261-272. doi:https://doi.org/10.1016/j.advwatres.2005.11.015

Ahmed, N. (1967). Physical Properties of Porous Medium Affecting Laminar and Turbulent Flow of Water. *PhD dissertation, Colorado State University, Fort Collins, Colorado*.

Amiri, H. A., & Hamouda, A. A. (2013). Evaluation of level set and phase field methods in modeling two phase flow with viscosity contrast through dual-permeability porous medium. *International Journal of Multiphase Flow, 52*, 22-34. doi:http://dx.doi.org/10.1016/j.ijmultiphaseflow.2012.12.006

Al-Gharbi, M. S., & Blunt, M. J. (2005). Dynamic network modeling of two-phase drainage in porous media. *Physical Review E, 71*(1), 016308. Retrieved from http://0-link.aps.org.pugwash.lib.warwick.ac.uk/doi/10.1103/PhysRevE.71.016308

Al-Raoush, R., Thompson, K., & Willson, C. S. (2003). Comparison of Network Generation Techniques for Unconsolidated Porous Media. *Soil Science Society of America Journal, 67*(6), 1687-1700. doi:10.2136/sssaj2003.1687

Al-Zoubi, A. (2014). Fundamentals of Lattice Boltzmann Method. Retrieved from https://sites.google.com/site/ahmad6alzoubi/introduction-to-lattice-boltzmann-method

Alfonsi, G. (2011). On Direct Numerical Simulation of Turbulent Flows. *Applied Mechanics Reviews, 64*(2), 020802-020802-020833. doi:10.1115/1.4005282

Algive, L., Bekri, S., & Vizika, O. (2010). Pore-Network Modeling Dedicated to the Determination of the Petrophysical-Property Changes in the Presence of Reactive Fluid. doi:10.2118/124305-PA

Aly, A. M., & Asai, M. (2015). Modelling of Non-Darcy Flows through Porous Media Using Extended Incompressible Smoothed Particle Hydrodynamics. *Numerical Heat Transfer, Part B: Fundamentals, 67*(3), 255-279. doi:10.1080/10407790.2014.955772

Ananthakrishnan, V., Gill, W. N., & Barduhn, A. J. (1965). Laminar dispersion in capillaries: Part I. Mathematical analysis. *AIChE Journal, 11*(6), 1063-1072. doi:10.1002/aic.690110620

Andrade, J. S., Costa, U. M. S., Almeida, M. P., Makse, H. A., & Stanley, H. E. (1999). Inertial Effects on Fluid Flow through Disordered Porous Media. *Physical Review Letters, 82*(26), 5249-5252. doi:10.1103/PhysRevLett.82.5249

Andrew, M., Bijeljic, B., & Blunt, M. J. (2013). Pore-scale imaging of geological carbon dioxide storage under in situ conditions. *Geophysical Research Letters, 40*(15), 3915-3918. doi:10.1002/grl.50771

Aris, R. (1956). On the dispersion of a solute in a fluid flowing through a tube. *Proceedings of the Royal Society of London. Series A. Mathematical and Physical Sciences, 235*(1200), 67-77. doi:10.1098/rspa.1956.0065

Babaei, M., & Joekar-Niasar, V. (2016). A transport phase diagram for pore-level correlated porous media. *Advances in Water Resources, 92*, 23-29. doi:http://dx.doi.org/10.1016/j.advwatres.2016.03.014

Bağcı, Ö., Dukhan, N., & Özdemir, M. (2014). Flow Regimes in Packed Beds of Spheres from Pre-Darcy to Turbulent. *Transport in Porous Media, 104*(3), 501-520. doi:10.1007/s11242-014-0345-0

Bailey, H. R., & Gogarty, W. B. (1962). Numerical and experimental results on the dispersion of a solute in a fluid in laminar flow through a tube. *Proceedings of the Royal Society of London. Series A. Mathematical and Physical Sciences, 269*(1338), 352-367. doi:10.1098/rspa.1962.0182

Balhoff, M. T., & Wheeler, M. F. (2009). A Predictive Pore-Scale Model for Non-Darcy Flow in Porous Media. *SPE Journal, 14*(03), 579-587.

Bandara, U. C., Tartakovsky, A. M., Oostrom, M., Palmer, B. J., Grate, J., & Zhang, C. (2013). Smoothed particle hydrodynamics pore-scale simulations of unstable immiscible flow in porous media. *Advances in Water Resources, 62, Part C*, 356-369. doi:http://dx.doi.org/10.1016/j.advwatres.2013.09.014

Barree, R. D., & Conway, M. W. (2004). *Beyond Beta Factors: A Complete Model for Darcy, Forchheimer, and Trans-Forchheimer Flow in Porous Media*. Paper presented at the SPE Annual Technical Conference and Exhibition, Houston, Texas.

Barree, R. D., & Conway, M. W. (2005). Reply to Discussion of "Beyond Beta Factors: A Complete Model for Darcy, Forchheimer, and Trans-Forchheimer Flow in Porous Media". *J. Pet. Tech. 57 (8): 73–74*. doi:10.2118/0805-0073-JPT

Bear, J. (1972). *Dynamics of Fluids in Porous Media*. Elsevier, New York.

Bear, J., & Cheng, H.-D. A. (2010). Groundwater Motion *Modeling Groundwater Flow and Contaminant Transport*. Dordrecht: Springer Netherlands.

Belhaj, H. A., Agha, K. R., Nouri, A. M., Butt, S. D., Vaziri, H. H., & Islam, M. R. (2003). *Numerical Modeling of Forchheimer's Equation to Describe Darcy and Non-Darcy Flow in Porous Media*. Paper presented at the SPE Asia Pacific Oil and Gas Conference and Exhibition, Jakarta, Indonesia. https://doi.org/10.2118/80440-MS

Bhatti, M. S., & Shah, R. K. (1987). Turbulent and Transition Flow Convective Heat Transfer in Ducts. *Handbook of Single-Phase Convective Heat Transfer, Kakac, Shah, and Aung, eds., John Wiley & Son, New York, pp. 4.1–4.166.*

Bijeljic, B., & Blunt, M. J. (2006). Pore-scale modeling and continuous time random walk analysis of dispersion in porous media. *Water Resources Research, 42*(1), W01202. doi:10.1029/2005WR004578

Bijeljic, B., & Blunt, M. J. (2007). Pore-scale modeling of transverse dispersion in porous media. *Water Resources Research, 43*(12), W12S11. doi:10.1029/2006WR005700

Bijeljic, B., Mostaghimi, P., & Blunt, M. J. (2013a). Insights into non-Fickian solute transport in carbonates. *Water Resources Research, 49*(5), 2714-2728. doi:10.1002/wrcr.20238

Bijeljic, B., Muggeridge, A. H., & Blunt, M. J. (2004). Pore-scale modeling of longitudinal dispersion. *Water Resources Research, 40*(11), W11501. doi:10.1029/2004WR003567

Bijeljic, B., Raeini, A., Mostaghimi, P., & Blunt, M. J. (2013b). Predictions of non-Fickian solute transport in different classes of porous media using direct simulation on pore-scale images. *Physical Review E, 87*(1), 013011. Retrieved from http://link.aps.org/doi/10.1103/PhysRevE.87.013011

Bird, R. B., Stewart, W. E., & Lightfoot, E. N. (1960). *Transport phenomena. New York: John Wiley and Sons.*

Blackwell, R. J. (1959). Experiments on mixing by fluid flow in porous media. *52nd Ann. Meeting Soc. Pet. Eng., San Francisco, Preprint 29*.

Blackwell, R. J., Rayne, J. R., & Terry, W. M. (1959). Factors Influencing the Efficiency of Miscible Displacement (pp. 8): Society of Petroleum Engineers.

Blake, F. C. (1922). The Resistance of Packing to Fluid Flow. *Trans. Am. Inst. Chem. Engrs. 14: 415–421*.

Blasius, H. (1913). Das Aehnlichkeitsgesetz bei Reibungsvorgängen in Flüssigkeiten *Mitteilungen über Forschungsarbeiten auf dem Gebiete des Ingenieurwesens: insbesondere aus den Laboratorien der technischen Hochschulen* (pp. 1-41). Berlin, Heidelberg: Springer Berlin Heidelberg.

Blick, E. F., & Civan, F. (1988). Porous-Media Momentum Equation for Highly Accelerated Flow. *Society of Petroleum Engineers*. doi:10.2118/16202-PA

Blunt, M. J. (1998). Physically-based network modeling of multiphase flow in intermediate-wet porous media. *Journal of Petroleum Science and Engineering, 20*(3), 117-125. doi:https://doi.org/10.1016/S0920-4105(98)00010-2

Blunt, M. J., Bijeljic, B., Dong, H., Gharbi, O., Iglauer, S., Mostaghimi, P., Paluszny, A., & Pentland, C. (2013). Pore-scale imaging and modelling. *Advances in Water Resources, 51*, 197-216. doi:http://dx.doi.org/10.1016/j.advwatres.2012.03.003

Blunt, M. J., Jackson, M. D., Piri, M., & Valvatne, P. H. (2002). Detailed physics, predictive capabilities and macroscopic consequences for pore-network models of multiphase flow. *Advances in Water*

Resources, 25(8), 1069-1089. doi:https://doi.org/10.1016/S0309-1708(02)00049-0

Bora, R., Maini, B. B., & Chakma, A. (2000). Flow Visualization Studies of Solution Gas Drive Process in Heavy Oil Reservoirs Using a Glass Micromodel. *SPE Reservoir Evaluation & Engineering, 3*(03), 224-229. doi:10.2118/64226-PA

Brigham, W. E., P. W. Reed, and J. N. Dew. (1969). Experiments on mixing by fluid flow in porous media. *Amer. Inst. Chem. Eng. and SOC. Petrol. Eng. Joint Symp. Oil Recovery Methods, Sun Francisco*.

Brownell, L. E., Dombrowski, H. S., & Dickey, C. A. (1947). Pressure drop through porous media. *Chem. Eng. Prog. 43: 537–548*.

Bruderer, C., & Bernabé, Y. (2001). Network modeling of dispersion: Transition from Taylor Dispersion in homogeneous networks to mechanical dispersion in very heterogeneous ones. *Water Resources Research, 37*(4), 897-908. doi:10.1029/2000WR900362

Bryant, S., & Blunt, M. (1992). Prediction of relative permeability in simple porous media. *Physical Review A, 46*(4), 2004-2011. Retrieved from http://link.aps.org/doi/10.1103/PhysRevA.46.2004

Bryant, S., King, P. R., & Mellor, D. W. (1993). Network model evaluation of permeability and spatial correlation in a real random sphere packing. *Transport in Porous Media, 11*(1), 53-70. doi:10.1007/bf00614635

Budwig, R. (1994). Refractive index matching methods for liquid flow investigations. *Experiments in Fluids, 17*(5), 350-355. doi:10.1007/bf01874416

Buselli, G., & Lu, K. (2001). Groundwater contamination monitoring with multichannel electrical and electromagnetic methods. *Journal of Applied Geophysics, 48*(1), 11-23. doi:https://doi.org/10.1016/S0926-9851(01)00055-6

Carberry, J. J., & Bretton, R. H. (1958). Axial dispersion of mass in flow through fixed beds. *AIChE Journal, 4*(3), 367-375. doi:10.1002/aic.690040327

Carman, P. C. (1937). Fluid flow through granular beds. *Chemical Engineering Research and Design, 75*, S32-S48. doi:https://doi.org/10.1016/S0263-8762(97)80003-2

Celia, M. A., Reeves, P. C., & Ferrand, L. A. (1995). Recent advances in pore scale models for multiphase flow in porous media. *Reviews of Geophysics, 33*(S2), 1049-1057. doi:10.1029/95RG00248

Çengel, Y. A., & Cimbala, J. M. (2006). *Fluid mechanics: Fundamentals and applications.* Boston: McGraw-HillHigher Education.

Chandler, I. D. (2012). Vertical variation in diffusion coefficient within sediments. (PhD Thesis), University of Warwick.

Chan, S. K., & Ng, K. M. (1988). Geometrical characteristics of the pore space in a random packing of equal spheres. *Powder Technology, 54*(2), 147-155. doi:http://dx.doi.org/10.1016/0032-5910(88)80072-X

Chatwin, P. C. (1977). The initial development of longitudinal dispersion in straight tubes. *Journal of Fluid Mechanics, 80*(1), 33-48. doi:10.1017/S0022112077001529

Chen, S., & Doolen, G. D. (1998). Lattice Boltzmann method for fluid flows. *Annual Review of Fluid Mechanics, 30*(1), 329-364. doi:10.1146/annurev.fluid.30.1.329

Chilton, T. H., & Colburn, A. P. (1931). Pressure Drop in Packed Tubes. *Industrial & Engineering Chemistry, 23*(8), 913-919. doi:10.1021/ie50260a016

Chukwudozie, C. P., Tyagi, M., Sears, S. O., & White, C. D. (2012). Prediction of Non-Darcy Coefficients for Inertial Flows Through the Castlegate Sandstone Using Image-Based Modeling. *Transport in Porous Media, 95*(3), 563-580. doi:10.1007/s11242-012-0062-5

Chung, P. M. Y., Kawaji, M., & Kawahara, A. (2002). Characteristics of Single-Phase Flow in Microchannels. (36150), 1219-1228. doi:10.1115/FEDSM2002-31211

Coats, K. H., & Smith, B. D. (1964). Dead-End Pore Volume and Dispersion in Porous Media. doi:10.2118/647-PA

Colebrook, C. F., & White, C. M. (1937). Experiments with Fluid Friction in Roughened Pipes. *Proceedings of the Royal Society of London. Series A, Mathematical and Physical Sciences, 161*(906), 367-381. Retrieved from http://www.jstor.org/stable/96790

Coles, M. E., & Hartman, K. J. (1998). Non-Darcy Measurements in Dry Core and the Effect of Immobile Liquid. *Society of Petroleum Engineers*. doi:10.2118/39977-MS

Comiti, J., Sabiri, N. E., & Montillet, A. (2000). Experimental characterization of flow regimes in various porous media — III: limit of Darcy's or creeping flow regime for Newtonian and purely viscous non-Newtonian fluids. *Chemical Engineering Science, 55*(15), 3057-3061. doi:http://dx.doi.org/10.1016/S0009-2509(99)00556-4

Costanza-Robinson, M. S., Estabrook, B. D., & Fouhey, D. F. (2011). Representative elementary volume estimation for porosity, moisture saturation, and air-water interfacial areas in unsaturated porous media: Data quality implications. *Water Resources Research, 47*(7). doi:10.1029/2010WR009655

Crane. (1942). *Flow of fluids through valves, fittings and pipe*. Chicago, III: Crane co.

Darcy, H. (1856). Les Fontaines Publiques de la Vile de Dijon. Victor Dalmond, Paris.

Darcy, H. (1857). Recherches expérimentales relatives au mouvement de l'eau dans les tuyaux, Mallet-Bachelier, Paris. 268 pages and atlas (in French).

Day, P. R. (1956). Dispersion of a moving salt-water boundary advancing through saturated sand. *Eos, Transactions American Geophysical Union, 37*(5), 595-601. doi:10.1029/TR037i005p00595

Ding, A., & Candela, D. (1996). Probing nonlocal tracer dispersion in flows through random porous media. *Physical Review E, 54*(1), 656-660. doi:10.1103/PhysRevE.54.656

Dong, H. (2007). *Micro CT Imaging and Pore Network Extraction.* (PhD thesis), Department of Earth Science and Engineering, Imperial College London.

Dong, H., & Blunt, M. J. (2009). Pore-network extraction from micro-computerized-tomography images. *Physical Review E, 80*(3), 036307. Retrieved from http://0-link.aps.org.pugwash.lib.warwick.ac.uk/doi/10.1103/PhysRevE.80.036307

Dong, H., Touati, M., & Blunt, M. J. (2007). Pore Network Modeling: Analysis of Pore Size Distribution of Arabian Core Samples. *in Proceedings of the SPE Middle East Oil and Gas Show and Conference, Manama, Bahrain.*

Du Plessis, J. P., & Masliyah, J. H. (1988). Mathematical modelling of flow through consolidated isotropic porous media. *Transport in Porous Media, 3*(2), 145-161. doi:10.1007/bf00820342

Duda, A., Koza, Z., & Matyka, M. (2011). Hydraulic tortuosity in arbitrary porous media flow. *Physical Review E, 84*(3), 036319. Retrieved from http://link.aps.org/doi/10.1103/PhysRevE.84.036319

Dullien, F. A. L. (1992). *Porous Media: Fluid Transport and Pore Structure*. San Diego: Academic Press.

Durlofsky, L., & Brady, J. F. (1987). Analysis of the Brinkman equation as a model for flow in porous media. *The Physics of Fluids, 30*(11), 3329-3341. doi:10.1063/1.866465

Dwivedi, P. N., & Upadhyay, S. N. (1977). Particle-Fluid Mass Transfer in Fixed and Fluidized Beds. *Industrial & Engineering Chemistry Process Design and Development, 16*(2), 157-165. doi:10.1021/i260062a001

Dybbs, A., & Edwards, R. V. (1984). A new look at porous media fluid mechanics-Darcy to turbulent. *In: Bear, J., Corapcioglu, M.Y. (Eds.), Fundamentals of Transport Phenomena in Porous Media, NATO ASI Series, vol. 82. Springer, Netherlands, pp. 199–256.*

Ebach, E. A., & White, R. R. (1958). Mixing of fluids flowing through beds of packed solids. *AIChE Journal, 4*(2), 161-169. doi:10.1002/aic.690040209

Ellis, J. S., & Bazylak, A. (2012). Dynamic pore network model of surface heterogeneity in brine-filled porous media for carbon sequestration. Physical Chemistry Chemical Physics, 14(23), 8382-8390. doi:10.1039/C2CP40812K

El-Zehairy, A. A., Nezhad, M. M., Joekar-Niasar, V., Guymer, I., Kourra, N., & Williams, M. A. (2019). Pore-network modelling of non-Darcy flow through heterogeneous porous media. *Advances in Water Resources, 131,* 103378. doi:https://doi.org/10.1016/j.advwatres.2019.103378

Enright, D. P. (2002). *Use of the particle level set method for enhanced resolution of free surface flows.* (PhD thesis), Stanford University.

Ergun, S. (1952). Fluid Flow through Packed Columns. *Chem. Eng. Prog., 48*, 89–94.

Ergun, S., & Orning, A. A. (1949). Fluid Flow through Randomly Packed Columns and Fluidized Beds. *Industrial & Engineering Chemistry, 41*(6), 1179-1184. doi:10.1021/ie50474a011

Fancher, G. H., & Lewis, J. A. (1933). Flow of Simple Fluids through Porous Materials. *Industrial & Engineering Chemistry, 25*(10), 1139-1147. doi:10.1021/ie50286a020

Fand, R. M., Kim, B. Y. K., Lam, A. C. C., & Phan, R. T. (1987). Resistance to the Flow of Fluids Through Simple and Complex Porous Media Whose Matrices Are Composed of Randomly Packed Spheres. *Journal of Fluids Engineering, 109*(3), 268-273. doi:10.1115/1.3242658

Fatt, I. (1956a). The Network Model of Porous Media I. Capillary Pressure Characteristics. *Pet. Trans. AIME, 207,144-159.*

Fatt, I. (1956b). The network model of porous media II. Dynamic properties of a single size tube network. *Pet. Trans. AIME, 207,160-163*.

Fatt, I. (1956c). The network model of porous media III. Dynamic properties of networks with tube radius distribution. *Pet Trans. AIME, 207,164-181*.

Ferdos, F., & Dargahi, B. (2016). A study of turbulent flow in large-scale porous media at high Reynolds numbers. Part I: numerical validation. *Journal of Hydraulic Research, 54*(6), 663-677. doi:10.1080/00221686.2016.1211184

Finney, J. L. (1968). *Random packing and the structure of liquid state.* (Ph.D. thesis), University of London.

Finney, J. L. (1970). Random packings and the structure of simple liquids. I. The geometry of random close packing. *Proceedings of the Royal Society of London. A. Mathematical and Physical Sciences, 319*(1539), 479-493. doi:doi:10.1098/rspa.1970.0189

Flory, P. J. (1941). Molecular Size Distribution in Three Dimensional Polymers. I. Gelation1. *Journal of the American Chemical Society, 63*(11), 3083-3090. doi:10.1021/ja01856a061

Forchheimer, P. (1901). Wasserbewegung durch Boden. *Zeitschrift des Vereins deutscher Ingenieure 45, no. 1: 1782–1788.*

Forchheimer, P. (1930). Hydraulik, third edition, 54. Leipzig: Druck und Verlag Von B.G. Teubner.

Freitas, D. S., & Prat, M. (2000). Pore Network Simulation of Evaporation of a Binary Liquid from a Capillary Porous Medium. *Transport in Porous Media, 40*(1), 1-25. doi:10.1023/a:1006651524722

Fried, J. J., & Combarnous, M. A. (1971). Dispersion in Porous Media. In V. T. Chow (Ed.), *Advances in Hydroscience* (Vol. 7, pp. 169-282): Elsevier.

Friedel, T., & Voigt, H.-D. (2006). Investigation of non-Darcy flow in tight-gas reservoirs with fractured wells. *Journal of Petroleum Science and Engineering, 54*(3–4), 112-128. doi:http://dx.doi.org/10.1016/j.petrol.2006.07.002

Frisch, U., Hasslacher, B., & Pomeau, Y. (1986). Lattice-Gas Automata for the Navier-Stokes Equation. *Physical Review Letters, 56*(14), 1505-1508. Retrieved from https://link.aps.org/doi/10.1103/PhysRevLett.56.1505

Gaganis, P., Skouras, E. D., Theodoropoulou, M. A., Tsakiroglou, C. D., & Burganos, V. N. (2005). On the evaluation of dispersion coefficients from visualization experiments in artificial porous media. *Journal of Hydrology, 307*(1), 79-91. doi:https://doi.org/10.1016/j.jhydrol.2004.09.023

Gao, S., Meegoda, J. N., & Hu, L. (2012). Two methods for pore network of porous media. *International Journal for Numerical and Analytical Methods in Geomechanics, 36*(18), 1954-1970. doi:10.1002/nag.1134

Geertsma, J. (1974). Estimating the Coefficient of Inertial Resistance in Fluid Flow Through Porous Media. *Society of Petroleum Engineers Journal, 14*(05), 445-450. doi:10.2118/4706-PA

Geiger, G. E. (1964). *Sudden contraction losses in single and two-phase flow.* (Ph.D. thesis), University of Pittsburgh, Pittsburgh, PA.

Ghanbarian, B., Hunt, A. G., Sahimi, M., Ewing, R. P., & Skinner, T. E. (2013). Percolation Theory Generates a Physically Based Description of Tortuosity in Saturated and Unsaturated Porous Media. *Soil Science Society of America Journal, 77*(6), 1920-1929. doi:10.2136/sssaj2013.01.0089

Gill, W. N., & Sankarasubramanian, R. (1970). Exact Analysis of Unsteady Convective Diffusion. *Proceedings of the Royal Society of London. Series A, Mathematical and Physical Sciences, 316*(1526), 341-350. Retrieved from http://www.jstor.org/stable/77597

Gist, G. A., Thompson, A. H., Katz, A. J., & Higgins, R. L. (1990). Hydrodynamic dispersion and pore geometry in consolidated rock. *Physics of Fluids A: Fluid Dynamics, 2*(9), 1533-1544. doi:10.1063/1.857602

Green, L., & Duwez, P. (1951). Fluid flow through porous metals. *J Appl Mech 3(2): 39–45*.

Guadagnini, A., Blunt, M. J., Riva, M., & Bijeljic, B. (2014). Statistical Scaling of Geometric Characteristics in Millimeter Scale Natural Porous Media. *Transport in Porous Media, 101*(3), 465-475. doi:10.1007/s11242-013-0254-7

Gui, F., & Scaringe, R. P. (1995). *Enhanced heat transfer in the entrance region of microchannels*: American Society of Mechanical Engineers, New York, NY (United States).

Guo, H., Wang, L., Yu, J., Ye, F., Ma, C., & Li, Z. (2010). Local resistance of fluid flow across sudden contraction in small channels. *Frontiers of Energy and Power Engineering in China, 4*(2), 149-154. doi:10.1007/s11708-009-0060-7

Guymer, I., & Stovin, V. R. (2011). One-Dimensional Mixing Model for Surcharged Manholes. *Journal of Hydraulic Engineering, 137*(10), 1160-1172. doi:doi:10.1061/(ASCE)HY.1943-7900.0000422

Hagen, G. (1839). Ueber die Bewegung des Wassers in engen cylindrischen Röhren. *Annalen der Physik, 122*(3), 423-442. doi:10.1002/andp.18391220304

Harms, T. M., Kazmierczak, M. J., & Gerner, F. M. (1999). Developing convective heat transfer in deep rectangular microchannels. *International Journal of Heat and Fluid Flow, 20*(2), 149-157. Retrieved from http://inis.iaea.org/search/search.aspx?orig_q=RN:31019107

Hart, J. R. (2013). *Longitudinal dispersion in steady and unsteady pipe flow.* (PhD), University of Warwick.

Hart, J. R., Guymer, I., Sonnenwald, F., & Stovin, V. R. (2016). Residence Time Distributions for Turbulent, Critical, and Laminar Pipe Flow. *Journal of Hydraulic Engineering, 142*(9), 04016024. doi:doi:10.1061/(ASCE)HY.1943-7900.0001146

Hashim, M. A., Mukhopadhyay, S., Sahu, J. N., & Sengupta, B. (2011). Remediation technologies for heavy metal contaminated groundwater. *Journal of Environmental Management, 92*(10), 2355-2388. doi:https://doi.org/10.1016/j.jenvman.2011.06.009

Hassanizadeh, S. M., & Gray, W. G. (1987). High velocity flow in porous media. *Transport in Porous Media, 2*(6), 521-531. doi:10.1007/bf00192152

Hegab, H. E., Bari, A., & Ameel, T. (2002). FRICTION AND CONVECTION STUDIES OF R-134a IN MICROCHANNELS WITHIN THE TRANSITION AND TURBULENT FLOW REGIMES. *Experimental Heat Transfer, 15*(4), 245-259. doi:10.1080/08916150290082658

Held, R. J., & Celia, M. A. (2001). Modeling support of functional relationships between capillary pressure, saturation, interfacial area and common lines. *Advances in Water Resources, 24*(3), 325-343. doi:https://doi.org/10.1016/S0309-1708(00)00060-9

Hilton, J. E. (2012). *A multiphase fluid-solid model based on the level set method*. Paper presented at the Ninth International Conference on CFD in the Minerals and Process Industries, CSIRO, Melbourne, Australia.

Hlushkou, D., & Tallarek, U. (2006). Transition from creeping via viscous-inertial to turbulent flow in fixed beds. *Journal of Chromatography A, 1126*(1–2), 70-85. doi:https://doi.org/10.1016/j.chroma.2006.06.011

Holdich, R. G. (2002). *Fundementals of particle technology*. Midland Information Technology and Publishing, Shepshed.

Horton, N. A., & Pokrajac, D. (2009). Onset of turbulence in a regular porous medium: An experimental study. *Physics of Fluids, 21*(4), 045104. doi:doi:http://dx.doi.org/10.1063/1.3091944

HSL. (2013). A collection of Fortran codes for large scale scientific computation. *http://www.hsl.rl.ac.uk.*

Huysmans, M., & Dassargues, A. (2005). Review of the use of Péclet numbers to determine the relative importance of advection and diffusion in low permeability environments. *Hydrogeology Journal, 13*(5), 895-904. doi:10.1007/s10040-004-0387-4

Jamiolahmady, M., Danesh, A., Tehrani, D. H., & Duncan, D. B. (2000). A Mechanistic Model of Gas-Condensate Flow in Pores. *Transport in Porous Media, 41*(1), 17-46. doi:10.1023/a:1006645515791

Janicek, J., & Katz, D. (1955). Applications of unsteady state gas flow calculations. *In: Proceedings of University of Michigan research conference*.

Jha, R. K., Bryant, S., & Lake, L. W. (2011). Effect of Diffusion on Dispersion. *SPE Journal, 16*(01), 65-77. doi:10.2118/115961-PA

Joekar-Niasar, V., & Hassanizadeh, S. (2011). Effect of fluids properties on non-equilibrium capillarity effects: Dynamic pore-network

modeling. *International Journal of Multiphase Flow, 37*(2), 198-214. doi:http://dx.doi.org/10.1016/j.ijmultiphaseflow.2010.09.007

Joekar-Niasar , V., & Hassanizadeh, S. M. (2012). Analysis of Fundamentals of Two-Phase Flow in Porous Media Using Dynamic Pore-Network Models: A Review. *Critical Reviews in Environmental Science and Technology, 42*(18), 1895-1976. doi:10.1080/10643389.2011.574101

Joekar-Niasar, V., Hassanizadeh, S. M., & Leijnse, A. (2008). Insights into the Relationships Among Capillary Pressure, Saturation, Interfacial Area and Relative Permeability Using Pore-Network Modeling. *Transport in Porous Media, 74*(2), 201-219. doi:10.1007/s11242-007-9191-7

Joekar-Niasar, V., Prodanović, M., Wildenschild, D., & Hassanizadeh, S. M. (2010). Network model investigation of interfacial area, capillary pressure and saturation relationships in granular porous media. *Water Resources Research, 46*(6), W06526. doi:10.1029/2009WR008585

Joekar Niasar, V., Hassanizadeh, S. M., Pyrak-Nolte, L. J., & Berentsen, C. (2009). Simulating drainage and imbibition experiments in a high-porosity micromodel using an unstructured pore network model. *Water Resources Research, 45*(2), W02430. doi:10.1029/2007WR006641

Johansson, N. (2011). Implementation of a standard level set method for incompressible two-phase flow simulations. *Tech. rep. Disciplinary Domain of Science and Technology, Uppsala University*.

Jones, S. C. (1987). Using the Inertial Coefficient, B, To Characterize Heterogeneity in Reservoir Rock. *Society of Petroleum Engineers*. doi:10.2118/16949-MS

Ju, B., Fan, T., & Ma, M. (2006). Enhanced oil recovery by flooding with hydrophilic nanoparticles. *China Particuology, 4*(1), 41-46. doi:https://doi.org/10.1016/S1672-2515(07)60232-2

Judy, J., Maynes, D., & Webb, B. W. (2002). Characterization of frictional pressure drop for liquid flows through microchannels. *International Journal of Heat and Mass Transfer, 45*(17), 3477-3489. doi:https://doi.org/10.1016/S0017-9310(02)00076-5

Junk, M. (2001). A finite difference interpretation of the lattice Boltzmann method. *Numerical Methods for Partial Differential Equations, 17*(4), 383-402. doi:doi:10.1002/num.1018

Kandhai, D., Hlushkou, D., Hoekstra, A. G., Sloot, P. M. A., Van As, H., & Tallarek, U. (2002). Influence of Stagnant Zones on Transient and Asymptotic Dispersion in Macroscopically Homogeneous Porous Media. *Physical Review Letters, 88*(23), 234501. doi:10.1103/PhysRevLett.88.234501

Kays, W. M. (1950). Loss Coefficient for Abrupt Changes in Flow Cross Section with Reynolds Number Flow in Single and Multiple Mube Systems. *Transactions of the American Society of Mechanical Engineers, 72*, 1067-1074.

Kays, W. M., & Crawford, M. E. (1993). *Convective heat and mass transfer*: (3rd ed., International ed). McGraw-Hill, New York ; Singapore.

Kececioglu, I., & Jiang, Y. (1994). Flow Through Porous Media of Packed Spheres Saturated With Water. *Journal of Fluids Engineering, 116*(1), 164-170. doi:10.1115/1.2910229

Kesten, H. (1987). Percolation Theory and First-Passage Percolation. *Ann. Probab., 15*(4), 1231-1271. doi:10.1214/aop/1176991975

Khrapitchev, A. A., & Callaghan, P. T. (2003). Reversible and irreversible dispersion in a porous medium. *Physics of Fluids, 15*(9), 2649-2660. doi:10.1063/1.1596914

Kim, B. Y. K. (1985). The resistance to flow in simple and complex porous media whose matrices are composed of spheres. *MSc thesis, University of Hawaii at Manoa, Honolulu, Hawaii.*

Kim, D., Peters, C. A., & Lindquist, W. B. (2011). Upscaling geochemical reaction rates accompanying acidic CO2-saturated brine flow in sandstone aquifers. *Water Resources Research, 47*(1). doi:doi:10.1029/2010WR009472

Kirby, B. J. (2010). Micro- and Nanoscale Fluid Mechanics: Transport in Microfluidic Devices. *New York: Cambridge University Press*. Retrieved from http://www.kirbyresearch.com/index.cfm/wrap/textbook/microfluidicsnanofluidicsch8.html#x53-1690008

Koch, D. L., & Brady, J. F. (1985). Dispersion in fixed beds. *J. Fluid Mech., 154*, 399.

Köhne, J. M., Schlüter, S., & Vogel, H.-J. (2011). Predicting Solute Transport in Structured Soil Using Pore Network Models. *Vadose Zone Journal*, *10*(3), 1082-1096. doi:10.2136/vzj2010.0158

Koplik, J. (1982). Creeping flow in two-dimensional networks. *Journal of Fluid Mechanics, 119*, 219-247. doi:10.1017/S0022112083001196

Koponen, A., Kataja, M., & Timonen, J. (1996). Tortuous flow in porous media. *Physical Review E, 54*(1), 406-410. Retrieved from http://link.aps.org/doi/10.1103/PhysRevE.54.406

Kozeny, J. (1927). Über kapillare Leitung des Wassers im Boden. *Akad. Wiss. Wien, 136*, 271-306. doi:citeulike-article-id:4155258

Kruyer, S. (1958). The penetration of mercury and capillary condensation in packed spheres. *Transactions of the Faraday Society, 54*(0), 1758-1767. doi:10.1039/TF9585401758

Kulasiri, D. (2013). Non-fickian Solute Transport *Non-fickian Solute Transport in Porous Media: A Mechanistic and Stochastic Theory* (pp. 1-27). Berlin, Heidelberg: Springer Berlin Heidelberg.

Kumblad, L., Kautsky, U., & Næslund, B. (2006). Transport and fate of radionuclides in aquatic environments – the use of ecosystem modelling for exposure assessments of nuclear facilities. *Journal of*

Environmental Radioactivity, 87(1), 107-129. doi:https://doi.org/10.1016/j.jenvrad.2005.11.001

Kundu, P., Kumar, V., & Mishra, I. M. (2016). Experimental and numerical investigation of fluid flow hydrodynamics in porous media: Characterization of pre-Darcy, Darcy and non-Darcy flow regimes. *Powder Technology, 303*, 278-291. doi:http://dx.doi.org/10.1016/j.powtec.2016.09.037

Kuwata, Y., & Suga, K. (2015). Large eddy simulations of pore-scale turbulent flows in porous media by the lattice Boltzmann method. *International Journal of Heat and Fluid Flow, 55*, 143-157. doi:http://dx.doi.org/10.1016/j.ijheatfluidflow.2015.05.015

Lage, J. L., Antohe, B. V., & Nield, D. A. (1997). Two Types of Nonlinear Pressure-Drop Versus Flow-Rate Relation Observed for Saturated Porous Media. *Journal of Fluids Engineering, 119*(3), 700-706. doi:10.1115/1.2819301

Lal, R., & Shukla, M. (2004). *Principles of soil physics*. Marcel Dekker; London : Taylor & Francis, New York.

Lao, H. W., Neeman, H. J., & Papavassiliou, D. V. (2004). A pore network model for the calculation of non-Darcy flow coefficients in fluid flow through porous media. *Chemical Engineering Communications, 191*(10), 1285-1322. doi:10.1080/00986440490464200

Lawrence, M., & Jiang, Y. (2017). Porosity, Pore Size Distribution, Micro-structure. In S. Amziane & F. Collet (Eds.), *Bio-aggregates Based Building Materials : State-of-the-Art Report of the RILEM Technical Committee 236-BBM* (pp. 39-71). Dordrecht: Springer Netherlands.

Lee, T. C., Kashyap, R. L., & Chu, C. N. (1994). Building Skeleton Models via 3-D Medial Surface Axis Thinning Algorithms. *CVGIP: Graphical Models and Image Processing, 56*(6), 462-478. doi:http://dx.doi.org/10.1006/cgip.1994.1042

Lee, Y. (2004). *Mass dispersion in intermittent laminar flow.* (PhD thesis), Univ. of Cincinnati, Cincinnati.

Lee, Y., & Buchberger, S. G. (2001). Estimation of Dispersion in Unsteady Random Flow Condition in Dead-End Pipes of Water Distribution System. *Bridging the Gap: Meeting the World's Water and Environmental Resources Challenges.*

Lemley, E. C., Papavassiliou, D. V., & Neeman, H. J. (2007). *Non-Darcy Flow Pore Network Simulation: Development and Validation of a 3D Model.* Paper presented at the ASME/JSME 2007 5th Joint Fluids Engineering Conference.

Leva, M. (1959). Fluidization. *New York: McGraw-Hill Book Co*.

Li, D., Svec, R. K., Engler, T. W., & Grigg, R. B. (2001). *Modeling and Simulation of the Wafer Non-Darcy Flow Experiments*. Paper presented at the SPE western regional meeting,SPE-68822-MS. Society of Petroleum Engineers.

Li, H., Ewoldt, R., & Olsen, M. G. (2005). Turbulent and transitional velocity measurements in a rectangular microchannel using microscopic particle image velocimetry. *Experimental Thermal and Fluid Science, 29*(4), 435-446. doi:https://doi.org/10.1016/j.expthermflusci.2004.06.001

Li, L., Peters, C. A., & Celia, M. A. (2006). Upscaling geochemical reaction rates using pore-scale network modeling. *Advances in Water Resources, 29*(9), 1351-1370. doi:https://doi.org/10.1016/j.advwatres.2005.10.011

Lighthill, M. J. (1966). Initial Development of Diffusion in Poiseuille Flow. *IMA Journal of Applied Mathematics, 2*(1), 97-108. doi:10.1093/imamat/2.1.97

Lindquist, E. (1933). On the flow of water through porous soil. *Proc., 1er Congres des Grands Barrages, Commission internationale des grands barrages, Stockholm, Sweden, 81–101*.

Lindquist, W. B., Lee, S.-M., Coker, D. A., Jones, K. W., & Spanne, P. (1996). Medial axis analysis of void structure in three-dimensional tomographic images of porous media. *Journal of Geophysical Research: Solid Earth, 101*(B4), 8297-8310. doi:10.1029/95JB03039

Lopez, X., Valvatne, P. H., & Blunt, M. J. (2003). Predictive network modeling of single-phase non-Newtonian flow in porous media. *Journal of Colloid and Interface Science, 264*(1), 256-265. doi:https://doi.org/10.1016/S0021-9797(03)00310-2

Ma, H., & Ruth, D. W. (1993). The microscopic analysis of high forchheimer number flow in porous media. *Transport in Porous Media, 13*(2), 139-160. doi:10.1007/bf00654407

Macdonald, I. F., El-Sayed, M. S., Mow, K., & Dullien, F. A. L. (1979). Flow through Porous Media-the Ergun Equation Revisited. *Industrial & Engineering Chemistry Fundamentals, 18*(3), 199-208. doi:10.1021/i160071a001

Macedo, H. H., Costa, U. M. S., & Almeida, M. P. (2001). Turbulent effects on fluid flow through disordered porous media. *Physica A: Statistical Mechanics and its Applications, 299*(3–4), 371-377. doi:http://dx.doi.org/10.1016/S0378-4371(01)00257-6

Maier, R. S., Kroll, D. M., Bernard, R. S., Howington, S. E., Peters, J. F., & Davis, H. T. (2000). Pore-scale simulation of dispersion. *Physics of Fluids, 12*(8), 2065-2079. doi:10.1063/1.870452

Marquardt, D. W. (1963). An Algorithm for Least-Squares Estimation of Nonlinear Parameters. *Journal of the Society for Industrial and Applied Mathematics, 11*(2), 431-441. doi:10.1137/0111030

Marry, V., & Rotenberg, B. (2015). Upscaling Strategies for Modeling Clay-Rock Properties. In C. Tournassat, C. I. Steefel, I. C. Bourg, & F. Bergaya (Eds.), *Developments in Clay Science* (Vol. 6, pp. 399-417): Elsevier.

Martins, A. A., Laranjeira, P. E., Lopes, J. C. B., & Dias, M. M. (2007). Network modeling of flow in a packed bed. *AIChE Journal, 53*(1), 91-107. doi:10.1002/aic.11047

Mason, G. (1967). General discussion. *Discussions of the Faraday Society, 43*(0), 75-88. doi:10.1039/DF9674300075

Mason, G. (1971). A model of the pore space in a random packing of equal spheres. *Journal of Colloid and Interface Science, 35*(2), 279-287. doi:http://dx.doi.org/10.1016/0021-9797(71)90121-4

Mason, G., & Morrow, N. R. (1991). Capillary behavior of a perfectly wetting liquid in irregular triangular tubes. *Journal of Colloid and Interface Science, 141*(1), 262-274. doi:http://dx.doi.org/10.1016/0021-9797(91)90321-X

Mehmani, Y. (2014). *Modeling single-phase flow and solute transport across scales.* (Ph.D. thesis), University of Texas Austin.

Mehmani, Y., Oostrom, M., & Balhoff, M. T. (2014). A streamline splitting pore-network approach for computationally inexpensive and accurate simulation of transport in porous media. *Water Resources Research, 50*(3), 2488-2517. doi:10.1002/2013WR014984

Meng, X., & Yang, D. (2017). Determination of dynamic dispersion coefficients for passive and reactive particles flowing in a circular tube. *Colloids and Surfaces A: Physicochemical and Engineering Aspects, 524*, 96-110. doi:https://doi.org/10.1016/j.colsurfa.2017.04.030

Middleton, R. S., Keating, G. N., Stauffer, P. H., Jordan, A. B., Viswanathan, H. S., Kang, Q. J., Carey, J. W., Mulkey, M. L., Sullivan, E. J., Chu, S. P., Esposito, R., & Meckel, T. A. (2012). The cross-scale science of CO2 capture and storage: from pore scale to regional scale. Energy & Environmental Science, 5(6), 7328-7345. doi:10.1039/C2EE03227A

Mobasheri, F., & Todd, D. K. (1963). Investigation of the hydraulics of flow near recharge wells. *Water Resources Center Contribution No. 72, University of California Berkeley, Berkeley, California.*

Mala, G. M., & Li, D. (1999). Flow characteristics of water in microtubes. *International Journal of Heat and Fluid Flow, 20*(2), 142-148. doi:https://doi.org/10.1016/S0142-727X(98)10043-7

Moin, P., & Mahesh, K. (1998). DIRECT NUMERICAL SIMULATION: A Tool in Turbulence Research. *Annual Review of Fluid Mechanics, 30*(1), 539-578. doi:10.1146/annurev.fluid.30.1.539

Momen, A. M., Sherif, S. A., & Lear, W. (2016). An Analytical-Numerical Model for Two-Phase Slug Flow through a Sudden Area Change in Microchannels. *Journal of Applied Fluid Mechanics, Vol. 9, No. 4, pp. 1839-1850.*

Moody, L. F. (1944). Friction Factors for Pipe Flow. *Transactions of the American Society of Mechanical Engineers, 66, 671-681*.

Moroni, M., & Cushman, J. H. (2001). Three-dimensional particle tracking velocimetry studies of the transition from pore dispersion to Fickian Dispersion for homogeneous porous media. *Water Resources Research, 37*(4), 873-884. doi:10.1029/2000WR900364

Mostaghimi, P. (2012). *Transport phenomena modelled on pore-space images.* (Ph.D. thesis), Department of Earth & Science Engineering, Imperial College, London.

Mostaghimi, P., Bijeljic, B., & Blunt, M. (2012). Simulation of Flow and Dispersion on Pore-Space Images. doi:10.2118/135261-PA

Muljadi, B. P., Blunt, M. J., Raeini, A. Q., & Bijeljic, B. (2015). The impact of porous media heterogeneity on non-Darcy flow behaviour from pore-scale simulation. *Advances in Water Resources*. doi:http://dx.doi.org/10.1016/j.advwatres.2015.05.019

Newman, M. S., & Yin, X. (2011). *The Effect of Pore Heterogeneity on Non-Darcy Flow by Lattice Boltzmann Simulation*. Paper presented

at the In: SPE 146689, presented at SPE Annual Technical Conference and Exhibition. Denver, Colorado, USA; October 30-November 2.

Nezhad, M. M., Rezania, M., & Baioni, E. (2019). Transport in Porous Media with Nonlinear Flow Condition. *Transport in Porous Media, 126*(1), 5-22. doi:10.1007/s11242-018-1173-4

Niven, R. K. (2002). Physical insight into the Ergun and Wen & Yu equations for fluid flow in packed and fluidised beds. *Chemical Engineering Science, 57*(3), 527-534. doi:http://dx.doi.org/10.1016/S0009-2509(01)00371-2

Nowak, W., Schwede, R. L., Cirpka, O. A., & Neuweiler, I. (2008). Probability density functions of hydraulic head and velocity in three-dimensional heterogeneous porous media. *Water Resources Research, 44*(8), W08452. doi:10.1029/2007WR006383

Ogata, A., & Banks, R. B. (1961). *A solution of the differential equation of longitudinal dispersion in porous media* (411A). Retrieved from http://pubs.er.usgs.gov/publication/pp411A

Olsen, M. G. (2008). Turbulence in Microchannels. In D. Li (Ed.), *Encyclopedia of Microfluidics and Nanofluidics* (pp. 2119-2125). Boston, MA: Springer US.

Oostrom, M., Mehmani, Y., Romero-Gomez, P., Tang, Y., Liu, H., Yoon, H., Kang, Q., Joekar-Niasar, V., Balhoff, M. T., Dewers, T., Tartakovsky, G. D., Leist, E. A., Hess, N. J., Perkins, W. A., Rakowski, C. L., Richmond, M. C., Serkowski, J. A., Werth, C. J., Valocchi, A. J., Wietsma, T. W., & Zhang, C. (2016). Pore-scale and continuum simulations of solute transport micromodel benchmark experiments. *Computational Geosciences, 20*(4), 857-879. doi:10.1007/s10596-014-9424-0

Oren, P. E., Bakke, S., & Arntzen, O. J. (1998). Extending Predictive Capabilities to Network Models. doi:10.2118/52052-PA

Orszag, S. A., & Patterson, G. S. (1972). Numerical Simulation of Three-Dimensional Homogeneous Isotropic Turbulence. *Physical Review Letters, 28*(2), 76-79. Retrieved from https://0-link-aps-org.pugwash.lib.warwick.ac.uk/doi/10.1103/PhysRevLett.28.76

Osher, S., & Fedkiw, R. (2003). *Level Set Methods and Dynamic Implicit Surfaces*: New York: Springer.

Osher, S., & Sethian, J. A. (1988). Fronts propagating with curvature-dependent speed: Algorithms based on Hamilton-Jacobi formulations. *Journal of Computational Physics, 79*(1), 12-49. doi:https://doi.org/10.1016/0021-9991(88)90002-2

Packman, A., Salehin, M., & Zaramella, M. (2004). Hyporheic Exchange with Gravel Beds: Basic Hydrodynamic Interactions and Bedform-Induced Advective Flows. *Journal of Hydraulic Engineering, 130*(7), 647-656. doi:10.1061/(ASCE)0733-9429(2004)130:7(647)

Pamuk, M. T., & Özdemir, M. (2012). Friction factor, permeability and inertial coefficient of oscillating flow through porous media of packed balls. *Experimental Thermal and Fluid Science, 38*, 134-139. doi:http://dx.doi.org/10.1016/j.expthermflusci.2011.12.002

Pan, C., Hilpert, M., & Miller, C. T. (2001). Pore-scale modeling of saturated permeabilities in random sphere packings. *Phys Rev E Stat Nonlin Soft Matter Phys, 64*(6 Pt 2), 066702. doi:10.1103/PhysRevE.64.066702

Pan, C., Hilpert, M., & Miller, C. T. (2004). Lattice-Boltzmann simulation of two-phase flow in porous media. *Water Resources Research, 40*(1), W01501. doi:10.1029/2003WR002120

Patzek, T. W., & Silin, D. B. (2001). Shape Factor and Hydraulic Conductance in Noncircular Capillaries. *Journal of Colloid and Interface Science, 236*(2), 295-304. doi:http://dx.doi.org/10.1006/jcis.2000.7413

Pedras, M. H. J., & de Lemos, M. J. S. (2000). On the definition of turbulent kinetic energy for flow in porous media. *International Communications in Heat and Mass Transfer, 27*(2), 211-220. doi:http://dx.doi.org/10.1016/S0735-1933(00)00102-0

Pedras, M. H. J., & de Lemos, M. J. S. (2001). On the Mathematical Description and Simulation of Turbulent Flow in a Porous Medium Formed by an Array of Elliptic Rods. *Journal of Fluids Engineering, 123*(4), 941-947. doi:10.1115/1.1413244

Peiyi, W., & Little, W. A. (1983). Measurement of friction factors for the flow of gases in very fine channels used for microminiature Joule-Thomson refrigerators. *Cryogenics, 23*(5), 273-277. doi:https://doi.org/10.1016/0011-2275(83)90150-9

Peng, X. F., Peterson, G. P., & Wang, B. X. (1994). Frictional flow characteristics of water flowing through rectangular microchannels. *Experimental Heat Transfer, 7*(4), 249-264. doi:10.1080/08916159408946484

Pfannkuch, H.-O. (1963). *Contribution à l'étude des déplacements de fluides miscibles dans un milieu poreux. Rev. Inst. Franc, du Petrole XVIII (2), 1–54.*

Piri, M., & Blunt, M. J. (2005). Three-dimensional mixed-wet random pore-scale network modeling of two- and three-phase flow in porous media. I. Model description. *Physical Review E, 71*(2), 026301. Retrieved from https://link.aps.org/doi/10.1103/PhysRevE.71.026301

Poinsot, T., Candel, S., & Trouvé, A. (1995). Applications of direct numerical simulation to premixed turbulent combustion. *Progress in Energy and Combustion Science, 21*(6), 531-576. doi:https://doi.org/10.1016/0360-1285(95)00011-9

Poiseuille, J. L. M. (1841). Recherches expérimentales sur le mouvement des liquides dans les tubes de très petits diamèstres. *Memoires*

Presentes par Divers Savants a l Academie Royal de l Institut de France,9: 433-544.

Prodanović, M., & Bryant, S. (2006). A level set method for determining critical curvatures for drainage and imbibition. *Journal of Colloid and Interface Science, 304*(2), 442-458. doi:http://dx.doi.org/10.1016/j.jcis.2006.08.048

Raeini, A. Q., Bijeljic, B., & Blunt, M. J. (2017). Generalized network modeling: Network extraction as a coarse-scale discretization of the void space of porous media. *Physical Review E, 96*(1), 013312. doi:10.1103/PhysRevE.96.013312

Raeini, A. Q., Bijeljic, B., & Blunt, M. J. (2018). Generalized network modeling of capillary-dominated two-phase flow. *Physical Review E, 97*(2), 023308. doi:10.1103/PhysRevE.97.023308

Raimondi, P., Gardner, G. H. F., & Petrick, C. B. (1959). Effect of pore structure and molecular diffusion on the mixing of miscible liquids flowing in porous media. *Amer. Inst. Chem. Eng. and Soc. Petrol. Eng. Joint Symp. Oil Recovery Methods, Sun Francisco. Preprint 43*.

Rands, C., Webb, B. W., & Maynes, D. (2006). Characterization of transition to turbulence in microchannels. *International Journal of Heat and Mass Transfer, 49*(17), 2924-2930. doi:https://doi.org/10.1016/j.ijheatmasstransfer.2006.02.032

Raoof, A., & Hassanizadeh, S. M. (2012). A new formulation for pore-network modeling of two-phase flow. *Water Resources Research, 48*(1), n/a-n/a. doi:10.1029/2010WR010180

Rennels, D. C., & Hudson, H. M. (2012). Incompressible Flow, *in Pipe Flow* (pp. 23-30): John Wiley & Sons, Inc., Hoboken, NJ, USA. doi: 10.1002/9781118275276.ch3.

Richardson, J. (2019). *Investigating a suitable characteristic length for demarcating flow regime boundaries for fluid flow through porous*

media. Individual research project report, School of Engineering, the University of Warwick.

Rifai, M. N. E., Kaufman, W. J., & Todd, D. K. (1956). Dispersion phenomena in laminar flow through porous media. *Sanitary Engineering Rep. No. 3, I.E.R., Series 90, University of California, Berkeley*.

Rogallo, R. S. (1981). Numerical experiments in homogeneous turbulence. *NASA Technical Memorandum B1315*.

Romero-Gomez, P., & Choi, C. Y. (2011). Axial Dispersion Coefficients in Laminar Flows of Water-Distribution Systems. *Journal of Hydraulic Engineering, 137*(11), 1500-1508. doi:doi:10.1061/(ASCE)HY.1943-7900.0000432

Ruth, D., & Ma, H. (1992). On the derivation of the Forchheimer equation by means of the averaging theorem. *Transport in Porous Media, 7*(3), 255-264. doi:10.1007/bf01063962

Ruth, D. W., & Ma, H. (1993). Numerical analysis of viscous, incompressible flow in a diverging-converging RUC. *Transport in Porous Media, 13*(2), 161-177. doi:10.1007/bf00654408

Sahimi, M. (2011a). Characterization of Pore Space Connectivity: Percolation Theory. In M. Sahimi (Ed.), *Flow and Transport in Porous Media and Fractured Rock* (pp. 15-37): Wiley-VCH Verlag GmbH & Co. KGaA.

Sahimi, M. (2011b). *Flow and Transport in Porous Media and Fractured Rock: From Classical Methods to Modern Approaches, Second Edition* (M. Sahimi Ed.): John Wiley and Sons.

Scheidegger, A. E. (1974). *The physics of flow through porous media*. Toronto; Buffalo [N.Y.]: University of Toronto Press.

Seymour, J. D., & Callaghan, P. T. (1997). Generalized approach to NMR analysis of flow and dispersion in porous media. *AIChE Journal, 43*(8), 2096-2111. doi:10.1002/aic.690430817

Shadloo, M. S., Oger, G., & Le Touzé, D. (2016). Smoothed particle hydrodynamics method for fluid flows, towards industrial applications: Motivations, current state, and challenges. *Computers & Fluids, 136*, 11-34. doi:https://doi.org/10.1016/j.compfluid.2016.05.029

Shah, R. K., & Bhatti, M. S. (1987). Laminar Convective Heat Transfer in Ducts. *Handbook of Single-Phase Convective Heat Transfer, Kakac, Shah and Aung, eds., John Wiley & Son, New York, pp. 3.1–3.3*.

Sharp, K. V., & Adrian, R. J. (2004). Transition from laminar to turbulent flow in liquid filled microtubes. *Experiments in Fluids, 36*(5), 741-747. doi:10.1007/s00348-003-0753-3

Shen, H. H., Cheng, A. H., Wang, K.-H., Teng, M. H., & Liu, C. C. (2002). *Environmental Fluid Mechanics: Theories and Applications* ASCE Publications.

Sittel, C. N., Threadgill, W. D., & Schnelle, K. B. (1968). Longitudinal Dispersion for Turbulent Flow in Pipes. *Industrial & Engineering Chemistry Fundamentals, 7*(1), 39-43. doi:10.1021/i160025a007

Sorbie, K. S., Clifford, P. J., & Jones, E. R. W. (1989). The rheology of pseudoplastic fluids in porous media using network modeling. *Journal of Colloid and Interface Science, 130*(2), 508-534. doi:https://doi.org/10.1016/0021-9797(89)90128-8

Sorbie, K. S., Parker, A., & Clifford, P. J. (1987). Experimental and Theoretical Study of Polymer Flow in Porous Media. *SPE Reservoir Engineering, 2*(03), 281-304. doi:10.2118/14231-PA

Stockmayer, W. H. (1943). Theory of Molecular Size Distribution and Gel Formation in Branched-Chain Polymers. *The Journal of Chemical Physics, 11*(2), 45-55. doi:10.1063/1.1723803

Stöhr, M. (2003). *Analysis of flow and transport in refractive index matched porous media (Ph.D. thesis).* University of Heidelberg, Heidelberg, Germany.

Sunada, D. K. (1965). Laminar and turbulent flow of water through homogeneous porous media. *PhD dissertation, University of California at Berkeley, Berkeley, California*.

Tartakovsky, A. M., Trask, N., Pan, K., Jones, B., Pan, W., & Williams, J. R. (2015). Smoothed particle hydrodynamics and its applications for multiphase flow and reactive transport in porous media. *Computational Geosciences,* 1-28. doi:10.1007/s10596-015-9468-9

Taylor, G. (1953). Dispersion of soluble matter in solvent flowing slowly through a tube. *Proceedings of the Royal Society of London. Series A. Mathematical and Physical Sciences, 219*(1137), 186-203. doi:10.1098/rspa.1953.0139

Taylor, G. (1954a). Conditions under which dispersion of a solute in a stream of solvent can be used to measure molecular diffusion. *Proceedings of the Royal Society of London. Series A. Mathematical and Physical Sciences, 225*(1163), 473. Retrieved from http://rspa.royalsocietypublishing.org/content/225/1163/473.abstract

Taylor, G. (1954b). The dispersion of matter in turbulent flow through a pipe. *Proceedings of the Royal Society of London. Series A. Mathematical and Physical Sciences, 223*(1155), 446-468. doi:doi:10.1098/rspa.1954.0130

Tek, M. R. (1957). Development of a Generalized Darcy Equation. *Journal of Petroleum Technology*. doi:10.2118/741-G

Thauvin, F., & Mohanty, K. K. (1998). Network Modeling of Non-Darcy Flow Through Porous Media. *Transport in Porous Media, 31*(1), 19-37. doi:10.1023/a:1006558926606

Theodoropoulou, M. A. (2007). Dispersion of Dissolved Contaminants in Groundwater: from Visualization Experiments to Macroscopic Simulation. *Water, Air, and Soil Pollution, 181*(1), 235-245. doi:10.1007/s11270-006-9296-6

Thompson, A. C. (1996). *Minkowski Geometry (Encyclopedia of Mathematics and its Applications)*. Cambridge: Cambridge University Press.

Toride, N., Leij, F. J., & Van Genuchten, M. T. (1995). *The CXTFIT Code for Estimating Transport Parameters from Laboratory Or Field Tracer Experiments: Version 2.0*: U.S. Salinity Laboratory.

Vafai, K., & Tien, C. L. (1981). Boundary and inertia effects on flow and heat transfer in porous media. *International Journal of Heat and Mass Transfer, 24*(2), 195-203. doi:http://dx.doi.org/10.1016/0017-9310(81)90027-2

Valvatne, P. H., & Blunt, M. J. (2004). Predictive pore-scale modeling of two-phase flow in mixed wet media. *Water Resources Research, 40*(7), W07406. doi:10.1029/2003WR002627

Valvatne, P. H., Piri, M., Lopez, X., & Blunt, M. J. (2005). Predictive Pore-Scale Modeling of Single and Multiphase Flow. *Transport in Porous Media, 58*(1), 23-41. doi:10.1007/s11242-004-5468-2

van der Zee, S. E. A. T. M., & Leijnse, A. (2013). Solute Transport in Soil. In M. C. H. Soriano (Ed.), *Soil Processes and Current Trends in Quality Assessment* (pp. Ch. 02). Rijeka: InTech.

Vedel, S., & Bruus, H. (2011). Transient Taylor–Aris dispersion for time-dependent flows in straight channels. *Journal of Fluid Mechanics, 691*, 95-122. doi:10.1017/jfm.2011.444

Vogel, H. J., & Roth, K. (2001). Quantitative morphology and network representation of soil pore structure. *Advances in Water Resources, 24*(3), 233-242. doi:https://doi.org/10.1016/S0309-1708(00)00055-5

Wang, S., Feng, Q., & Han, X. (2014). A Hybrid Analytical/Numerical Model for the Characterization of Preferential Flow Path with Non-Darcy Flow. *PLoS ONE, 8*(12), e83536. doi:10.1371/journal.pone.0083536

Wang, X., & Mohanty, K. K. (1999). Critical Condensate Saturation in Porous Media. *Journal of Colloid and Interface Science, 214*(2), 416-426. doi:https://doi.org/10.1006/jcis.1999.6223

Wang, X., Thauvin, F., & Mohanty, K. K. (1999). Non-Darcy flow through anisotropic porous media. *Chemical Engineering Science, 54*(12), 1859-1869. doi:http://dx.doi.org/10.1016/S0009-2509(99)00018-4

Wang, Z-B., Chen, R., Wang, H., Liao, Q., Zhu, X., & Li, S.-Z. (2016). An overview of smoothed particle hydrodynamics for simulating multiphase flow. *Applied Mathematical Modelling, 40*(23), 9625-9655. doi:https://doi.org/10.1016/j.apm.2016.06.030

Weilin, Q., Mala, G. M., & Dongqing, L. (2000). Pressure-driven water flows in trapezoidal silicon microchannels. *International Journal of Heat and Mass Transfer, 43*(3), 353-364. doi:https://doi.org/10.1016/S0017-9310(99)00148-9

Weisbach, J. (1845). Lehrbuch der Ingenieur- und Maschinen-Mechanik, Vol. 1. Theoretische Mechanik, Vieweg und Sohn, Braunschweig. 535 pages (in German).

Whitaker, S. (1996). The Forchheimer equation: A theoretical development. *Transport in Porous Media, 25*(1), 27-61. doi:10.1007/bf00141261

Whitaker, S. (1999). The Method of Volume Averaging (Vol. 13): Springer.

Wibel, W., & Ehrhard, P. (2009). Experiments on the Laminar/Turbulent Transition of Liquid Flows in Rectangular Microchannels. *Heat Transfer Engineering, 30*(1-2), 70-77. doi:10.1080/01457630802293449

Wierman, J. C. (1982). Percolation Theory. *Ann. Probab., 10*(3), 509-524. doi:10.1214/aop/1176993764

Wilkinson, D. (1984). Percolation model of immiscible displacement in the presence of buoyancy forces. *Physical Review A, 30*(1), 520-531. Retrieved from http://link.aps.org/doi/10.1103/PhysRevA.30.520

Winter, T. C., Harvey, J. W., Franke, O. L., & Alley, W. M. (1998). *Ground water and surface water; a single resource* (1139). Retrieved from http://pubs.er.usgs.gov/publication/cir1139

Wood, B. D. (2007). Inertial effects in dispersion in porous media. *Water Resources Research, 43*(12). doi:doi:10.1029/2006WR005790

Wood, B. D., Radakovich, K., & Golfier, F. (2007). Effective reaction at a fluid–solid interface: Applications to biotransformation in porous media. *Advances in Water Resources, 30*(6), 1630-1647. doi:https://doi.org/10.1016/j.advwatres.2006.05.032

Wu, H. Y., & Cheng, P. (2003). Friction factors in smooth trapezoidal silicon microchannels with different aspect ratios. *International Journal of Heat and Mass Transfer, 46*(14), 2519-2525. doi:https://doi.org/10.1016/S0017-9310(03)00106-6

Wu, J., Hu, D., Li, W., & Cai, X. I. N. (2016). A review on non-Darcy flow-Forchheimer equation, Hydraulic radius model, fractal model and experiment. *Fractals, 24*(02), 1630001. doi:10.1142/S0218348X16300014

Xiong, Q., Baychev, T. G., & Jivkov, A. P. (2016). Review of pore network modelling of porous media: Experimental characterisations, network constructions and applications to reactive transport. *Journal of Contaminant Hydrology, 192*, 101-117. doi:http://dx.doi.org/10.1016/j.jconhyd.2016.07.002

Xiong, Q., & Jivkov, A. P. (2015). Analysis of pore structure effects on diffusive transport in Opalinus clay via pore network models. *Mineralogical Magazine, 79*(6), 1369-1377. doi:10.1180/minmag.2015.079.6.12

Yanuka, M., Dullien, F. A. L., & Elrick, D. E. (1986). Percolation processes and porous media: I. Geometrical and topological model of porous media using a three-dimensional joint pore size distribution. *Journal of Colloid and Interface Science, 112*(1), 24-41. doi:https://doi.org/10.1016/0021-9797(86)90066-4

Zaretskiy, Y., Geiger, S., Sorbie, K., & Förster, M. (2010). Efficient flow and transport simulations in reconstructed 3D pore geometries. *Advances in Water Resources, 33*(12), 1508-1516. doi:http://dx.doi.org/10.1016/j.advwatres.2010.08.008

Zeighami, R., Laser, D., Zhou, P., Asheghi, M., Devasenathipathy, S., Kenny, T., Santiago, J., & Goodson, K. (2000, 23-26 May 2000). *Experimental investigation of flow transition in microchannels using micron-resolution particle image velocimetry.* Paper presented at the ITHERM 2000. The Seventh Intersociety Conference on Thermal and Thermomechanical Phenomena in Electronic Systems (Cat. No.00CH37069).

Zeng, Z., & Grigg, R. (2006). A Criterion for Non-Darcy Flow in Porous Media. *Transport in Porous Media, 63*(1), 57-69. doi:10.1007/s11242-005-2720-3

Zhang, J., & Xing, H. (2012). Numerical modeling of non-Darcy flow in near-well region of a geothermal reservoir. *Geothermics, 42*, 78-86. doi:https://doi.org/10.1016/j.geothermics.2011.11.002

Zheng, C., & Bennett, G. D. (2002). *Applied contaminant transport modeling* (2nd ed.): Wiley-Interscience, New York.

Zhi-qing, W. (1982). Study on correction coefficients of liminar and turbulent entrance region effect in round pipe. *Applied Mathematics and Mechanics, 3*(3), 433-446. doi:10.1007/bf01897224

Zimmerman, R. W., Al-Yaarubi, A., Pain, C. C., & Grattoni, C. A. (2004). Non-linear regimes of fluid flow in rock fractures. *International Journal of Rock Mechanics and Mining Sciences, 41*, 163-169. doi:https://doi.org/10.1016/j.ijrmms.2004.03.036

Appendices

Appendix A: Algorithm of the Non-Darcy flow regime PNM code

A-1. Code flow chart

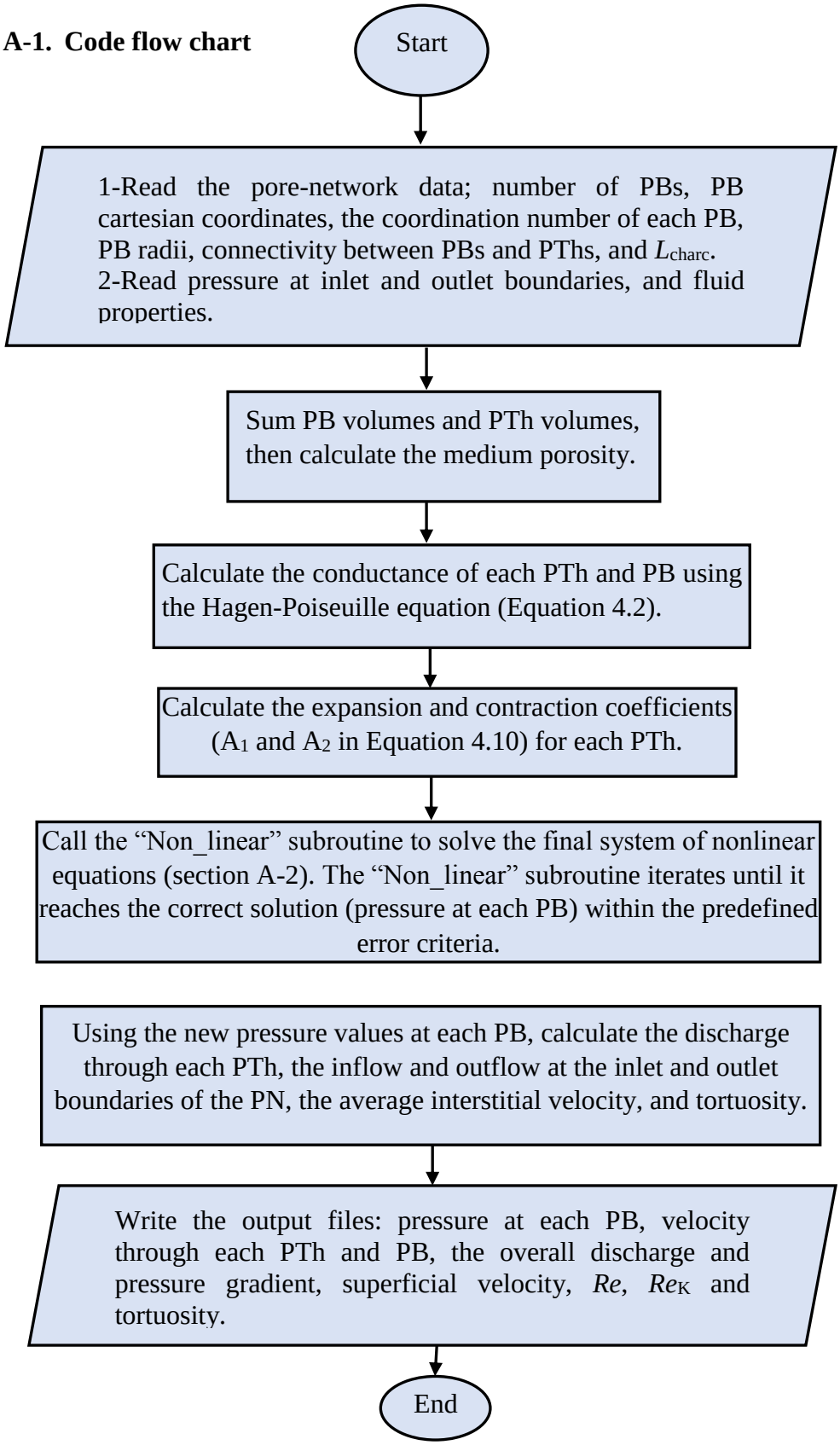

A-2. Solving the nonlinear system of equations

Assuming the following simple pore-network:

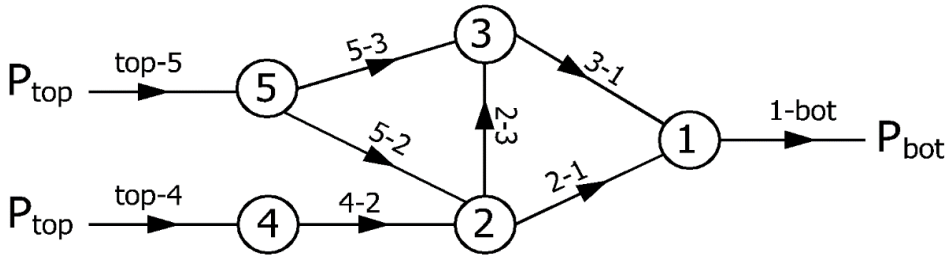

Figure 1A A simple example of a pore-network.

Starting from Equation 4.10:

$$A_1\, q_{\mathrm{i-j}}^2 + A_2\, q_{\mathrm{i-j}} + A_3 = 0.0 \qquad 4.10$$

where

$$A_1 = (K_e + K_c)\frac{\rho}{2a_{\mathrm{i-j}}^2},\ A_2 = \left[\frac{L_{\mathrm{i-j,tot}}}{g_{\mathrm{i-j,tot}}}\right],\ A_3 = -\Delta P_{\mathrm{i-j}}^{\mathrm{tot}}$$

$$q_{\mathrm{i-j}} = \frac{-A_2 + \sqrt{{A_2}^2 - 4A_1A_3}}{2A_1} \qquad 9.1$$

And by applying the continuity equation (Equation 4.11) at each node (pore body) in Figure 1A, the following system of equations can be obtained:

<u>At node 1:</u>

$\Sigma q_{i\text{-}j} = 0.0$

Then

$$q_{2-1} + q_{3-1} - q_{1-\mathrm{bot}} = 0.0$$

Then

$$\frac{-A_{2_{2-1}} + \sqrt{{A_{2_{2-1}}}^2 + 4(A_{1_{2-1}})\Delta P_{2-1}^{tot}}}{2(A_{1_{2-1}})} + \frac{-A_{2_{3-1}} + \sqrt{{A_{2_{3-1}}}^2 + 4(A_{1_{3-1}})\Delta P_{3-1}^{tot}}}{2(A_{1_{3-1}})} - \frac{-A_{2_{1-bot}} + \sqrt{{A_{2_{1-bot}}}^2 + 4(A_{1_{1-bot}})\Delta P_{1-bot}^{tot}}}{2(A_{1_{1-bot}})} = 0.0$$

Then

$$\frac{-A_{2_{2-1}} + \sqrt{{A_{2_{2-1}}}^2 + 4(A_{1_{2-1}})[P_2 - P_1]}}{2(A_{1_{2-1}})} + \frac{-A_{2_{3-1}} + \sqrt{{A_{2_{3-1}}}^2 + 4(A_{1_{3-1}})[P_3 - P_1]}}{2(A_{1_{3-1}})} - \frac{-A_{2_{1-bot}} + \sqrt{{A_{2_{1-bot}}}^2 + 4(A_{1_{1-bot}})[P_1 - P_{bot}]}}{2(A_{1_{1-bot}})} = 0.0$$

Then

$$\frac{-A_{2_{2-1}}+\sqrt{A_{2_{2-1}}{}^2+4(A_{1_{2-1}})[P_2-P_1]}}{2(A_{1_{2-1}})}+\frac{-A_{2_{3-1}}+\sqrt{A_{2_{3-1}}{}^2+4(A_{1_{3-1}})[P_3-P_1]}}{2(A_{1_{3-1}})}-$$
$$\frac{-A_{2_{1-bot}}+\sqrt{A_{2_{1-bot}}{}^2+4(A_{1_{1-bot}})[P_1-P_{bot}]}}{2(A_{1_{1-bot}})}+P_1-P_1=0.0 \quad 9.2$$

At node 2:

$$q_{4-2}+q_{5-2}-q_{2-3}-q_{2-1}=0.0$$

Then

$$\frac{-A_{2_{4-2}}+\sqrt{A_{2_{4-2}}{}^2+4(A_{1_{4-2}})[P_4-P_2]}}{2(A_{1_{4-2}})}+\frac{-A_{2_{5-2}}+\sqrt{A_{2_{5-2}}{}^2+4(A_{1_{5-2}})[P_5-P_2]}}{2(A_{1_{5-2}})}-$$
$$\frac{-A_{2_{2-3}}+\sqrt{A_{2_{2-3}}{}^2+4(A_{1_{2-3}})[P_2-P_3]}}{2(A_{1_{2-3}})}-\frac{-A_{2_{2-1}}+\sqrt{A_{2_{2-1}}{}^2+4(A_{1_{2-1}})[P_2-P_1]}}{2(A_{1_{2-1}})}=0.0$$

Then

$$\frac{-A_{2_{4-2}}+\sqrt{A_{2_{4-2}}{}^2+4(A_{1_{4-2}})[P_4-P_2]}}{2(A_{1_{4-2}})}+\frac{-A_{2_{5-2}}+\sqrt{A_{2_{5-2}}{}^2+4(A_{1_{5-2}})[P_5-P_2]}}{2(A_{1_{5-2}})}-$$
$$\frac{-A_{2_{2-3}}+\sqrt{A_{2_{2-3}}{}^2+4(A_{1_{2-3}})[P_2-P_3]}}{2(A_{1_{2-3}})}-\frac{-A_{2_{2-1}}+\sqrt{A_{2_{2-1}}{}^2+4(A_{1_{2-1}})[P_2-P_1]}}{2(A_{1_{2-1}})}+P_2-P_2=$$
0.0 9.3

At node 3:

$$q_{5-3}+q_{2-3}-q_{3-1}=0.0$$

Then

$$\frac{-A_{2_{5-3}}+\sqrt{A_{2_{5-3}}{}^2+4(A_{1_{5-3}})[P_5-P_3]}}{2(A_{1_{5-3}})}+\frac{-A_{2_{2-3}}+\sqrt{A_{2_{2-3}}{}^2+4(A_{1_{2-3}})[P_2-P_3]}}{2(A_{1_{2-3}})}-$$
$$\frac{-A_{2_{3-1}}+\sqrt{A_{2_{3-1}}{}^2+4(A_{1_{3-1}})[P_3-P_1]}}{2(A_{1_{3-1}})}=0.0$$

Then

$$\frac{-A_{2_{5-3}}+\sqrt{A_{2_{5-3}}{}^2+4(A_{1_{5-3}})[P_5-P_3]}}{2(A_{1_{5-3}})}+\frac{-A_{2_{2-3}}+\sqrt{A_{2_{2-3}}{}^2+4(A_{1_{2-3}})[P_2-P_3]}}{2(A_{1_{2-3}})}-$$
$$\frac{-A_{2_{3-1}}+\sqrt{A_{2_{3-1}}{}^2+4(A_{1_{3-1}})[P_3-P_1]}}{2(A_{1_{3-1}})}+P_3-P_3=0.0 \quad 9.4$$

At node 4:

$$q_{top-4}-q_{4-2}=0.0$$

Then

$$\frac{-A_{2_{top-4}}+\sqrt{A_{2_{top-4}}{}^2+4\left(A_{1_{top-4}}\right)[P_{top}-P_4]}}{2\left(A_{1_{top-4}}\right)}-\frac{-A_{2_{4-2}}+\sqrt{A_{2_{4-2}}{}^2+4\left(A_{1_{4-2}}\right)[P_4-P_2]}}{2\left(A_{1_{4-2}}\right)}=$$

0.0

Then

$$\frac{-A_{2_{top-4}}+\sqrt{A_{2_{top-4}}{}^2+4\left(A_{1_{top-4}}\right)[P_{top}-P_4]}}{2\left(A_{1_{top-4}}\right)}-\frac{-A_{2_{4-2}}+\sqrt{A_{2_{4-2}}{}^2+4\left(A_{1_{4-2}}\right)[P_4-P_2]}}{2\left(A_{1_{4-2}}\right)}+$$

$P_4 - P_4 = 0.0$ 9.5

<u>At node 5:</u>

$q_{top-5} - q_{5-3} - q_{5-2} = 0.0$

Then

$$\frac{-A_{2_{top-5}}+\sqrt{A_{2_{top-5}}{}^2+4\left(A_{1_{top-5}}\right)[P_{top}-P_5]}}{2\left(A_{1_{top-5}}\right)}-\frac{-A_{2_{5-3}}+\sqrt{A_{2_{5-3}}{}^2+4\left(A_{1_{5-3}}\right)[P_5-P_3]}}{2\left(A_{1_{5-3}}\right)}-$$

$$\frac{-A_{2_{5-2}}+\sqrt{A_{2_{5-2}}{}^2+4\left(A_{1_{5-2}}\right)[P_5-P_2]}}{2\left(A_{1_{5-2}}\right)}=0.0$$

Then

$$\frac{-A_{2_{top-5}}+\sqrt{A_{2_{top-5}}{}^2+4\left(A_{1_{top-5}}\right)[P_{top}-P_5]}}{2\left(A_{1_{top-5}}\right)}-\frac{-A_{2_{5-3}}+\sqrt{A_{2_{5-3}}{}^2+4\left(A_{1_{5-3}}\right)[P_5-P_3]}}{2\left(A_{1_{5-3}}\right)}-$$

$$\frac{-A_{2_{5-2}}+\sqrt{A_{2_{5-2}}{}^2+4\left(A_{1_{5-2}}\right)[P_5-P_2]}}{2\left(A_{1_{5-2}}\right)}+P_5-P_5=0.0$$ 9.6

The final five equations (9.2, 9.3, 9.4, 9.5 and 9.6) can be written in the form required by the of HSL NS23 routine (HSL, 2013), used to solve a system of nonlinear equations in FORTRAN, as follows:

$$\frac{-A_{2_{2-1}}+\sqrt{A_{2_{2-1}}{}^2+4(A_{1_{2-1}})[P_2-P_1]}}{2(A_{1_{2-1}})}+\frac{-A_{2_{3-1}}+\sqrt{A_{2_{3-1}}{}^2+4(A_{1_{3-1}})[P_3-P_1]}}{2(A_{1_{3-1}})}-$$

$$\frac{-A_{2_{1-bot}}+\sqrt{A_{2_{1-bot}}{}^2+4(A_{1_{1-bot}})[P_1-P_{bot}]}}{2(A_{1_{1-bot}})}+P_1-P_1=F_1(P_1,P_2,P_3)-P_1=0$$ 9.2`

where $F_1(P_1,P_2,P_3)=\frac{-A_{2_{2-1}}+\sqrt{A_{2_{2-1}}{}^2+4(A_{1_{2-1}})[P_2-P_1]}}{2(A_{1_{2-1}})}+$

$$\frac{-A_{2_{3-1}}+\sqrt{A_{2_{3-1}}{}^2+4(A_{1_{3-1}})[P_3-P_1]}}{2(A_{1_{3-1}})}-\frac{-A_{2_{1-bot}}+\sqrt{A_{2_{1-bot}}{}^2+4(A_{1_{1-bot}})[P_1-P_{bot}]}}{2(A_{1_{1-bot}})}+P_1$$

And

$$\frac{-A_{2_{4-2}}+\sqrt{{A_{2_{4-2}}}^2+4(A_{1_{4-2}})[P_4-P_2]}}{2(A_{1_{4-2}})}+\frac{-A_{2_{5-2}}+\sqrt{{A_{2_{5-2}}}^2+4(A_{1_{5-2}})[P_5-P_2]}}{2(A_{1_{5-2}})}-$$
$$\frac{-A_{2_{2-3}}+\sqrt{{A_{2_{2-3}}}^2+4(A_{1_{2-3}})[P_2-P_3]}}{2(A_{1_{2-3}})}-\frac{-A_{2_{2-1}}+\sqrt{{A_{2_{2-1}}}^2+4(A_{1_{2-1}})[P_2-P_1]}}{2(A_{1_{2-1}})}+P_2\ -$$
$$P_2=F_2(P_1,P_2,P_3,P_4,P_5)-P_2=0.0 \qquad 9.3`$$

And

$$\frac{-A_{2_{5-3}}+\sqrt{{A_{2_{5-3}}}^2+4(A_{1_{5-3}})[P_5-P_3]}}{2(A_{1_{5-3}})}+\frac{-A_{2_{2-3}}+\sqrt{{A_{2_{2-3}}}^2+4(A_{1_{2-3}})[P_2-P_3]}}{2(A_{1_{2-3}})}-$$
$$\frac{-A_{2_{3-1}}+\sqrt{{A_{2_{3-1}}}^2+4(A_{1_{3-1}})[P_3-P_1]}}{2(A_{1_{3-1}})}+P_3-P_3=F_3(P_1,P_2,P_3,P_5)-P_3=0.0 \qquad 9.4`$$

And

$$\frac{-A_{2_{top-4}}+\sqrt{{A_{2_{top-4}}}^2+4\left(A_{1_{top-4}}\right)[P_{top}-P_4]}}{2\left(A_{1_{top-4}}\right)}-\frac{-A_{2_{4-2}}+\sqrt{{A_{2_{4-2}}}^2+4(A_{1_{4-2}})[P_4-P_2]}}{2(A_{1_{4-2}})}+$$
$$P_4-P_4=F_4(P_2,P_4)-P_4=0 \qquad 9.5`$$

And

$$\frac{-A_{2_{top-5}}+\sqrt{{A_{2_{top-5}}}^2+4\left(A_{1_{top-5}}\right)[P_{top}-P_5]}}{2\left(A_{1_{top-5}}\right)}-\frac{-A_{2_{5-3}}+\sqrt{{A_{2_{5-3}}}^2+4(A_{1_{5-3}})[P_5-P_3]}}{2(A_{1_{5-3}})}-$$
$$\frac{-A_{2_{5-2}}+\sqrt{{A_{2_{5-2}}}^2+4(A_{1_{5-2}})[P_5-P_2]}}{2(A_{1_{5-2}})}+P_5-P_5=F_5(P_2,P_3,P_5)-P_5=0 \qquad 9.6`$$

The HSL NS23 routine (HSL, 2013), requires nonzero derivatives of each equation (the Jacobian matrix) as shown below:

$$\frac{\partial F_i}{\partial P_j} = \begin{bmatrix} \frac{\partial F_1}{\partial P_1} & \frac{\partial F_1}{\partial P_2} & \frac{\partial F_1}{\partial P_3} & \frac{\partial F_1}{\partial P_4} & \frac{\partial F_1}{\partial P_5} \\ \frac{\partial F_2}{\partial P_1} & \frac{\partial F_2}{\partial P_2} & \frac{\partial F_2}{\partial P_3} & \frac{\partial F_2}{\partial P_4} & \frac{\partial F_2}{\partial P_5} \\ \frac{\partial F_3}{\partial P_1} & \frac{\partial F_3}{\partial P_2} & \frac{\partial F_3}{\partial P_3} & \frac{\partial F_3}{\partial P_4} & \frac{\partial F_3}{\partial P_5} \\ \frac{\partial F_4}{\partial P_1} & \frac{\partial F_4}{\partial P_2} & \frac{\partial F_4}{\partial P_3} & \frac{\partial F_4}{\partial P_4} & \frac{\partial F_4}{\partial P_5} \\ \frac{\partial F_5}{\partial P_1} & \frac{\partial F_5}{\partial P_2} & \frac{\partial F_5}{\partial P_3} & \frac{\partial F_5}{\partial P_4} & \frac{\partial F_5}{\partial P_5} \end{bmatrix}$$

$$= \begin{bmatrix} \frac{\partial F_1}{\partial P_1} & \frac{\partial F_1}{\partial P_2} & \frac{\partial F_1}{\partial P_3} & 0 & 0 \\ \frac{\partial F_2}{\partial P_1} & \frac{\partial F_2}{\partial P_2} & \frac{\partial F_2}{\partial P_3} & \frac{\partial F_2}{\partial P_4} & \frac{\partial F_2}{\partial P_5} \\ \frac{\partial F_3}{\partial P_1} & \frac{\partial F_3}{\partial P_2} & \frac{\partial F_3}{\partial P_3} & 0 & \frac{\partial F_3}{\partial P_5} \\ 0 & \frac{\partial F_4}{\partial P_2} & 0 & \frac{\partial F_4}{\partial P_4} & 0 \\ 0 & \frac{\partial F_5}{\partial P_2} & \frac{\partial F_5}{\partial P_3} & 0 & \frac{\partial F_5}{\partial P_5} \end{bmatrix}$$

$$F_1(P_1, P_2, P_3) = \frac{-A_{2_{2-1}} + \sqrt{A_{2_{2-1}}{}^2 + 4(A_{1_{2-1}})[P_2 - P_1]}}{2(A_{1_{2-1}})} +$$

$$\frac{-A_{2_{3-1}} + \sqrt{A_{2_{3-1}}{}^2 + 4(A_{1_{3-1}})[P_3 - P_1]}}{2(A_{1_{3-1}})} - \frac{-A_{2_{1-bot}} + \sqrt{A_{2_{1-bot}}{}^2 + 4(A_{1_{1-bot}})[P_1 - P_{bot}]}}{2(A_{1_{1-bot}})} +$$

$P_1 = 0.0$

Then

$$\frac{\partial F_1(P_1,P_2,P_3)}{\partial P_1} = \frac{\partial}{\partial P_1}\left[\frac{-A_{2_{2-1}} + \sqrt{A_{2_{2-1}}{}^2 + 4(A_{1_{2-1}})[P_2 - P_1]}}{2(A_{1_{2-1}})} +\right.$$

$$\left.\frac{-A_{2_{3-1}} + \sqrt{A_{2_{3-1}}{}^2 + 4(A_{1_{3-1}})[P_3 - P_1]}}{2(A_{1_{3-1}})} - \frac{-A_{2_{1-bot}} + \sqrt{A_{2_{1-bot}}{}^2 + 4(A_{1_{1-bot}})[P_1 - P_{bot}]}}{2(A_{1_{1-bot}})}\right] +$$

$$\frac{\partial}{\partial P_1} P_1 = -\frac{1}{\sqrt{A_{2_{2-1}}{}^2 + 4(A_{1_{2-1}})[P_2 - P_1]}} - \frac{1}{\sqrt{A_{2_{3-1}}{}^2 + 4(A_{1_{3-1}})[P_3 - P_1]}} -$$

$$\frac{1}{\sqrt{A_{2_{1-bot}}{}^2 + 4(A_{1_{1-bot}})[P_1 - P_{bot}]}} + 1$$

and

$$\frac{\partial F_1(P_1,P_2,P_3)}{\partial P_2} = \frac{\partial}{\partial P_2}\left[\frac{-A_{2_{2-1}}+\sqrt{A_{2_{2-1}}{}^2+4(A_{1_{2-1}})[P_2-P_1]}}{2(A_{1_{2-1}})}\right] = \frac{1}{\sqrt{A_{2_{2-1}}{}^2+4(A_{1_{2-1}})[P_2-P_1]}}$$

and

$$\frac{\partial F_1(P_1,P_2,P_3)}{\partial P_3} = \frac{\partial}{\partial P_3}\left[\frac{-A_{2_{3-1}}+\sqrt{A_{2_{3-1}}{}^2+4(A_{1_{3-1}})[P_3-P_1]}}{2(A_{1_{3-1}})}\right] = \frac{1}{\sqrt{A_{2_{3-1}}{}^2+4(A_{1_{3-1}})[P_3-P_1]}}$$

$$F_2(P_1,P_2,P_3,P_4,P_5) = \frac{-A_{2_{4-2}}+\sqrt{A_{2_{4-2}}{}^2+4(A_{1_{4-2}})[P_4-P_2]}}{2(A_{1_{4-2}})} + \frac{-A_{2_{5-2}}+\sqrt{A_{2_{5-2}}{}^2+4(A_{1_{5-2}})[P_5-P_2]}}{2(A_{1_{5-2}})} - \frac{-A_{2_{2-3}}+\sqrt{A_{2_{2-3}}{}^2+4(A_{1_{2-3}})[P_2-P_3]}}{2(A_{1_{2-3}})} - \frac{-A_{2_{2-1}}+\sqrt{A_{2_{2-1}}{}^2+4(A_{1_{2-1}})[P_2-P_1]}}{2(A_{1_{2-1}})} + P_2 = 0.0$$

then

$$\frac{\partial F_2(P_1,P_2,P_3,P_4,P_5)}{\partial P_1} = \frac{\partial}{\partial P_1}\left[-\frac{-A_{2_{2-1}}+\sqrt{A_{2_{2-1}}{}^2+4(A_{1_{2-1}})[P_2-P_1]}}{2(A_{1_{2-1}})}\right] = \frac{1}{\sqrt{A_{2_{2-1}}{}^2+4(A_{1_{2-1}})[P_2-P_1]}}$$

and

$$\frac{\partial F_2(P_1,P_2,P_3,P_4,P_5)}{\partial P_2} = \frac{\partial}{\partial P_2}\left[\frac{-A_{2_{4-2}}+\sqrt{A_{2_{4-2}}{}^2+4(A_{1_{4-2}})[P_4-P_2]}}{2(A_{1_{4-2}})} + \frac{-A_{2_{5-2}}+\sqrt{A_{2_{5-2}}{}^2+4(A_{1_{5-2}})[P_5-P_2]}}{2(A_{1_{5-2}})} - \frac{-A_{2_{2-3}}+\sqrt{A_{2_{2-3}}{}^2+4(A_{1_{2-3}})[P_2-P_3]}}{2(A_{1_{2-3}})} - \frac{-A_{2_{2-1}}+\sqrt{A_{2_{2-1}}{}^2+4(A_{1_{2-1}})[P_2-P_1]}}{2(A_{1_{2-1}})} + P_2\right] = -\frac{1}{\sqrt{A_{2_{4-2}}{}^2+4(A_{1_{4-2}})[P_4-P_2]}} - \frac{1}{\sqrt{A_{2_{5-2}}{}^2+4(A_{1_{5-2}})[P_5-P_2]}} - \frac{1}{\sqrt{A_{2_{2-3}}{}^2+4(A_{1_{2-3}})[P_2-P_3]}} - \frac{1}{\sqrt{A_{2_{2-1}}{}^2+4(A_{1_{2-1}})[P_2-P_1]}} + 1$$

and

$$\frac{\partial F_2(P_1,P_2,P_3,P_4,P_5)}{\partial P_3} = \frac{\partial}{\partial P_3}\left[-\frac{-A_{2_{2-3}}+\sqrt{A_{2_{2-3}}{}^2+4(A_{1_{2-3}})[P_2-P_3]}}{2(A_{1_{2-3}})}\right] = \frac{1}{\sqrt{A_{2_{2-3}}{}^2+4(A_{1_{2-3}})[P_2-P_3]}}$$

and

$$\frac{\partial F_2(P_1,P_2,P_3,P_4,P_5)}{\partial P_4} = \frac{\partial}{\partial P_4}\left[\frac{-A_{2_{4-2}}+\sqrt{A_{2_{4-2}}{}^2+4(A_{1_{4-2}})[P_4-P_2]}}{2(A_{1_{4-2}})}\right] = \frac{1}{\sqrt{A_{2_{4-2}}{}^2+4(A_{1_{4-2}})[P_4-P_2]}}$$

and

$$\frac{\partial F_2(P_1,P_2,P_3,P_4,P_5)}{\partial P_5} = \frac{\partial}{\partial P_5}\left[\frac{-A_{2_{5-2}}+\sqrt{A_{2_{5-2}}{}^2+4(A_{1_{5-2}})[P_5-P_2]}}{2(A_{1_{5-2}})}\right] = \frac{1}{\sqrt{A_{2_{5-2}}{}^2+4(A_{1_{5-2}})[P_5-P_2]}}$$

$$F_3(P_1,P_2,P_3,P_5) = \frac{-A_{2_{5-3}}+\sqrt{A_{2_{5-3}}{}^2+4(A_{1_{5-3}})[P_5-P_3]}}{2(A_{1_{5-3}})} + \frac{-A_{2_{2-3}}+\sqrt{A_{2_{2-3}}{}^2+4(A_{1_{2-3}})[P_2-P_3]}}{2(A_{1_{2-3}})} - \frac{-A_{2_{3-1}}+\sqrt{A_{2_{3-1}}{}^2+4(A_{1_{3-1}})[P_3-P_1]}}{2(A_{1_{3-1}})} + P_3$$

then

$$\frac{\partial F_3(P_1,P_2,P_3,P_5)}{\partial P_1} = \frac{\partial}{\partial P_1}\left[-\frac{-A_{2_{3-1}}+\sqrt{A_{2_{3-1}}{}^2+4(A_{1_{3-1}})[P_3-P_1]}}{2(A_{1_{3-1}})}\right] = \frac{1}{\sqrt{A_{2_{3-1}}{}^2+4(A_{1_{3-1}})[P_3-P_1]}}$$

and

$$\frac{\partial F_3(P_1,P_2,P_3,P_5)}{\partial P_2} = \frac{\partial}{\partial P_2}\left[\frac{-A_{2_{2-3}}+\sqrt{A_{2_{2-3}}{}^2+4(A_{1_{2-3}})[P_2-P_3]}}{2(A_{1_{2-3}})}\right] = \frac{1}{\sqrt{A_{2_{2-3}}{}^2+4(A_{1_{2-3}})[P_2-P_3]}}$$

and

$$\frac{\partial F_3(P_1,P_2,P_3,P_5)}{\partial P_3} = \frac{\partial}{\partial P_3}\left[\frac{-A_{2_{5-3}}+\sqrt{A_{2_{5-3}}{}^2+4(A_{1_{5-3}})[P_5-P_3]}}{2(A_{1_{5-3}})}+\right.$$
$$\left.\frac{-A_{2_{2-3}}+\sqrt{A_{2_{2-3}}{}^2+4(A_{1_{2-3}})[P_2-P_3]}}{2(A_{1_{2-3}})}-\frac{-A_{2_{3-1}}+\sqrt{A_{2_{3-1}}{}^2+4(A_{1_{3-1}})[P_3-P_1]}}{2(A_{1_{3-1}})}+P3\right] =$$
$$-\frac{1}{\sqrt{A_{2_{5-3}}{}^2+4(A_{1_{5-3}})[P_5-P_3]}}-\frac{1}{\sqrt{A_{2_{2-3}}{}^2+4(A_{1_{2-3}})[P_2-P_3]}}-$$
$$\frac{1}{\sqrt{A_{2_{3-1}}{}^2+4(A_{1_{3-1}})[P_3-P_1]}}+1$$

and

$$\frac{\partial F_3(P_1,P_2,P_3,P_5)}{\partial P_5} = \frac{\partial}{\partial P_5}\left[\frac{-A_{2_{5-3}}+\sqrt{A_{2_{5-3}}{}^2+4(A_{1_{5-3}})[P_5-P_3]}}{2(A_{1_{5-3}})}\right] =$$
$$\frac{1}{\sqrt{A_{2_{5-3}}{}^2+4(A_{1_{5-3}})[P_5-P_3]}}$$

$$F_4(P_2,P_4) = \frac{-A_{2_{top-4}}+\sqrt{A_{2_{top-4}}{}^2+4\left(A_{1_{top-4}}\right)[P_{top}-P_4]}}{2\left(A_{1_{top-4}}\right)}-$$
$$\frac{-A_{2_{4-2}}+\sqrt{A_{2_{4-2}}{}^2+4(A_{1_{4-2}})[P_4-P_2]}}{2(A_{1_{4-2}})}+P_4=0.0$$

then

$$\frac{\partial F_4(P_2,P_4)}{\partial P_2} = \frac{\partial}{\partial P_2}\left[-\frac{-A_{2_{4-2}}+\sqrt{A_{2_{4-2}}{}^2+4(A_{1_{4-2}})[P_4-P_2]}}{2(A_{1_{4-2}})}\right] = \frac{1}{\sqrt{A_{2_{4-2}}{}^2+4(A_{1_{4-2}})[P_4-P_2]}}$$

and

$$\frac{\partial F_4(P_2,P_4)}{\partial P_4} = \frac{\partial}{\partial P_4}\left[\frac{-A_{2_{top-4}}+\sqrt{A_{2_{top-4}}{}^2+4\left(A_{1_{top-4}}\right)[P_{top}-P_4]}}{2\left(A_{1_{top-4}}\right)}-\right.$$
$$\left.\frac{-A_{2_{4-2}}+\sqrt{A_{2_{4-2}}{}^2+4(A_{1_{4-2}})[P_4-P_2]}}{2(A_{1_{4-2}})}+P_4\right] = -\frac{1}{\sqrt{A_{2_{top-4}}{}^2+4\left(A_{1_{top-4}}\right)[P_{top}-P_4]}}-$$
$$\frac{1}{\sqrt{A_{2_{4-2}}{}^2+4(A_{1_{4-2}})[P_4-P_2]}}+1$$

$$F_5(P_2,P_3,P_5) = \frac{-A_{2_{top-5}}+\sqrt{A_{2_{top-5}}{}^2+4\left(A_{1_{top-5}}\right)[P_{top}-P_5]}}{2\left(A_{1_{top-5}}\right)}-$$
$$\frac{-A_{2_{5-3}}+\sqrt{A_{2_{5-3}}{}^2+4(A_{1_{5-3}})[P_5-P_3]}}{2(A_{1_{5-3}})}-\frac{-A_{2_{5-2}}+\sqrt{A_{2_{5-2}}{}^2+4(A_{1_{5-2}})[P_5-P_2]}}{2(A_{1_{5-2}})}+P_5$$

then

$$\frac{\partial_5(P_2,P_3,P_5)}{\partial P_2} = \frac{\partial}{\partial P_2}\left[-\frac{-A_{2_{5-2}}+\sqrt{A_{2_{5-2}}{}^2+4(A_{1_{5-2}})[P_5-P_2]}}{2(A_{1_{5-2}})}\right] =$$

$$\frac{1}{\sqrt{A_{2_{5-2}}{}^2+4(A_{1_{5-2}})[P_5-P_2]}}$$

and

$$\frac{\partial F_5(P_2,P_3,P_5)}{\partial P_3} = \frac{\partial}{\partial P_3}\left[-\frac{-A_{2_{5-3}}+\sqrt{A_{2_{5-3}}{}^2+4(A_{1_{5-3}})[P_5-P_3]}}{2(A_{1_{5-3}})}\right] =$$

$$\frac{1}{\sqrt{A_{2_{5-3}}{}^2+4(A_{1_{5-3}})[P_5-P_3]}}$$

and

$$\frac{\partial F_5(P_2,P_3,P_5)}{\partial P_5} = \frac{\partial}{\partial P_5}\left[\frac{-A_{2_{top-5}}+\sqrt{A_{2_{top-5}}{}^2+4\left(A_{1_{top-5}}\right)[P_{top}-P_5]}}{2\left(A_{1_{top-5}}\right)} - \right.$$

$$\left.\frac{-A_{2_{5-3}}+\sqrt{A_{2_{5-3}}{}^2+4(A_{1_{5-3}})[P_5-P_3]}}{2(A_{1_{5-3}})} - \frac{-A_{2_{5-2}}+\sqrt{A_{2_{5-2}}{}^2+4(A_{1_{5-2}})[P_5-P_2]}}{2(A_{1_{5-2}})} + P_5\right] =$$

$$-\frac{1}{\sqrt{A_{2_{top-5}}{}^2+4\left(A_{1_{top-5}}\right)[P_{top}-P_5]}} - \frac{1}{\sqrt{A_{2_{5-3}}{}^2+4(A_{1_{5-3}})[P_5-P_3]}} -$$

$$\frac{1}{\sqrt{A_{2_{5-2}}{}^2+4(A_{1_{5-2}})[P_5-P_2]}} + 1$$

After providing the previous equations and derivatives to the HSL NS23 routine (HSL, 2013), the HSL NS23 routine iterates until the correct solution of each equation is achieved. Then the pressure value at each PB (i.e. $\boldsymbol{P_1}, \boldsymbol{P_2}, \ldots, \boldsymbol{P_N}$) is the output of the HSL NS23 routine.

A-3. Semi-variograms of pore body radii and pore body coordination numbers for Beadpack, Bentheimer, Estaillades, packed spheres and Berea samples.

A semi-variogram describes how data are correlated with distance. The semi-variogram function, $\gamma(h)$, represents half of the average squared difference between a group of points (in pairs) separated by a distance (h), and is given by

$$\gamma(h) = \frac{1}{2|N(h)|}\sum_{N(h)}\left(Z_i - Z_j\right)^2 \qquad 9.7$$

where $N(h)$ is the number of point pairs (i and j) separated by a distance h. Z_i and Z_j are the data values at the location of points i and j.

In the following figures, semi-variograms are presented for pore body radii and pore body coordination numbers. Because the five samples (beadpack, Bentheimer, Estaillades, packed spheres and Berea) are different in size and characteristics, in both figures, the separation distance (h) of each sample is normalized by the maximum separation distance. While $\gamma(h)$ is normalized by the mean value of the data presented for each sample. The figures show that Estaillades is the most heterogeneous sample as the variations of pore body radii and coordination numbers increase when the separation distance between pore bodies increases. The variation in $\gamma(h)$ for Estaillades is larger compared to the other four samples.

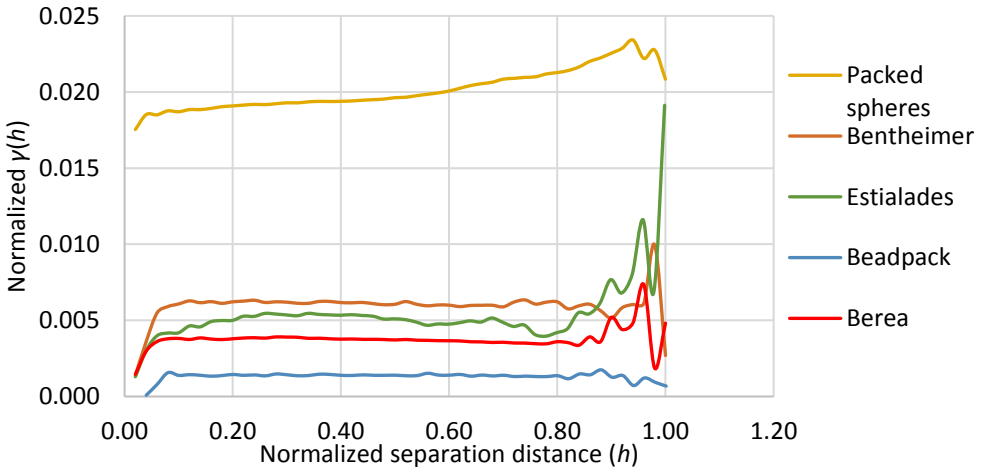

Figure 2A Pore body radii semi-variograms.

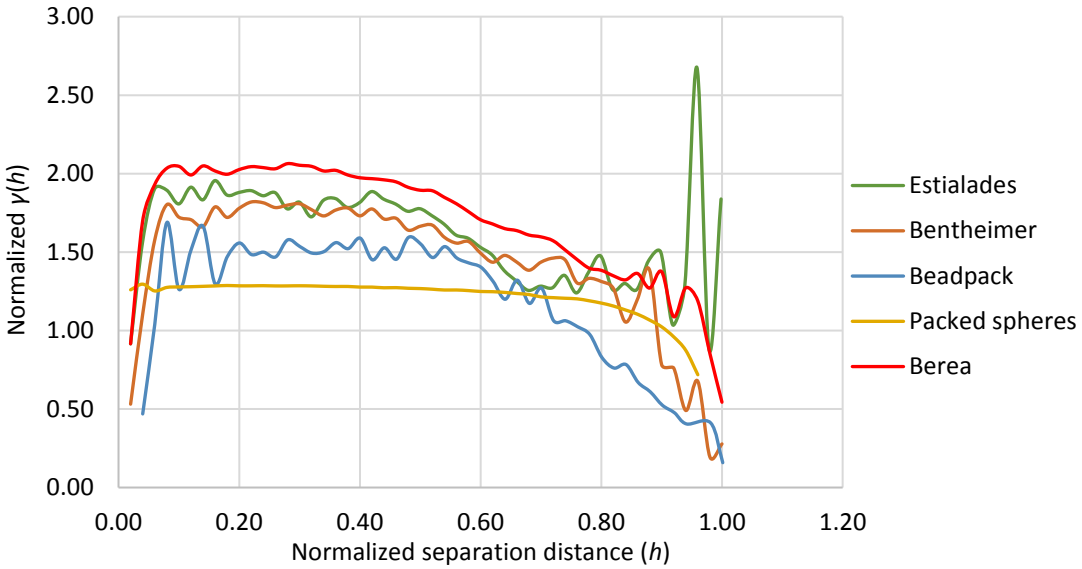

Figure 3A Pore body coordination numbers semi-variograms.

A-4. The developed FORTRAN code

Main code:

```
program pore_tubes
implicit none
integer:: step,porebody_vol_index,
Non_Zero_deriv,non_zero_deriv_bot,non_zero_deriv_top
Real:: KK,KK_F,BB, max_h,dh,dh_upper,dh_lower
real::deltaStep,diffusion, sum_1, sum_2, sum_3
integer::n_pore, m_throat,max_coord
integer::n_bot, n_top
real, dimension(:,:), allocatable::pb_coordinates, h,
gamma_h,gamma_h_2
integer, dimension(:), allocatable::bndry_pores,exclude
real::deltaZ,network_length, r_eff, charc_L
real,dimension (:),allocatable::L,PB_shp,PTh_shp,PB_vol, PTh_vol,
PTh_length_c2c, g_PTh, g_tot,A_PB,A_PTh,HA_A_PTh,A_Kw_tot
real,dimension (:),allocatable::R ,R_2
real,dimension(:),allocatable:: D,poreunit
real,dimension(:),allocatable:: Velocity, VELOCITY_2, VELOCITY_3,
VELOCITY_4, VELOCITY_5, VELOCITY_x,
VELOCITY_2_x,VELOCITY_3_x,VELOCITY_4_x,VELOCITY_5_x,theta
real,dimension(:,:),allocatable:: PB_Velocity, PB_length, g_PB
real,dimension(:),allocatable:: max_nod_velocity
integer,dimension(:),allocatable:: out_nod
real,dimension(:),allocatable:: Concent
real,dimension(:),allocatable:: Concent_old
real:: cross_section, min_x, max_x, max_y,max_z
real:: alpha
real::nrpowr
real::Vthroat
real::Vpore
real::Vtot
real::ff
double precision,dimension(:),allocatable::KW
double precision,dimension(:),allocatable::KW1
double precision,dimension(:),allocatable::Kb
double precision,dimension(:),allocatable::Ke
double precision,dimension(:),allocatable::Kc
double precision,dimension(:),allocatable::K3
double precision,dimension(:),allocatable::Wet_P
double precision,dimension(:),allocatable::new_P
double precision,dimension(:),allocatable::X
real::Ptop
real::Pbot
real::Inflow
real::outflow
Integer, dimension(:),allocatable::COORDMAT
Integer, dimension(:),allocatable::ConThrCounter
Integer, dimension(:,:),allocatable::CONNODTHRT
Integer, dimension(:,:),allocatable::CONTHRTNOD
double precision, dimension(:),allocatable::B_Mat
real::MuW
real::RoW
integer:: generator
real:: pi=3.141592653589793D0
character filename*8
character satOutputFormat*12
character presOutputFormat*12
character Long_SatFormat*12
real::term1,term2
```

```
integer:: i,j,k,m,n,TODAY(3),NOW(3), iterm1, iterm2
integer:: IERR
real::lowBoundary
integer::SUMNODSTATIC
integer::SUMTUBSTATIC
real::R_min
real::R_max
real::r_mean
real::var
integer:: Distribution_graph
integer:: snapshot_graph
integer::no_snapoff=0
real,dimension(:), allocatable::Pressure_BC
REAL::LOWCUT,HIGHCUT,BINS=30.0d0, BINSIZE,LOWERBIN,HIGHERBIN
integer:: counter, counter_2
REAL, DIMENSION(:),  ALLOCATABLE::PTH_BIN,PB_BIN
CALL system('mkdir result_folder')
CALL system('mkdir .\result_folder\snapshots')
CALL system('mkdir .\result_folder\snapshots\PN')
CALL system('mkdir .\result_folder\snapshots\PW')
CALL system('mkdir .\result_folder\snapshots\SW')
CALL system('mkdir .\result_folder\snapshots\Tube')
CALL system('mkdir .\result_folder\snapshots\Visu')
print*, 'PROGRAM READS FROM THE INPUT DATA!'
open(unit=10, file="./result_folder/output_T_C.txt")
open(unit=20, file="./result_folder/nodes_coordinations.txt")
open(unit=60, file="./result_folder/aspect ratio.txt")
open(unit=70, file="./result_folder/long_averag_c.txt")
open(unit=444, file="./result_folder/linear_pressure.txt")
open(unit=445, file="./result_folder/linear_PTH_velocities.txt")
open(unit=446, file="./result_folder/Frochheimer_PTH_velocities.txt")
open(unit=555, file="./result_folder/Frochheimer_pressure.txt")
open(unit=666, file="./result_folder/PTh_length.txt")
open(unit=777, file="./result_folder/PTH_Radii_output.txt")
open(unit=888, file="./result_folder/PB_radii_output.txt")
open(unit=999, file="./result_folder/Ke.txt")
open(unit=998, file="./result_folder/Kc.txt")
open(unit=997, file="./result_folder/calculations_dp=.txt")
open(unit=996, file="./result_folder/K3.txt")
open(unit=995, file="./result_folder/Kw.txt")
open(unit=994, file="./result_folder/velocity_2.txt")
open(unit=993, file="./result_folder/velocity_3.txt")
open(unit=992, file="./result_folder/A_PTH.txt")
open(unit=5001, file="./result_folder/D_velocity.txt")
open(unit=5002, file="./result_folder/D_velocity_x.txt")
open(unit=5003, file="./result_folder/D_velocity_3.txt")
open(unit=5004, file="./result_folder/D_velocity_3_x.txt")
open(unit=5005, file="./result_folder/D_theta.txt")
open(unit=1001, file="./result_folder/F_theta.txt")
open(unit=1002, file="./result_folder/F_velocity.txt")
open(unit=1003, file="./result_folder/F_velocity_4.txt")
open(unit=1004, file="./result_folder/F_velocity_5.txt")
open(unit=1005, file="./result_folder/F_velocity_x.txt")
open(unit=1006, file="./result_folder/F_velocity_2_x.txt")
open(unit=1007, file="./result_folder/F_velocity_3_x.txt")
open(unit=1008, file="./result_folder/F_velocity_4_x.txt")
open(unit=1009, file="./result_folder/F_velocity_5_x.txt")
open(unit=1010, file="./result_folder/exclude_2.txt")
open(unit=1012, file="./result_folder/A_PTh_exclude.txt")
open(unit=2000, file="./result_folder/Vari_PB_radii.txt")
open(unit=2001, file="./result_folder/Vari_coord_no.txt")
write(10,*) "time(s) "," concentration(-)"
```

```
open(unit=30, file="input.txt")

filename="pore.txt"
read (30,*)r_min
print*,"r_min",r_min
read (30,*)r_mean
print*,"r_mean",r_mean
read (30,*)r_max
print*,"r_max",r_max
read (30,*)var
print*,"var",var
read (30,*)MuW
print*,"MuW", MuW
read (30,*)RoW
print*,"RoW", RoW
read (30,*)alpha
print*,"alpha",alpha
read (30,*)nrpowr
print*,"nrpowr",nrpowr
read (30,*)Distribution_graph
print*,"Distribution_graph",Distribution_graph
read (30,*)snapshot_graph
print*,"snapshot_graph",snapshot_graph
read (30,*)generator

print*,"generator",generator
read(30,*)ptop
print*,"ptop",ptop
read(30,*)pbot
print*,"pbot",pbot
read(30,*) satOutputFormat
print*,"satOutputFormat",satOutputFormat
read(30,*) presOutputFormat
print*,"presOutputFormat",presOutputFormat
read(30,*) Long_SatFormat
print*,"Long_SatFormat",Long_SatFormat
read (30,*)iterm1
step=iterm1
print*, "number of window along the flow", step
read (30,*)DeltaStep
print*, "spacing of moving window along the flow", deltaStep
read (30,*) porebody_vol_index
read (30,*) lowBoundary
read (30,*)ff
print*, "The friction factor", ff
read (30,*)min_x
read (30,*)max_x
read (30,*)max_y
read (30,*)max_z
read (30,*)charc_L
close(30)

SUMNODSTATIC=0
SUMTUBSTATIC=0
diffusion=1.0D-3
open(unit=21, file="./result_folder/generalinfo.txt")
call idate(today)
call itime(now)
write ( *, 1000 )  today(2), today(1), today(3), now
write (55, 1000 )  today(2), today(1), today(3), now
1000  format ( 'Date ', i2.2, '/', i2.2, '/', i4.4, '; time ', i2.2,
':', i2.2, ':', i2.2 )
```

```
write(55,554) "time ","sat ","<Pc> ","<Pc>_all ","<Pn>-<Pw>_all
","GlobalPc ","Ca ","Int_area ", "<pc_arith> ", "<Pc>_front "
write(90,301) "Time ","Sat ","NW_ph_ALL ","NW_ph_CNT ","NW_simp ",
"W_ph_ALL ","W_ph_CNT ","W_simp ", "NW-W(Ph_All) ","NW-W(Ph_CNT)
","NW_W(Simp) ","Pc_front ","Pc_Ph_UCnt ","Pc_Ph_All ","Pc_Sim "
554    Format (A7,A6,A7,A12, A12,A11,A5,A11,A13, A18)
555    Format (F10.7,F7.4, 2F11.2,F11.2,F10.2,F15.10,2F11.2,F11.2)
301    Format (15A16)

open (unit = 100, file = "pb2pth.txt")!
read(100,*) n_pore
read(100,*) max_coord

open (unit = 200, file = "coord_nr.txt")
allocate (COORDMAT(n_pore))
do
read(200,FMT=*, end=1111) CoordMat
end do
1111  close(200)

allocate (CONNODTHRT(max_coord,n_pore))
CONNODTHRT=0
i=1
do
read(100,FMT=*, end=1112) CONNODTHRT(1:CoordMat(i),i)
i=i+1
If (i.eq.(n_pore+1)) goto 1112
end do
1112 close (100)

open (unit = 100, file = "pth2pb.txt")
read(100,*) m_throat
read(100,*) n_bot
read(100,*) n_top
allocate (CONTHRTNOD(2,m_throat))
CONTHRTNOD=0
do i=1,n_top+n_bot
read(100,*)CONTHRTNOD(1:2,i)
end do

i=n_top+n_bot+1
do
read(100,*,end=1113) CONTHRTNOD(1:2,i)
i=i+1
end do
1113  close (100)

open (unit = 100, file = "pb_coordinates.txt")!
allocate (pb_coordinates(3,n_pore))
i=1
do
read(100,*, end=1114)pb_coordinates(1:3,i)
i=i+1
end do
1114 close (100)

network_length=(max_x-min_x)
write(70,'(A5,9999F10.6)')  'time', (k/real(step),k=1,step)

open (unit = 100, file = "bndry_pores.txt")!
allocate (bndry_pores(n_top+n_bot))
```

```
do i=1, n_top+n_bot
read(100,*)bndry_pores(i)
end do
close (100)

allocate (L(m_throat),PTh_shp(m_throat))
allocate (R(m_throat),R_2(m_throat))
allocate (D(n_pore),PB_shp (n_pore))
allocate (poreunit(n_pore))
allocate (ConThrCounter(m_throat))
allocate (KW(m_throat))
allocate (KW1(m_throat))
allocate (Kb(m_throat))
allocate (Ke(m_throat))
allocate (Kc(m_throat))
allocate (K3(m_throat))
allocate(velocity(m_throat),VELOCITY_x(m_throat),
theta(m_throat),VELOCITY_2_x(m_throat),VELOCITY_3_x(m_throat),VELOCITY
_4_x(m_throat),VELOCITY_5_x(m_throat) )
allocate(velocity_2(m_throat), VELOCITY_3(m_throat),
VELOCITY_4(m_throat), VELOCITY_5(m_throat),exclude(m_throat))
allocate(PB_Velocity(2,m_throat))
allocate(Concent_old(n_pore))
allocate(Concent(n_pore))
allocate(PB_length(2,m_throat))
allocate(g_Pth(m_throat))
allocate(g_tot(m_throat))
allocate(g_PB(2,m_throat))
allocate(PTh_length_c2c(m_throat))
allocate (A_PB(n_pore),A_PTh(m_throat),PB_vol(n_pore),
PTh_vol(m_throat),HA_A_PTh(m_throat),A_Kw_tot(m_throat))
allocate ( h(n_pore,n_pore),
gamma_h(n_pore,n_pore),gamma_h_2(n_pore,n_pore) )

A_PB=0.0
HA_A_PTh=0.0
A_PTh=0.0
A_Kw_tot=0.0
velocity=0.0D0
velocity_2=0.0d0
velocity_3=0.0d0
velocity_4=0.0d0
VELOCITY_5=0.0
VELOCITY_x=0.0
VELOCITY_2_x=0.0
VELOCITY_3_x=0.0
VELOCITY_4_x=0.0
VELOCITY_5_x=0.0
exclude=0
sum_1=0.0
sum_2=0.0
sum_3=0.0
h=0.0
gamma_h=0
gamma_h_2=0
theta=0.0
PB_Velocity=0.0d0
max_nod_velocity=0.0D0
out_nod=0.0
g_Pth=0
g_Pb=0
g_tot=0
```

```
PTh_length_c2c=0
PB_vol=0
PTh_vol=0

write(1011,*) exclude

allocate (B_Mat(n_pore))
allocate (Pressure_BC(1))
ALLOCATE(PTH_BIN(INT(BINS)),PB_BIN(INT(BINS)))
allocate (Wet_P(n_pore))
allocate (new_P(n_pore))
allocate (X(n_pore))

PB_length=0.0

open (unit = 81, file = "pb_length.txt")
do i = 1, m_throat
read (81,*) PB_length(1,i), PB_length(2,i)
end do
CLOSE(81)
open (unit = 82, file = "pth_tot_length_c2c.txt")
do i = 1, m_throat
read (82,*) PTh_length_c2c(i)
end do
CLOSE(82)

L=0
R=0
D=0
open (unit = 4, file = "pb_radii.txt")
read (4,*) n_pore
read (4,*) (D(i),i=1,n_pore)
D=2.0D0*D
CLOSE(4)

L=0.0D0

open (unit = 31, file = "pth_length.txt")
read (31,*) (L(i),i=1,M_THROAT)
CLOSE(31)

if(minval(D).LE.0) then
PRINT*, "WARNING D"
PAUSE
end if

if(minval(L).LE.0) then
PRINT*, "WARNING L"
PAUSE
end if

open (unit = 32, file = "pth_radii.txt")
read (32,*) (r(i),i=1,M_THROAT)
CLOSE(32)

open (unit = 33, file = "pth_shp.txt")
read (33,*) (PTh_shp(i),i=1,M_THROAT)
CLOSE(33)

open (unit = 34, file = "pb_shp.txt")
read (34,*) (PB_shp(i),i=1,n_pore)
CLOSE(34)
```

```
open (unit = 35, file = "pb_vol.txt")
read (35,*) (PB_vol(i),i=1,n_pore)
CLOSE(35)

open (unit = 36, file = "pth_vol.txt")
read (36,*) (PTh_vol(i),i=1,m_throat)
CLOSE(36)

Do i=1,m_throat
A_PTh(i)=r(i)*r(i)/(4.0*Pth_shp(i))
write(992,*) A_PTh(i)
end do

Do i=1, n_pore
A_PB(i)=D(i)*D(i)/(16.0*Pb_shp(i))
end do


Vthroat=sum(A_PTh*L)
write (*,*)"Vthroat:", Vthroat

Vpore=sum(PB_vol)
write (*,*)"Vpore:", Vpore
write (*,*)"Vth/Vpore:",Vthroat/Vpore

Vtot=(maxval(pb_coordinates(1,:))-
minval(pb_coordinates(1,:)))*(maxval(pb_coordinates(2,:))-
minval(pb_coordinates(2,:)))*(maxval(pb_coordinates(3,:))-
minval(pb_coordinates(3,:)))

write (*,*)"Total Vol:", Vtot
write (*,*)"initial Porosity:",(Vthroat+Vpore)/(max_x*max_y*max_z)
write (997,*)"initial Porosity:",(Vthroat+Vpore)/(max_x*max_y*max_z)
cross_section= (max_y*max_z)
write (997,*)"cross_section(mm2)=",cross_section

if (minval(R).LT.0) then
print*, "wrong radius"
pause
end if

if (minval(L).LT.0) then
print*, "wrong Length"
pause
end if

if (minval(D).LT.0) then
print*, "wrong diameter"
pause
end if

WRITE(*,*)'network generation accomplished'
CALL SLEEP (3)

Vthroat=sum((Pth_vol))
write (*,*)"Vthroat:", Vthroat
Vpore=sum(PB_vol)
write (*,*)"Vpore:", Vpore
write (*,*)"final Porosity:",(Vthroat+Vpore)/(max_x*max_y*max_z)
write (997,*)"final Porosity:",(Vthroat+Vpore)/(max_x*max_y*max_z)
```

```
KW=0.0d0
KW1=0.0d0
Kb=0.0d0
Ke=0.0d0
Kc=0.0d0
K3=0.0d0
ConThrCounter=0

WRITE(*,*)'network generation accomplished'
CALL SLEEP (3)

poreunit=0
do i=1,n_pore
poreunit(i)=(4.0/3.0*pi*(D(i)/2.0D0)**3)*porebody_vol_index
do j=1,coordmat(i)
poreunit(i)=poreunit(i)+0.5*pi*R(connodthrt(j,i))**2.0D0*L(connodthrt(
j,i))
enddo
end do

lowcut=minval(R)
highcut=maxval(D/2.0d0)
binsize=(highcut-lowcut)/bins
lowerbin=minval(R)
higherbin=lowerbin+binsize
PTH_bin=0

counter=1
do while (higherbin.LE.highcut)
do i=1,m_throat
if(R(i).LE.higherbin.and.R(i).GE.lowerbin) then
PTH_bin(counter)=PTH_bin(counter)+1
end if
end do
lowerbin=higherbin
higherbin=higherbin+binsize
counter=counter+1
end do

lowerbin=minval(R)
higherbin=lowerbin+binsize
PB_bin=0
counter=1
do while (higherbin.LE.highcut)
do i=1,n_pore
if(D(i)/2.0d0.LE.higherbin.and.D(i)/2.0d0.GE.lowerbin) then
PB_bin(counter)=PB_bin(counter)+1
end if
end do
lowerbin=higherbin
higherbin=higherbin+binsize
counter=counter+1
end do

PB_bin=PB_bin/real(n_pore)
PTH_bin=PTH_bin/real(m_throat)

OPEN (UNIT=4,file="./result_folder/histogram.txt")
do i=1,int(bins)
write(4,*) i, lowcut+binsize*(i-1),PB_bin(i),PTH_bin(i)
end do
write (4,*)"Min R=", minval(R)
```

```
write (4,*)"avg R=", sum(R)/m_throat
write (4,*)"Max R=", maxval(R)
write (4,*)"Max D/2=", maxval(D)/2.0d0
write (4,*)"avg D/2=", sum(D)/2.0d0/n_pore
write (4,*)"Min D/2=", minval(D)/2.0d0
close(4)
print*, "probabality summation,", sum(PB_bin),sum(PTH_bin)

do j=1, m_throat
if (CONTHRTNOD(2,j).le.0) then
write(60,*)0.5d0*D(CONTHRTNOD(1,j))/R(j)
else
write(60,*)min(0.5d0*D(CONTHRTNOD(1,j))/R(j),0.5d0*D(CONTHRTNOD(2,j))/
R(j)),max(0.5d0*D(CONTHRTNOD(1,j))/R(j),0.5d0*D(CONTHRTNOD(2,j))/R(j))
endif
end do
CLOSE(60)

counter=0
sum_1=0
sum_2=0
k=0

Do i=1,n_pore
Do j=1, n_pore
h(i,j)=sqrt((pb_coordinates(1,i)-pb_coordinates(1,j))**2 +
(pb_coordinates(2,i)-pb_coordinates(2,j))**2+(pb_coordinates(3,i)-
pb_coordinates(3,j))**2)
end do
end do

Do i=1,n_pore
Do j=1, n_pore
gamma_h(i,j)=0.5*(( (D(i)/2)-(D(j)/2) )**2)
end do
end do

max_h=maxval(h)
dh=max_h/50

do k=1,50
sum_1=0.0
counter_2=0
dh_upper=dh*k+0.499*dh
dh_lower=dh*k-0.4999*dh

Do i=1,n_pore
Do j=1, n_pore
if ((i.le.j).and.(h(i,j).ge.dh_lower).and.(h(i,j).le.dh_upper)) then
counter_2=counter_2+1
sum_1=sum_1+gamma_h(i,j)

end if
end do
end do
write (2000,*)dh*k, sum_1/counter_2
end do

sum_1=0.0
counter=0
sum_1=0
sum_2=0
```

```
k=0

Do i=1,n_pore
Do j=1, n_pore
gamma_h_2(i,j)=0.5*(( coordmat(i)-coordmat(j) )**2)
end do
end do
max_h=maxval(h)
dh=max_h/50
do k=1,50
sum_1=0.0
counter_2=0
dh_upper=dh*k+0.499*dh
dh_lower=dh*k-0.4999*dh

Do i=1,n_pore
Do j=1, n_pore
if ((i.le.j).and.(h(i,j).ge.dh_lower).and.(h(i,j).le.dh_upper)) then
counter_2=counter_2+1
sum_1=sum_1+gamma_h_2(i,j)

end if
end do
end do
write (2001,*)dh*k, sum_1/counter_2
end do

sum_1=0.0
77     PI = 3.14159265358979d0
B_Mat=0.0d0

Do i=1,m_throat
if(pth_shp(i).le.0.049) then
kw(i)=(3*((a_pth(i))**2.0d0)*pth_shp(i))/(5*MuW*L(i))
else if ((pth_shp(i).le.0.0625).and.(pth_shp(i).gt.0.049)) then
kw(i)=(0.5623*((a_pth(i))**2.0d0)*pth_shp(i))/(MuW*L(i))
else if (pth_shp(i).gt.0.0625)then
kw(i)=(0.5*((a_pth(i))**2.0d0)*pth_shp(i))/(MuW*L(i))
else if (pth_shp(i).gt.0.0796) then
write (*,*) "warning, shape factor greater than 0.0796 for a circle"
end if
end do
g_pth=kw*L

Do i=1,m_throat
if (conthrtnod(2,i).le.0) then
iterm1=conthrtnod(1,i)

if(pb_shp(iterm1).le.0.049) then
g_PB(1,i)=(3*((a_pb(iterm1))**2.0d0)*pb_shp(iterm1))/(5*MuW)
else if ((pb_shp(iterm1).le.0.0625).and.(pb_shp(iterm1).gt.0.049))
then
g_PB(1,i)=(0.5623*((a_pb(iterm1))**2.0d0)*pb_shp(iterm1))/(MuW)
else if (pb_shp(iterm1).gt.0.0625)then
g_PB(1,i)=(0.5*((a_pb(iterm1))**2.0d0)*pb_shp(iterm1))/(MuW)
else if (pb_shp(iterm1).gt.0.0796) then
write (*,*) "warning, shape factor greater than 0.0796 for a circle"
end if

endif
end do
```

```
Do i=1, m_throat
if (conthrtnod(2,i).gt.0) then
iterm1=conthrtnod(1,i)
iterm2=conthrtnod(2,i)

if(pb_shp(iterm1).le.0.049) then
g_PB(1,i)=(3*((a_pb(iterm1))**2.0d0)*pb_shp(iterm1))/(5*MuW)
else if ((pb_shp(iterm1).le.0.0625).and.(pb_shp(iterm1).gt.0.049))
then
g_PB(1,i)=(0.5623*((a_pb(iterm1))**2.0d0)*pb_shp(iterm1))/(MuW)
else if (pb_shp(iterm1).gt.0.0625)then
g_PB(1,i)=(0.5*((a_pb(iterm1))**2.0d0)*pb_shp(iterm1))/(MuW)
else if (pb_shp(iterm1).gt.0.0796) then
write (*,*) "warning, shape factor greater than 0.0796 for a circle"
end if

if(pb_shp(iterm2).le.0.049) then
g_PB(2,i)=(3*((a_pb(iterm2))**2.0d0)*pb_shp(iterm2))/(5*MuW)
else if ((pb_shp(iterm2).le.0.0625).and.(pb_shp(iterm2).gt.0.049))
then
g_PB(2,i)=(0.5623*((a_pb(iterm2))**2.0d0)*pb_shp(iterm2))/(MuW)
else if (pb_shp(iterm2).gt.0.0625)then
g_PB(2,i)=(0.5*((a_pb(iterm2))**2.0d0)*pb_shp(iterm2))/(MuW)
else if (pb_shp(iterm2).gt.0.0796) then
write (*,*) "warning, shape factor greater than 0.0796 for a circle"
end if
endif
end do

Do i=1,m_throat
if (conthrtnod(2,i).le.0) then
g_tot(i)=(PB_length(1,i)+L(i))/((PB_length(1,i)/g_PB(1,i))+(L(i)/g_pth
(i)))
kw(i)= g_tot(i)/(PB_length(1,i)+L(i))
endif
end do

Do i=1, m_throat
if (conthrtnod(2,i).gt.0) then
g_tot(i)=(PTh_length_c2c(i))/((PB_length(1,i)/g_PB(1,i))+(L(i)/g_pth(i
))+(PB_length(2,i)/g_PB(2,i)))
kw(i)= g_tot(i)/PTh_length_c2c(i)
endif
end do

do i=1,m_throat
write (995,*) KW(i)
end do

DO i=1,m_throat
iterm1=ConThrtNod(1,i)
iterm2=ConThrtNod(2,i)
if (iterm2.eq.0) then
B_Mat(iterm1)=B_Mat(iterm1)+KW(i)*Pbot
else if (iterm2.eq.-1) then
B_Mat(iterm1)=B_Mat(iterm1)+KW(i)*Ptop
endif
end do

Wet_P=0.5*(pbot+ptop)
```

```
call
A_B_Matrix_single_phase(n_pore,m_throat,KW,CONTHRTNOD,ConThrCounter,We
t_P,ptop,pbot,B_Mat,ConNodThrt,coordmat,n_bot,n_top,max_coord,IERR)
Write(*,*)"Linear initialization is done."

KK=0.0
KK_F=0.0
BB=0.0
inflow=0
outflow=0
term1=0
term2=0
DO i=1,m_throat
if (ConThrtNod(2,i).eq.0) then
term1=Kw(i)*(Wet_P(ConThrtNod(1,i))-pbot)
outflow=outflow+term1
end if
END DO

Do i=1, m_throat
if (ConThrtNod(2,i).eq.-1) then
term2=Kw(i)*(ptop-Wet_P(ConThrtNod(1,i)))
inflow=inflow+term2
end if
END Do

KK=inflow*muw/(real(ptop-pbot)*cross_section)*1.0D6*network_length
write(*,263)"linear permeability(* 10^-6 to be in m2):"
write(*,*) KK
KK=inflow*muw/(real(ptop-pbot)*cross_section)*network_length
call sleep(1)

Write (997,*)"pressure gradient(pa/mm)=", (Ptop-Pbot)/network_length
Write (997,*)"Darcian inflow (mm3/s)=", inflow
Write (997,*)"Darcian outflow (mm3/s)=", outflow
Write (997,*)"Darcian permeability [KD] in mm2)=",KK

263 FORMAT(A35,f15.12)

DO i=1,m_throat
if (ConThrtNod(2,i).eq.0) then
VELOCITY(i)=KW(i)*(WET_P(ConThrtNod(1,i))-pbot)/(a_pth(i))
VELOCITY_x(i)=VELOCITY(i)
end if
END DO

DO i=1,m_throat
if (ConThrtNod(2,i).eq.-1) then
VELOCITY(i)=KW(i)*(ptop-WET_P(ConThrtNod(1,i)))/(a_pth(i))
VELOCITY_x(i)=VELOCITY(i)
endif
END DO

DO i=1,m_throat
if (ConThrtNod(2,i).gt.0) then
VELOCITY(i)=abs(KW(i)*(WET_P(ConThrtNod(1,i))-
WET_P(ConThrtNod(2,i))))/(a_pth(i))
VELOCITY_x(i)=VELOCITY(i)
endif
END DO

do i=1, m_throat
```

```
if (ConThrtNod(2,i).gt.0) then
m=conthrtnod(1,i)
n=conthrtnod(2,i)

if (wet_p(m).GT.wet_p(n)) then
theta(i)=acosd(abs(pb_coordinates(1,n)-
pb_coordinates(1,m))/PTh_length_c2c(i))

if (pb_coordinates(1,m).le.pb_coordinates(1,n))then
VELOCITY_x(i)=VELOCITY(i)*cosd(theta(i))
elseif (pb_coordinates(1,m).gt.pb_coordinates(1,n))then
VELOCITY_x(i)=-1.0*VELOCITY(i)*cosd(theta(i))
endif

else
theta(i)=acosd(abs(pb_coordinates(1,n)-
pb_coordinates(1,m))/PTh_length_c2c(i))

if (pb_coordinates(1,m).le.pb_coordinates(1,n))then
VELOCITY_x(i)=-1.0*VELOCITY(i)*cosd(theta(i))
elseif (pb_coordinates(1,m).gt.pb_coordinates(1,n))then

VELOCITY_x(i)=VELOCITY(i)*cosd(theta(i))
endif

endif
end if
end do

Do i=1,m_throat
do j=1,m_throat
if (exclude(j).eq.i)goto 5010
end do
Write(5001,*)VELOCITY(i)
write (5002,*)VELOCITY_x(i)
write (5005,*)theta(i)
5010 end do

sum_1=0.0
sum_2=0.0
sum_3=0.0

Do i=1, m_throat
do j=1,m_throat
if (exclude(j).eq.i)goto 5011
end do
sum_1= sum_1+VELOCITY(i)*A_PTh(i)
sum_2= sum_2+A_PTh(i)
sum_3=sum_3+VELOCITY_x(i)*A_PTh(i)

5011 end do

write(*,*)    sum_1, sum_2,sum_3
do i=1,m_throat
write(1010,*) exclude(i)
enddo
Write (997,*)"Darcy Turtosity1: intererstial V/V_x",
(sum_1/sum_2)/(sum_3/sum_2)
Write (997,*)"sum_1",sum_1,"sum_2",sum_2,"sum_3",sum_3

Do i=1,m_throat
if (ConThrtNod(2,i).eq.0) then
```

```
PB_Velocity(1,i)=Kw(i)*(WET_P(conthrtnod(1,i))-
Pbot)/(A_PB(conthrtnod(1,i)))
end if
end do

Do i=1,m_throat
if (ConThrtNod(2,i).eq.-1) then
PB_Velocity(1,i)=Kw(i)*abs(Ptop-
WET_P(conthrtnod(1,i)))/(A_PB(conthrtnod(1,i)))
end if
end do

DO i=1,m_throat
if (ConThrtNod(2,i).gt.0) then
PB_Velocity(1,i)=Kw(i)*abs(WET_P(conthrtnod(1,i))-
WET_P(conthrtnod(2,i)))/(A_PB(conthrtnod(1,i)))
PB_Velocity(2,i)=Kw(i)*abs(WET_P(conthrtnod(1,i))-
WET_P(conthrtnod(2,i)))/(A_PB(conthrtnod(2,i)))
end if
end do

do i=1,m_throat
if (ConThrtNod(2,i).le.0) then
VELOCITY_3(i)=(PB_length(1,i)+L(i))/(((PB_length(1,i))/PB_Velocity(1,i
))+(L(i)/VELOCITY(i)))
end if
enddo

do i=1, m_throat
if (ConThrtNod(2,i).gt.0) then
VELOCITY_3(i)=(PTh_length_c2c(i))/((PB_length(1,i)/PB_Velocity(1,i))+(
L(i)/VELOCITY(i))+(PB_length(2,i)/PB_Velocity(2,i)))
end if
enddo

VELOCITY_3_x=VELOCITY_3*cosd(theta)
Do i=1,m_throat
if (velocity_x(i).lt.0) then
VELOCITY_3_x(i)=-1.0*VELOCITY_3_x(i)
end if
end do

Do i=1,m_throat
do j=1,m_throat
if (exclude(j).eq.i)goto 5012
end do
write(5003,*) VELOCITY_3(i)
write(5004,*) VELOCITY_3_x(i)
5012    enddo

sum_1=0.0
sum_2=0.0
sum_3=0.0

Do i=1, m_throat
do j=1,m_throat
if (exclude(j).eq.i)goto 5013
end do
sum_1= sum_1+VELOCITY_3(i)*A_PTh(i)
sum_2= sum_2+A_PTh(i)
sum_3=sum_3+VELOCITY_3_x(i)*A_PTh(i)
```

```
5013 end do
Write (997,*)"Darcy_Turtosity3(PTH_Area): intererstial V3/V3_x",
(sum_1/sum_2)/(sum_3/sum_2)
Write (997,*)"sum_1",sum_1,"sum_2",sum_2,"sum_3",sum_3
Write(*,*)"[linear]inters.velocity(mm/s): ",
sum(VELOCITY*a_pth)/sum(a_pth)
Write (997,*)"[linear]inters.velocity(mm/s)=",
sum(VELOCITY*a_pth)/sum(a_pth)
Write (997,*)"[linear]inters.velocity_3(mm/s)=",
sum(VELOCITY_3*a_pth)/sum(a_pth)
KK_F=(sum(VELOCITY_3*a_pth)/sum(a_pth))*((Vthroat+Vpore)/(max_x*max_y*
max_z))*muw/(real(ptop-pbot))*network_length
Write (997,*)"Darcian permeability [KD_F] from Vpore mm2=",KK_F

Write(997,*)"[linear]Pore_Peclet: ",
sum(abs(VELOCITY)*R/diffusion)/real(m_throat)
Write(997,*)"[linear]Charc_L_Peclet: ",
(sum(VELOCITY*a_pth)/sum(a_pth))*charc_L/diffusion
Write(*,*)"[linear]inflow (mm3/s): ", inflow
Write(*,*)"[linear]outflow (mm3/s): ", outflow
Write (997,*)"Darcian (KD) superficial velocity (mm/s)=",
outflow/cross_section
Write (997,*)"Darcian ReL based on charc_L & superficial V=", Row*1e-
6*outflow*charc_L/cross_section/MuW
call sleep(2)

Do i =1, n_pore
Write (444,*) pb_coordinates(1,i),
pb_coordinates(2,i),pb_coordinates(3,i),Wet_P(i)
End do

VELOCITY=0.0
VELOCITY_x=0.0
PB_Velocity=0.0
VELOCITY_2_x=0.0
VELOCITY_3=0.0
VELOCITY_3_x=0.0


Write(*,*) "Start of Forchheimer calculations"

KW1=1/kw
DO i=1,m_throat
if (ConThrtNod(2,i).eq.0) then
Ke(i)=0.0d0
m=conthrtnod(1,i)
Kc(i)=((0.45d0-0.45d0*(A_PTh(i)/A_PB(m)))*(row*(1e-
6)/2.0d0))/((A_PTh(i))**2)
if (A_PTh(i).ge.A_PB(m)) kc(I)=0.0
iF (kc(I).lt.0.0d0) THEN
Kc(i)=0.0d0
end if
K3(i)= Ke(i)+Kc(i)
If (k3(i).le.0) then
k3(i)=1e-6
end if
end if
end do

50  DO i=1,m_throat
if (ConThrtNod(2,i).eq.-1) then
Kb=0
```

```
Kc(i)=0.0d0
m=conthrtnod(1,i)
Ke(i)=(((1.0d0-(A_PTh(i)/A_PB(m)))**2)*ROW*(1e-
6)/2.0d0)/((A_PTh(i))**2)
if (A_PTh(i).ge.A_PB(m)) Ke(i)=0.0d0
iF (ke(i).lt.0.0d0) THEN
Ke(i)=0.0d0
end if
K3(i)= Ke(i)+Kc(i)
If (k3(i).le.0) then
k3(i)=1e-6
end if
endif
end do

do i=1, m_throat
if (ConThrtNod(2,i).gt.0) then
Kb(i)=0
m=conthrtnod(1,i)
n=conthrtnod(2,i)
if (wet_p(m).GT.wet_p(n)) then
Kc(i)=((0.45d0-0.45d0*(A_PTh(i)/A_PB(m)))*(row*(1e-
6)/2.0d0))/((A_PTh(i))**2)
Ke(i)=(((1.0d0-(A_PTh(i)/A_PB(n)))**2)*ROW*(1e-
6)/2.0d0)/((A_PTh(i))**2)
if (A_PTh(i).ge.A_PB(m)) Kc(i)=0.0
if (A_PTh(i).ge.A_PB(n)) Ke(i)=0.0
else
Kc(i)=((0.45d0-0.45d0*(A_PTh(i)/A_PB(n)))*(row*(1e-
6)/2.0d0))/((A_PTh(i))**2)
Ke(i)=(((1.0d0-(A_PTh(i)/A_PB(m)))**2)*ROW*(1e-
6)/2.0d0)/((A_PTh(i))**2)
if (A_PTh(i).ge.A_PB(n)) Kc(i)=0.0
if (A_PTh(i).ge.A_PB(m)) Ke(i)=0.0
endif
K3(i)= Ke(i)+Kc(i)
If (k3(i).le.0) then
k3(i)=1e-6
end if
end if
end do

Do i =1, m_throat
Write (999,*) ke(i)
End do

Do i =1, m_throat
Write (998,*) kc(i)
End do

Do i =1, m_throat
Write (996,*) k3(i)
End do

X=0.0d0
New_P=0.0d0

Non_Zero_deriv=0d0
non_zero_deriv_bot=0d0
non_zero_deriv_top=0d0
Non_Zero_deriv=Sum(Coordmat)+n_pore-n_bot-n_top
Do i=1, n_bot
```

```
non_zero_deriv_bot=non_zero_deriv_bot+Coordmat(i)
end do
Do i=n_bot+1, n_bot+n_top
non_zero_deriv_top=non_zero_deriv_top+Coordmat(i)
end do
call
Non_linear(n_pore,m_throat,CONTHRTNOD,Ptop,Pbot,ConNodThrt,coordmat,n_
bot,n_top,Wet_p,K3,Kw1,max_coord,X,Non_Zero_deriv)

New_p=X
inflow=0d0
outflow=0d0
term1=0.0d0
term2=0.0d0
theta=0.0
K=0
DO i=1,m_throat
if (ConThrtNod(2,i).eq.0) then
term1=(-Kw1(i)+sqrt
(abs(Kw1(i)**2.0d0+4.0d0*K3(i)*(new_P(conthrtnod(1,i))-
Pbot))))/(2.0d0*K3(i))
outflow=outflow+term1
endif
END DO

DO i=1,m_throat
if (ConThrtNod(2,i).eq.-1) then
term2=(-Kw1(i)+sqrt(abs(Kw1(i)**2.0d0+4.0d0*K3(i)*abs(Ptop-
new_P(conthrtnod(1,i))))))/(2.0d0*K3(i))
inflow=inflow+term2
Endif
END DO

Write(*,*)"Forchheimer inflow (mm3/s): ", inflow
Write(*,*)"Forchheimer outflow (mm3/s): ", outflow

Do i=1, m_throat
if ((conthrtnod(2,i)).gt.0) then
If
((wet_p(conthrtnod(1,i)).gt.wet_p(conthrtnod(2,i))).and.(New_p(conthrt
nod(1,i)).lt.New_p(conthrtnod(2,i))))then
wet_p=x
go to 50
else
if((wet_p(conthrtnod(1,i)).lt.wet_p(conthrtnod(2,i))).and.(New_p(conth
rtnod(1,i)).gt.New_p(conthrtnod(2,i))))then
wet_p=X
go to 50
endif
end if
end do

call sleep(1)
223 FORMAT(A25,f15.12)
VELOCITY=0.0d0

DO i=1,m_throat
if (ConThrtNod(2,i).eq.0) then
VELOCITY(i)=((-
Kw1(i)+sqrt((Kw1(i)**2.0d0+4.0d0*K3(i)*(new_P(conthrtnod(1,i))-
Pbot))))/(2.0d0*K3(i)))/(A_PTh(i))
VELOCITY_x(i)=VELOCITY(i)
```

```
end if
END DO

DO i=1,m_throat
if (ConThrtNod(2,i).eq.-1) then
VELOCITY(i)=((-Kw1(i)+sqrt((Kw1(i)**2.0d0+4.0d0*K3(i)*abs(Ptop-
new_P(conthrtnod(1,i))))))/(2.0d0*K3(i)))/(A_PTh(i))
VELOCITY_x(i)=VELOCITY(i)
endif
END DO

DO i=1,m_throat
if (ConThrtNod(2,i).gt.0) then
VELOCITY(i)=((-
Kw1(i)+sqrt((Kw1(i)**2.0d0+4.0d0*K3(i)*abs(new_P(conthrtnod(1,i))-
new_P(conthrtnod(2,i))))))/(2.0d0*K3(i)))/(A_PTh(i))
VELOCITY_x(i)=VELOCITY(i)
end if
END DO

do i=1, m_throat
if (ConThrtNod(2,i).gt.0) then
m=conthrtnod(1,i)
n=conthrtnod(2,i)

if (new_p(m).GT.new_p(n)) then
theta(i)=acosd(abs(pb_coordinates(1,n)-
pb_coordinates(1,m))/PTh_length_c2c(i))

if (pb_coordinates(1,m).le.pb_coordinates(1,n))then
VELOCITY_x(i)=VELOCITY(i)*cosd(theta(i))
elseif (pb_coordinates(1,m).gt.pb_coordinates(1,n))then
VELOCITY_x(i)=-1.0*VELOCITY(i)*cosd(theta(i))
endif

else
theta(i)=acosd(abs(pb_coordinates(1,n)-
pb_coordinates(1,m))/PTh_length_c2c(i))

if (pb_coordinates(1,m).le.pb_coordinates(1,n))then
VELOCITY_x(i)=-1.0*VELOCITY(i)*cosd(theta(i))
elseif (pb_coordinates(1,m).gt.pb_coordinates(1,n))then

VELOCITY_x(i)=VELOCITY(i)*cosd(theta(i))
endif
endif
end if
end do

Do i=1, m_throat
do j=1,m_throat
if (exclude(j).eq.i)goto 202
end do
write (1002,*)VELOCITY(i)
write (1005,*)VELOCITY_x(i)
write (1001,*)theta(i)

202 end do
Write (997,*)"[froch]inters.velocity[V](mm/s)=",
sum(VELOCITY*a_pth)/sum(a_pth)

sum_1=0.0
```

```
sum_2=0.0
sum_3=0.0

Do i=1, m_throat
do j=1,m_throat
if (exclude(j).eq.i)goto 203
end do
sum_1= sum_1+VELOCITY(i)*A_PTh(i)
sum_2= sum_2+A_PTh(i)
sum_3=sum_3+VELOCITY_x(i)*A_PTh(i)
203 end do

write(*,*)    sum_1, sum_2,sum_3
do i=1,m_throat
write(1010,*) exclude(i)
enddo
Write (997,*)"Turtosity1: intererstial V/V_x",
(sum_1/sum_2)/(sum_3/sum_2)
Write (997,*)"sum_1",sum_1,"sum_2",sum_2,"sum_3",sum_3

Do i=1,m_throat
if (ConThrtNod(2,i).eq.0) then
PB_Velocity(1,i)=((-
Kw1(i)+sqrt((Kw1(i)**2.0d0+4.0d0*K3(i)*(new_P(conthrtnod(1,i))-
Pbot))))/(2.0d0*K3(i)))/(A_PB(conthrtnod(1,i)))
end if
end do

Do i=1, m_throat
if (ConThrtNod(2,i).eq.-1) then
PB_Velocity(1,i)=((-Kw1(i)+sqrt((Kw1(i)**2.0d0+4.0d0*K3(i)*abs(Ptop-
new_P(conthrtnod(1,i))))))/(2.0d0*K3(i)))/(A_PB(conthrtnod(1,i)))
end if
end do

DO i=1,m_throat
if (ConThrtNod(2,i).gt.0) then
PB_Velocity(1,i)=((-
Kw1(i)+sqrt((Kw1(i)**2.0d0+4.0d0*K3(i)*abs(new_P(conthrtnod(1,i))-
new_P(conthrtnod(2,i))))))/(2.0d0*K3(i)))/(A_PB(conthrtnod(1,i)))
PB_Velocity(2,i)=((-
Kw1(i)+sqrt((Kw1(i)**2.0d0+4.0d0*K3(i)*abs(new_P(conthrtnod(1,i))-
new_P(conthrtnod(2,i))))))/(2.0d0*K3(i)))/(A_PB(conthrtnod(2,i)))
end if
end do

do i=1,m_throat
if (ConThrtNod(2,i).le.0) then
VELOCITY_2(i)=2/((1/PB_Velocity(1,i))+(1/VELOCITY(i)))
end if
enddo

do i=1, m_throat
if (ConThrtNod(2,i).gt.0) then
VELOCITY_2(i)=3/((1/PB_Velocity(1,i))+(1/VELOCITY(i))+(1/PB_Velocity(2
,i)))
end if
enddo

VELOCITY_2_x=VELOCITY_2*cosd(theta)

Do i=1,m_throat
```

```
if (velocity_x(i).lt.0) then
VELOCITY_2_x(i)=-1.0*VELOCITY_2_x(i)
end if
end do

Do i=1,m_throat
do j=1,m_throat
if (exclude(j).eq.i)goto 208
end do
write(994,*) VELOCITY_2(i)
write(1006,*) VELOCITY_2_x(i)

208 enddo
Write (997,*)"[froch]inters.velocity[V2](mm/s)=",
sum(VELOCITY_2*a_pth)/sum(a_pth)

sum_1=0.0
sum_2=0.0
sum_3=0.0

Do i=1, m_throat
do j=1,m_throat
if (exclude(j).eq.i)goto 204
end do
sum_1= sum_1+VELOCITY_2(i)*A_PTh(i)
sum_2= sum_2+A_PTh(i)
sum_3=sum_3+VELOCITY_2_x(i)*A_PTh(i)

204 end do
Write (997,*)"Turtosity2(PTH_Area): intererstial V2/V2_x",
(sum_1/sum_2)/(sum_3/sum_2)
Write (997,*)"sum_1",sum_1,"sum_2",sum_2,"sum_3",sum_3

do i=1, m_throat
if (ConThrtNod(2,i).le.0) then
VELOCITY_3(i)=(PB_length(1,i)+L(i))/(((PB_length(1,i))/PB_Velocity(1,i
))+(L(i)/VELOCITY(i)))
end if
enddo

do i=1, m_throat
if (ConThrtNod(2,i).gt.0) then
VELOCITY_3(i)=(PTh_length_c2c(i))/((PB_length(1,i)/PB_Velocity(1,i))+(
L(i)/VELOCITY(i))+(PB_length(2,i)/PB_Velocity(2,i)))
end if
enddo

VELOCITY_3_x=VELOCITY_3*cosd(theta)
Do i=1,m_throat
if (velocity_x(i).lt.0) then
VELOCITY_3_x(i)=-1.0*VELOCITY_3_x(i)
end if
end do

Do i=1,m_throat
do j=1,m_throat
if (exclude(j).eq.i)goto 209
end do
write(993,*) VELOCITY_3(i)
write(1007,*) VELOCITY_3_x(i)
209    enddo
```

```
Write (997,*)"[froch]inters.velocity[V3](mm/s)=",
sum(VELOCITY_3*a_pth)/sum(a_pth)

sum_1=0.0
sum_2=0.0
sum_3=0.0

Do i=1, m_throat
do j=1,m_throat
if (exclude(j).eq.i)goto 205
end do
sum_1= sum_1+VELOCITY_3(i)*A_PTh(i)
sum_2= sum_2+A_PTh(i)
sum_3=sum_3+VELOCITY_3_x(i)*A_PTh(i)

205 end do
Write (997,*)"Turtosity3(PTH_Area): intererstial V3/V3_x",
(sum_1/sum_2)/(sum_3/sum_2)
Write (997,*)"sum_1",sum_1,"sum_2",sum_2,"sum_3",sum_3

Do i=1,m_throat
if (ConThrtNod(2,i).le.0) then
HA_A_PTh(i)=(PB_length(1,i)+L(i))/(((PB_length(1,i))/A_PB(conthrtnod(1
,i)))+(L(i)/A_PTh(i)))
end if
enddo

Do i=1, m_throat
if (ConThrtNod(2,i).gt.0) then
HA_A_PTh(i)=(PTh_length_c2c(i))/((PB_length(1,i)/A_PB(conthrtnod(1,i))
)+(L(i)/A_Pth(i))+(PB_length(2,i)/A_PB(conthrtnod(2,i))))
end if
enddo

DO i=1,m_throat
if (ConThrtNod(2,i).eq.0) then
VELOCITY_4(i)=((-
Kw1(i)+sqrt((Kw1(i)**2.0d0+4.0d0*K3(i)*(new_P(conthrtnod(1,i))-
Pbot))))/(2.0d0*K3(i)))/(HA_A_PTh(i))
endif
END DO

DO i=1,m_throat
if (ConThrtNod(2,i).eq.-1) then
VELOCITY_4(i)=((-Kw1(i)+sqrt((Kw1(i)**2.0d0+4.0d0*K3(i)*abs(Ptop-
new_P(conthrtnod(1,i))))))/(2.0d0*K3(i)))/(HA_A_PTh(i))
endif
END DO

DO i=1,m_throat
if (ConThrtNod(2,i).gt.0) then
VELOCITY_4(i)=((-
Kw1(i)+sqrt((Kw1(i)**2.0d0+4.0d0*K3(i)*abs(new_P(conthrtnod(1,i))-
new_P(conthrtnod(2,i))))))/(2.0d0*K3(i)))/(HA_A_PTh(i))
end if
END DO

VELOCITY_4_x=VELOCITY_4*cosd(theta)

Do i=1,m_throat
if (velocity_x(i).lt.0) then
VELOCITY_4_x(i)=-1.0*VELOCITY_4_x(i)
```

```
end if
end do

Do i=1,m_throat
do j=1,m_throat
if (exclude(j).eq.i)goto 211
end do
write(1003,*) VELOCITY_4(i)
write(1008,*) VELOCITY_4_x(i)
211   enddo
Write (997,*)"[froch]inters.velocity[V4](mm/s)=",
sum(VELOCITY_4*a_pth)/sum(a_pth)

sum_1=0.0
sum_2=0.0
sum_3=0.0

Do i=1, m_throat
do j=1,m_throat
if (exclude(j).eq.i)goto 206
end do
sum_1= sum_1+VELOCITY_4(i)*A_PTh(i)
sum_2= sum_2+A_PTh(i)
sum_3=sum_3+VELOCITY_4_x(i)*A_PTh(i)

206 end do
Write (997,*)"Turtosity4(PTH_Area): intererstial V4/V4_x",
(sum_1/sum_2)/(sum_3/sum_2)
Write (997,*)"sum_1",sum_1,"sum_2",sum_2,"sum_3",sum_3

R_2=0.0

Do i=1,m_throat
if (ConThrtNod(2,i).le.0) then
if(pth_shp(i).le.0.049) then
R_2(i)=(80*kw(i)*MuW*(PB_length(1,i)+L(i))*pth_shp(i)/3)**0.25d0
A_Kw_tot(i)=R_2(i)*R_2(i)/(4*pth_shp(i))

else if ((pth_shp(i).le.0.0625).and.(pth_shp(i).gt.0.049)) then
R_2(i)=(kw(i)*MuW*(PB_length(1,i)+L(i))/0.5623)**0.25d0
A_Kw_tot(i)=R_2(i)*R_2(i)/(4*pth_shp(i))

else if (pth_shp(i).gt.0.0625)then
R_2(i)=(kw(i)*8.0d0*MuW*(PB_length(1,i)+L(i))/pi)**0.250d0
A_Kw_tot(i)=R_2(i)*R_2(i)/(4*pth_shp(i))
end if
end if
end do

Do i=1,m_throat
if (ConThrtNod(2,i).gt.0) then
if(pth_shp(i).le.0.049) then
R_2(i)=(80*kw(i)*MuW*(PTh_length_c2c(i))*pth_shp(i)/3)**0.25d0
A_Kw_tot(i)=R_2(i)*R_2(i)/(4*pth_shp(i))

else if ((pth_shp(i).le.0.0625).and.(pth_shp(i).gt.0.049)) then
R_2(i)=(kw(i)*(MuW*PTh_length_c2c(i))/0.5623)**0.25d0
A_Kw_tot(i)=R_2(i)*R_2(i)/(4*pth_shp(i))

else if (pth_shp(i).gt.0.0625)then
R_2(i)=(kw(i)*(8.0d0*MuW*PTh_length_c2c(i))/pi)**0.250d0
A_Kw_tot(i)=R_2(i)*R_2(i)/(4*pth_shp(i))
```

```
end if
end if
end do

DO i=1,m_throat
if (ConThrtNod(2,i).eq.0) then
VELOCITY_5(i)=((-
Kw1(i)+sqrt((Kw1(i)**2.0d0+4.0d0*K3(i)*(new_P(conthrtnod(1,i))-
Pbot))))/(2.0d0*K3(i)))/(A_Kw_tot(i))
endif
END DO

DO i=1,m_throat
if (ConThrtNod(2,i).eq.-1) then
VELOCITY_5(i)=((-Kw1(i)+sqrt((Kw1(i)**2.0d0+4.0d0*K3(i)*abs(Ptop-
new_P(conthrtnod(1,i))))))/(2.0d0*K3(i)))/(A_Kw_tot(i))
endif
END DO

DO i=1,m_throat
if (ConThrtNod(2,i).gt.0) then
VELOCITY_5(i)=((-
Kw1(i)+sqrt((Kw1(i)**2.0d0+4.0d0*K3(i)*abs(new_P(conthrtnod(1,i))-
new_P(conthrtnod(2,i))))))/(2.0d0*K3(i)))/(A_Kw_tot(i))
end if
END DO

VELOCITY_5_x=VELOCITY_5*cosd(theta)

Do i=1,m_throat
if (velocity_x(i).lt.0) then
VELOCITY_5_x(i)=-1.0*VELOCITY_5_x(i)
end if
end do

Do i=1,m_throat
do j=1,m_throat
if (exclude(j).eq.i)goto 212
end do
write(1004,*) VELOCITY_5(i)
write(1009,*) VELOCITY_5_x(i)
212 enddo
Write (997,*)"[froch]inters.velocity[V5](mm/s)=",
sum(VELOCITY_5*a_pth)/sum(a_pth)

sum_1=0.0
sum_2=0.0
sum_3=0.0

Do i=1, m_throat
do j=1,m_throat
if (exclude(j).eq.i)goto 207
end do
sum_1= sum_1+VELOCITY_5(i)*A_PTh(i)
sum_2= sum_2+A_PTh(i)
sum_3=sum_3+VELOCITY_5_x(i)*A_PTh(i)

207 end do
Write (997,*)"Turtosity5(PTH_Area): intererstial V5/V5_x",
(sum_1/sum_2)/(sum_3/sum_2)
Write (997,*)"sum_1",sum_1,"sum_2",sum_2,"sum_3",sum_3
```

```
Do i=1,m_throat
Write(446,*)VELOCITY(i)
End do

Do i=1,m_throat
Write(447,*)VELOCITY_2(i)
End do

Write(997,*)"inters.velocity_2(mm/s): ",
sum(VELOCITY_2*A_PTh)/sum(A_PTh)
Write(*,*)"inters.velocity(mm/s): ", sum(VELOCITY_2*A_PTh)/sum(A_PTh)
Write(997,*)"Pore_Peclet:V_1",
sum(abs(VELOCITY)*R/diffusion)/real(m_throat)
Write(997,*)"[froch]Charc_L_Peclet:V1",
(sum(VELOCITY*a_pth)/sum(a_pth))*charc_L/diffusion
Write(997,*)"Pore_Peclet:V_2 ",
sum(abs(VELOCITY_2)*R/diffusion)/real(m_throat)
Write(*,*)"Pore_Peclet: V_2",
sum(abs(VELOCITY_2)*R/diffusion)/real(m_throat)
BB=((real(ptop-pbot)/network_length)-
MuW*inflow/(KK*cross_section))/(RoW*(1e-6)*inflow**2/cross_section**2)
Write(*,*)"Frochheimer Coefficient (units[mm^-1] because Row in
Kg/(mm2*m)): "
write(*,*) BB, " *10^3 to be in 1/m"
write (*,*) " Row*1e-6=", Row*1e-6

20     call idate(today)
print*,no_snapoff
call itime(now)
write (21, 1000 )  today(2), today(1), today(3), now

Do i =1, n_pore
Write (444,*) pb_coordinates(1,i),
pb_coordinates(2,i),pb_coordinates(3,i),Wet_P(i)
End do

Do i =1, n_pore
Write (555,*) pb_coordinates(1,i),
pb_coordinates(2,i),pb_coordinates(3,i), New_p(i)
End do
Do i =1, m_throat
Write (666,*) L(i)
End do

Do i =1, m_throat
Write (777,*) R(i)
End do

write(888,*)n_pore
Do i =1, n_pore
Write (888,*) D(i)/2
End do

Write (997,*)"Forchheimer inflow (mm3/s)=", inflow
Write (997,*)"Forchheimer outflow (mm3/s)=", outflow
Write (997,*)"Forchheimer coefficient[mm^-1] as Row in Kg/(mm2*m))not
exact",BB
write(997,*) "Forchheimer coefficient*10^3 to be in 1/m"
Write (997,*)"top pressure (Pa)=", Ptop
Write (997,*)"bottom pressure (Pa)=", Pbot
Write (997,*)"Forchheimer superficial velocity (mm/s)=",
outflow/cross_section
```

```
Write (997,*)"Forchheimer ReL based on charc_L & superficial V=",
Row*1e-6*outflow*charc_L/cross_section/MuW
Write (997,*)"Forchheimer ReK based on KD & superficial V=", Row*1e-
6*outflow*sqrt(kk)/cross_section/MuW
Write (997,*)"Forchheimer 1/Kapp=DP/(L*mu*V)[1/mm2]", (Ptop-
Ptop)/((max_x-min_x)*muw*outflow/cross_section)
Write (997,*)"Forchheimer row*V/mu[1/mm])", (row*1e-
6*outflow/cross_section)/muw
deallocate(L,R,D,poreunit,ConThrCounter,Kw,kw1,kb,ke,kc,k3,
velocity,velocity_2,PB_Velocity,
Concent_old,Concent,B_Mat,Pressure_BC,PTH_BIN,PB_BIN,Wet_P,new_P,X)
end program  pore_tubes
```

Subroutine A_B_Matrix_single_phase:

```
SUBROUTINE
A_B_Matrix_single_phase(n_pore,m_throat,KW,CONTHRTNOD,ConThrCounter,Pb
ar,Ptop,Pbot,B_Mat,ConNodThrt,coordmat,n_bot,n_top,max_coord,IERR)
implicit none
integer::i,j,k,n_pore,m_throat,n_top,n_bot,counter,max_coord
integer::
ConThrCounter(m_throat),ConThrtNod(2,m_throat),ConNodThrt(max_coord,n_
pore),coordmat(n_pore)
double precision,dimension(m_throat):: KW
double precision, dimension(n_pore)::B_Mat
double precision::term1,term2
real::ptop,pbot,SUMT
integer::
MatrixOrder,nonzero,ISYM,NSAVE,ITOL,ITMAX,ITER,IERR,IUNIT,LENW,LENIW,N
L,NU
double precision::Pbar(n_pore)
double precision::TOL,ERR

integer,dimension(:), allocatable::ArrI,ArrJ
Double Precision,dimension(:), allocatable::AA
Double Precision, dimension(:),ALLOCATABLE::RWORK
Integer, dimension(:),ALLOCATABLE::IWORK

ITMAX=3000
ISYM=1
NSAVE=400
ITOL=2
TOL=1.0E-7
MatrixOrder=n_pore
nonzero=0
term1=0.0_8
term2=0.0_8

nonzero=n_pore+(m_throat-n_top-n_bot)
allocate(ArrI(nonzero),ArrJ(nonzero),AA(nonzero))
ArrI=0
ArrJ=0
AA=0.0
nonzero=0
Do i=1,n_pore
nonzero=nonzero+1
ArrI(nonzero)=i
ArrJ(nonzero)=i
Do j=1,coordmat(i)
AA(nonzero)=AA(nonzero)+KW(connodthrt(j,i))
End Do
End Do

Do i=1, m_throat
if (CONTHRTNOD(2,i).gt.0) then
nonzero=nonzero+1
ArrI(nonzero)=min(CONTHRTNOD(1,i),CONTHRTNOD(2,i))
ArrJ(nonzero)=max(CONTHRTNOD(1,i),CONTHRTNOD(2,i))
AA(nonzero)=-(KW(i))
endif
End Do

IUNIT=0
NL=n_pore+2*(m_throat-n_top-n_bot)
NU=NL
```

```
LENW=1+MatrixOrder*(NSAVE+7) + NSAVE*(NSAVE+3)+NL+NU
LENIW =(NL+NU+4*MatrixOrder+32.0)
Allocate (RWORK(LENW),IWORK(LENIW))
RWORK=0
IWORK=0
call DSDBCG
(MatrixOrder,B_Mat,Pbar,nonzero,ArrI,ArrJ,AA,ISYM,ITOL,TOL,ITMAX,
ITER, ERR, IERR, IUNIT, RWORK, LENW, IWORK, LENIW)
if (IERR.ne.0) then
print*, "wrong solution of A-B-Matrix"
print*,"IERR=",IERR
pause
end if
deallocate (ArrI,ArrJ,AA,RWORK,IWORK)
return
END SUBROUTINE
```

Subroutine Non_linear:

```
SUBROUTINE Non_linear(n_pore,m_throat,CONTHRTNOD,Ptop
,Pbot,ConNodThrt,coordmat,n_bot,n_top,Wet_p,K3,Kw1,
 max_coord,X,Non_Zero_deriv)
integer:: ConThrtNod(2,m_throat),ConNodThrt(max_coord,n_pore),
coordmat(n_pore),m_throat, max_coord
Real ::Ptop, pbot
Double precision:: Kw1(m_throat),Kw(m_throat),k3(m_throat),
 wet_p(n_pore),X(n_pore)
EXTERNAL NS23AD, FUNC
INTEGER:: M,N,LIW,LW,K,K1,k2,k4,n_pore,iterm1,iterm2,iterm3
PARAMETER (LIW=8500000, LW=8500000)
DOUBLE PRECISION:: SAC,STPMIN,HMAX
INTEGER MAXFUN,IPRINT,IFLAG, I, J
INTEGER, dimension(:), allocatable::IW,IRN,IP,IRNA,IPA
INTEGER, dimension(:,:), allocatable::Row_indices
DOUBLE PRECISION, dimension(:), allocatable::W,F,A,DERIV
DOUBLE PRECISION, dimension(:,:), allocatable::F1_DERIV,F1
PARAMETER (SAC=1D-10, STPMIN=1D-10, MAXFUN=3000000, IPRINT=1)
INTEGER ICNTL(5),INFO(10),KEEP(130)
DOUBLE PRECISION CNTL(5),RINFO(5),RKEEP(72)
LOGICAL LKEEP(10)
Allocate (IW(LIW),IRN(Non_Zero_deriv+1), IP(n_pore+1),
 IRNA(n_pore), IPA(n_pore+1),F(n_pore),A(n_pore),
 DERIV(Non_Zero_deriv))
 Allocate (W(LW))
Allocate (Row_indices(n_pore,n_pore),F1_DERIV(n_pore,n_pore),
 F1(n_pore,n_pore))
M=n_pore
N=n_pore
CALL NS23ID(ICNTL,CNTL,KEEP,RKEEP,LKEEP)
WRITE(6,'(A,I7,A,1P,E11.4,A,E11.4)')
     ' N =',N, ',  SAC =',SAC, ',  STPMIN =',STPMIN

  X=Wet_p
  F=0.0d0
  K1=0
  K2=0
  iterm1=0
  iterm2=0
  iterm3=0
  Row_indices=0
  IRN=0
  IRNA=0
  K4=1
  A=0

Do I=1, m_throat
if (ConThrtNod(2,i).eq.0) then
K2=CONTHRTNOD(1,i)
Do K=1, Coordmat(K2)
iterm3=Connodthrt(K,K2)
iterm1=Conthrtnod(1,iterm3)
iterm2=Conthrtnod(2,iterm3)
IF (iterm2.LE.0) then
Row_indices(iterm1,iterm1)=iterm1
go to 11
End if
IF (iterm1.NE.K2) then
Row_indices(iterm1,k2)=iterm1
else
```

```
      Row_indices(iterm2,k2)=iterm2
      End if
11    end do
      endif
      end do

      Do I=1,n_pore
      Do K=1, Coordmat(I)+1
      If (K==(Coordmat(I)+1))then
          Row_indices(I,I)=I
          goto 55
      endif
      iterm3=Connodthrt(K,I)
      iterm1=Conthrtnod(1,iterm3)
      iterm2=Conthrtnod(2,iterm3)
      IF (iterm2.LE.0) go to 66
      IF (iterm1.NE.I) then
      Row_indices(iterm1,I)=iterm1
      else
      Row_indices(iterm2,I)=iterm2
      End if
55    end do
66    end do

      Do I=1, m_throat
      if (ConThrtNod(2,i).eq.-1) then
      K2=CONTHRTNOD(1,i)
      Do K=1, Coordmat(K2)
      iterm3=Connodthrt(K,K2)
      iterm1=Conthrtnod(1,iterm3)
      iterm2=Conthrtnod(2,iterm3)
      IF (iterm2.LE.0) then
      Row_indices(iterm1,iterm1)=iterm1
      go to 44
      End if
      IF (iterm1.NE.K2) then
      Row_indices(iterm1,k2)=iterm1
      else
      Row_indices(iterm2,k2)=iterm2
      End if
44    end do
      endif
      end do
      Do I=1, n_pore
      Do j=1, n_pore
       If (Row_indices(J,I).NE.0)then
      IRN(K4)=Row_indices(J,I)
      K4=K4+1
      else
      go to 43
      end if
43    end do
      end do
      IP(1) = 1
      Do I =1, n_pore
      K4=0
      Do J=1,n_pore
      If (Row_indices(J,I).NE.0)then
      K4=K4+1
      end if
      End do
      IP(I+1)= IP(I)+ k4
```

```
      End do
      DO I=1,n_pore
         A(I)=-1
         IRNA(I)=I
         IPA(I)=I
      end do
      IPA(n_pore+1)=n_pore+1
      IFLAG = 1
      HMAX = 0
   40 CONTINUE
      CALL FUNC ( N, X, F,F1, DERIV,coordmat,connodthrt,CONTHRTNOD
      ,Kw1,k3,Wet_p,Pbot,Ptop,n_bot, n_top, n_pore,
      m_throat, max_coord,F1_DERIV,Non_Zero_deriv)

      CALL NS23AD( M, N, SAC, STPMIN, MAXFUN, IPRINT, IRN, IP,
              A, IRNA, IPA, HMAX, LIW, IW, LW, W, X, F, DERIV, IFLAG,
              ICNTL,CNTL,INFO,RINFO,KEEP,RKEEP,LKEEP)
      IF(IFLAG.GT.0) GO TO 40
      IF (IFLAG.EQ.0) THEN
      WRITE(*,*) ' INFO matrix',(INFO(I),I=1,5)
      WRITE(*,*) ' IFLAG =',IFLAG
      WRITE(6,'(A,/,(5I9))') 'ICNTL vector',(ICNTL(I),I=1,5)
      WRITE(6,'(A,/,(5F9.5))') 'CNTL vector',(CNTL(I),I=1,5)
      WRITE(*,*) ' Solution is',(X(I),I=1,5)
      ELSE
          WRITE(6,'(A,I4)') ' Failure. INFO(1:5) =',(INFO(I),I=1,5)
          WRITE(6,'(A,/,(5I9))') 'ICNTL vector',(ICNTL(I),I=1,5)
          WRITE(6,'(A,/,(5F9.5))') 'CNTL vector',(CNTL(I),I=1,5)
      END IF
      deallocate (IW,W,IRN,IP,IRNA,IPA,F,A,Deriv,Row_indices,F1_deriv
       ,F1)
      END SUBROUTINE

      SUBROUTINE FUNC ( N, X, F,F1,
DERIV,coordmat,connodthrt,CONTHRTNOD
      ,Kw1,k3,Wet_p,Pbot,Ptop,n_bot, n_top, n_pore,
      m_throat, max_coord,F1_DERIV,Non_Zero_deriv)
      INTEGER:: N, i, j, k, K1,k2,n_bot, n_top, n_pore, m_throat,
       coordmat(n_pore),ConThrtNod(2,m_throat),max_coord,
       ConNodThrt(max_coord,n_pore),PB_index_2nd_end(max_coord,n_pore)
      DOUBLE PRECISION
X(N),F(N),DERIV(Non_Zero_deriv),F1(N,N),Wet_p(N),
      Kw1(m_throat),k3(m_throat), bb_mat(n_pore),F1_DERIV(N,N), term1
      ,c(5), term2
      Real Pbot,Ptop
      F1=0.0d0
      F1_DERIV=0.0d0
      PB_index_2nd_end=0
      bb_mat(n_pore)=0.0
      term1=0

      Do i =1, m_throat
      if (ConThrtNod(2,i).eq.0) then
      K2=CONTHRTNOD(1,i)
      do j=1,coordmat(k2)
      K=connodthrt(j,K2)
      iterm1=CONTHRTNOD(1,k)
      iterm2=CONTHRTNOD(2,k)
      PB_index_2nd_end(j,k2)=iterm1
      if (k2==iterm1) then
      PB_index_2nd_end(j,k2)=iterm2
      end if
```

```
      If (i/=k) then
      If (wet_p(PB_index_2nd_end(j,k2)).GT.wet_p(k2)) then
      If (((x(PB_index_2nd_end(j,k2)).ne.0).and.(x(k2).ne.0)).and.
       (x(PB_index_2nd_end(j,k2)).GT.x(k2))) then
      F1(PB_index_2nd_end(j,k2),K2)=(-Kw1(k)+sqrt(Kw1(k)**2.0d0+4.0d0*
      k3(k)*(X(PB_index_2nd_end(j,k2))-X(k2))))/(2.0d0*k3(k))
      F1_DERIV(K2,PB_index_2nd_end(j,k2))=1.0d0/(sqrt(Kw1(k)**2.0d0+
      4.0d0*k3(k)*(X(PB_index_2nd_end(j,k2))-X(k2))))
      else if
(((x(PB_index_2nd_end(j,k2)).ne.0).and.(x(k2).ne.0)).and.
       (x(PB_index_2nd_end(j,k2)).LT.x(k2))) then
      F1(PB_index_2nd_end(j,k2),K2)=-1.0d0*(-
Kw1(k)+sqrt(Kw1(k)**2.0d0+
      4.0d0*k3(k)*(X(k2)-X(PB_index_2nd_end(j,k2)))))/(2.0d0*k3(k))
      F1_DERIV(k2,PB_index_2nd_end(j,k2))=1.0d0/(sqrt(Kw1(k)**2.0d0+
      4.0d0*k3(k)*(X(k2)-X(PB_index_2nd_end(j,k2))))
      else
      F1(PB_index_2nd_end(j,k2),K2)=(-Kw1(k)+sqrt(Kw1(k)**2.0d0+4.0d0*
      k3(k)*(X(PB_index_2nd_end(j,k2))-X(k2))))/(2.0d0*k3(k))
      F1_DERIV(K2,PB_index_2nd_end(j,k2))=1.0d0/(sqrt(Kw1(k)**2.0d0+
      4.0d0*k3(k)*(X(PB_index_2nd_end(j,k2))-X(k2))))
       end if
      else

      if (((x(PB_index_2nd_end(j,k2)).ne.0).and.(x(k2).ne.0)).and.
       (x(PB_index_2nd_end(j,k2)).LT.x(k2))) then
      F1(PB_index_2nd_end(j,k2),K2)=-1.0d0*(-
Kw1(k)+sqrt(Kw1(k)**2.0d0+
      4.0d0*k3(k)*(X(k2)-X(PB_index_2nd_end(j,k2)))))/(2.0d0*k3(k))
      F1_DERIV(k2,PB_index_2nd_end(j,k2))=1.0d0/(sqrt(Kw1(k)**2.0d0+
      4.0d0*k3(k)*(X(k2)-X(PB_index_2nd_end(j,k2)))))
      else if(((x(PB_index_2nd_end(j,k2)).ne.0).and.(x(k2).ne.0)).and.
       (x(PB_index_2nd_end(j,k2)).GT.x(k2))) then
      F1(PB_index_2nd_end(j,k2),K2)=(-Kw1(k)+sqrt(Kw1(k)**2.0d0+4.0d0*
      k3(k)*(X(PB_index_2nd_end(j,k2))-X(k2))))/(2.0d0*k3(k))

      F1_DERIV(K2,PB_index_2nd_end(j,k2))=1.0d0/(sqrt(Kw1(k)**2.0d0+
      4.0d0*k3(k)*(X(PB_index_2nd_end(j,k2))-X(k2))))
      else
      F1(PB_index_2nd_end(j,k2),K2)=-1.0d0*(-
Kw1(k)+sqrt(Kw1(k)**2.0d0+
      4.0d0*k3(k)*(X(k2)-X(PB_index_2nd_end(j,k2)))))/(2.0d0*k3(k))

      F1_DERIV(k2,PB_index_2nd_end(j,k2))=1.0d0/(sqrt(Kw1(k)**2.0d0+
      4.0d0*k3(k)*(X(k2)-X(PB_index_2nd_end(j,k2)))))
      end if
      end if
      elseIf (i==k) then
      F1(k2,K2)=-1.0d0*(-Kw1(k)+sqrt(Kw1(k)**2.0d0+
       4.0d0*k3(k)*(X(k2)-Pbot)))/(2.0d0*k3(k))

      F1_DERIV(k2,K2)=-1.0d0/(sqrt(Kw1(k)**2.0d0+
       4.0d0*k3(k)*(X(k2)-Pbot)))

      End if
      End do
      Term2=F1_DERIV(k2,K2)
      F1_DERIV(k2,K2)=0
      F1_DERIV(k2,K2)=-1.0d0*sum((F1_DERIV(k2,1:n_pore)))+term2+1
      F(k2)=sum(F1(1:n_pore,k2))+x(k2)
      endif
      end do
```

```
      Do i =1, m_throat
      if (ConThrtNod(2,i).eq.-1) then
      K2=CONTHRTNOD(1,i)
      do j=1,coordmat(k2)
      K=connodthrt(j,K2)
      iterm1=CONTHRTNOD(1,k)
      iterm2=CONTHRTNOD(2,k)
      PB_index_2nd_end(j,k2)=iterm1
      if (k2==iterm1) then
      PB_index_2nd_end(j,k2)=iterm2
      end if
      If (i/=k) then
      If (wet_p(PB_index_2nd_end(j,k2)).GT.wet_p(k2))then
      If (((x(PB_index_2nd_end(j,k2)).ne.0).and.(x(k2).ne.0)).and.
       (x(PB_index_2nd_end(j,k2)).GT.x(k2))) then

      F1(PB_index_2nd_end(j,k2),K2)=(-Kw1(k)+sqrt(Kw1(k)**2.0d0+4.0d0
      *k3(k)*(X(PB_index_2nd_end(j,k2))-X(k2))))/(2.0d0*k3(k))

      F1_DERIV(K2,PB_index_2nd_end(j,k2))=1.0d0/(sqrt(Kw1(k)**2.0d0+
      4.0d0*k3(k)*(X(PB_index_2nd_end(j,k2))-X(k2))))

      else if
(((x(PB_index_2nd_end(j,k2)).ne.0).and.(x(k2).ne.0)).and.
       (x(PB_index_2nd_end(j,k2)).LT.x(k2))) then
      F1(PB_index_2nd_end(j,k2),K2)=-1.0d0*(-
Kw1(k)+sqrt(Kw1(k)**2.0d0+
       4.0d0*k3(k)*(X(k2)-X(PB_index_2nd_end(j,k2)))))/
      (2.0d0*k3(k))
      F1_DERIV(K2,PB_index_2nd_end(j,k2))=1.0d0/(sqrt(Kw1(k)**2.0d0+
      4.0d0*k3(k)*abs(X(k2)-X(PB_index_2nd_end(j,k2))))
      else
      F1(PB_index_2nd_end(j,k2),K2)=(-Kw1(k)+sqrt(Kw1(k)**2.0d0+4.0d0
      *k3(k)*(X(PB_index_2nd_end(j,k2))-X(k2))))/(2.0d0*k3(k))
      F1_DERIV(K2,PB_index_2nd_end(j,k2))=1.0d0/(sqrt(Kw1(k)**2.0d0+
      4.0d0*k3(k)*(X(PB_index_2nd_end(j,k2))-X(k2))))
      endif
      else

      if (((x(PB_index_2nd_end(j,k2)).ne.0).and.(x(k2).ne.0)).and.
       (x(PB_index_2nd_end(j,k2)).LT.x(k2))) then
      F1(PB_index_2nd_end(j,k2),K2)=-1.0d0*(-
Kw1(k)+sqrt(Kw1(k)**2.0d0+
       4.0d0*k3(k)*(X(k2)-X(PB_index_2nd_end(j,k2)))))/
      (2.0d0*k3(k))
      F1_DERIV(K2,PB_index_2nd_end(j,k2))=1.0d0/(sqrt(Kw1(k)**2.0d0+
      4.0d0*k3(k)*abs(X(k2)-X(PB_index_2nd_end(j,k2))))
      else if
(((x(PB_index_2nd_end(j,k2)).ne.0).and.(x(k2).ne.0)).and.
       (x(PB_index_2nd_end(j,k2)).GT.x(k2))) then
      F1(PB_index_2nd_end(j,k2),K2)=(-Kw1(k)+sqrt(Kw1(k)**2.0d0+4.0d0
      *k3(k)*(X(PB_index_2nd_end(j,k2))-X(k2))))/(2.0d0*k3(k))
      F1_DERIV(K2,PB_index_2nd_end(j,k2))=1.0d0/(sqrt(Kw1(k)**2.0d0+
      4.0d0*k3(k)*(X(PB_index_2nd_end(j,k2))-X(k2))))
      Else
      F1(PB_index_2nd_end(j,k2),K2)=-1.0d0*(-
Kw1(k)+sqrt(Kw1(k)**2.0d0+
       4.0d0*k3(k)*(X(k2)-X(PB_index_2nd_end(j,k2)))))/
      (2.0d0*k3(k))
      F1_DERIV(K2,PB_index_2nd_end(j,k2))=1.0d0/(sqrt(Kw1(k)**2.0d0+
      4.0d0*k3(k)*abs(X(k2)-X(PB_index_2nd_end(j,k2))))
```

```
      endif
      end if
      elseIf (i==k) then
      F1(k2,K2)=(-Kw1(k)+sqrt(Kw1(k)**2.0d0+4.0d0*
       k3(k)*abs(ptop-X(k2))))/(2.0d0*k3(k))
      F1_DERIV(k2,K2)=-1.0d0/(sqrt(Kw1(k)**2.0d0+4.0d0*
       k3(k)*abs(ptop-X(k2))))

      End if
      End do
      Term2=F1_DERIV(k2,K2)
      F1_DERIV(k2,K2)=0
      F1_DERIV(k2,K2)=-1.0d0*sum((F1_DERIV(k2,1:n_pore)))+term2+1
      F(k2)=sum(F1(1:n_pore,k2))+x(k2)
      endif
      end do

      Do i =1, n_pore
      Do K=1, Coordmat(I)
      iterm3=Connodthrt(K,I)
      iterm1=Conthrtnod(1,iterm3)
      iterm2=Conthrtnod(2,iterm3)
      IF (iterm2.LE.0) go to 7
      End do
      do j=1,coordmat(I)
      K=connodthrt(j,I)
      iterm1=CONTHRTNOD(1,k)
      iterm2=CONTHRTNOD(2,k)
      PB_index_2nd_end(j,I)=iterm1
      if (I==iterm1) then
      PB_index_2nd_end(j,I)=iterm2
      end if
      If (wet_p(PB_index_2nd_end(j,I)).GT.wet_p(I))then
      If (((x(PB_index_2nd_end(j,I)).ne.0).and.(x(I).ne.0)).and.
       (x(PB_index_2nd_end(j,I)).GT.x(I))) then
       F1(PB_index_2nd_end(j,I),I)=(-Kw1(k)+sqrt(Kw1(k)**2.0d0+4.0d0*
       k3(k)*(X(PB_index_2nd_end(j,I))-X(I))))/(2.0d0*k3(k))
      F1_DERIV(I,PB_index_2nd_end(j,I))=1.0d0/(sqrt(Kw1(k)**2.0d0+
      4.0d0*k3(k)*(X(PB_index_2nd_end(j,I))-X(I))))
      else if (((x(PB_index_2nd_end(j,I)).ne.0).and.(x(I).ne.0)).and.
       (x(PB_index_2nd_end(j,I)).LT.x(I))) then
      F1(PB_index_2nd_end(j,I),I)=-1*(-
Kw1(k)+sqrt(Kw1(k)**2.0d0+4.0d0*
       k3(k)*(X(I)-X(PB_index_2nd_end(j,I)))))/(2.0d0*k3(k))
      F1_DERIV(I,PB_index_2nd_end(j,I))=1.0d0/(sqrt(Kw1(k)**2.0d0+
      4.0d0*k3(k)*(X(I)-X(PB_index_2nd_end(j,I))))
      else
       F1(PB_index_2nd_end(j,I),I)=(-Kw1(k)+sqrt(Kw1(k)**2.0d0+4.0d0*
       k3(k)*(X(PB_index_2nd_end(j,I))-X(I))))/(2.0d0*k3(k))
      F1_DERIV(I,PB_index_2nd_end(j,I))=1.0d0/(sqrt(Kw1(k)**2.0d0+
      4.0d0*k3(k)*(X(PB_index_2nd_end(j,I))-X(I))))

      end if
      else
      if (((x(PB_index_2nd_end(j,I)).ne.0).and.(x(I).ne.0)).and.
       (x(PB_index_2nd_end(j,I)).LT.x(I))) then
       F1(PB_index_2nd_end(j,I),I)=-1*(-
Kw1(k)+sqrt(Kw1(k)**2.0d0+4.0d0*
       k3(k)*(X(I)-X(PB_index_2nd_end(j,I)))))/(2.0d0*k3(k))
      F1_DERIV(I,PB_index_2nd_end(j,I))=1.0d0/(sqrt(Kw1(k)**2.0d0+
      4.0d0*k3(k)*(X(I)-X(PB_index_2nd_end(j,I))))
      else if (((x(PB_index_2nd_end(j,I)).ne.0).and.(x(I).ne.0)).and.
```

```
        (x(PB_index_2nd_end(j,I)).GT.x(I))) then
       F1(PB_index_2nd_end(j,I),I)=(-Kw1(k)+sqrt(Kw1(k)**2.0d0+4.0d0*
        k3(k)*(X(PB_index_2nd_end(j,I))-X(I))))/(2.0d0*k3(k))
       F1_DERIV(I,PB_index_2nd_end(j,I))=1.0d0/(sqrt(Kw1(k)**2.0d0+
       4.0d0*k3(k)*(X(PB_index_2nd_end(j,I))-X(I))))
       else
       F1(PB_index_2nd_end(j,I),I)=-1*(-
Kw1(k)+sqrt(Kw1(k)**2.0d0+4.0d0*
        k3(k)*(X(I)-X(PB_index_2nd_end(j,I)))))/(2.0d0*k3(k))
       F1_DERIV(I,PB_index_2nd_end(j,I))=1.0d0/(sqrt(Kw1(k)**2.0d0+
       4.0d0*k3(k)*(X(I)-X(PB_index_2nd_end(j,I)))))
       end if
        end if
       end do
       F1_DERIV(I,I)=-1.0d0*sum((F1_DERIV(I,1:n_pore)))+1
       F(I)=sum(F1(1:n_pore,I))+x(I)
7      End do
       K=1
       Do I =1, n_pore
       Do j = 1, n_pore
       If (F1_DERIV(J,I).NE.0.0) then
       Deriv(K)=F1_DERIV(J,I)
       K=K+1
       endif
       end do
       end do
       END SUBROUTINE
```

Appendix B: Algorithm of the laminar, Forchheimer and turbulent flow regimes PNM code

B-1. Code flow chart

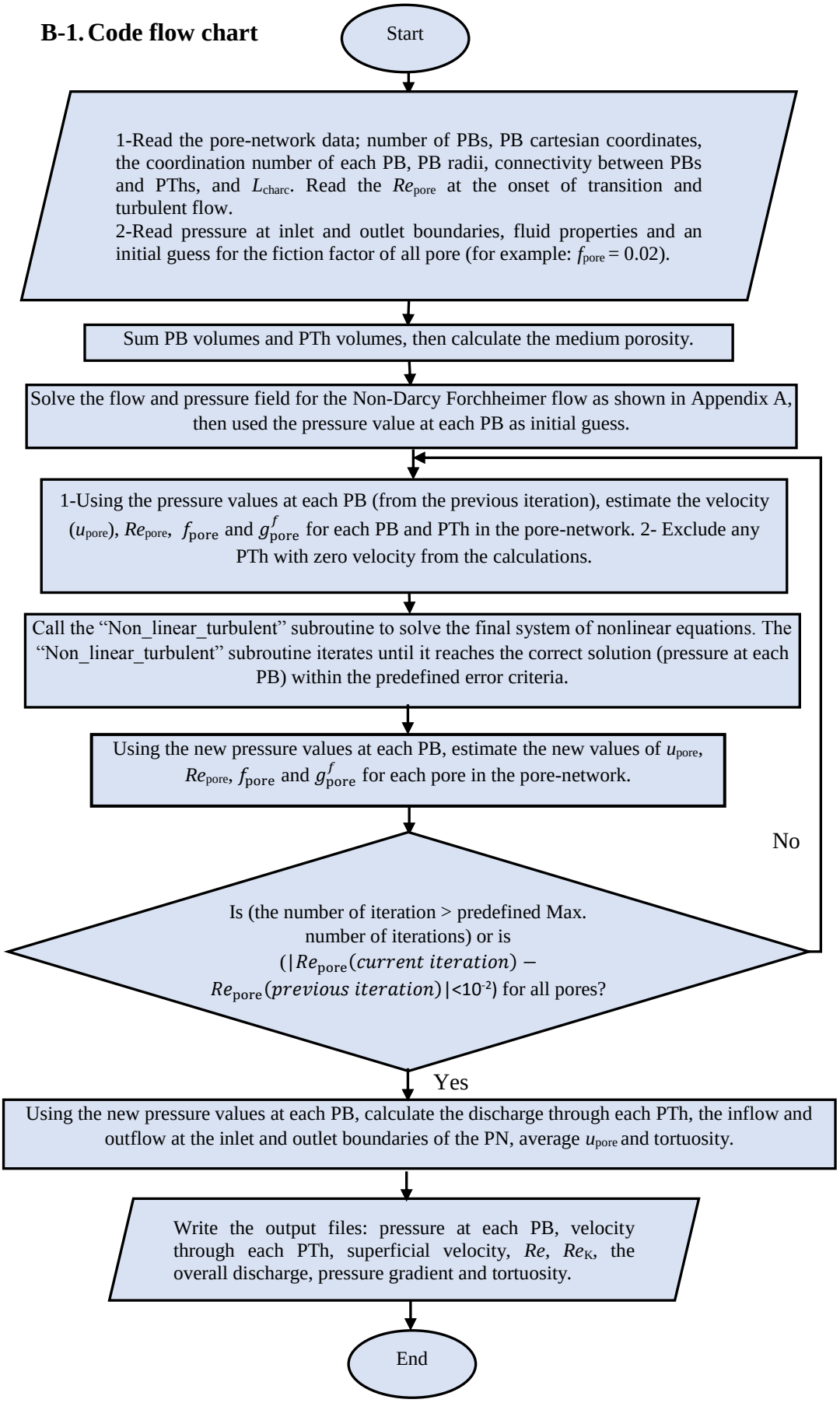

B-2. Solving the nonlinear system of equations

Assuming the following simple pore-network:

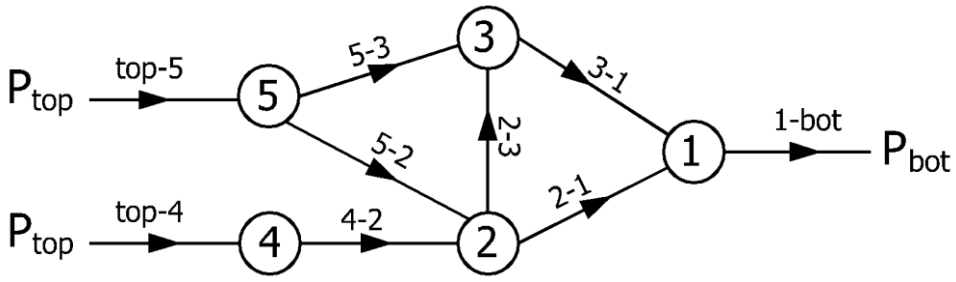

Figure 1B A simple example of a pore-network.

Starting from Equation 5.7:

$$q_{\mathrm{i-j}} = \sqrt{\frac{\Delta P_{\mathrm{i-j}}^{\mathrm{tot}}}{\left[\frac{L_{\mathrm{i-j,tot}}}{g_{i-j,tot}^{f}}\right] + K_e \frac{\rho}{2a_{\mathrm{i-j}}^2} + K_c \frac{\rho}{2a_{\mathrm{i-j}}^2}}} \qquad 5.7$$

Equation 5.7 can be written as

$$q_{\mathrm{i-j}} = \sqrt{\frac{\Delta P_{\mathrm{i-j}}^{\mathrm{tot}}}{K3}} \qquad 9.8$$

Where $K3 = \left[\frac{L_{\mathrm{i-j,tot}}}{g_{i-j,tot}^{f}}\right] + K_e \frac{\rho}{2a_{\mathrm{i-j}}^2} + K_c \frac{\rho}{2a_{\mathrm{i-j}}^2}$

And by applying the continuity equation (Equation 4.11) at each node (pore body) in Figure 1B, the following system of equations can be obtained:

<u>At node 1:</u>

$q_{2-1} + q_{3-1} - q_{1-bot} = 0.0$

Then

$$\sqrt{\frac{\Delta P_{2-1}^{tot}}{K3_{2-1}}} + \sqrt{\frac{\Delta P_{3-1}^{tot}}{K3_{3-1}}} - \sqrt{\frac{\Delta P_{1-bot}^{tot}}{K3_{1-bot}}} = 0.0$$

Then

$$\sqrt{\frac{[P_2 - P_1]}{K3_{2-1}}} + \sqrt{\frac{[P_3 - P_1]}{K3_{3-1}}} - \sqrt{\frac{[P_1 - P_{bot}]}{K3_{1-bot}}} + P_1 - P_1 = 0.0 \qquad 9.9$$

<u>At node 2:</u>

$q_{4-2} + q_{5-2} - q_{2-3} - q_{2-1} = 0.0$

Then

$$\sqrt{\frac{\Delta P_{4-2}}{K3_{4-2}}} + \sqrt{\frac{\Delta P_{5-2}}{K3_{5-2}}} - \sqrt{\frac{\Delta P_{2-3}}{K3_{2-3}}} - \sqrt{\frac{\Delta P_{2-1}}{K3_{2-1}}} = 0.0$$

Then

$$\sqrt{\frac{[P_4-P_2]}{K3_{4-2}}}+\sqrt{\frac{[P_5-P_2]}{K3_{5-2}}}-\sqrt{\frac{[P_2-P_3]}{K3_{2-3}}}-\sqrt{\frac{[P_2-P_1]}{K3_{2-1}}}+P_2-P_2=0.0 \quad 9.10$$

At node 3:

$q_{5-3}+q_{2-3}-q_{3-1}=0.0$

Then

$$\sqrt{\frac{[P_5-P_3]}{K3_{5-3}}}+\sqrt{\frac{[P_2-P_3]}{K3_{2-3}}}-\sqrt{\frac{[P_3-P_1]}{K3_{3-1}}}=0$$

Then

$$\sqrt{\frac{[P_5-P_3]}{K3_{5-3}}}+\sqrt{\frac{[P_2-P_3]}{K3_{2-3}}}-\sqrt{\frac{[P_3-P_1]}{K3_{3-1}}}+P_3-P_3=0.0 \quad 9.11$$

At node 4:

$q_{top-4}-q_{4-2}=0.0$

Then

$$\sqrt{\frac{\Delta P_{top-4}}{K3_{top-4}}}-\sqrt{\frac{\Delta P_{4-2}}{K3_{4-2}}}=0.0$$

Then

$$\sqrt{\frac{[P_{top}-P_4]}{K3_{top-4}}}-\sqrt{\frac{[P_4-P_2]}{K3_{4-2}}}+P_4-P_4=0.0 \quad 9.12$$

At node 5:

$q_{top-5}-q_{5-3}-q_{5-2}=0.0$

Then

$$\sqrt{\frac{[P_{top}-P_5]}{K3_{top-5}}}-\sqrt{\frac{[P_5-P_3]}{K3_{5-3}}}-\sqrt{\frac{[P_5-P_2]}{K3_{5-2}}}=0.0$$

Then

$$\sqrt{\frac{[P_{top}-P_5]}{K3_{top-5}}}-\sqrt{\frac{[P_5-P_3]}{K3_{5-3}}}-\sqrt{\frac{[P_5-P_2]}{K3_{5-2}}}+P_5-P_5=0.0 \quad 9.13$$

The final five equations (9.9, 9.10, 9.11, 9.12 and 9.13) can be written in the form required by the of HSL NS23 routine (HSL, 2013), used to solve a system of nonlinear equations in FORTRAN, as follows:

$$\sqrt{\frac{[P_2-P_1]}{K3_{2-1}}}+\sqrt{\frac{[P_3-P_1]}{K3_{3-1}}}-\sqrt{\frac{[P_1-P_{bot}]}{K3_{1-bot}}}+P_1-P_1=F_1(P_1,P_2,P_3)-P_1=0 \quad 9.9`$$

Where $F_1(P_1, P_2, P_3) = \sqrt{\frac{[P_2 - P_1]}{K3_{2-1}}} + \sqrt{\frac{[P_3 - P_1]}{K3_{3-1}}} - \sqrt{\frac{[P_1 - P_{bot}]}{K3_{1-bot}}} + P_1$

And

$$\sqrt{\frac{[P_4 - P_2]}{K3_{4-2}}} + \sqrt{\frac{[P_5 - P_2]}{K3_{5-2}}} - \sqrt{\frac{[P_2 - P_3]}{K3_{2-3}}} - \sqrt{\frac{[P_2 - P_1]}{K3_{2-1}}} + P_2 - P_2 = F_2(P_1, P_2, P_3, P_4, P_5) - P_2 = 0.0 \quad 9.10`$$

And

$$\sqrt{\frac{[P_5 - P_3]}{K3_{5-3}}} + \sqrt{\frac{[P_2 - P_3]}{K3_{2-3}}} - \sqrt{\frac{[P_3 - P_1]}{K3_{3-1}}} + P_3 - P_3 = F_3(P_1, P_2, P_3, P_5) - P_3 = 0.0 \quad 9.11`$$

And

$$\sqrt{\frac{[P_{top} - P_4]}{K3_{top-4}}} - \sqrt{\frac{[P_4 - P_2]}{K3_{4-2}}} + P_4 - P_4 = F_4(P_2, P_4) - P_4 = 0 \quad 9.12`$$

And

$$\sqrt{\frac{[P_{top} - P_5]}{K3_{top-5}}} - \sqrt{\frac{[P_5 - P_3]}{K3_{5-3}}} - \sqrt{\frac{[P_5 - P_2]}{K3_{5-2}}} + P_5 - P_5 = F_5(P_2, P_3, P_5) - P_5 = 0 \quad 9.13`$$

The of HSL NS23 routine (HSL, 2013), requires the nonzero derivatives of each equation (the Jacobian matrix) as shown below:

$$\frac{\partial F_i}{\partial P_j} = \begin{bmatrix} \frac{\partial F_1}{\partial P_1} & \frac{\partial F_1}{\partial P_2} & \frac{\partial F_1}{\partial P_3} & \frac{\partial F_1}{\partial P_4} & \frac{\partial F_1}{\partial P_5} \\ \frac{\partial F_2}{\partial P_1} & \frac{\partial F_2}{\partial P_2} & \frac{\partial F_2}{\partial P_3} & \frac{\partial F_2}{\partial P_4} & \frac{\partial F_2}{\partial P_5} \\ \frac{\partial F_3}{\partial P_1} & \frac{\partial F_3}{\partial P_2} & \frac{\partial F_3}{\partial P_3} & \frac{\partial F_3}{\partial P_4} & \frac{\partial F_3}{\partial P_5} \\ \frac{\partial F_4}{\partial P_1} & \frac{\partial F_4}{\partial P_2} & \frac{\partial F_4}{\partial P_3} & \frac{\partial F_4}{\partial P_4} & \frac{\partial F_4}{\partial P_5} \\ \frac{\partial F_5}{\partial P_1} & \frac{\partial F_5}{\partial P_2} & \frac{\partial F_5}{\partial P_3} & \frac{\partial F_5}{\partial P_4} & \frac{\partial F_5}{\partial P_5} \end{bmatrix}$$

$$= \begin{bmatrix} \frac{\partial F_1}{\partial P_1} & \frac{\partial F_1}{\partial P_2} & \frac{\partial F_1}{\partial P_3} & 0 & 0 \\ \frac{\partial F_2}{\partial P_1} & \frac{\partial F_2}{\partial P_2} & \frac{\partial F_2}{\partial P_3} & \frac{\partial F_2}{\partial P_4} & \frac{\partial F_2}{\partial P_5} \\ \frac{\partial F_3}{\partial P_1} & \frac{\partial F_3}{\partial P_2} & \frac{\partial F_3}{\partial P_3} & 0 & \frac{\partial F_3}{\partial P_5} \\ 0 & \frac{\partial F_4}{\partial P_2} & 0 & \frac{\partial F_4}{\partial P_4} & 0 \\ 0 & \frac{\partial F_5}{\partial P_2} & \frac{\partial F_5}{\partial P_3} & 0 & \frac{\partial F_5}{\partial P_5} \end{bmatrix}$$

$$F_1(P_1,P_2,P_3)=\sqrt{\frac{[P_2-P_1]}{K3_{2-1}}}+\sqrt{\frac{[P_3-P_1]}{K3_{3-1}}}-\sqrt{\frac{[P_1-P_{bot}]}{K3_{1-bot}}}+P_1=0.0$$

Then

$$\frac{\partial F_1(P_1,P_2,P_3)}{\partial P_1}=\frac{\partial}{\partial P_1}\left[\sqrt{\frac{[P_2-P_1]}{K3_{2-1}}}+\sqrt{\frac{[P_3-P_1]}{K3_{3-1}}}-\sqrt{\frac{[P_1-P_{bot}]}{K3_{1-bot}}}\right]+\frac{\partial}{\partial P_1}P_1=$$
$$-\frac{1}{2\sqrt{(K3_{2-1})[P_2-P_1]}}-\frac{1}{2\sqrt{(K3_{3-1})[P_3-P_1]}}-\frac{1}{2\sqrt{(K3_{1-bot})[P_1-P_{bot}]}}+1$$

and

$$\frac{\partial F_1(P_1,P_2,P_3)}{\partial P_2}=\frac{\partial}{\partial P_2}\left[\sqrt{\frac{[P_2-P_1]}{K3_{2-1}}}\right]=\frac{1}{2\sqrt{(K3_{2-1})[P_2-P_1]}}$$

and

$$\frac{\partial F_1(P_1,P_2,P_3)}{\partial P_3}=\frac{\partial}{\partial P_3}\left[\sqrt{\frac{[P_3-P_1]}{K3_{3-1}}}\right]=\frac{1}{2\sqrt{(K3_{3-1})[P_3-P_1]}}$$

$$F_2(P_1,P_2,P_3,P_4,P_5)=\sqrt{\frac{[P_4-P_2]}{K3_{4-2}}}+\sqrt{\frac{[P_5-P_2]}{K3_{5-2}}}-\sqrt{\frac{[P_2-P_3]}{K3_{2-3}}}-\sqrt{\frac{[P_2-P_1]}{K3_{2-1}}}+P_2=0.0$$

then

$$\frac{\partial F_2(P_1,P_2,P_3,P_4,P_5)}{\partial P_1}=\frac{\partial}{\partial P_1}\left[-\sqrt{\frac{[P_2-P_1]}{K3_{2-1}}}\right]=\frac{1}{2\sqrt{(K3_{2-1})[P_2-P_1]}}$$

and

$$\frac{\partial F_2(P_1,P_2,P_3,P_4,P_5)}{\partial P_2}=\frac{\partial}{\partial P_2}\left[\sqrt{\frac{[P_4-P_2]}{K3_{4-2}}}+\sqrt{\frac{[P_5-P_2]}{K3_{5-2}}}-\sqrt{\frac{[P_2-P_3]}{K3_{2-3}}}-\sqrt{\frac{[P_2-P_1]}{K3_{2-1}}}+P_2\right]=$$
$$-\frac{1}{2\sqrt{(K3_{4-2})[P_4-P_2]}}-\frac{1}{2\sqrt{(K3_{5-2})[P_5-P_2]}}-\frac{1}{2\sqrt{(K3_{2-3})[P_2-P_3]}}-\frac{1}{2\sqrt{(K3_{2-1})[P_2-P_1]}}+1$$

and

$$\frac{\partial F_2(P_1,P_2,P_3,P_4,P_5)}{\partial P_3}=\frac{\partial}{\partial P_3}\left[-\sqrt{\frac{[P_2-P_3]}{K3_{2-3}}}\right]=\frac{1}{2\sqrt{(K3_{2-3})[P_2-P_3]}}$$

and

$$\frac{\partial F_2(P_1,P_2,P_3,P_4,P_5)}{\partial P_4}=\frac{\partial}{\partial P_4}\left[\sqrt{\frac{[P_4-P_2]}{K3_{4-2}}}\right]=\frac{1}{2\sqrt{(K3_{4-2})[P_4-P_2]}}$$

and

$$\frac{\partial F_2(P_1,P_2,P_3,P_4,P_5)}{\partial P_5}=\frac{\partial}{\partial P_5}\left[\sqrt{\frac{[P_5-P_2]}{K3_{5-2}}}\right]=\frac{1}{2\sqrt{(K3_{5-2})[P_5-P_2]}}$$

$$F_3(P_1,P_2,P_3,P_5)=\sqrt{\frac{[P_5-P_3]}{K3_{5-3}}}+\sqrt{\frac{[P_2-P_3]}{K3_{2-3}}}-\sqrt{\frac{[P_3-P_1]}{K3_{3-1}}}+P_3$$

then

$$\frac{\partial F_3(P_1,P_2,P_3,P_5)}{\partial P_1}=\frac{\partial}{\partial P_1}\left[-\sqrt{\frac{[P_3-P_1]}{K3_{3-1}}}\right]=\frac{1}{2\sqrt{(K3_{3-1})[P_3-P_1]}}$$

and

$$\frac{\partial F_3(P_1,P_2,P_3,P_5)}{\partial P_2}=\frac{\partial}{\partial P_2}\left[\sqrt{\frac{[P_2-P_3]}{K3_{2-3}}}\right]=\frac{1}{2\sqrt{(K3_{2-3})[P_2-P_3]}}$$

and

$$\frac{\partial F_3(P_1,P_2,P_3,P_5)}{\partial P_3}=\frac{\partial}{\partial P_3}\left[\sqrt{\frac{[P_5-P_3]}{K3_{5-3}}}+\sqrt{\frac{[P_2-P_3]}{K3_{2-3}}}-\sqrt{\frac{[P_3-P_1]}{K3_{3-1}}}+P_3\right]=$$
$$-\frac{1}{2\sqrt{(K3_{5-3})[P_5-P_3]}}-\frac{1}{2\sqrt{(K3_{2-3})[P_2-P_3]}}-\frac{1}{2\sqrt{(K3_{3-1})[P_3-P_1]}}+1$$

and

$$\frac{\partial F_3(P_1,P_2,P_3,P_5)}{\partial P_5}=\frac{\partial}{\partial P_5}\left[\sqrt{\frac{[P_5-P_3]}{K3_{5-3}}}\right]=\frac{1}{2\sqrt{(K3_{5-3})[P_5-P_3]}}$$

$$F_4(P_2,P_4)=\sqrt{\frac{[P_{top}-P_4]}{K3_{top-4}}}-\sqrt{\frac{[P_4-P_2]}{K3_{4-2}}}+P_4=0.0$$

then

$$\frac{\partial F_4(P_2,P_4)}{\partial P_2}=\frac{\partial}{\partial P_2}\left[-\sqrt{\frac{[P_4-P_2]}{K3_{4-2}}}\right]=\frac{1}{2\sqrt{(K3_{4-2})[P_4-P_2]}}$$

and

$$\frac{\partial F_4(P_2,P_4)}{\partial P_4}=\frac{\partial}{\partial P_4}\left[\sqrt{\frac{[P_{top}-P_4]}{K3_{top-4}}}-\sqrt{\frac{[P_4-P_2]}{K3_{4-2}}}+P_4\right]=-\frac{1}{2\sqrt{(K3_{top-4})[P_{top}-P_4]}}-$$
$$\frac{1}{2\sqrt{(K3_{4-2})[P_4-P_2]}}+1$$

$$F_5(P_2,P_3,P_5)=\sqrt{\frac{[P_{top}-P_5]}{K3_{top-5}}}-\sqrt{\frac{[P_5-P_3]}{K3_{5-3}}}-\sqrt{\frac{[P_5-P_2]}{K3_{5-2}}}+P_5$$

then

$$\frac{\partial F_5(P_2,P_3,P_5)}{\partial P_2}=\frac{\partial}{\partial P_2}\left[-\sqrt{\frac{[P_5-P_2]}{K3_{5-2}}}\right]=\frac{1}{2\sqrt{(K3_{5-2})[P_5-P_2]}}$$

and

$$\frac{\partial F_5(P_2,P_3,P_5)}{\partial P_3}=\frac{\partial}{\partial P_3}\left[-\sqrt{\frac{[P_5-P_3]}{K3_{5-3}}}\right]=\frac{1}{2\sqrt{(K3_{5-3})[P_5-P_3]}}$$

and

$$\frac{\partial F_5(P_2,P_3,P_5)}{\partial P_5} = \frac{\partial}{\partial P_5}\left[\sqrt{\frac{[P_{top}-P_5]}{K3_{top-5}}} - \sqrt{\frac{[P_5-P_3]}{K3_{5-3}}} - \sqrt{\frac{[P_5-P_2]}{K3_{5-2}}} + P_5\right] =$$

$$-\frac{1}{2\sqrt{(K3_{top-5})[P_{top}-P_5]}} - \frac{1}{2\sqrt{(K3_{5-3})[P_5-P_3]}} - \frac{1}{2\sqrt{(K3_{5-2})[P_5-P_2]}} + 1$$

After providing the previous equations and derivatives to the HSL NS23 routine (HSL, 2013), the HSL NS23 routine iterates until the correct solution of each equation is achieved. Then the pressure value at each PB (i.e. P_1, P_2, ... , P_N) is the output of the HSL NS23 routine.

Appendix C: A regular structured pore-network generation code

C-1. Introduction

As explained in Chapter 2, there are three approaches that can be followed to generate a pore-network that represents a real porous medium. The first approach is to directly map the porous media, e.g. from a CT-image, while the second method is to construct a representative pore-network using statistical distributions of basic morphologic parameters. The third approach is called the grain-based model and is used to generate a pore-network equivalent to a packing of grains by considering information about the grain diameters and locations. All these approaches may have some uncertainties due to the simplification done while converting from the irregular complex shape of a porous medium to its equivalent simplified pore-network or due to the difficulties in determining the location of grains. Therefore, to initially test the performance of the proposed models, a regular structured medium (Figure 1C) with known grain locations and dimensions can be used, experimentally and numerically, to avoid the effect of these uncertainties on the simulation results.

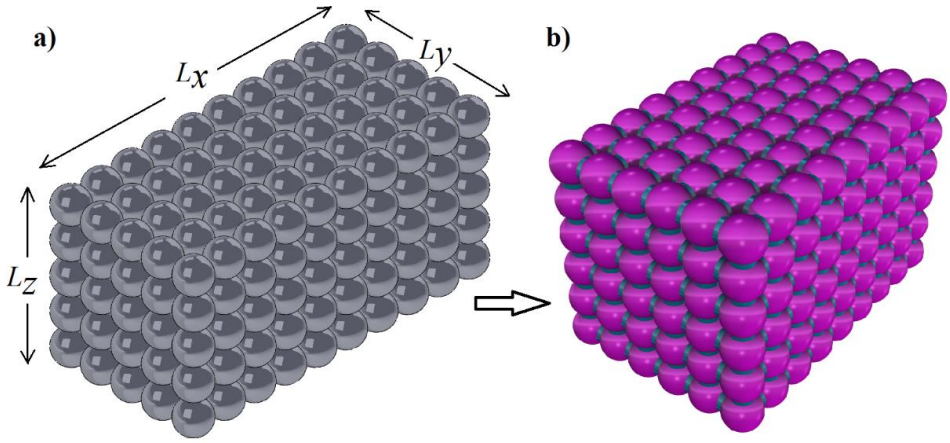

Figure 1C a) Regularly structured uniform packed spheres and b) its equivalent pore-network.

C-2. Method

The following method explains the procedures used to generate a pore-network equivalent to regularly structured uniform spherical beads, as

shown in Figure 1C. All pore bodies are assigned a spherical shape and all pore throats are assumed to have a cylindrical shape.

- The required inputs are the beads uniform diameter (D_{beads}), the external dimensions of the porous medium (L_x, L_y and L_z) and the number of pore bodies (N_x, N_y and N_z) in *x*, *y*, and *z* directions.
- The total number of pore bodies (N_{PB}) is equal to $N_x \times N_y \times N_z$, and each pore body is assigned an index from 1 to N_{PB}.
- The total number of pore throats (N_{PTh}) is equal to

$$N_{PTh} = 3N_x \times N_y \times N_z - N_x \times N_z - N_x \times N_y + N_y \times N_z \qquad 9.14$$

The above equation comes from the fact that the pore-network can be constructed by repeating a unit composed of one pore body and three pore throats perpendicular on each other's (Figure 2C) in the *x*, *y*, and *z* directions. Then, the excess pore throats at the boundaries are removed and additional pore throats are added at the inlet boundary.

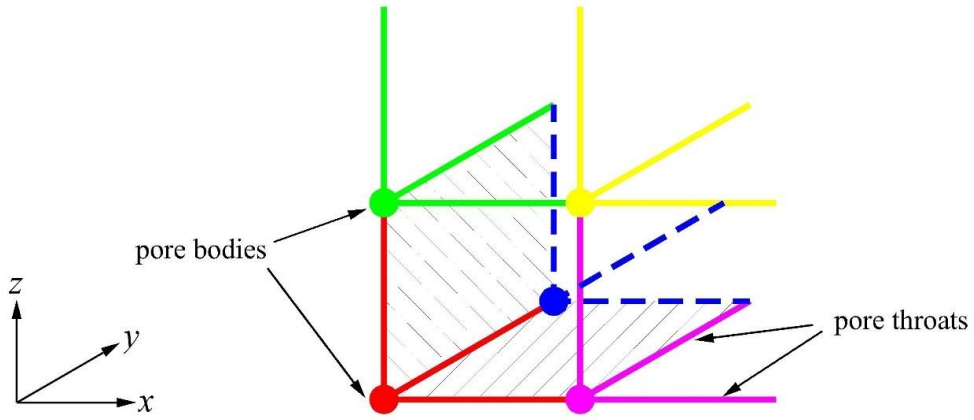

Figure 2C The basic elements of a regular structured pore-network, each colour represents a unit composed of one pore body and three pore throats perpendicular on each other's.

- The first pore body is assigned (0, 0, 0) coordinates, then the remaining pore body coordinates are assigned by adding a step equal to D_{beads} in the *x*, *y*, and *z* directions based on the number of pore bodies in *x*, *y*, and *z* direction.

- Each pore throat is assigned an index from 1 to N_{PTh}, and the *x*, *y*, and *z* coordinates of each pore throat are calculated at the middle of its centreline.
- Based on pore body and pore throat coordinates, the connectivity of the whole pore-network is assigned, i.e. each pore throat, except the pore throats located at the inlet and outlet boundaries, is connected to the nearest two pore bodies.
- Then, the coordination number of each pore body is calculated and checked not to exceed 6, which is the maximum coordination number for any pore body in the proposed regular structured pore-network.
- The pore body and pore throat geometries are calculated according to Section C-3 below.

C-3. Pore body and pore throat geometries

Regularly packed uniform spheres with a constant diameter (D_{beads}) have the advantage of having known geometries, i.e. known pore body inscribed radii, pore throat inscribed radii, pore body coordination numbers and equal distances between each two neighbouring pore bodies. Following Kruyer (1958), Al-Raoush et al. (2003), Gao et al. (2012) and Bryant and Blunt (1992), the following methodology is adapted to define the pore throat and pore body geometries. The medium is divided into cells, each cell is a cube that has eight corners located at the eight nearest sphere centres (Figure 3C-a, b). The interior of the cell represents a pore body while the six faces of each cell represent pore throats connected to the pore body located inside the cell, i.e. the coordination number of each pore body is equal to six, except those pore bodies at the boundaries.

The volume of a pore body space can be calculated as the cell volume minus the volumes of the sphere segments contained within it. If the pore body volume is represented by a sphere, then its radius $\left(r_{\mathrm{PB,e}}\right)$ is equal to 0.485 D_{beads} following Equation 9.15.

$$\text{Pore body volume} = \frac{4}{3}\pi\left(r_{\mathrm{PB,e}}\right)^3 = (D_{\mathrm{beads}})^3 - \frac{4}{3}\pi\left(\frac{D_{\mathrm{beads}}}{2}\right)^3 \qquad 9.15$$

Inside the pore body volume, the radius of the inscribed sphere $\left(r_{\mathrm{PB,c}}\right)$ that just touches the external surface of the beads is given as

$$r_{\mathrm{PB,c}} = \frac{\sqrt{3\left(D_{beads}{}^{2}\right)}}{2} - \frac{D_{\mathrm{beads}}}{2} = 0.366\, D_{\mathrm{beads}} \quad (9.16)$$

For flow simulation and for estimating the medium parameters, the pore body effective radius $\left(r_{\mathrm{PB,eff}}\right)$ is used, which can be calculated using Equation 9.17.

$$r_{\mathrm{PB,eff}} = \frac{\left(r_{\mathrm{PB,c}} + r_{\mathrm{PB,e}}\right)}{2} = 0.4255\, D_{\mathrm{beads}} \quad (9.17)$$

For each pore throat, the radius of the maximum inscribed circle within the cell face (r_{c}) is equal to 0.207 D_{beads} (Figure 3C-c), while the radius of the circle that has an area equivalent to the cell face area minus the area of sphere segments contained within it (the red area in Figure 3C-d), r_e, is 0.261 D_{beads} according to Equation 9.18.

$$\text{Pore throat equivalent area} = \pi\,(r_e)^2 = (D_{\mathrm{beads}})^2 - \pi\left(\frac{D_{\mathrm{beads}}}{2}\right)^2 \quad (9.18)$$

For flow simulation and for estimating the medium parameters, the pore throat effective radius (r_{eff}) is used, which is calculated using Equation 9.19.

$$r_{\mathrm{eff}} = \frac{(r_{\mathrm{c}} + r_{\mathrm{e}})}{2} = 0.234\, D_{\mathrm{beads}} \quad (9.19)$$

The pore throat and pore body lengths are assigned from the geometry of Figure 3C-e and they are equal to 0.289 D_{beads} and 0.355 D_{beads}, respectively.

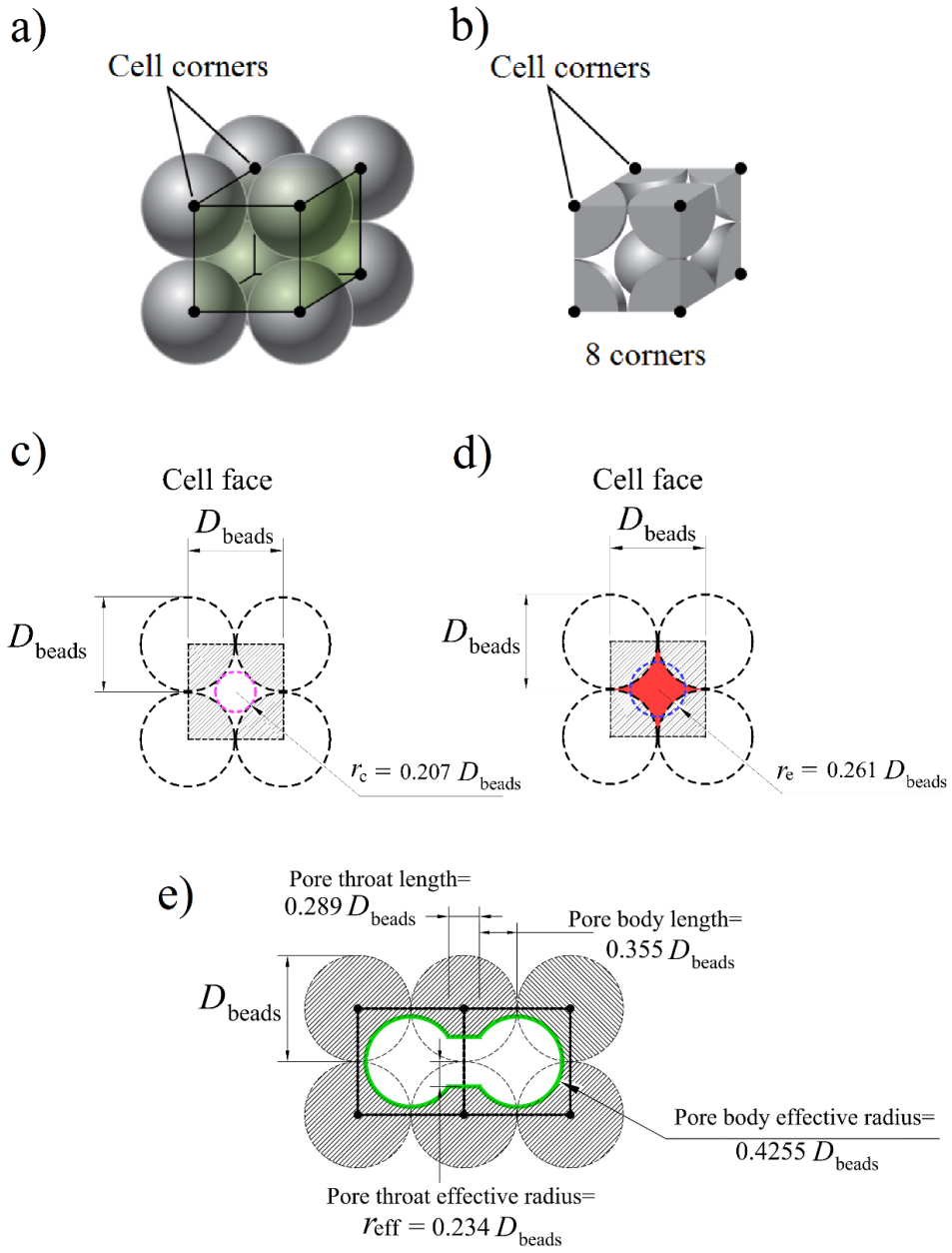

Figure 3C a) An eight corners cell, the centre of the cell represents a void space (pore body) and **b)** the cell faces represent six narrower restrictions (pore throats), the vertices of the cells are located at the sphere centres. **c)** One cell face with the radius of the maximum inscribed circle inside the cell face (r_c). **d)** One cell face with the radius of the circle (r_e) whose area is equal to the void area (shaded in red). **e)** The geometry of one pore throat and the connected two pore bodies (shown in green). Hint: **a)** and **b)** are obtained from: (https://commons.wikimedia.org/wiki/File:CNX_Chem_10_06_SimpleCub3.png).

Appendix D: Details of the proposed pore-network model used to simulate solute transport for the Darcy and Non-Darcy flow regimes

D-1. Code flow chart

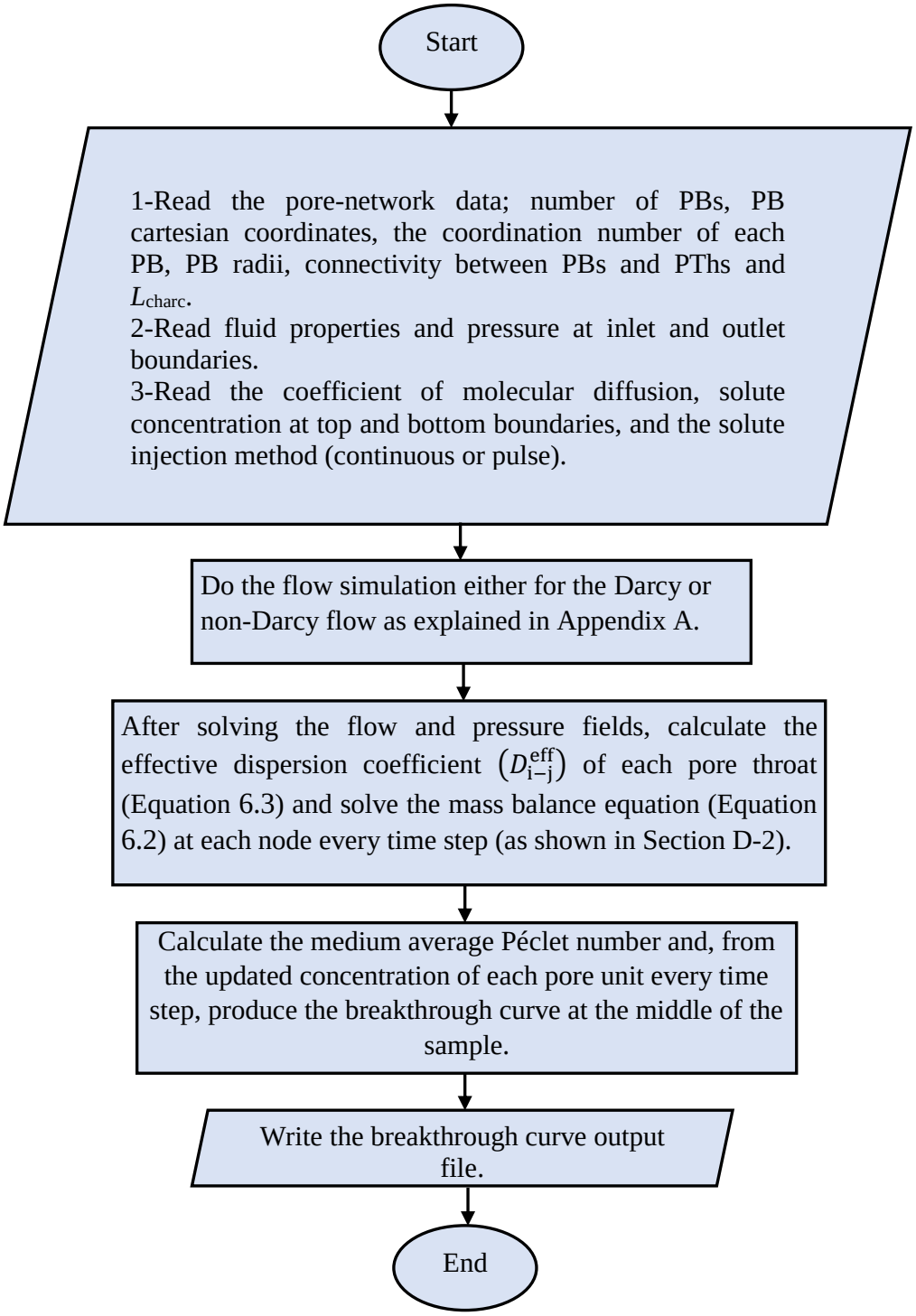

D-2. Solving the mass balance (Equation 6.2) explicitly at each time step

Assuming the following simple pore-network:

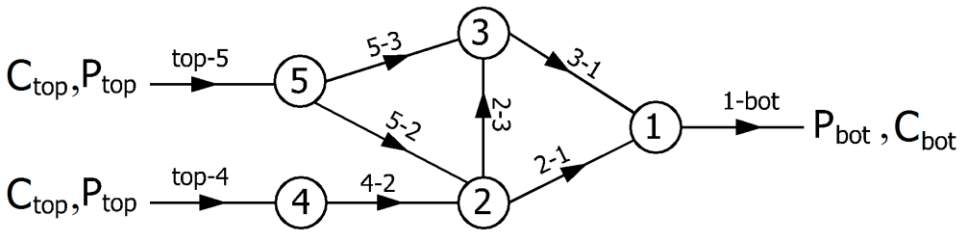

Figure 1D A simple example of a pore-network and its boundary conditions.

Applying Equation 5.7 at each pore-unit (pore body) in Figure 1D, the following system of equations can be obtained:

At node 1:

$$C_1(t+dt) = C_1(t) + \frac{dt}{V_1}\Big[q_{3-1}C_3(t) + q_{2-1}C_2(t) - q_{1-\text{bot}}C_1(t) + a_{3-1}D^{\text{eff}}_{3-1}\frac{C_3(t)-C_1(t)}{L_{3-1}} + a_{2-1}D^{\text{eff}}_{2-1}\frac{C_2(t)-C_1(t)}{L_{2-1}} + a_{1-\text{bot}}D^{\text{eff}}_{1-\text{bot}}\frac{C_{\text{bot}}(t)-C_1(t)}{L_{1-\text{bot}}}\Big] \quad 9.20$$

At node 2:

$$C_2(t+dt) = C_2(t) + \frac{dt}{V_2}\Big[q_{5-2}C_5(t) + q_{4-2}C_4(t) - q_{2-3}C_2(t) - q_{2-1}C_2(t) + a_{5-2}D^{\text{eff}}_{5-2}\frac{C_5(t)-C_2(t)}{L_{5-2}} + a_{4-2}D^{\text{eff}}_{4-2}\frac{C_4(t)-C_2(t)}{L_{4-2}} + a_{2-3}D^{\text{eff}}_{2-3}\frac{C_3(t)-C_2(t)}{L_{2-3}} + a_{2-1}D^{\text{eff}}_{2-1}\frac{C_1(t)-C_2(t)}{L_{2-1}}\Big] \quad 9.21$$

At node 3:

$$C_3(t+dt) = C_3(t) + \frac{dt}{V_3}\Big[q_{5-3}C_5(t) + q_{2-3}C_2(t) - q_{3-1}C_3(t) + a_{5-3}D^{\text{eff}}_{5-3}\frac{C_5(t)-C_3(t)}{L_{5-3}} + a_{2-3}D^{\text{eff}}_{2-3}\frac{C_2(t)-C_3(t)}{L_{2-3}} + a_{3-1}D^{\text{eff}}_{3-1}\frac{C_1(t)-C_3(t)}{L_{3-1}}\Big] \quad 9.22$$

At node 4:

$$C_4(t+dt) = C_4(t) + \frac{dt}{V_4}\Big[q_{\text{top}-4}C_{\text{top}} - q_{4-2}C_4(t) + a_{\text{top}-4}D^{eff}_{\text{top}-4}\frac{C_{\text{top}}-C_4(t)}{L_{\text{top}-4}} + a_{4-2}D^{\text{eff}}_{4-2}\frac{C_2(t)-C_4(t)}{L_{4-2}}\Big] \quad 9.23$$

At node 5:

$$C_5(t+dt) = C_5(t) + \frac{dt}{V_5}\Big[q_{\text{top}-5}C_{\text{top}} - q_{5-2}C_5(t) - q_{5-3}C_5(t) + a_{top-5}D^{\text{eff}}_{\text{top}-5}\frac{C_{\text{top}}-C_5(t)}{L_{\text{top}-5}} + a_{5-2}D^{\text{eff}}_{5-2}\frac{C_2(t)-C_5(t)}{L_{5-2}} + a_{5-3}D^{\text{eff}}_{5-3}\frac{C_3(t)-C_5(t)}{L_{5-3}}\Big] \quad 9.24$$

The above system of equations is solved explicitly at each time step to evaluate the concentration values in each pore-unit. The simulation continues using an iterative process until the medium is fully saturated with the solute, i.e. the concentration is equal to C_{top} at every pore-unit in the pore-network.